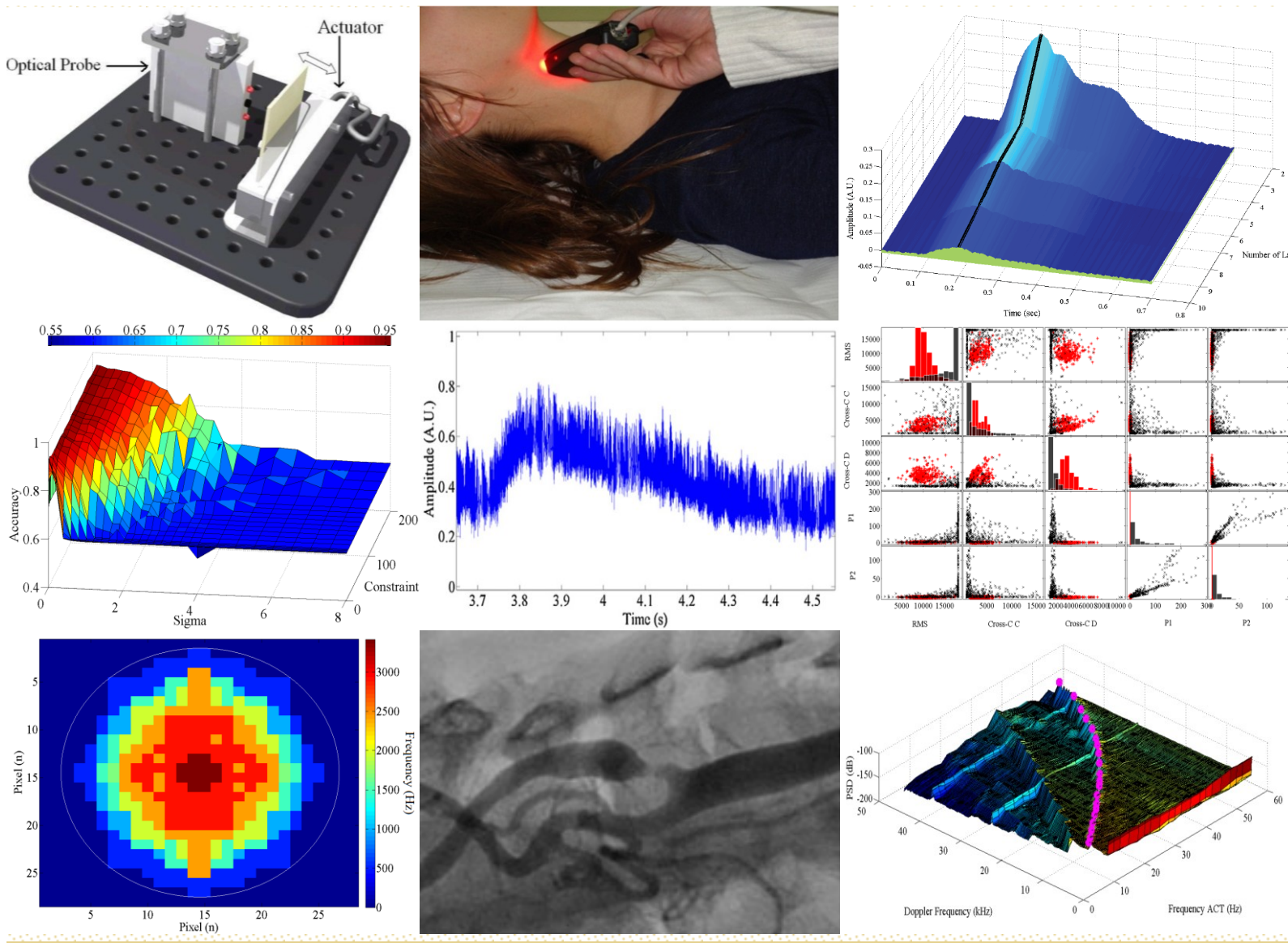

Tânia Maria Pereira Lopes

Non-Invasive Hemodynamic Parameters Assessment using Optoelectronic Devices

Thesis submitted to the University of Coimbra in fulfillment of the requirements for the degree of Doctor of Philosophy (PhD) in Biomedical Engineering under the scientific supervision of PhD João Manuel Rendeiro Cardoso and Full Professor Carlos Manuel Alexandre Correia

2014

· U C ·

UNIVERSIDADE DE COIMBRA

University of Coimbra

Faculty of Sciences and Technology

Department of Physics

Non-Invasive Hemodynamic Paramenters Assessment using Optoelectronic Devices

Thesis submitted to the University of Coimbra in fulfillment of the requirements for the degree of Doctor of Philosophy in Biomedical Engineering

Scientific Supervisor:
PhD João Manuel Rendeiro Cardoso

Co-Supervisor:
Full Professor Carlos Manuel Bolota Alexandre Correia

Tânia Maria Pereira

2014

This work was supported by Fundação para a Ciência e a Tecnologia, in the form of the grant SFRH / BD / 79334 / 2011.

Para a minha Mãe.
Poderiam tirar-me tudo, "mas nunca o teu riso,
porque então morreria."
(Pablo Neruda)

Acknowledgements

Antes de mais gostaria de agradecer o apoio logístico e financeiro do Laboratório de Electrónica e Instrumentação (LEI) do Departamento de Física da Universidade de Coimbra bem como da Fundação para a Ciência e a Tecnologia (bolsa de doutoramento SFRH / BD / 79334 / 2011). Ao meu país, Portugal, por me permitir o acesso a toda a formação que representou um período de 22 anos, que espero não ter terminado aqui, mas que será definitivamente o grande lançamento para a minha vida.

Ao Professor Carlos Correia pela orientação científica e permanente disponibilidade para discutir e ultrapassar os diversos obstáculos, e pelas inúmeras sugestões e ideias indispensáveis ao desenvolvimento deste trabalho.

Ao Doutor João Cardoso pela orientação científica e tecnológica, por todas as conversas científicas que representaram grandes degraus do meu crescimento académico e pessoal e por ter tornado todo este percurso um desafio estimulante e de grande exigência.

Ao Doutor Telmo Pereira e ao Doutor Helder Santos agradeço a transmissão de conhecimentos da prática clínica, a incansável disponibilidade e todo o apoio logístico, fundamentais para o desenvolvimento deste trabalho.

À minha equipa, família do LEI, Manuel, Tatiana, Tobias, Pedro e Inês, que tornaram os meus dias neste projecto tão alegres e interessantes, companheiros que tanto contribuíram para o meu crescimento e desenvolvimento deste trabalho, e alguns dos quais vou guardar para sempre na minha vida e no meu coração.

À minha família que fez de mim tudo aquilo que sou hoje, esculpiu em mim todas as características que agora reconheço e sem as quais não teria chegado aqui. Em especial à minha Mãe, refúgio do mundo, sol da minha vida, devo-lhe tudo, todos os dias de felicidade e todas as conquistas do meu ser. À minha irmã agradeço o exercício de paciência que todos os dias me obriga a fazer, e a animação e companheirismo que preenchem os meus dias. À minha tia Maria, por todos os conselhos e ensinamentos que me transmitiu com toda a doçura e sabedoria do seu coração, desejando que nunca desista de o fazer.

Às minhas pretinhas, as companheiras de sempre. À minha Doroti, amorzinho do meu coração, pela companhia de todos os serões de trabalho, por derreter o meu coração com os seus olhitos verdes que falam directamente com a minha alma, por todos os mimos e o arrependimento por todos os que ficaram por dar, que nunca poderei recompensar e que me faltarão para o resto da minha vida.

Aos meus amigos, que fizeram de mim a "Sultona", que aturaram as minhas manias e que me permitem crescer em opinião nas conversas que ocupam os nossos serões semanais e saborear a juventude nas nossas aventuras. Ao Hugo pelo oportunidade de crescimento que representou na minha vida e por me mostrar o mundo com a objectividade necessária.

Ao Beto, o filósofo do meu mundo, o meu companheiro de todos os tempos, de todas as histórias, de toda a minha vida. Obrigada por estares sempre a meu lado, porque ser amigo não significa compreender sempre mas sim estar para além do que não se compreende.

À minha fada Goreti, por me ter salvo nos dias mais negros, por desmontar os meus monstros em peças pequenas para que depois eu possa seguir em frente na minha vida. Toda a gente devia ter uma amiga psicóloga na sua vida, eu tive uma com poderes de fada!

Ao Francisco, que trouxe a primavera à minha vida, enchendo de cor e doçura os meus dias durante este percurso, que varreu o cinzento e me fez acreditar que a felicidade existe e é infinita.

"Por fim, a todos aqueles que não enuncio mas que com diligência, tranquilidade e subtileza configuraram os espaços e os tempos no meu crescimento científico e pessoal."

Dezembro 2013

Revisão: Maio 2014

Tânia Pereira

Abstract

Non-Invasive Hemodynamic Parameters Assessment using Optoelectronic Devices

The world wide incidence of cardiovascular diseases (CVDs), has spurred the research efforts targeting new solutions that may be able to perform an early detection of the pathological processes associated with these diseases. Special emphasis has been given to the methods that allow the monitoring of the blood pressure and the arterial pulse waveform, thus providing a more precise tool to complement the diagnosis process based on a multi-parameter assessment approach. From the analysis of arterial pulse pressure waveform features, and its propagation velocity, important clinical parameters can be extracted in order to evaluate the CVD risk, the vascular adaptation and the therapeutic efficacy. The use of multiple parameters allows to minimize the error when compared to the approach where a subject is classified solely based on a single parameter. Emerging trends in cardiovascular monitoring are moving away from invasive and costly technologies towards non-invasive and low-cost solutions. In this sense, optical solutions represent a great advantage due to the immense technological progresses observed in the recent decades. The truly non-contact nature of optical techniques allows measurements without distortion in the shape of the pulse curve, which is one of the main limitations of the current commercial devices used in hemodynamic parameters assessment. The main objective of this work consists in demonstrating that with an optical system it is possible to acquire the arterial pulse waveform with a configuration that allows the local pulse wave velocity (PWV) measurement and the determination of the most important clinical parameters using dedicated algorithms, without physical contact with the skin of the patient. Four prototypes were developed: three based in non-coherent light and one with coherent light. All the developed optical probes have a common design structure. They include two identical photodetectors placed 2 cm apart from each other to guarantee accurate determination of local pulse transit time. Relatively to the non-coherent light probes three different probes base on photodetectors were tested: an avalanche photodiode, a planar photodiode and a lateral effect photodiode (LEP). The optical system components (probe prototypes and acquisition box) were designed to meet specific requirements that allow the clinical use, such as portability, compact size and low weight, low cost, limited power consumption, ergonomics and easy user-interface in order to be considered as an interesting solution for commercial purposes. The *in vivo* tests allowed the selection of the best algorithm and probe combination to determine PWV: cross-correlation algorithm and the probe with planar photodiodes demonstrated to be the most efficient. This system showed good reproducibility, as evaluated by both inter-operator and intra-operator analysis. A large study was performed

in 131 young subjects, obtaining a mean value for PWV of 3.33 $\pm$ 0.72 ms^{-1}, thus confirming its significant increase with age. A comparative test between the distension waveform measured with the optical probe at the carotid artery and the invasive profile of the pulse pressure acquired by an intra arterial catheter showed a strong correlation (mean value of 0.958), and validates the ability of this non-invasive device to estimate the arterial pulse waveform. Also a coherent light probe was developed and tested using several processing techniques based on the short time Fourier transform and empirical mode decomposition algorithm. This approach demonstrated the ability to determine the main feature points in the waveform with low error in the pulse transit time determination (less than 5ms). An alternative configuration for the Doppler effect-based probe was tested, using a photodetector with a larger area in order to obtain the self-mixing effect outside the laser cavity. This feature opened the possibility to improve the quality of the signal which may foresee potential future biomedical applications. Globally, the results obtained with the developed methodologies (prototypes and associated algorithmic tools) proved that it is possible to measure the arterial pulse waveform in the carotid artery, to determine several clinical parameters and assess the cardiovascular condition with optical technology.

Keywords: biomedical instrumentation; optical system; arterial pulse waveform, cardiovascular diseases

Resumo

Avaliação Não-invasiva de Parâmetros Hemodinâmicos usando Dispositivos Optoeletronica

A grande incidência das doenças cardiovasculares no mundo estimulou a procura de novas soluções que permitam a deteção precoce de processos patológicos associados a este tipo de doenças. Especial ênfase foi dada a métodos que permitem a monitorização da pressão arterial e da forma de onda de pressão arterial, que fornecem uma ferramenta precisa que complementa o diagnóstico baseado em múltiplos parâmetros. Da análise das características da forma de onda da pressão arterial, e da sua velocidade de propagação, podem ser extraídas importantes parâmetros clínicos de modo a avaliar o risco cardiovascular, a adaptação vascular e a eficácia terapêutica. O uso de múltiplos parâmetros permite minimizar erros na estimação de um dos parâmetros. As soluções emergentes para a monitorização cardiovascular têm-se afastado de tecnologias invasivas e caras para soluções não invasivas e sem contacto. Neste sentido, os sistemas ópticos apresentam uma grande vantagem devido ao grande progresso tecnológico sofrido nas últimas décadas. A natureza de não contacto desta tecnologia permite a medição sem distorção da forma da onda arterial ultrapassando as limitações dos aparelhos comerciais usados para este tipo de avaliação. O principal objetivo deste trabalho consistia em demonstrar que é possível adquirir através do uso de uma metodologia óptica, a forma da onda de pressão arterial sem contacto, com uma configuração que permite medir a velocidade onda de pulso (VOP) local e determinar os principais parâmetros usando algoritmos dedicados. Foram desenvolvidos quatro protótipos: três baseados em luz não-coerente e um em luz coerente. As sondas foram desenvolvidas usando uma configuração comum, composta por dois fotodetectores distanciados de 2 cm, o que garante a deteção da onda de pulso em dois pontos distintos e permite uma determinação rigorosa do tempo de trânsito. Nas sondas de luz não-coerente foram testados três fotodetectores: fotodíodos de avalanche, fotodíodos planares, e fotodíodos de efeito lateral (LEP). Os componentes do sistema óptico (protótipos das sondas e caixa de aquisição) foram desenhados com as características físicas que permitem o uso clínico, como a portabilidade, o tamanho compacto, leves, de baixo consumo e com materiais de baixo custo, ergonómicas para o operador e confortáveis para o paciente, de modo a serem consideradas uma solução interessante para a comercialização. Os testes *in vivo* permitiram a seleção da melhor combinação sonda/algoritmo para a determinação da PWV, usando o método da correlação e a sonda baseada em fotodíodos planares que demonstrou ser mais eficiente para

a aquisição de sinais em humanos. O sistema óptico desenvolvido mostrou boa reprodutibilidade na avaliação inter e intra-operador. Um estudo alargado foi desenvolvido em 131 sujeitos jovens, com um valor médio PWV de $3.33 \pm 0.72\ ms^{-1}$ confirmando o seu aumento com a idade. O teste comparativo entre a onda de distensão medida com o sistema óptico na carótida e o perfil da onda de pressão adquirida invasivamente por um cateter intra-arterial mostrou uma grande correlação entre as duas ondas (valor médio de 0.958), validando a capacidade das sondas ópticas para estimar a forma da onda de pulso de modo não-invasivo e sem contacto. A sonda óptica baseada em luz coerente foi testada em combinação com algoritmos de processamento de sinal baseados nos métodos short time Fourier transform e empirical mode decomposition, demonstrando ser capaz de determinar os pontos característicos da forma de onda com baixo erro (menor que 5ms). Uma configuração alternativa foi testada usando um fotodetector com uma maior área que permitiu obter o efeito de self-mixing fora da cavidade laser. Esta característica abriu a possibilidade de construir uma nova sonda adaptada a esta nova técnica de modo a melhorar a qualidade do sinal e permitir uma aplicação biomédica. Globalmente, os resultados obtidos para a metodologias desenvolvidas (protótipos e ferramentas de processamento de sinal associados) mostraram ser possível de medir a onda de pulso arterial na carótida, para determinar vários parâmetros clínicos e avaliar a condição cardiovascular.

Keywords: instrumentação biomédica; sistemas ópticos; onda de pulso arterial; doenças cardiovasculares

List of Original Papers

This thesis presents the work published in the following fourteen papers:

I T. Pereira, M. Cabeleira, P. Matos, E. Borges, V. Almeida, J. Cardoso, C. Correia, "Optical methods for local pulse wave velocity". 4th International Joint Conference on Biomedical Engineering Systems and Technologies (BIOSIGNALS 2011). Rome, Italy.

II T. Pereira, T. Oliveira, M. Cabeleira, P. Matos, H. C. Pereira, V. Almeida, E. Borges, T. S. Pereira, H. Santos, J. Cardoso, C. Correia, "Signal Analysis in a new optical pulse waveform profiler for cardiovascular applications". International conference on signal and image processing and applications, SIPA 2011, 22-24 June, Crete, Greece.

III T. Pereira, T. Oliveira, M. Cabeleira, E. Borges, V. Almeida, J. Cardoso, C. Correia, "Visible and infrared optical probes for hemodynamic parameters assessment", IEEE Sensors 2011, 28-31 October, Limerick, Ireland.

IV T. Pereira, M. Cabeleira, P. Matos, E. Borges, H.C. Pereira, V. Almeida, J. Cardoso, C. Correia, "Non-invasive pulse wave velocity assessment using optical methods", Communications in Compute and Information Science (CCIS 273), pp. 246–257, 2012.

V T. Pereira, I. Santos, T. Oliveira, P. Vaz, T. S. Pereira, H. Santos, H. Pereira, V. Almeida,C. Correia, J. Cardoso, "Local PWV and other Hemodynamic Parameters Assessment: Validation of a New Optical Technique in an Healthy Population". 6th International Joint Conference on Biomedical Engineering Systems and Technologies (BIOSIGNALS 2013). Barcelona, Spain 11-14 February 2013.

VI T. Pereira, I. Santos, T. Oliveira, P. Vaz, T. Correia, H. Pereira, V. Almeida, T. S. Pereira, H. Santos, C. Correia, J. Cardoso, "Characterization of Optical System for Hemodynamic Multi-Parameter Assessment", Cardiovascular Engineering and Technology, Vol. 4, No. 1, March 2013 pp. 87–97.

VII T. Pereira, P. Vaz, I. Santos, T. Oliveira, H. Pereira, V. Almeida, C. Correia, J. Cardoso, "Empirical Mode Decomposition for Self-Mixing Doppler Signals of Hemodynamics Optical Probes", Physiol Meas. Vol. 34, No. 3, 2013 March pp. 377-90.

VIII T. Pereira, P. Vaz, I. Santos, T. Oliveira, H. Pereira, V. Almeida, C. Correia, J. Cardoso, "New optical probe approach using mixing effect in planar photodiode for biomedical applications", SPIE Optics + Optoelectronics, Prague, Czech Republic, 15 - 18 April 2013.

IX T. Pereira, T. Oliveira, M. Cabeleira, P. Matos, E. Borges, H.C. Pereira, V. Almeida, C. Correia, J. Cardoso, "Comparison of Low-Cost and Non-Invasive Optical Sensors for Cardiovascular Monitoring", IEEE SENSORS Journal, Vol. 13, No. 5, May 2013 pp. 1434 - 1441.

X T. Pereira, I. Santos, T. Oliveira, P. Vaz, T. S. Pereira, H. Santos, H. Pereira, V. Almeida, J. Cardoso, C. Correia, "Clinical test for validation of a new optical probe for hemodynamic parameters assessment", Communications in Compute and Information Science published by Springer-Verlag (Accepted).

XI T. Pereira, I. Santos, T. S. Pereira, H. Santos, H. Pereira, V. Almeida, C. Correia, J. Cardoso, "Reproducibility of pulse wave analysis and pulse wave velocity in healthy subjects", 7th International Joint Conference on Biomedical Engineering Systems and Technologies (BIOSIGNALS 2014). Angers, France 3-6 March 2014.

XII T. Pereira, M. Sequeira, P. Vaz, A. Tomé, H. Pereira, C. Correia, J. Cardoso, "Sub-Micron Surface Vibration Profiling using Doppler Self-Mixing Techniques", Advances in Optics, Vol. 2014, July 2014.

XIII T. Pereira, I. Santos, T. Oliveira, P. Vaz, T. S. Pereira, H. Santos, H. Pereira, C. Correia, J. Cardoso, "Pulse pressure waveform estimation using distension profiling with contactless optical probe", Medical Engineering and Physics Journal 36 (2014) 1515–1520.

XIV T. Pereira, T. S. Pereira, H. Santos, C. Correia, J. Cardoso, "Arterial Pulse Pressure Waveform Monitoring by Novel Optical Probe", International Journal of Cardiology 179 (2015) 95–96.

The main subject in all of these papers is the optical probes developed to measurement the arterial pulse wave profile at the carotid site for cardiovascular assessment. Paper I and IV discuss the multiple methods for pulse transit time determination for optical signals. Paper II focuses in a comparison test that was carried out between an ultrasound image system as source of reference data, and the optical probes.

Paper III and IX present probes with different light wavelength capable of crossing the epidermis and fat structures that could eventually exist.

Paper V and X establish the reference values for several hemodynamic parameters by the optical system.

Paper VI discusses the results obtained with optical probes in a small group of volunteers over 4 weeks and the consistency of the hemodynamic parameters determined using dedicated algorithms.

Paper VII and VIII focuses in self-mixing signals from the probe based in coherent light, the specific algorithms and the possible advantage in a new approach.

Paper XI presents a reproducibility study that was performed in 13 volunteers by two trained operators, covering inter-operator and intra-operator variability analysis.

Paper XII demonstrates the feasibility of the probe based on self-mixing technique, to accurately measure a sub-micron displacements.

Paper XIII presents a comparison between signals form non-invasive optical probe that measures carotid artery distension profiles and the waveforms of the pulse pressure acquired by intra-arterial catheter invasive measurement in the ascending aorta. This study validates the capability of acquiring the arterial pulse waveform with a non-invasive method, using a non-contact optical probe at the carotid site with residual differences from the aortic invasive measurements.

Paper XIV evidences the optical probe as an efficient tool for the non-invasive diagnostic and monitoring the stenosis events.

Contents

List of Figures

List of Tables

Acronyms

A	Accuracy
ACT	Actuator
AD	Area during Diastole
AIx	Augmentation Index
APD	Avalanche Photodiode
APW	Arterial Pulse Waveform
AS	Area during Systole
AU	Arbitrary Units
AUC	Area Under the Curve
AWG	Arbitrary Waveform Generator
bDBP	brachial Diastolic Blood Pressure
bMAP	brachial Mean Arterial Pressure
BP	Blood Pressure
bSBP	brachial Systolic Blood Pressure
cDBP	carotid Diastolic Blood Pressure
cMAP	carotid Mean Arterial Pressure
CoefV	Coefficients of Variation
cSBP	carotid Systolic Blood Pressure
CV	Cardiovascular
CVD	Cardiovascular Diseases
DAQ	Data Acquisition Box
DAS	Data Acquisition System
DBMS	Database Management System

DBP	Diastolic Blood Pressure
DN	Dicrotic Notch
DOB	Date of Birth
DP	Dicrotic Peak
EEG	Electroencephalogram
EC	Electronic Circuitry
ECG	Electrocardiogram
EIS	Electrical Impedance Spectroscopy
EMD	Empirical Mode Decomposition
ER	Entity-relationship
ETI	Ejection Time Index
FM	Fixed Mirror
F-M	F-Measure
FN	False Negatives
FP	False Positive
HR	Heart Rate
HV Amp	High Voltage Linear Power Driver
ICC	Intraclass Correlation Coefficients
ICNIRP	International Commission on Non-Ionizing Protection
IMF	Intrinsic Mode Functions
IR	Infrared
KNN	K-Nearest Neighbors
LA	Limits of Agreement
LD	Laser-diode
LDV	Laser Doppler Vibrometer
LED	Light-Emitting Diode
LEP	Lateral Effect Photodiode
LVET	Left Ventricular Ejection Time
MAP	Mean Arterial Pressure
MM	Moving Mirror
MPE	Maximum Permissible Exposure

MRI Magnetic Resonance Image

MS Mechanical Structure

OCT Optical Coherence Tomography

PCA Principal Component Analysis

PCB Printed Circuit Board

PD Photodiode

PDF Probability Density Function

PP Pulse Pressure

PPD Planar Photodiode

PPG Photoplethysmography

PSD Power Spectral Density

PZ Piezoelectric

PTT Pulse Transit Time

PWA Pulse Wave Analysis

PWV Pulse Wave Velocity

RMS Root Mean Square

RMSE Root Mean Square Error

ROI Region-of-interest

RC Regularisation Constant

RP Reflection Point

SBP Systolic Blood Pressure

SD Standard Deviation

SDu Systolic Duration

Se Sensitivity

SEM Standard Error of Measurement

SEVR Subendocardial Viability Ratio

SNR Signal-to-Noise Ratio

SP Systolic Peak

Sp Specificity

SQL Structured Query Language

STFT Short-Time Fourier Transform

SVM Support Vector Machine

SVM RFE Support Vector Machine Recursive Feature Elimination

TD Total Duration

TN True Negatives

TP True Positives

US Ultrasound

USB Universal Serial Bus

WHO World Health Organization

WSB Wedged Plate Beamsplitter

Symbols

C	Compliance
D	Distensibility
E	Elastic modulus
E_{laser}	Laser irradiance
L	Length of laser cavity
L_{ext}	Length of external cavity
M_1	Laser mirror located at the backside of laser cavity
M_2	Laser mirror located at light output
M_{ext}	External target
P	Pressure
c	Speed of light
dP/dt_{max}	Maximum rate of pressure change
f	Frequency
f'	Doppler frequency
g	Waveforms from one photodetector
g_c	Threshold gain for compound cavity in external feedback
g_{th}	Threshold gain without external feedback
h	Arterial thickness
h_n	Residue of level n
k_{ext}	Coupling coefficient
r_2	Amplitude reflection coefficient of effective mirror
r_{2s}	Amplitude reflection coefficient of laser mirror M2
r_{2ext}	Amplitude reflection coefficient of external target
v	Velocity
s	Waveforms from another photodetector
t	Time
$X(\tau, \psi)$	Fourier transform of x(t)
Δt	Time delay
Δx	Distance between the two locations
$\Psi(t)$	Window function
θ	Phase angle
λ	Wavelength
μ_e	Effective refractive index of laser cavity
ρ	Blood density
σ	Width of the gaussian function
τ	Time parameter
τ_{ext}	Round trip delay back and forth through the external cavity
ψ	Frequency parameter
ω	Angular frequency

Chapter 1

Introduction

The present chapter delineates the motivation of the performed work plan and describes the outlined objectives pursued during this study. The chapter closes with a description of the global structure of the thesis.

1.1 Motivation

Cardiovascular Diseases (CVD) are responsible for approximately 30% of global deaths and for the next decades an increase is expected, contrary to all the other major diseases that are expected to experience a decrease rate [1].

Over the last sixty years, there has been an extensive effort to find new techniques that allow an early detection of pathological processes [2]. According to World Health Organization (WHO), such tools are essential to decrease the incidence of CVD [3]. These facts illustrate the importance of focusing on the development of new methods and devices for everyday practical use and patient monitoring.

Blood pressure and the arterial pulse waveform have long been known as fundamental medical signals [4]. Measurement of the structural and functional properties of the arterial segment yields a host of indexes for the assessment of cardiovascular risk, vascular adaptation, and therapeutic efficacy [5]. Numerous non-invasive techniques have been developed to detect cardiovascular pulsation and blood pressure. The first methods developed were the oscillometric methods, stethoscopes, phonocardiograms, and manual palpation of superficial arteries, which were non-suitable for continuous monitoring. Emerging trends in cardiovascular monitoring are moving away from more invasive technologies to portable and non-invasive solutions. An optical method for non-contact measurement of skin surface vibrations with the distension of the carotid artery is promising nowadays [6].

Optical sensors represent greatest advantages in biomedical diagnostics compared to other types of sensors. The most important advantage of optical methods is the noncontact nature that allows the measurement without distortions in the shape of the pulse curve. The optical methods are safe to use, since there is not direct electrical contact between the measurement device and the measured person and also if the wavelength of light used is safe to be directly applied on human skin. On the other hand, the optical sensors allow the construction of systems based on low-cost components, which represents an important feature for an extensive use in the clinical routine.

1.2 Objectives

The main objective of this work was to demonstrate that with an optical system is possible to acquire the arterial pulse waveform, without contact with the skin of the patient, and determine the most important clinical parameters using dedicated algorithms. The major motivation of this work was to find a non-contact technique that allows to overcome the limitations of commercial devices used in this type of hemodynamic parameters assessment.

The optical system should meet some requirements that able the clinical use, such as portable, compact size, lightweight and it was designed to have low power consumption and low cost materials, to be ergonomic for the operator and user-friendly for the patient, in order to be considered an interesting solution for commercial purposes.

The algorithms implemented should make possible the Pulse Wave Analysis (PWA) and Pulse Wave Velocity (PWV) determination. The implemented algorithms should also determine more precisely the diagnosis based on multi-parameters assessment. The determination of several parameters based on the pulse pressure profile enables to overcome errors that are implicit when only one parameter is analyzed.

The probe's configuration was designed to make possible a local measurement of PWV, which can detect earlier atherosclerosis phenomena and gives a more rigorous measurement of PWV parameter in comparison with the current commercial devices.

The aim of this thesis was also to test probes based on coherent and non-coherent light, and explore the features of each type of signal. In non-coherent light relevant information is at the amplitude modulation of the signal, while in the coherent light probes the information is in the frequency modulation. This fact has required specific algorithms for signal processing.

For obese patients, it is difficult the assessment of pulse pressure waveform, therefore it was intended to test different light wavelengths capable of crossing the superficial layers of skin and fat tissue structures. Specifically for these patients were created different specialized probes and the results obtained from probes with visible light were compared with the results obtained with infrared probes.

To validate and characterize the developed optical probes and algorithms, several protocols and experimental benches were made. Some of the experimental benches were performed on a skin model that mimics the behavior and mechanical properties of the carotid distension mechanism.

Bench tests were also performed *in vivo* with the objective to compare the results obtained with the gold-standard devices. The result of the comparison has proven the capability and feasibility of the developed optical probes in the detection of the distension waveform, and determination of PWA and PWV.

1.3 Contents of this work

This dissertation is divided in eight chapters. Chapter 2 introduces the global health problem that cardiovascular diseases represents. The most important established risk factors are identified, and the correlation of the pulse pressure profile and pulse wave velocity with the main risk factors are analyzed. In this chapter, a detailed overview of studies performed on PWV based in regional or local assessment is presented. The commercial solutions are presented, their working principles exposed and the advantages and limitations of each method are discussed. It is presented also a summary of the current prototypes for CVD assessment.

Chapter 3 describes the developed optical system, the physical working principles and respective electronic circuits. The acquisition box is an important module of the entire work as it allows to digitize the signals from the four prototypes. It is disclosed with specific circuits appropriate for the characteristics of each prototype. Detailed information about software tools developed for signal acquisition, data processing and data organization are available in this chapter.

The algorithms involved in the analysis of the pulse pressure waveforms are presented in Chapter 4. Probes with coherent light and probes with non-coherent light were tested. That originated two different types of signal. The prototypes based in non-coherent light generate signals modulated in amplitude whereas for the prototype based in coherent light the main features are contained in the frequency modulation of the obtained signal. Therefore, different algorithms were implemented according to the type of emitted light. Several algorithms were developed to extract characteristic information from pulse pressure waveform. In particular, two main analyses are presented: for signals with amplitude modulation and for frequency modulation. Relatively to the amplitude modulation a differential method was implemented, which determined zero-crossing of the three first derivatives, and the pulse transit time was determined by time and frequency methods. The Doppler signals require time-frequency analysis to extract most of the physiological important parameters. An algorithm based on the short time Fourier transform and a new method based on Empirical Mode Decomposition (EMD) were used to find the feature points of the pulse waveform.

Further on, the results of the experiments accomplished on the global dataset are presented in Chapter 5 and 6, where the algorithms previously conceived for parameters assessment from the optical signals were tested and evaluated. Several test benches, which were performed to evaluate the optical probes and dedicated algorithms are described in these two chapters. The performance of the optical probes based on non-coherent light is evaluated in Chapter 5, and the results for the probe based on self-mixing effect are presented in Chapter 6.

Chapter 7 presents several studies on a preliminary validation of the optical system devoted to the clinical evaluation. These studies attempted to validate the proposed optical system as a reliable method to assess non-invasively local PWV and PWA parameters in the carotid artery. All studies presented in this chapter were approved by the ethical committee of the Centro Hospitalar e Universitário de Coimbra, EPE Portugal.

Finally, the conclusions of the work and possible future research are discussed in Chapter 8.

Chapter 2

Theoretical Background

This chapter describes the global problems associated to the cardiovascular diseases targeted by the present thesis. The most important risk factors are comprehensively identified and compared. Furthermore, the correlations between the pulse pressure wave profiles and velocities are analyzed. The identification of the risk factors, that account to the accurate diagnostics of cardiovascular system alterations, represent an objective of utmost importance in order to minimize hospitalization costs and to reduce CVD morbidity and mortality rates. Lastly, a detailed analysis of the commercial solutions is presented, as well as, an overview of the currently used prototypes used for CVD assessment.

2.1 Cardiovascular Diseases Incidence

Cardiovascular diseases are a group of disorders that includes several heart diseases and circulatory system, such as coronary heart disease, cerebrovascular disease, peripheral arterial disease, rheumatic heart disease and congenital heart disease [3].

The WHO refers the cardiovascular diseases as the leading death cause worldwide, resulting in a number of annually deceased people from CVD higher than from any other cause [3]. The improvements of diagnostics, treatments, medications, and cirurgical techniques were responsible to a significant decrease in total CVD mortality over the past few decades [3], [7]. Nonetheless, it is estimated that 17 million people died from CVD in 2011, are responsible for approximately 30% of global deaths and an increase is expected for the next decades [1].

The access to effective and equitable health care services, including early detection of pathological processes, is essential to decrease the incidence of CVD. Even though the existence of cost effective and high impact interventions in the daily practice, the WHO emphasizes and prioritizes the necessity to increase the investment in early detection through programmes that aim prevention and control of CVD in an earlier stage. According to WHO, "people at high risk can be identified early in primary care, using simple tools such as specific risk prediction charts. If people are identified early, inexpensive treatment is available to prevent many heart attacks and strokes" [3], [8].

An instantaneous and accurate diagnostic of changes in cardiovascular system and identification of risk factors is of utmost importance to avoid hospitalization and to reduce CVD morbidity and mortality rates. The early detection based in multi-parameters of pathological condition is the key to the patient survival. The European Guidelines on

cardiovascular disease prevention in clinical practice evidence that "More research into prevention of CVD is needed, starting early in life or even during fetal development" [9]. Consequently, there is an ever-increasing need and demand for novel and more efficient diagnostic tools to early detect cardiovascular diseases [3].

Due to the high variability of individual risk, methods that estimate the risk of future CVD events have been developed and applied [10]. Those methods identify relationships between biomedical and behavior variables and future CVD events [11]. Such scores not only stratify individual risk and identify those most likely to benefit from an intervention, but also inform the most cost-effective allocation of preventive therapies [11], [12].

2.1.1 Risk Factors

The most important behavioural risk factors of CVD in western society are well known. Among them, the unhealthy diet, sedentary, smoking habits and chronic ingestion of alcohol are the most common. Behavioural risk factors are responsible for about 80% of coronary heart disease and cerebrovascular disease [3]. In addition to the behavioural risk factors, there are some risk factors that cannot be changed like age, gender and family history [9]. Current risk-stratification systems are based on clinical judgment and traditional vital signals including heart rate, respiratory rate, blood pressure, temperature, and pulse oximetry. However, these vital signals have not been shown to correlate well with clinical outcomes and are not sufficient to predict and evaluate the cardiovascular diseases risk [3].

The appropriate management of classical risk factors (age, gender, smoking habits, hypertension, high body mass index) and biological analysis (cholesterol, glucose, triglycerides, potassium, sodium) together with new parameters (pulse wave velocity, augmentation index) represent larger potential for more accurate diagnosis [13], [14].

Arterial elastic properties are increasingly applied for risk stratification purposes in several populations. Recently, the European Society of Cardiology guidelines for the management of arterial hypertension suggested the measurement of aortic PWV, considered the gold standard method for assessing aortic stiffness, as a tool for assessment of arterial system damage [13]. Arterial stiffness is increasingly recognized as a surrogate end point for cardiovascular disease. Apart from invasive methods, it can also be measured with non-invasively, reproducible, and using relatively inexpensive techniques [14].

2.1.2 Arterial Stiffness

Arterial stiffness describes the reduced capability of an artery to expand and contract in response to pressure of confined fluid. Arterial stiffness is caused by reversible or irreversible changes in both the structural and cellular components of the arterial wall [15]. Parameters that describe vessel stiffness include compliance and distensibility.

Compliance *(C)* is the ratio between arterial volume change (ΔV) and pressure change (ΔP). In the arterial system compliance relates to the change in artery diameter caused by left ventricular ejection. The compliance value represents the arterial elasticity; for a low compliant artery, a substantial increase of pressure causes a small variation of diameter vessel. Therefore, compliance indicates how easily an artery wall can be stretched [15].

Distensibility is used to define compliance relative to the initial volume or diameter of an artery and is convenient in comparing arteries of different sizes. Arterial stiffness and its reciprocal arterial distensibility (or compliance), may provide indices of early vascular changes that predispose to the development of major vascular diseases [15].

Arterial stiffness is not uniformly disseminated throughout the vascular tree but is often patchy, occurring in central and conduit vessels with peripheral muscular arteries not exhibiting these stiffening changes.

On the other hand, arteriosclerosis is a diffuse and dilatory disorder that primarily affects the media, which is the thickest layer and is composed of smooth muscle, permitting the diameter and blood flow changes of the arteries. The cushioning function is affected due to the stiffening and dilation of major arteries, which results in raised blood pressure and pulse pressure, and the disturbance of the load upstream to the heart. The stiffening of large arteries reduces their capacitance and increase the velocity of propagation of arterial pulse pressure, thus contributing to a widening of pulse pressure and to the enlarged prevalence of isolated systolic hypertension with age [16], [17], [18].

The atherosclerosis is the process of plaque buildup, is a focal and occlusive disorder that primarily affects the intima (inner layer of the vessels and is composed by a single cell layer that interfaces the lumen of the vessel and the tunica media). The conduit function is affected due to narrowing of a major artery and ischaemia to the distal organ or tissues [19].

Most events of cardiovascular diseases are caused by atherosclerotic diseases, with most changes affecting the carotid bifurcation, where the common carotid divides into the internal and external carotid arteries. By implication, an arterial stenosis corresponds to the narrowing of the lumen of the artery. In extreme cases, the artery can become blocked, mainly due to the accumulation of lipids in the intima layer of the artery. This condition could lead to a decrease of the blood flow and subsequent oxygen supply reduction to different organs and tissues. In the specific case of carotid stenosis, cerebral perfusion is affected [19].

The most serious consequence of carotid stenosis is the stroke, which is fatal in one third of the cases and survivors usually have permanent disabilities. Although many patients have carotid stenosis, this disease is often only discovered after they have a stroke. Therefore, its early detection is crucial in order to avoid such cases [20]. Thus, the monitoring of the cardiovascular system has been growing in importance on the diagnosis and management of many disease states, including the carotid stenosis [16], [19].

2.2 Pulse Pressure Waveform

Hemodynamically, rather than merely consider its maximum and minimum values, should be taken into account the overall shape of the arterial blood pressure curve to describe the mechanical effects on the arterial wall and to give an adequate description of arterial system behaviour.

Central blood pressure waveforms contain specific features related to the cardiac and arterial functions as represented in Figure 2.1 [21]. The left ventricle contracts and ejects blood to the arterial system, creating the arterial blood flow and pressure. This phenomenon is easily conceived as a propagating pulse along the arterial bed. The maximum sharp peak at the end of the ascending limb is the systolic peak pressure. The dicrotic notch located on the systolic decline is caused by the closure of the aortic valve during early diastole. The pressure then gradually drops until the diastolic pressure is reached [18], [21].

Age related changes in aortic pressure waveforms exhibit early reflected waves and high systolic and pulse pressure amplitudes as a consequence of the arterial stiffness hence because of the early systolic wave reflections. These changes become noticeable

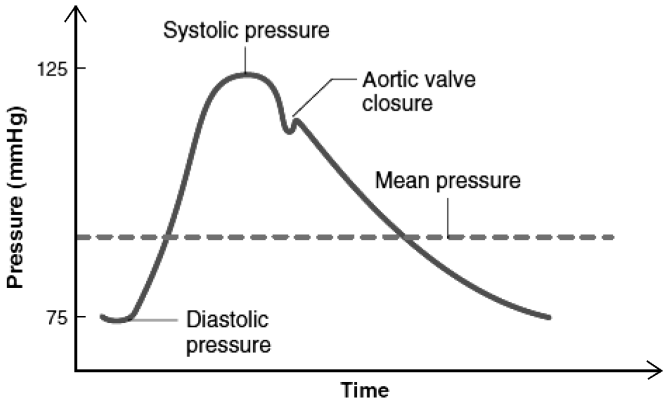

FIGURE 2.1: Central artery pressure wave, representing a single cardiac cycle. Adapted from [22].

after the third life decade, when the reflection peak comes together with the first rise thus becoming unnoticeable and augmenting the overall systolic amplitude [15], [23].

Information on the interaction between the left ventricle ejection and the physical properties of the arterial circulation can be determined by the descriptive and quantitative analysis of the arterial pulse pressure waveform [18]. Such properties arise from the reflective phenomena of the incident pressure wave generated by the left ventricle and its reflections from peripheral sites. The mechanical impedance mismatches in arteries and arterioles represents the major contribution to the appearance of the reflected wave in systole and eventual summation with the forward incident wave and result in the augmentation of the systolic blood pressure [15].

Four types of carotid pressure waveforms have been identified so far: type A, where systolic peak appears after the maximum wave; type B, which corresponds to cases of pronounced artery stiffness where the systolic peak appears after the inflection point (although the difference between them is very close to zero); type C waveforms, where the systolic peak appears before the inflection point, (commonly seen in healthy individuals that have low arterial stiffness and high elasticity); and type D, whose waves are similar to type A waveforms but the inflection point cannot be identified. These typical waveforms are shown in Figure 2.2 with amplitude in Arbitrary Units (AU) [24].

Morphologic features of individual arterial pressure waveforms provide diagnostic clues to various pathologic conditions [22]. Aortic stenosis produces a fixed obstruction to left ventricular ejection, resulting in a reduced stroke volume and an arterial pressure waveform that rises slowly *(pulsus tardus)* and peaks late in systole. In cases of systolic left ventricular failure the pulse pressure alternates in amplitude from beat to beat even though the rhythm is basically regular. Many others diseases are identified with abnormal pulse pressure waveform such as hypertrophic cardiomyopathy, left ventricular systolic dysfunction, chronic obstructive pulmonary disease, congestive heart failure, etc [25], [26]. These diseases have a typical pulse pressure profile. However many others might have typical and distinct patterns and therefore more studies are required to identify the waveform characteristics.

The pulse pressure waveform undergo alterations along the arterial tree. Pressure waveforms recorded simultaneously at different arterial sites have different morphologies due to the physical characteristics of the vascular tree (Figure 2.3). As the arterial pressure wave travels from the central aorta to the periphery, several characteristic changes occur [27], [28]. The pulse wave is more pronounced in the arteries but gradually diminishes in the peripheral blood vessels until it cannot be felt in the venous network

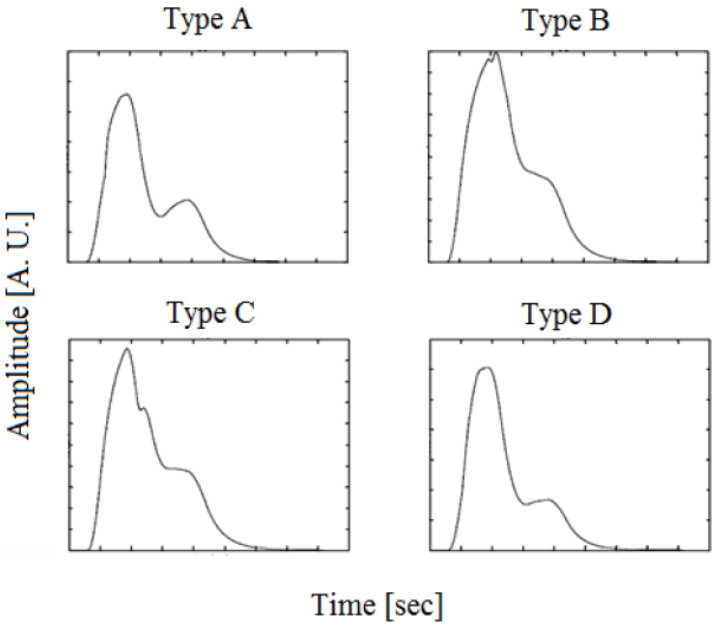

FIGURE 2.2: Types of pressure waveforms (synthesized waves). Type A, in which systolic peak appears after the peak of the wave; type B, the systolic peak appears after the inflection point with the difference between them close to zero; type C, where the systolic peak appears before the inflection point, commonly in healthy individuals; and type D, whose waves that the inflection point can not be identified.

that returns blood to the heart. The arterial upstroke becomes steeper, the systolic peak becomes higher, the dicrotic notch appears later, the diastolic wave becomes more prominent, and the end-diastolic pressure becomes lower. Thus, compared with central aortic pressure, peripheral arterial waveforms have higher systolic pressure, lower diastolic pressure, and wider pulse pressure [23].

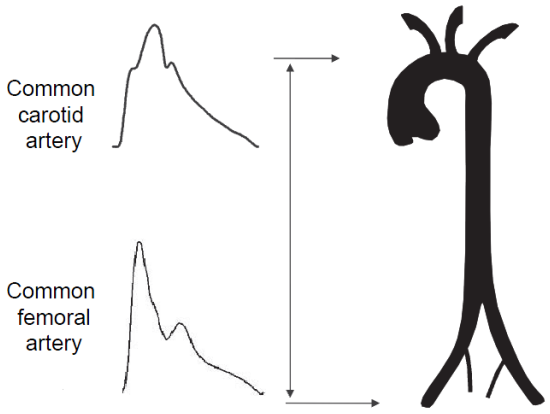

FIGURE 2.3: Differences in pressure waveforms along the arterial system. Adapted from [29].

In clinical practice, it is recognized an increase in the whole amplitude of the pulse pressure when it travels to a distal vessel. This amplification of the pressure wave with distance (spatial amplification) does not require additional energy input in the arterial

system, and so, by definition, is more a distortion than a true amplification, translated as an alteration in the morphology of the waveform [30], [31].

2.2.1 Pulse Wave Analysis

The assessment of the cardiovascular system condition based on multi-parameters allows a more precise and accurate diagnosis of the heart and the arterial tree condition. Risk indicators can be assessed from the main parameters extracted to the arterial waveform, its time characteristics and the pulse wave velocity. The PWA allows the non-invasive determination of the main indices of cardiovascular function: Augmentation Index (AIx), Subendocardial Viability Ratio (SEVR), Maximum rate of pressure change (dP/dt_{max}), Ejection Time Index (ETI) and Area Under the Curve (AUC). The most important points of the pulse pressure waveform are presented in Figure 2.4. The clinical definition for the referred parameters and the mathematical expressions for their determination are summarized in table 2.1.

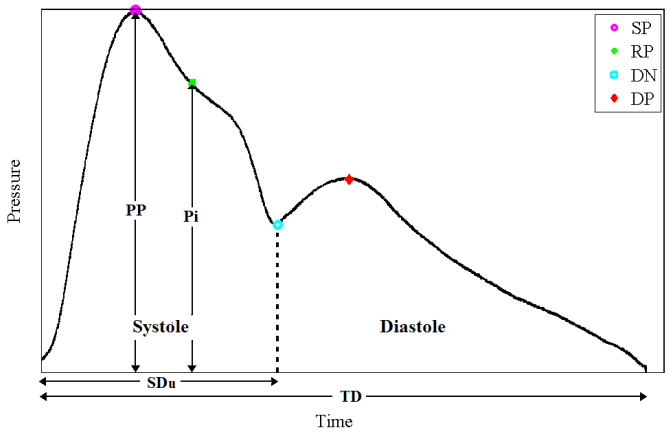

FIGURE 2.4: Typical pressure waveform of a healthy subject and its main features used to compute the indices of cardiovascular function: PP, SP, RP, DN, DP, SDu, TD and pressure in the reflection point (Pi).

In the pulse wave analysis, the AIx is the most widely studied index with several studies indicating that it is independently predictive of adverse cardiac events. AIx describes the increase of systolic blood pressure due to an early backward wave, produced by the reflection of the forward systolic wave on the peripheral arterial tree structure. This index is defined as the ratio of blood pressure amplitudes at the timings of the RP and SP, thus resulting in RP/SP expressed as a percentage. A convention for the AIx, defines positive value when the reflected wave arrival occurs earlier than the systolic peak the AIx, while a negative value of AIx indicates that the reflected wave is observed after the systolic peak [35].

Several studies have focused on the relationship between AIx and Heart Rate (HR) and a strong negative correlation between these two parameters is established. This is explained by the early return of the reflected wave in systole when the HR is lower. In this case, because heart is contracted during a longer period of time, the reflected wave returns during the systole. As the HR increases, the return of the reflected wave is shifted to diastole, thus, decreasing AIx [36], [37].

The Subendocardial Viability Ratio, or Buckberg Index, is a parameter that estimates the myocardial oxygen supply demand relative to the cardiac workload and is an

TABLE 2.1: Main parameters from pulse waveform analysis.

Parameter	Definition	Expression	Reference Values
AIx	Describes the increase of systolic blood pressure due to an early backward wave, produced by the reflection of the forward systolic wave on the peripheral arterial tree structure.	$\pm\frac{Pi}{PP}100$	- 22 to 40 (%) [32]
SEVR	Estimates the myocardial oxygen supply-demand relative to the cardiac workload. It is an indicator of subendocardial ischaemia.	$\frac{\int_{SDu}^{TD} Pdt}{\int_{0}^{SDu} Pdt}100$	119 to 254 (%) [32]
dP/dt_{max}	The ventricular contractility can be evaluated by the maximum rate of pressure change, which gives information about the initial velocity of the myocardial contraction. Is also an index of myocardial performance.	$\frac{dP}{dt}$	772 ± 229 (mmHg s^{-1}) [33]
ETI	Ventricular systolic ejection time between the aortic valve opening and closing. It is an important component on the evaluation of the left ventricular performance.	$\frac{SDu}{TD}100$	30 to 42 (%) [34]

indicator of subendocardial ischaemia [32], [36], [38]. The coronary perfusion, and consequently the oxygen supply of the heart, occurs mainly during diastole. In opposition, during the systole, due to the contraction of the heart, there is great energy consumption. Normal and healthy heart operation requires an energy balanced systole–diastole cycle, without which myocardial overload is expected and CVD risk increases. This heart cycle energy trade-off can be directly estimated by pulse wave analysis through the ratio of the diastole and systole areas (pressure–time integrals) on the pulse waveform. Results from some studies in healthy subjects show that SEVR varies between 119 and 254% [32], [35].

Ejection Time Index is another important cardiovascular parameter available through PWA. The ETI, also referred to Left Ventricular Ejection Time (LVET), corresponds to the ventricular systolic ejection time between the aortic valve opening and closing. Its ratio to the total duration of the cardiac cycle represents the ETI (%) and is an important component to evaluate the left ventricular performance. In healthy subjects the ejection time is inversely related to the heart rate and varies directly with the stroke volume. It is reported that in patients with cardiac failure the pre-ejection time increases while the LVET decreases [39], [40]. Several studies provided evidence that the ETI varies between 30 and 42% in healthy individuals [36], [41].

The ventricular contractility can also be evaluated by a parameter that reports the maximum rate of pressure change, dP/dt_{max}, in the systolic upstroke. It is known that this index gives information about the initial velocity of the myocardial contraction, which is also an index of myocardial performance. In situations where fluid edema enters the myocardial interstitium, affecting the stiffness of the heart and the myocardial function, the dP/dt_{max} index decreases. A study performed on a 10 healthy people group reported a carotid dP/dt_{max} of 772 ± 229 (mmHg s^{-1}) [33].

The AUC of arterial pulse waveform is calculated by means of an integral function. Using blood-pressure measurements recorded in 1655 women, the results show an area under the curve of 0.56 (95% CI, 0.54–0.58) [42].

2.2.2 Pulse Wave Velocity

PWV is defined as the velocity at which the pressure waves, generated by the systolic contraction of the heart, propagate along the arterial tree. This parameter is related to the elastic modulus (E) of the arterial wall which represents the intrinsic wall stiffness, and the arterial thickness (h) and blood density (ρ). The first relationship was formulated by Moens and Korteweg and expresses:

$$PWV = \sqrt{\frac{Eh}{d\rho}} \tag{2.1}$$

Later on, Bramwell and Hill described (2.1) the association in terms of distensibility (D), which is determined by the blood vessel's compliance (C), the former relation can be expressed:

$$PWV = \frac{1}{\sqrt{DC\rho}} \tag{2.2}$$

From the expression, is possible to deduce that higher PWV corresponds to lower vessel distensibility and compliance, and therefore to higher arterial stiffness.

As the mechanical properties of the arterial walls change along the arterial system, from the large arteries to the periphery, PWV is also affected by these changes. Normal PWV values are plotted in Figure 2.5. The pulse waves travel through the arteries at a speed of 4 to 15 meters per second depending on the vessel, PWV increases with the distance from the heart (see Figure 2.5), along with the elastic condition of the arterial wall, which is affected by a variety of factors in the pathological process [43].

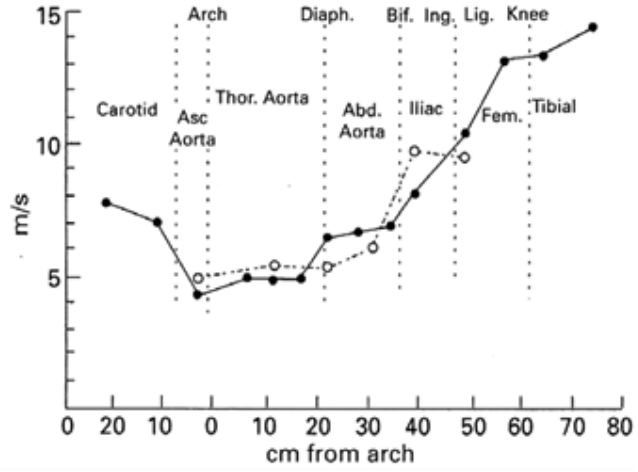

FIGURE 2.5: Pulse wave velocity along the arterial system. Adapted from [43]

2.2.2.1 Regional Pulse Wave Velocity

The regional PWV assessment is usually done in two different arteries (commonly the carotid and femoral arteries). The typical sites for pulse assessment are those where the pulsation can be easily felt, such as in the radial artery, in the common carotid artery or in the brachial or femoral arteries.

In 1961, Framingham study created multivariate risk scores to help to classify the risk level of CVD [2]. The first Framingham risk score was calculated by using information of

disease, age, gender, diabetes, smoking, blood pressure, and blood lipid concentrations. Several studies followed the Framingham work in order to improve and develop new guidelines for risk management based on many others parameters that could amend the assessing individual risk [2]. The multiple parameter risk response score is a useful tool to categorize patients for selection of appropriate therapeutics. In the following studies main focus was given to the regional PWV as a predictive factor of CVD [12].

In 1962, by using a piezoelectric crystal microphone to record the pressure pulse in radial and carotid arteries, Woolam *et al.* estimated the PWV in healthy subjects which ranged between 6.75 and 9.04 ms^{-1} and for diabetic subjects varying from 8.35 to 12.76 ms^{-1}. A significant increase in the pulse wave velocity was found in the diabetic subjects [44].

Isnard *et al.* studied in a small population the differences of PWV in normal subjects ($8.9 \pm 0.3\ ms^{-1}$) and hypertension patients ($11.8 \pm 0.5\ ms^{-1}$) [45].

In 1995, Asmar *et al.* studied the PWV in 418 subjects and concluded that the age and systolic pressure are the major determinants for the velocity of pulse propagation [46]. The differences between the PWV for normotensive, untreated hypertensive and treated subjects and concluded that antihypertensive drug increase of arterial stiffness with age [47].

Blacher *et al.* developed a study in a hypertensive population, that showed the correlation of PWV with atherosclerosis alterations and constitutes a predictor of cardiovascular risk in hypertensive patients [26].

The relationship of PWV and cardiovascular diseases was investigated in a hypertensive patients, and was verified higher PWV in patients with clinical vascular disease [48].

In 2001, pulse wave velocity was studied in subjects with 70 to 100 years old, which indicate that the increase in aortic PWV is an independent marker of cardiovascular risk in subjects with more than 70 years of age [49].

Lourent *et al.* performed a 9.3 years follow up study with 1980 patients, by assessing PWV, with the aim of determining if aortic stiffness is an independent predictor of cardiovascular mortality in hypertensive patients. Moreover, the authors related that an increasing in 5 ms^{-1} in PWV is equivalent to an aging of 10 years in terms of increasing the mortality risk [50].

A study with a cohort of 1045 hypertensive patients with a mean age 51 years and with a mean follow up period of 5.7 years, shows that relative risk of coronary event or any cardiovascular event increased with increasing level of pulse wave velocity and evidences that PWV is an independent predictor of primary coronary events in patients with hypertension [51].

Another study, with random sample of 1678 subjects aged 40 to 70 years, show similar values for PWV independently of gender, $10.8 \pm 3.2\ ms^{-1}$ for females and $11.8 \pm 3.6\ ms^{-1}$ for males. The authors refer the need to develop more sensitive techniques to measure the stiffness of various compartments of the arterial tree, which can be readily applied in routine clinical practice for risk stratification [52].

In the Reference Values for Arterial Stiffness Collaboration, an European cross-sectional study, performed in 11902 subjects, where PWV was assessed regionally (carotid-femoral) using several devices, showed that the obtained PWV values were lower in the group classified as normotensive (without cardiovascular risk factors subjects), from which the authors had established normal values of PWV [53]. The results also demonstrated that PWV increases with age and hypertension severity. The normotensive group had a PWV mean distribution between $6.6 \pm 0.8\ ms^{-1}$ for subjects under 30 years old, and $11.7 \pm 2.9\ ms^{-1}$ for the age category above 70 years old. This population was

separated by age decade and Blood Pressure (BP) category (optimal, <120/80; normal, ≥120/80 and <130/85; high normal, ≥130/85 and <140/90; grade I hypertension, ≥140/90 and <160/100; and grade II/III hypertension, >160/100 mmHg). The relations between PWV, age and BP in the reference populations are graphically explained in Figure 2.6 [53].

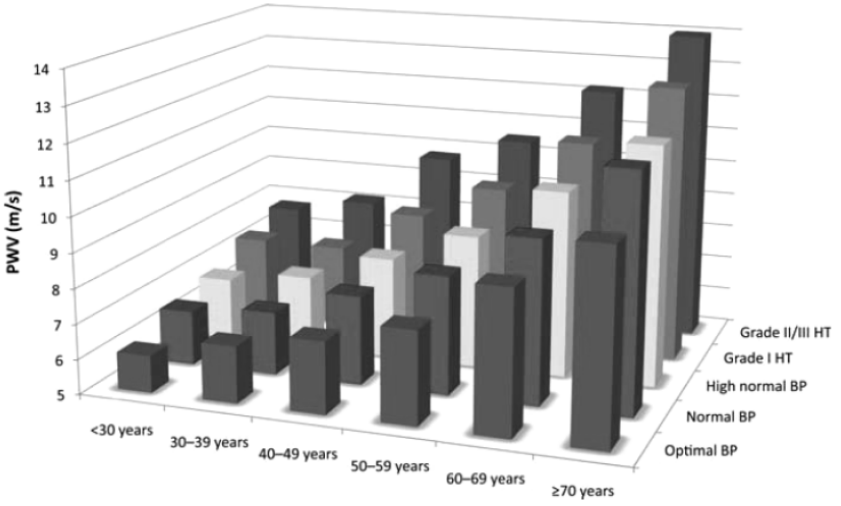

FIGURE 2.6: PWV according to age and BP in the reference value population. Adapted from [53].

In 2011, a multicenter, observational study included 2200 Portuguese subjects, underwent clinical assessment and annual PWV measurement, demonstrated that PWV was significantly higher in individuals with cardiovascular events ($11.76 \pm 2.13\ ms^{-1}$) than in those without events ($10.01 \pm 2.01\ ms^{-1}$), evidencing the clinical relevance of PWV as a cardiovascular risk marker [54].

Several studies have focused on the determination of normal and reference PWV values in groups with healthy subjects and patients with cardiovascular diseases, hypertension, diabetes or heart disease. Table 2.2 summarize the main results of these studies. Although all these studies have been performed for regional PWV, the local measurement of the PWV is pertinent because of the arteriosclerosis local nature.

TABLE 2.2: Studies of PWV caroti-femoral measurement and reference values.

Feature Population/Disease	**Number of subjects**	**Age (years ± SD)**	**PWV (ms^{-1})**	**Device**	**Reference**
Healthy	15	33 ± 3	8.9 ± 0.3	Pulse transducer probe (Siemens Elema AB) synchronism with ECG	Isnard *et al.* [45]
Hypertensive subjects	16	38 ± 3	11.8 ± 0.5		
Healthy	418	46 ± 12	0.07xSP+0.09xage-4.3	TY-360 Pressure transducer (Fukuda Co)	Asmar *et al.* [46]
Normotensive subjects	124	45 ± 13	8.5 ± 1.5	Doppler unit (SEGA-M842, Oregon, USA) synchronism with ECG	Asmar *et al.* [47]
Untreated hypertensive patients	224	48 ± 11	11.8 ± 2.7		
Treated hypertension patients	164	59 ± 11	10.1 ± 2.6		
Hypertensive without atherosclerosis	530	57 ± 13	12.4 ± 2.6	Complior®	Blacher *et al.* [26]
Hypertensive with atherosclerosis	180	67 ± 12	14.9 ± 4.0		
Hypertensive without vascular disease	196	57 ± 13	12.4 ± 2.7	Complior®	Bortollo *et al.* [48]
Hypertensive with vascular disease	40	62 ± 13	14.3 ± 4.0		
Subjects >70 years	141	87.1 ± 6.6	14.15 ± 3.11	Complior®	Meaume *et al.* [49]
Hypertensive patients	1980	50 ± 13	11.5 ± 63.4	Pulse transducer probes (Electronics for Medicine)	Laurent *et al.* [50]
Hypertensive without CV events	948	50 ± 12	11.4 ± 3.1	Pulse transducer probes (Electronics for Medicine)	Boutouyrie *et al.* [51]
Hypertensive with CV events	97	56 ± 13	12.8 ± 3.2		
Female	800	53.5	10.8 ± 3.2	2 piezoelectric pressure transducers (Hellige GmbH)	Willum-Hansen *et al.* [52]
Male	878	54.3	11.8 ± 3.6		
Female	1127	37	7.4	Complior®, Sphygmocor®, Pulsepen®	Vermeersch *et al.* [53]
Male	1080	39	8.2		
Smoker	444	43	8.0		
No smoker	2207	38	7.8		
General population (52% hypertensive, 11% diabetic, 17% smokers)	2200	46.33 ± 13.77	10.05 ± 2.03	Complior®	Maldonado *et al.* [54]

2.2.2.2 Local Pulse Wave Velocity

The local PWV measurement is made on a segment of an artery, whereas the regional PWV assessment is usually done in two different arteries. It has been attested invasively that PWV varies significantly along the entire arterial tree due to variations in both the geometry and structure of the arteries. The carotid-to-femoral PWV estimation therefore represents an average of the all local PWV values along the arterial segment [43]. In the early stage, fibrous spots with small diameter are scattered on the arterial wall and, in the final stage, the arterial wall becomes homogeneously hard. For this reason, it is important to have an early diagnosis tool able to measure the local stiffness of the arterial wall [55], [56].

Murgo *et al.* in 1980, measured the PWV in 18 patients by the catheterization in the ascending aorta and obtaining an average over all patients of 6.68 ms^{-1} [57]. In 1985, a smaller set of nine patients yielded a measured of 4.4 ± 0.4 ms^{-1} for the aortic root pulse wave velocity, also during the catheterization [58].

The relationship between carotid-femoral and aortic pulse wave velocity was studied in 107 patients [59]. The velocities were measured simultaneously during cardiac catheterization and comproved the higher values obtained in carotid-femoral velocity (10.65 ± 2.29 ms^{-1}) comparing to aortic velocity (8.78 ± 2.24 ms^{-1}) [59].

Using an ultrasound records in 21 adults were measured the local PWV in the left common carotid artery, obtained values in the range of 4 – 9 ms^{-1} and verified that the velocity is increasing with age [60]. In 2008, an experimental method, based on ultrassound data with higher frame rate, for the local determination of PWV in the carotid artery obtained values for PWV of 3 – 4 ms^{-1} [61].

Another technique uses magnetic resonance that allows direct imaging of the thoracic and abdominal aorta. The PWV can be determined by measuring the pulse wave at 2 points in the vasculature and by estimating the path length of the pulse wave. The mean PWV obtained with this method in patients with diabetes mellitus, was 5.65 ± 0.75 ms^{-1} [62].

2.3 State of the Art

One of the major objectives of a CVD detection programme should be to identify the persons who have asymptomatic arterial disease in order to slow the progression of atherosclerotic disease and in particular to reduce the risk of clinical manifestations. The revolution in technology has a clear influence in the decision making of cardiovascular patients diagnostics, and can be applied in the early disease detection in asymptomatic patients. A number of devices to measure arterial stiffness are currently commercially available. The non-invasive measurement of arterial stiffness is usually acomplished by a set of devices that measure PWV and that provide assessments of pulse pressure waveform and PWA.

The most common technique to non-invasively assess PWV is based on the acquisition of pulse waves generated by the systolic ejection at two distinct locations, separated by a distance d, by determining the time delay, or pulse transit time Pulse Transit Time (PTT), due to the pulse wave propagation along the arterial tree. The PWV parameter is then simply calculated as the linear ratio between d and the PTT [63].

Many different pulse waveforms have been used to assess pulse wave velocity, such as pressure wave, distension wave or flow wave. In previous studies, the comparison between pressure and distension waveforms had shown that, these waves can be used interchangeably for many analyses due to their similar wave contour. The results of a

TABLE 2.3: Devices and methods used to determine arterial stiffness. Adapted from [65].

Method	Measurement	Device
Non-Invasive	Regional PWV	PulsePen® Complior® Sphygmocor® Ultrassound
	Local PWV	Magnetic Resonance Image (MRI) Ultrasound
Invasive	Pulse pressure Waveform	Angiography

number of studies have concluded that the distension waves are slightly less peaked than the pressure ones [64].

Some of the described equipment is able to determine regional PWV and others for a local PWV measurement, and the most relevante are summarized in table 2.3. More recently some of these devices had implemented others functionalities such as computation of PWA parameters, like AIx.

2.3.1 Commercial Devices

In order to non-invasively assess the cardiovascular system, several techniques have been developed. Some devices are routinely used in diagnostic work-up programmes in the clinic environment but they have rarely been used in the population as image screening tools such as MRI or Ultrasonic sensors, however, these are usually seen as a costly technique and difficult to operate. More recently, new techniques have become available to detect new and several hemodynamic parameters. Pressure sensors, such as the tonometer, is considered the gold standard method for measuring PWV, but some operating skill is required to use this method which may influence the measurement. As a result, the tonometry technique of PWV assessment is usually used in research and clinical settings by well trained operators, but not widespread use in clinical or in ambulatory environments.

PulsePen®

The PulsePen® (DiaTecne Milan, Italy) is composed of one tonometer and an integrated Electrocardiogram (ECG) unit. The delay between pulse waves is determined by applanation tonometery to obtain the carotid and femoral synchronized with the ECG R peak and the foot of the wave determined [66].

Complior®

The Complior® (Colson, France) uses two dedicated piezoelectric pressure mechanotransducers directly applied to the skin in a simultaneous measurement of pressure pulses. The Complior® was validated through a range of epidemiological studies that demonstrate the predictive value of PWV in cardiovascular diseases. A first probe is positioned at the common carotid artery, the central detection site, whereas a second probe was is placed at the femoral artery site. However it is possible to determine the PWV in several pathways like carotid-femoral, carotid-brachial or femoral-dorsalis pedis without the need of ECG recordings [67].

SphygmoCor®

SphygmoCor® (AtCor Medical, Sydney, Australia) analyzes the pulse wave of the carotid and femoral arteries, estimating the delay with respect to the electrocardiogram wave and calculating the PWV. SphygmoCor offers the possibility of carotid–femoral PWV measurements in two steps. The first step is used to simultaneously record carotid pulse wave and ECG, while the second step is the recording of femoral pulse wave and ECG. ECG recording during measurements is necessary for synchronization of carotid and femoral pulse wave times [67], [68].

In the previously described techniques, PulsePen®, Complior® and SphygmoCor®, raveling pathway is measured on the body surface. Distance measurements are taken with a measuring tape from the sternal notch to the carotid and femoral arteries at the sensor location. In fact, this measured distance is an estimation of the true distance travelled by the front wave and largely depends on body habitus [67], thus introducing a significant systematic error on the PWV estimation.

Arteriograph®

Arteriograph® (TensioMed, Budapest, Hungary) does not measure propagation time from carotid–femoral waveform recordings or the distance between carotid and femoral arterial recording sites. The main principle of PWV estimation behind the Arteriograph® device is to record oscillometric pressure curves based on plethysmography and register pulsatile pressure changes in an artery on the upper arm [67]. Since fluctuations in pulsatile pressure in the artery beneath the inflated pressure cuff induce periodic pressure changes in the inflated cuff, the oscillometric method measures these periodic pressure changes (oscillations) as an indirect measure for the pulsatile pressure changes in the artery beneath [69]. The pressure fluctuations in the brachial artery detected by the cuff are analyzed and the difference in time between the beginning of the first wave and the beginning of the second (reflected wave) is related to the distance from the jugulum to the symphysis, resulting in the PWV. The software of the Arteriograph decomposes the early, late systolic and diastolic waves and also determines the onset and the peaks of the waves [69]. One important feature of this device is that it does not need auxiliary methods for pulse wave calibration. Since it uses an arm cuff like a sphygmomanometer, systolic and diastolic blood pressures are "intrinsically" calibrated.

Photoplethysmography

Photoplethysmography (PPG) is another non-invasive method for the detection of pressure waves propagated around the human body. The advantages of this method are: movement artefacts reduction (Infrared (IR) probes lightly held against the skin without perturbing the physiological system); infrared can then explore deep arteries according to the wavelength and to the distance between the light source and the detector. This latter characteristic is very interesting for assessing PWV in overweight populations. However this technique can only be applied to peripheral sites of the body. Pressure wave of blood undergoes changes in arterial tree, so that the waves obtained by this method don't give reliable information from one central system.

The measurements of PWV in overweight and obese subjects may be of major interest in assessing cardiovascular risk. However, obesity is a well known factor of technical operator bias when assessing PWV. The image techniques are a commercial solution to acquire signals when the fatty deposit prevents the acquisition by other methods.

Ultrasound

The ultrasound technique allows the determination of the PWV by estimating the time delay between the diameter waveforms recorded simultaneously at two close positions along the vessels. The PWV is determined by the ratio of the temporal and the longitudinal diameter gradients. Alternatively the US may analyze the carotid and femoral waves simultaneously and separately normalized with the electrocardiogram [65]. These techniques depend on a reliable identification of the foot of the diameter waveforms and a sufficiently high sampling frequency. Another method from ultrasound measurements estimated local PWV as the ratio between change in flow and change in cross-sectional area during a cardiac cycle [60].

Magnetic Resonance Imaging

PWV measured by Magnetic Resonance Imaging allows the accurate assessment of the blood flow velocity with a enough temporal and spatial resolution to study the propagation of the aortic systolic flow wave [70]. MRI is a non-invasive technique that allows direct imaging of the thoracic and abdominal aorta without the use of geometric assumptions. The accurate and direct measurement of the path length of pulse waves in the proximal and distal aorta, even in the presence of a tortuous vessel, is a major advantage over other techniques [62].

The MRI allows the assessment of PWV, or another aortic vascular parameters (aortic distensibility, aortic compliance, aortic elastic modulus, and aortic stiffness index) [62]. Aortic PWV was calculated as $\Delta x/\Delta t$, where Δx is the aortic path length between the 2 imaging levels and Δt is the time delay between the arrival of the foot of the flow pulse wave at these levels, represented in Figure 2.7 [62], [71]. To extract ascending and descending aorta flow curves, aortic lumen contours are segmented. The intersection of the tangent line to the upstroke and the baseline were considered as the arrival time of the pulse wave [70].

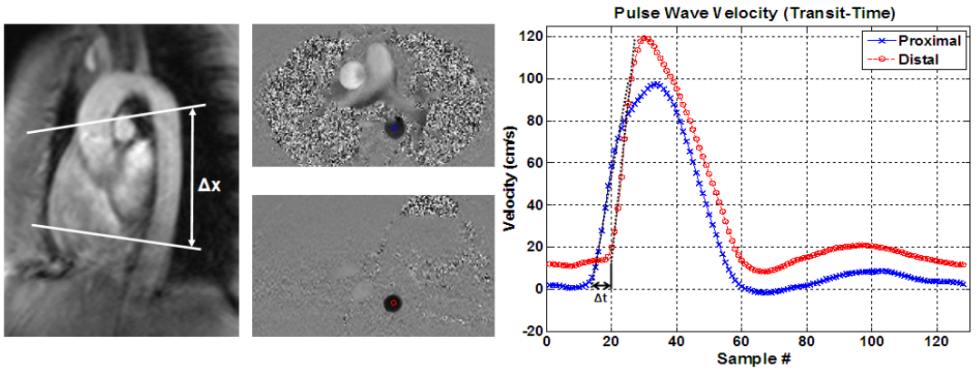

FIGURE 2.7: Transit-time method for calculating PWV in MRI. Velocity curves (right) from a volunteer scan are computed at two distant cross sections (middle) along the descending aorta (left). PWV = $\Delta x/\Delta t$, where Δx is the distance between the two locations and Δt is the time difference between the two velocity curves. Adapted from [71].

Invasive Measurement

The best method for measuring aortic and pulse pressure waveform is the threaded catheterization from a peripheral artery, during an angiography procedure. However,

the invasive nature has several disadvantages and this method cannot be justified except during a cardiac diagnostic or vascular procedure [72].

2.3.2 Non-Commercial Devices: Prototypes

In the Electronics and Instrumentation Group of the University of Coimbra, several prototypes for non-invasive hemodynamic parameters assessment, including local PWV, have been developed over the last years.

One probe based on piezoelectric transducers and another based on acoustic sensors have been developed targeting local PWV assessment and are currently under clinical validation studies [73]. The developed double headed probe consists of two piezoelectric sensors, and the functionality of this probe allows the determination of local PWV and AIx [73]. On the other hand, acoustic double probe consists of two sensors that detect the main cardiac sounds when placed over the carotid artery. This probe is able to determine the PWV, HR and LVET, from the detected waveform [74].

The clinical application of the novel non-invasive instrumentation can overcome practical and technical limitations inherent to the currently used methods such as arterial applanation tonometry, ultrasound and plethysmography that require physical contact of the probe with the patient and compress the artery throughout an entire cardiac cycle. Due to the contact nature, the exact positioning of the sensors is crucial for the correct measurement of PWV, and in consequence the quality of the recordings is strongly dependent of the operator. Several efforts have been done in the last decade for to develop novel instrumentation which provides non-contact measurements. The following prototypes describe several systems based in optical techniques that allow the monitoring the PWV and other vital signals without contact with patient, which representing a promising techniques for PWV measurement without distortion.

Meigas *et al.* [75] presented an optical device based on self-mixing interferometry coupled with fiber optics to measure the carotid artery displacement. Along the optical sensor, an ECG was performed in order to determine pulse time delay.

Jukka *et al.* [76] developed a self-mixing interferometry prototype applied to cardiovascular pulse measurements. The technique is used for pulse pressure waveform detection over the radial artery.

Scalise *et al.* [77] proposed an optical procedure, with two optical head based in Doppler vibrometer for measurements at long distances, suitable for monitoring the cardiac activity.

Mirko *et al.* [78] developed a system based in optical vibrocardiography for measure the regional pulse wave velocity at the carotid and femoral site, with ECG signal for the synchronism.

Yanlu Li *et al.* [79] suggested a system with two laser Doppler vibrometry as a potential technique to measurement the local carotid PWV in two locations along the common carotid artery from skin vibrations.

Recently, Adriaan Campo *et al.* [80] presented an instrument with a double laser Doppler vibrometer to assess the local pulse wave velocity at the carotid site PWV estimation.

An ideal method for arterial stiffness assessment: would be able to measure the parameter directly, without any intermediate model or transfer function; be an independent predictor for cardiovascular events, providing accurate information about the health condition of the patient; be easy to use in daily clinical practice; allow a non-invasive and non-contact measurement and, be validated in numerous studies with different groups of patients providing reference values that are accepted by the clinical community.

Chapter 3

Measurement System

This chapter presents several aspects related with the design and assembly of the prototypes and the data acquisition and management system. A detailed description of the different non-invasive optical probes, used to assess PWV and PWA parameters along with its portable system, is performed. Four distinct prototypes were developed with different sensor technologies and light sources. A data Acquisition Box and a dedicated database were designed in order to integrate the requirements of all the prototypes.

3.1 Overall Vision

The challenge in the development of hemodynamic devices is that the sensor should be able to measure the arterial pulse waveform from a far distance, without disturbing the wave profile. Optical techniques offer a lot of potential to address this challenge due to the fact that they offer a very fast response to an external stimulus and allow non-contact measurements. To study this issue, four different prototypes were developed and evaluated both in test benches and *in vivo*.

To accomplish the requirement of a completely portable system, suitable for health centers and hospital units involved in large-scale validation studies, the system should be as portable as possible. In this way, the acquisition box circuit comprises both the supply circuit for the probes and an acquisition system of analog data.

The portable optical system represented in Figure 3.1, that for referral simplicity is and dubbed as *GetPulse*, is composed by a Data Acquisition Box (DAQ); a set of probes; data processing software and a database.

3.2 Optical Probes

Emerging innovations in cardiovascular monitoring are moving away from more invasive technologies to portable and non-invasive solutions, particularly to those able to perform multi-parameter assessment. An optical method, for non-contact measurement of skin surface vibrations associated with the distension of the carotid artery, yielded promising results [75], [76]. The carotid artery is the natural probing site for pulse waveform measurement, due to the heart proximity and because it is easily accessible due to its proximity to the skin surface.

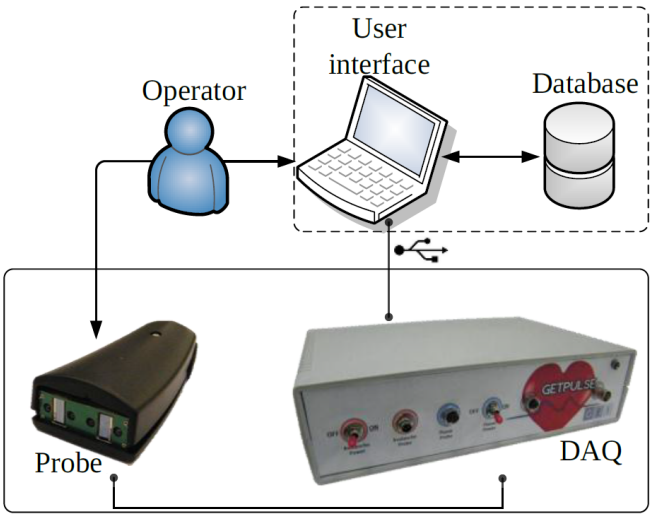

FIGURE 3.1: Components of the *GetPulse*, the portable optical system for hemodynamic multi-parameters assessment. Adapted from [81].

Beyond the ability to acquire a high definition non-invasive carotid distension waveform, the presented optical system shows several advantages over actual commercial devices. The clinical application of this non-invasive method can overcome practical and technical limitations inherent to the currently used methods such as arterial applanation tonometry, ultrasound and plethysmography, that require physical contact of the probe with the patient and compress the artery throughout an entire cardiac cycle. This measurement technique is affected by the Bernoulli effect that distorts the shape of the pulse curve itself [82], [83].

In tonometry, the probe needs to be placed over the widest pulsation area, and requires support from solid structures like the bone. For this reason, it is difficult to make valid measurements with applanation tonometry over the carotid artery, since they are usually involved in soft tissues [84].

The major limitation inherent to the current commercial devices is that they simply measure regional PWV [85]. However, and as mentioned before, peripheral arteries are significantly stiffer than central arteries and this fact skews the interpretation of the real value of PWV. Besides, the PWV in large central elastic arteries, such as the aorta or carotid, increases with age, whereas brachial or femoral arteries PWV does not increase so markedly [86]. Therefore the large heterogeneity of the structure of arterial walls at different sites constitutes an important limitation of PWV regional measurement [16]. In fact, the Expert Consensus Document in Arterial Stiffness states that the PWV increases from 4–5 ms^{-1} in the ascending aorta, 5–6 ms^{-1} in the abdominal aorta and 8–9 ms^{-1} in the iliac and femoral arteries. A local PWV measurement technique is hence preferred [85]. Furthermore, this convenient approach to analyse PWV on an artery segment avoids coarse approximations of the distance between test points, constituting an important advance in PWV assessment. In fact, the carotid-femoral PWV assessment implies measuring the distance between carotid and femoral sites over the body surface. The accuracy of this measurement is markedly influenced by either the distance determination protocols or the presence of abdominal obesity [85]. For these reasons optical sensors are an attractive instrumental solution in this kind of time assessment applications due to their truly non-contact that allows a measurement local PWV and PWA in the carotid artery. Moreover, its simple architecture, its time resolution and the low cost of production makes this prototype very interesting, competitive and allows to

build a data set with interest for clinical studies, with a range of important dimensions not available for other devices.

The developed optical probes are capable of emitting a constant beam of light while simultaneously acquiring the reflected light. When the pressure wave travels underneath a deformable surface like the skin, the deformation of the artery, close to the skin surface, will alter the reflection light and thus, the signal generated on each sensor is correlated to the passing pressure wave (Figure 3.2).

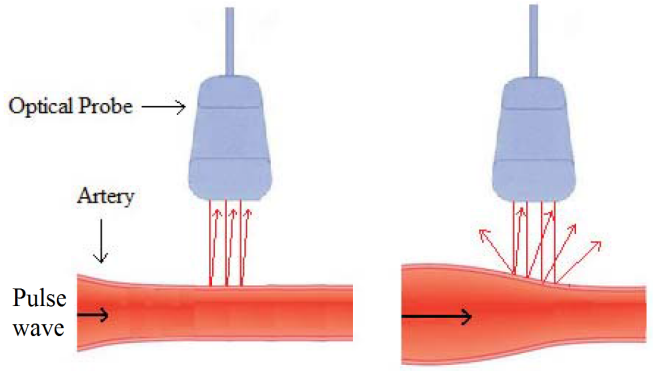

FIGURE 3.2: Effect on the reflectivity with a passing pressure pulse.

The developed probes are based on emission and detection of light and were designed to detect the distension of arterial wall. Throughout the development process, the probes were designed to detect the signal more efficiently. The Printed Circuit Board (PCB) is cased in a plastic box with an ergonomic configuration to ensure a safe and user-friendly probe for both operator and patient (Figure 3.3).

The developed probes can be arranged in 2 main groups depending whether of coherent a non-coherent light is need.

FIGURE 3.3: Optical probe method for non-contact measurement of skin surface in carotid local.

3.2.1 Probes based in Non-coherent Light

The probes have a common design structure which includes two Light-Emitting Diode (LED) in the vicinity of two identical photodiodes sensors placed 20 mm apart. This guarantees the local pulse wave profile assessment at two distinct spots, providing the precise local determination of pulse transit time and thus of the local PWV. Both elements (light source and sensor) are integrated in the probe's PCB which also includes basic electronics for signal conditioning.

Three distinct types of silicon optical sensors are used in this work: Planar Photodiode (PPD), Avalanche Photodiode (APD) and Lateral Effect Photodiode (LEP) each one requiring a particular electronic circuitry. Semiconductor sensors generate a photocurrent which depends on the intensity and energy of the incident light, depending on the materials and manufacturing technology.

Silicon photodiodes are semiconductor devices able to response to high energy particles and photons. Photodiodes operate by absorption of photons or charged particles and generate a current flow in an external circuit, proportional to the incident light intensity.

The photodetectors used in this work are not sensitive to position nor to the angle of incidence of the light, integrating the number of photons per unit area and converting them into electric current. The illumination is provided by LED and the photodetector was disposed in an axial symmetry. The LED approximately act as a point source of light. However, the skin is a dispersive media and this fact ensures that an homogeneous distribution of the reflected light is achieved at the sensor level.

A silicon photodiode can be operated in either photovoltaic or photoconductive mode. Mode selection depends upon the speed requirements of the application, and the amount of dark current that is tolerable. In this case the photodiodes were operated in the photoconductive mode in order to achieve their fastest switching speeds. The electronic circuit is composed by op-amps on trans-impedance amplifier configuration.

The spectral response curve represents the responsivity as a function of the wavelength, represented in the Figure 3.4 for the APD. The response of the silicon photodiode to the wavelength of the incident light goes from 400 nm to 1100 nm, for both the PPD and APD. The responsivity is low, close to zero (A/W) at the short wavelengths, increasing until the maximum sensitivity wavelength is reached (930 nm for the PPD and 830 nm for APD) and decreases thereafter [87], [88].

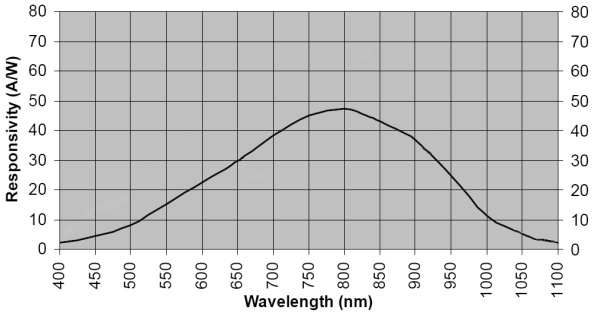

FIGURE 3.4: Curve of APD spectral response.

3.2.1.1 Non-coherent Light Source

For each type of sensor (planar and avalanche photodiode), two probes were built; one designed to work with visible red light wavelength (625 nm) and another with IR (830

nm and 940 nm for APD probe and PPD probe, respectively) [89], [90], [91].

The visible light used in optical probes is Mega Brightness LED (Multicomp® OVL-3328) composed by AlGaInP/Si with a dominant wavelength in 625 nm (red), with a luminous intensity of the 80 mW/sr, a viewing angle of the 30º, with a forward voltage of the 2.6 V and 30 mA for the forward current [89].

The IR light probes were built regarding that in obese subjects the carotid artery is frequently not at the surface due to the adipose tissue accumulation around the neck. In those cases the use of a wavelength that could penetrate more deeply into the tissues was considered a required to allow the determination of the distension waveform, reason for the use of the infrared light.

The IR LED peak wavelength is 850 nm and has a very high radiant intensity (about 110 mW/sr) and emission angle of the 26º with a forward voltage of the 1.5 V and 100 mA for the forward current [90]. For the infrared LED with dominant wavelength in the 940 nm the typical forward voltage of the 1.25V and 50 mA for the forward current, a viewing angle of the 30º and a radiant intensity of 14 mW/sr [89].

In each probe, two LEDs provide skin illumination with the intensity controlled by a variable resistor to ensure a uniform light distribution.

LEDs are current driven devices. The light they produce is proportional to the current flowing through them. One way to maintain constant luminescence is to keep the current through the LED as stable as possible, even it the supply voltage changes.

Thus, LEDs require a perfectly regulated constant-current power supply. It follows that the primary role of the LED driver is to set the current to the nominal value as represented in Figure 3.5. The LEDs are connected to the output of the op-amp with a transistor to increase power. The feedback loop which is responsible for the accuracy of regulation requires an extremely precise current source.

The architecture of a common constant-current is a closed-loop-control LED driver circuit. The current is sensed through a resistor R_{sense}. The voltage across the resistor, proportional to the LEDs current, is then used by the feedback input pin of the regulator to adjust the control mechanisms and modify the voltage applied to the LEDs in order to maintain the current through it constant.

A precision current source requires the use of a highly accurate op-amp with offset compensation [92]. The op-amp actuates both as a voltage reference buffer and a constant current control. A fixed DC voltage needs to be applied to V_{ref} to establish the current for the LED.

The simple transistor 2STN 1360 [93] current source was improved by inserting the base-emitter junction of the transistor in the feedback loop of an op-amp. Now the op-amp increases its output voltage to compensate VBE. The circuit is actually a buffered non-inverting amplifier driven by a constant input voltage. It keeps up this constant voltage across the constant sense resistor. As a result, the current, flowing through the load, is constant as well.

3.2.1.2 Planar Photodiode Probe

The photodiode is a device in which the electric field of the depletion layer of a P–N junction is used to collect current carriers generated by photonic absorption. The diffused area defines the photodiode active area. The electron-hole pairs generated by light incidence are swept away by drifting in the depletion region and are collected by diffusion from the undepleted region. In this way generated current is proportional to the incident light or radiation power.

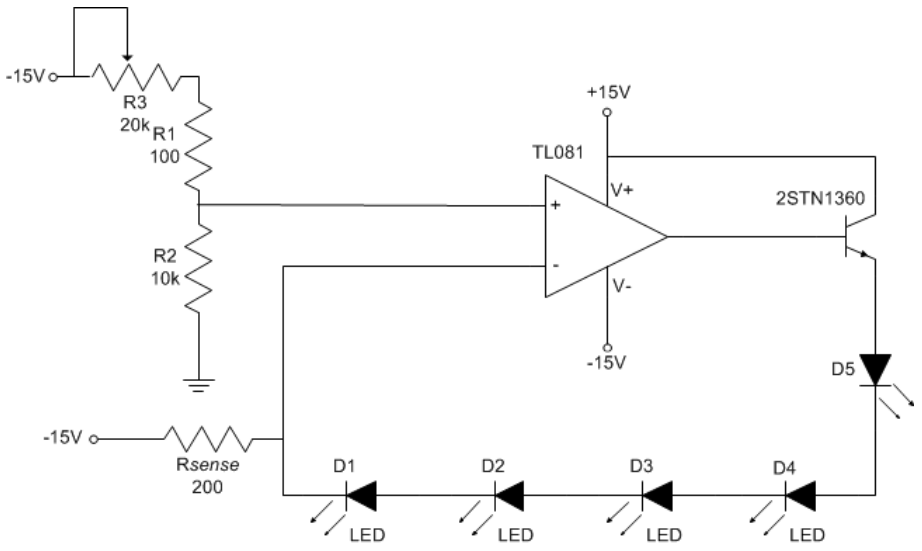

FIGURE 3.5: Schematic circuit of LEDs current drive. D5 represents the LED for a reference to the operator position the probe. D1 to D4 represents the LEDs that are responsible to provide skin illumination.

In this work a planar type from Silonex® (SLCD-61N3), rectangular shaped photodiode, 10.2 mm x 5.1 mm, biased at 15 V on the photoconductive mode, with a maximum sensitivity wavelength for 930 nm, was used and, consequently, the infrared LEDs selected for this probe have also approximately this wavelength [87].

In photoconductive mode, an external reverse bias is applied to the photodiode junction. The photocurrent generated on the device originates a voltage across the load resistance (R1 represented in Figure 3.6). The current measured through the circuit indicates illumination of the device; the measured output current is linearly proportional to the input optical power. Applying a reverse bias increases the width of the depletion junction producing an increased responsivity with a decrease in junction capacitance and produces a very linear response. This operation mode is the one that exhibits the fastest response. The TL081 was used for trans-impedance amplifier for current-to-voltage conversion [92].

Figure 3.6 shows only half of the components of the probe that further comprises a second photodetector and two more LEDs, which are not represented in the figure for simplicity. The probe was designed in order to measure the PWV and the final version was composed by two planar photodiodes 20 mm apart and four LEDs, two for each sensor.

During the development of this project, tree configurations for the probe were projected and implemented. The first version of the PPD based probe is presented on Figure 3.7(a). This configuration was difficult to operate because the sensors establish contact with the skin thus increasing the noise in the signal. The signal was also very difficult to reach, because the probe did not adapt well to the anatomy of the neck. The direct flow of light from the LED to the sensors combined with the reflected light with no information resulted in a baseline that limited the amplitude of the signal containing the relevant information.

The second version of the PPD based probe is presented on Figure 3.7(b). The main improvement of this probe relatively to its preceding is the external architecture. Here both the sensors and the LEDs are buried on the "chassis" of the probe limiting, in this way, the contact of the sensor with the skin and also the amount of reflected clear

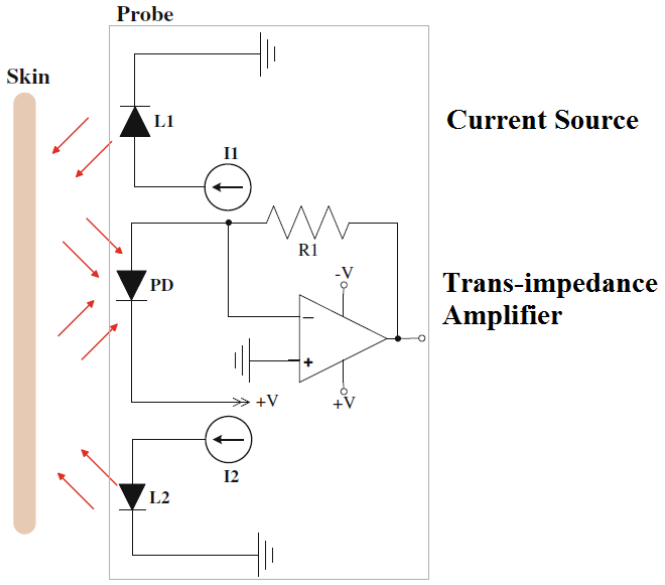

FIGURE 3.6: Schematic of one PD and light sources (L1 and L2) of the probe and light interaction with skin.

light and direct back-flow of light diminishing the baseline amplitude. The LEDs are also arranged in a configuration that provides an even illumination of the skin under the sensor. This probe was still not ergonomic enough making the signal acquisition process difficult.

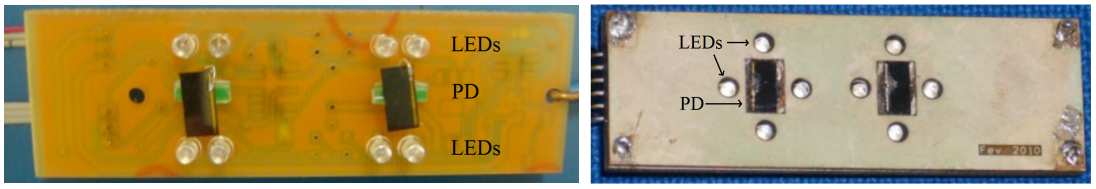

(a) First version. (b) Second version.

FIGURE 3.7: Details of the first versions the PPDs probe.

The probes usability and the operator ergonomic requirements were also considered when developing the new configuration. Their design concerned the functional requirements and their hardware is enclosed in an ergonomic plastic box that ensures easeful handling to the operator (Figure 3.8). Also the security for both the patient and the operator is guaranteed. Indeed, neither the LEDs, the photodetectors nor the printed circuit board directly contacts with the patient skin. The electronic components remain at a fixed distance from the skin (3 mm) ensuring a totally non-contact assessment.

The next step, after the design optimization, was developed on prototype with infrared light. LEDs with a 940 nm are chosen according the maximum sensitivity wavelength for the planar photodiode. In order to better distinguish the probe types of illumination, two different plastic casing (white and black) were chosen to enclose IR light probe and visible light probe, respectively (Figure 3.9).

Probe casing also has an extra LED, in the right side of the plastic case, used as a reference to the operator position the probe, in order to each acquisition could be done in the same position as previous measurements.

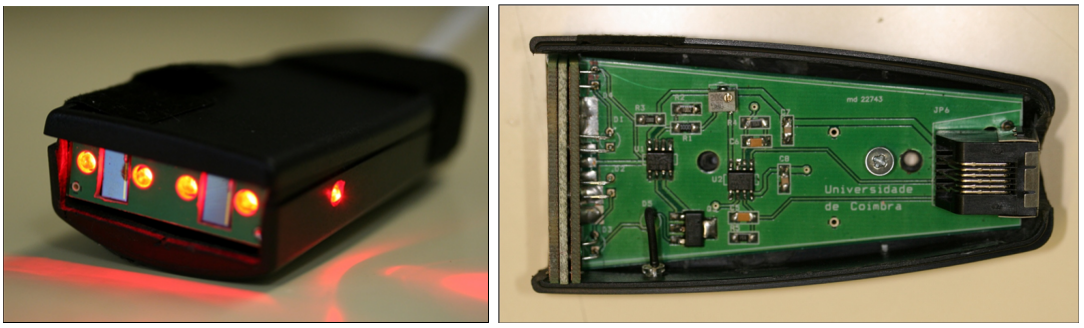

(a) Ergonomic probe design. (b) PCB of PPD probe.

FIGURE 3.8: Structure of last version of optical probe with two planar photodetectors and light sources, inside an ergonomic plastic box.

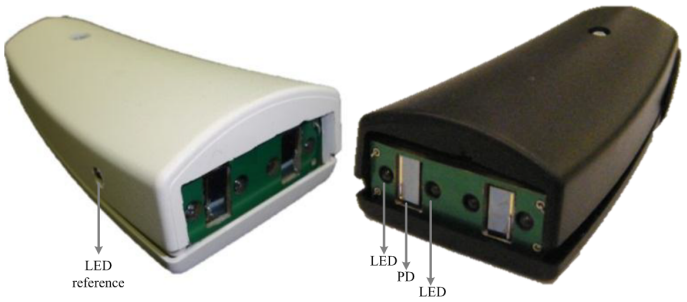

FIGURE 3.9: Infrared light PPDs probe (white box) and visible red light PPDs probe (black box).

3.2.1.3 Avalanche Photodiode Probe

Analogously to the conventional photodiodes, APDs operate from the electron-hole pairs created by the absorption of incident photons. An avalanche photodiode is a photodiode that internally amplifies the photocurrent by an avalanche process. In APDs, a large reverse-bias voltage, typically over 150 Volts, is applied across the active region. The high voltage causes the photoelectrons, initially generated by the incident radiation to accelerate as they move through the APD active region. As these electrons collide with other electrons in the semiconductor material, they cause a fraction of them to become part of the photocurrent. This process is known as avalanche multiplication. Avalanche multiplication continues to occur until the electrons move out of the active area of the APD. Under these conditions, gains of around 50 will result from the avalanche effect, providing a larger signal from small variations of light reflected from the skin and will, at least theoretically, improve the Signal-to-Noise Ratio (SNR).

On the other hand, since the sensitive area of this sensor is very small (1 mm^2), the accuracy of the estimations increases. In fact, comparatively to the planar photodiode, in which the detection of light takes place over a much larger area, this sensor can measure an almost point of the skin, thus decreasing the error associated to the detection solid angle.

APDs used in the probes (Advanced Photonics® (SD 012-70-62-541)) show a maximum light sensivity in the infrared wavelength region, specifically at 830 nm [88]. A probe with visible red light wavelength (625 nm), along with another with infrared light of 830 nm wavelength was developed.

The APD probe includes the high voltage biasing circuitry (-150V) necessary to guarantee the avalanche effect, showed in Figure 3.10. TS Series, TS 0.25N (Matsusada®) was used for a high voltage DC-DC converter suited for biasing APDs with low ripple (less than 10mVpp), input current of the 70 mA, and input voltage of 12V. The LM7812 is responsible for the regulation of the 12V for the input of the high voltage converter [94]. The output voltage of TS 0.25 N is controlled by a remote control voltage (0 to 10Vdc) and guarantees continuous output short circuit protection [95]. For the remote control voltage a circuit based on TL071, that provides a voltage of 6V was used. The small input capacitors in the circuit (C4 and C5 of 100 nF) have low inductance giving it excellent high frequency response and noise filtering capabilities. The C1 and C2 filter out ripple changes and large load transients. The TL082 was used for trans-impedance amplifier for current-to-voltage conversion for the dual photodetectors in the probe (the op-amp in the Figure 3.6 configuration).

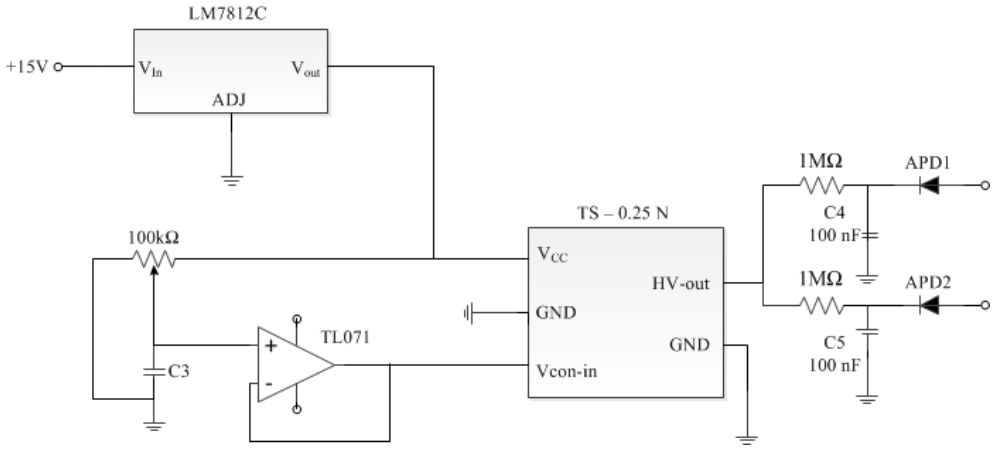

FIGURE 3.10: Schematic of the high voltage biasing circuit of APDs.

For the optical probe based in APD sensors an interface based in silicone structure was tested in order to ensure the non-contact of the optical elements with the sensing media. In this way is also possible to reduce the distress of the patient by the silicone characteristics of soft texture and adaptable form (Figure 3.11).

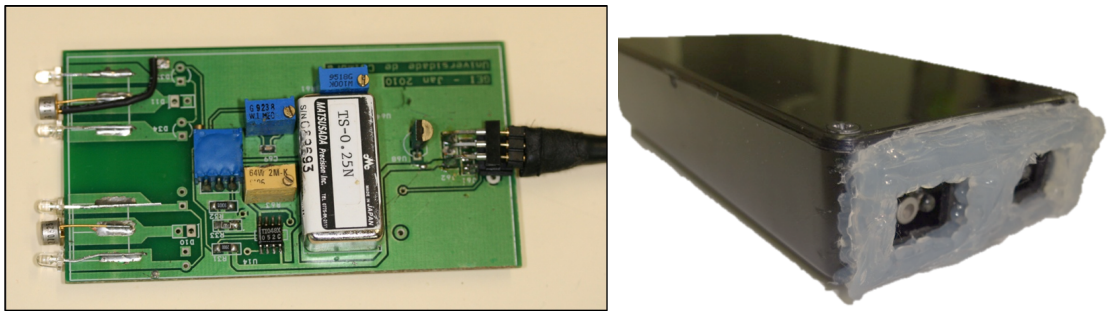

(a) PCB of APD probe.

(b) Optical probe inside the plastic box, with silicone interface.

FIGURE 3.11: Structure of optical probe with each APD in the center of two visible LEDs.

The next diagram (Figure 3.12) shows the configuration of the probe elements, LEDs and the photodetector, and the light interaction with skin. The radiation pattern in far field is characterized by the angular intensity distribution. Radiant intensity is the

radiant flux per solid angle in a given direction from the source. In the Lambertian pattern the maximum light intensity is at 0°. As the angular displacement increases the light intensity falls and for high angle amplitude the light intensity is almost negligible. The illumination profile at the skin level results from the typical Lambertian radiation pattern form LED emitters [96], [97]. The small distance between the two LEDs merge a fusion of the respective radiation pattern in the spatial distribution that correspond the photodetector sensitive area.

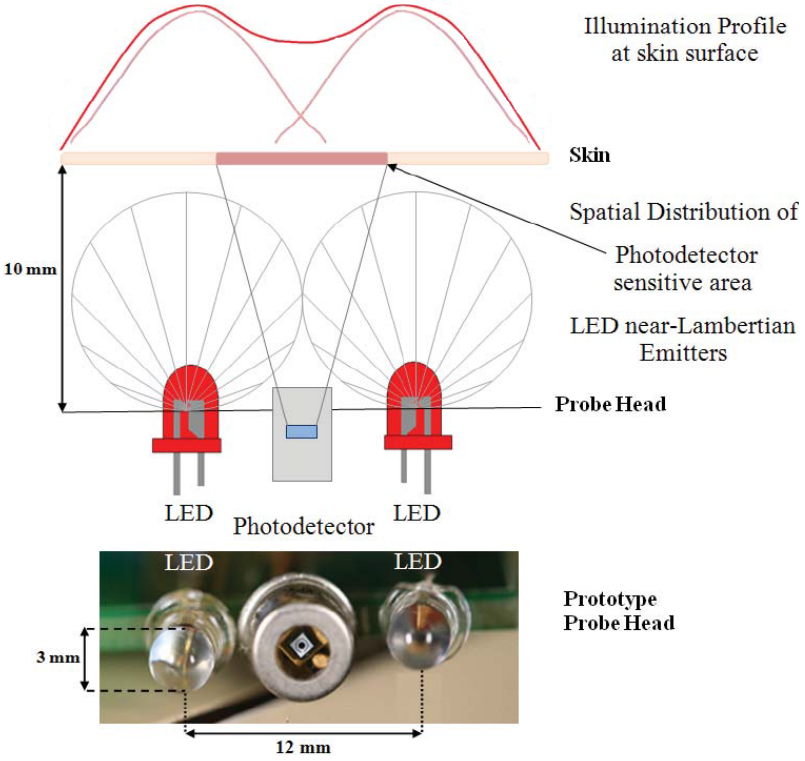

FIGURE 3.12: Structure of the optical probe with APD photodiode sensor and light sources. Schematic of the light interaction with skin.

The skin surface act as a diffuse reflector that scatters light over a wide angle range. This characteristic contributes for the homogeneous distribution of the reflected light. Thus, a uniform illumination scheme is provided in the area (about 140 mm^2) where the reflection occurs, neglecting the influence of the light incidence angle.

The scheme represented in the Figure 3.12 for light emission and interaction with skin is the same for two prototypes based in non-coherent light, the PPD and APD probe.

3.2.1.4 Lateral Effect Photodiode Probe

Another prototype using non-coherent light was created based in LEP. This probe presents a different configuration due to the dimensions of the LEP. However, has a similar architecture, LEDs for the illumination and a position sensing photodetector, the LEP [98]. A LEP is a continuous photodiode along all its detective area, without gaps or dead points. It is a position sensing detector, as it provides direct information on light spot displacements across the detective area. When light reaches the photosensor, two currents are generated, proportional to the light intensity and spot position on the photodetector area (Figure 3.13(a)) [99].

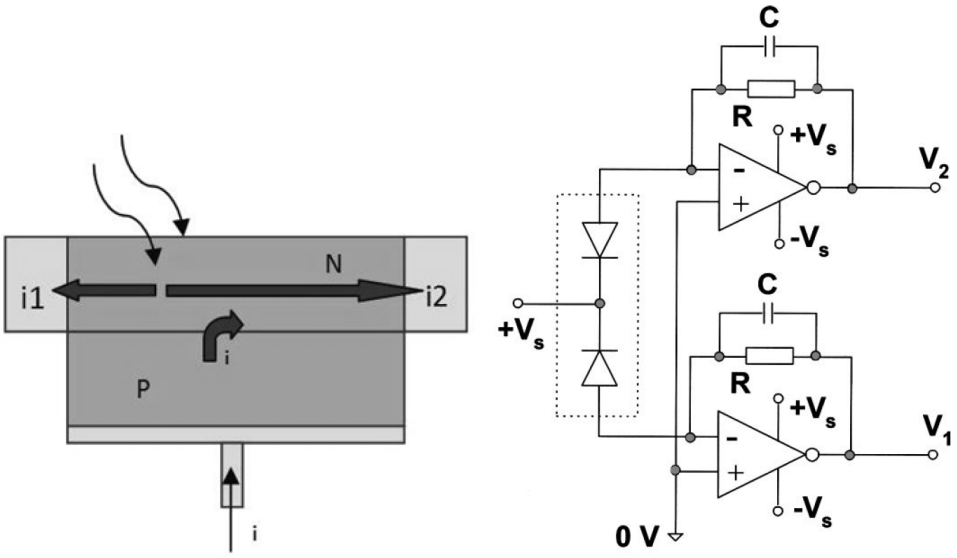

(a) Schematic of LEP. (b) Circuit of LEP.

FIGURE 3.13: The lateral effect photodiode. a) Schematic diagram of LEP and b) equivalent circuit for the LEP and the amplifiers used [99].

When the light reaches the center of the photosensor, two equal currents are generated, I_1 and I_2. As long as the beam light moves along the length of the active area, the currents generated are used to determine the position, X, of the light beam for each time instant using equation 3.1, from which PWV would be determined.

$$X = \frac{I_1 - I_2}{I_2 + I_1}. \tag{3.1}$$

Position sensitive detectors can achieve spacial resolutions of 1 μm without any signal amplification, which makes them suitable for accurate measurements [99].

The developed probe contains a LEP operating on the photoconductive mode (bias voltage applied was 15V) whose output signals are amplified (Figure 3.13(b)). The illumination circuit of this probe is composed of two lines of 9 LEDs placed on either side of the sensor (30 x 5 mm) to provide illumination and form the entire probe that shown in Figure 3.14.

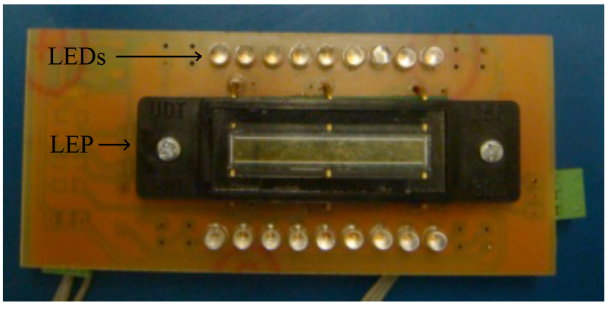

FIGURE 3.14: Photo of lateral effect photodiode probe.

The light emitted by the LEDs is reflected on the skin and its intensity and spot position detected by the LEP. For a passing pressure wave, the position of the intensity maximum is recorded over time, thus allowing the pressure waveform assessments.

3.2.2 Self-Mixing Coherent Light Probe

One great advantage in the use of coherent light consists in the possibility of using components which act simultaneously as emitters and receivers of light thus simplifying the optical alignment. The theory of self-mixing is based on laser Doppler effect and the interference between the emitted and reflected waves in a moving target, *i.e.* different wavelengths [100], [101]. This approach allow an simple optical scheme, with only one optical axis, as an alternative to the multi-axis schemes using several optical components. These characteristics reduce the size required by the optical probe and allow improvements in the ergonomics design.

The laser-based technique has been applied in biomedical areas due to its advantageous metrological characteristics that represent one opportunity to develop one interesting solution for to help in the diagnostic the CVD with potential to be an alternative to current research methodologies. The self-mixing effect has been used in several hemodynamic applications for PWV analysis [6], [76], [77], [102], [103], [104], but their clinical applications and commercial development are still in the emergent stage.

The construction of a new device, using simple low cost optical and electronic components, along with a new algorithm that improves the accuracy in the extraction of parameters, fills the existent gaps in the assessment of the arterial pulse pressure. The optical probe based in coherent light was developed for recording the pulse pressure waveform by sensing the skin vibration profile using a self-mixing laser Doppler vibrometry.

3.2.2.1 Theory of Self-mixing interferometry

The self-mixing effect can be modelled as a three-mirror Fabry-Perot structure. The schematic arrangement of the self-mixing effect in a semiconductor laser is presented in Figure 3.15.

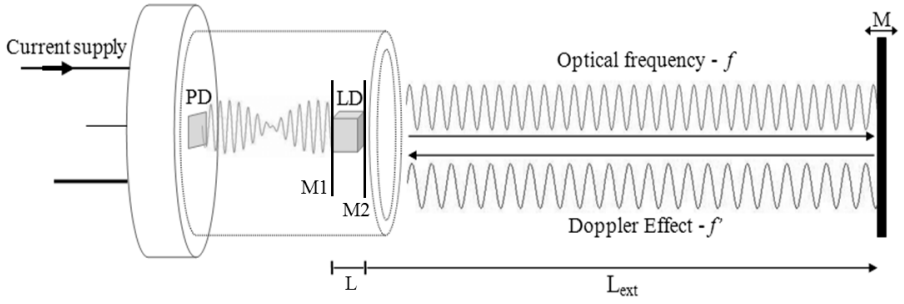

FIGURE 3.15: Schematic of self-mixing effect in a laser-diode.

Mirrors M_1 and M_2 form a laser cavity, of which L has an effective refractive index of μ_e. The external target, M, is located on the optical axis at distance L_{ext}. Photodiode is located in the laser package behind the laser cavity to measure power fluctuations within it.

According to the theory, mirror M_2 is replaced with an effective mirror, which combines the laser cavity and the external cavity to form a compound cavity. The amplitude reflection coefficient of the effective mirror r_2 is:

$$r_2(v) = r_{2s} + (1 - |r_{2s}|^2).r_{2ext}.exp^{-j2\pi v\tau_{ext}} \tag{3.2}$$

where r_{2s} and r_{2ext} are the amplitude reflection coefficients of laser mirror M_2 and external target M_{ext}, respectively [6], [105]. The optical frequency is v and τ_{ext} corresponds to the round trip delay back and forth through the external cavity, $\tau_{ext} = 2L_{ext}/c$, which is assumed to be air in this case and c is the speed of light. Multiple reflections are ignored in the external cavity since $|r_{2ext}| << |r_{2s}|$.

The optical power fluctuations ΔP of the laser-diode are related to gain variations and follow the equation:

$$\Delta P \simeq g_c - g_{th} = -\frac{k_{ext}}{L}.\cos(2\pi v\tau_{ext}) \tag{3.3}$$

where g_c is the threshold gain in optical feedback and g_{th} is the threshold gain without optical feedback [6], [105]. The coupling coefficient, k_{ext}, varies between zero and unity, defined as $k_{ext} = (1-|(r_{2s})^2 r_{2ext}/r_{2s})$. The gain in the laser-diode is produced by driving a high current density into the active area. Because external optical feedback causes gain variations, the self-mixing phenomenon can also be measured from the pump current of the laser-diode.

Self-mixing effect occurs when the laser emitted light with frequency (f), reflected from an object (M in Figure 3.15), re-enter the laser cavity with a frequency-shifted (f')and interacts with the original laser light, causing fluctuations to the laser power [106].

If the reflector object is moving, the reflected light presents a different frequency from the original light. The theoretical relation of the Doppler frequency, f', is given by equation 3.4, where v is the vector magnitude of the target's velocity, θ is the angle between the optical axis of the sensor and the velocity vector, and λ is the laser light wavelength [107].

$$f' = \frac{2v\cos(\theta)}{\lambda} \tag{3.4}$$

If the measurement is perpendicular to the target, equation 3.4 is reduced to $f = 2v/\lambda$ and further, solving the velocity, $v = f\lambda/2$. Replacing this to equation 3.3, it can be seen that the power fluctuations of the laser-diode are related to the Doppler frequency. Thus, it is possible to determine the velocity of the target measuring these power fluctuations.

When two sinusoidal waves with the same amplitude and similar frequencies interfere inside the laser cavity, the resulting wave is a sinusoidal waveform with modulated amplitude. These variations of amplitude are called "beats". To show this mathematically, one can consider the superposition of the two sinusoidal waves: $s1 = A\sin(\alpha t)$ and $s2 = A\sin(\beta t)$ where A is the amplitude of each wave and α and β are the angular frequencies $w = 2\pi f$.

The resulting wave is:

$$A\sin(\alpha) + A\sin(\beta) = 2A\sin(\frac{\alpha+\beta}{2})\cos(\frac{\alpha-\beta}{2}) \tag{3.5}$$

The following Figure 3.16 shows two signals with close frequencies (upper), which result in beats after interference (lower).

By mixing the Doppler-shifted wave with a reference wave (original frequency), a low frequency beat is produced with exactly the frequency shift produced by the Doppler effect. The Doppler shift of scattered light is proportional to the component of its axial velocity. Its magnitude can be evaluated by measuring the frequency of the beats produced by the scattered light.

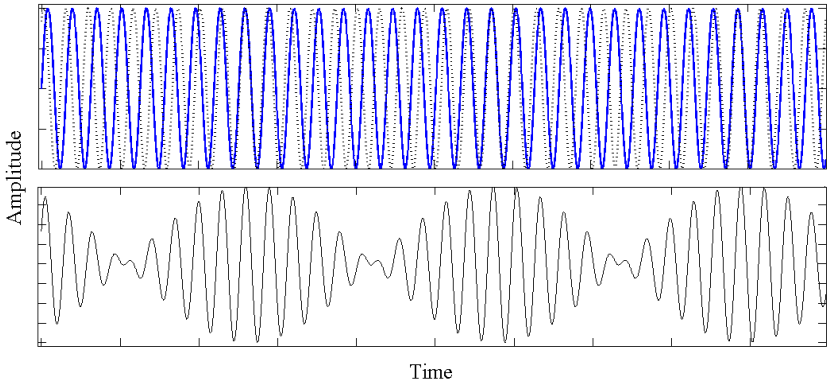

FIGURE 3.16: Amplitude modulation resulting from interfering waves (upper) and the resulting beat wave (lower).

3.2.2.2 Hardware Prototype

In the developed probe, Laser-diode (LD) were mounted perpendicularly to a printed circuit board layer. The probe includes a LD driven by a constant current as well as signal conditioning electronics based on a trans-impedance amplifier.

The prototype uses a laser-diode from Laser Components (Visible Laser-Diode ADL-65075TL) with a peak wavelength of 635 nm, 5 mW output power and an operating current of the 30 mA [108]. The relevant regulations according to International Commission on Non-Ionizing Protection (ICNIRP) Guidelines and the applicable accident prevention roles were taken into account [109].

Lasers are specified sources that should have particular safety handling procedure. Photochemical effects are more dangerous in lasers with small wavelengths (ultraviolet radiation). According to ICNIRP international standard, the Maximum Permissible Exposure (MPE) determine the level of laser radiation to which, under normal conditions, persons may be exposed without suffering adverse effects. The maximum MPE of skin to laser radiation, for long time (10^3 to 3x10^4 seconds) for wavelengths between 400 to 700 nm, is 2000 W m^{-2} [109].

The irradiance is then calculated by the light output power and the approximate diameter of laser beam of the 3.5 x 10^{-3} mm for check if the selected LD is safe for skin long time exposures.

$$E_{laser} = \frac{P}{A} = \frac{5 \times 10^{-3}}{\pi \times (1.75 \times 10^{-3})^2} = 520 W m^{-2} \tag{3.6}$$

This value is therefore lower them the maximum MPE allowed and hence suitable for the proposed uses.

The laser-diode component is composed of two parts, a light emitter (laser-diode) and receiver (photodiode), allowing the acquisition of self-mixing interferometry signals. The linear relation between monitor current and power is extremely important. This parameter allows monitoring the laser output power through the changes in photodiode reverse current. Since self-mixing effect produces power variations proportional, in frequency, to the target object velocity, through the acquisition of the photodiode current is possible to monitor its velocity.

Laser power is strongly influenced by the operating current and temperature, mainly above the threshold current. To maintain a constant output power it is necessary to maintain in the LD a constant current which can be achieved using a current driver. The laser-diode is fed with a constant current by a simple driver. This driver is composed

of a LM337T, which is a negative voltage regulator [110]. The LM337T set a constant potential difference of -1.25 V between V_{out} pin and ADJ pin. By using a constant resistance between these pins is possible to control the supply current. For an operating current of 30 mA, for the laser-diode, the appropriate value for source resistance is 42 Ω. The circuit schematics is represented in the Figure 3.17.

As previously mentioned, the self-mixing signals are extracted from the photodiode reverse current. Current signals are difficult to measure and photocurrents are usually very small and require amplification. In order to convert the current intensity into voltage potential, a trans-impedance amplification stage is necessary.

The trans-amplification stage was constructed by using an operational amplifier. Since all the current must be preserved, an op-amp with a low bias current is essential to perform a better amplification. The OPA 129 ultra-low bias current was used with this purposed since its input bias current OPA 129 is very low (30 fA) [111]. This component was used in a trans-impedance amplifier configuration that converts the photocurrent generated by the PD to voltage as the Figure 3.18 shows. The OPA129 is biased with ± 15V to ensure that it does not saturate when the op-amp have a high gain.

The optical probe was designed to allow for PWV measurements and for this reason two LD with 2.78 cm between then were used. This spatial limitation has to be balanced with a good time resolution in the signal acquisition and with fast sensor responses. Driver and trans-amplifier are independent circuits for each LD to minimize

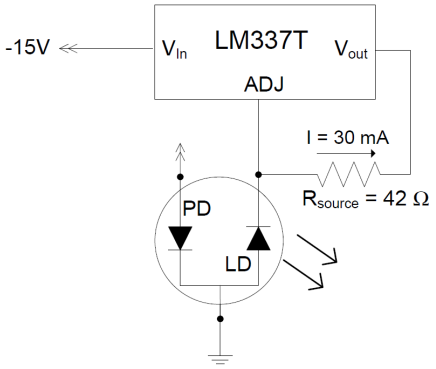

FIGURE 3.17: Functional diagram of laser-diode driver using the LM337T.

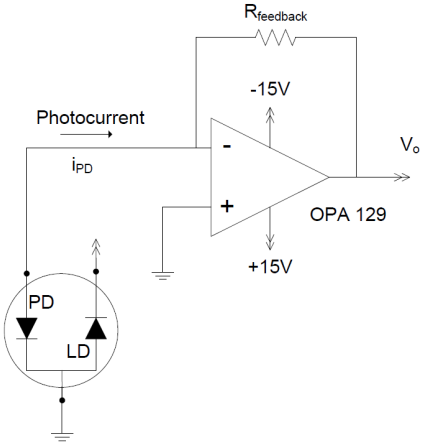

FIGURE 3.18: Functional diagram of trans-amplification stage for laser-diode and photodiode.

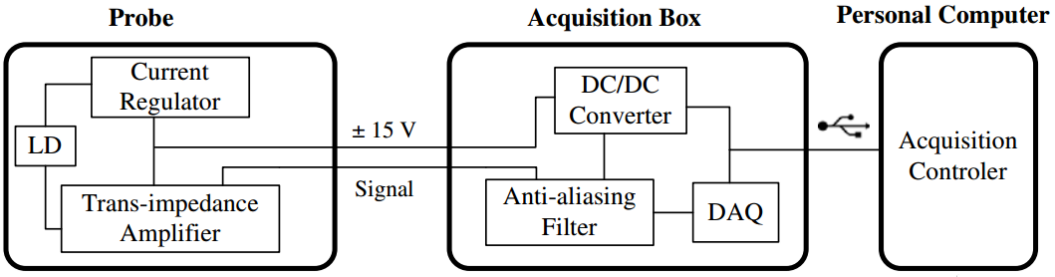

FIGURE 3.19: Block diagram of the optical system and all its minor components.

the possibility of electrical crosstalk. The probe is cased in a plastic box with holes for each of the laser-diodes in the front face which permits the emission and reception of light (Figure 3.20).

FIGURE 3.20: Photography of the laser-diode prototype.

The developed probe was designed in order to minimize the forces applied and improve the procedure of positioning the probe in the measuring site. The probe should be shaped and textured to be comfortable for both the user and patient. The complete design should be easy to stow and transportable in a clinical setting, compact and agile system.

3.3 Acquisition Box

The acquisition box integrates interfaces to all the optical probes with specific circuits appropriate for the characteristics of each prototype. The acquisition box is an important module of the entire work as it digitizes the signals from all the prototypes, allows to send and store data in a personal computer and power supplies the probes. The box main modules are the power supply, anti-aliasing filter and the acquisition system.

On the back panel of the acquisition box there are two input entries for Universal Serial Bus (USB) connection to the computer. The Data Acquisition System (DAS) uses a USB connector to transfer data and power supply while the DC/DC converter uses another USB connector for power supply. The use of two USB connectors was a necessity to reduce the digitalization noise of DAS.

In the front panel of the box, represented in Figure 3.21 there are three inputs for corresponding prototype probes, power switch buttons, and a LED to indicate the connection status of the acquisition box with the host computer. Each probe has its own

entrance, with different types of plug to prevent incorrect connections. Attached to each entry exist one ON/OFF button which is responsible for connecting the probe. Although probes have a common acquisition box, they are not supposed to be used simultaneously.

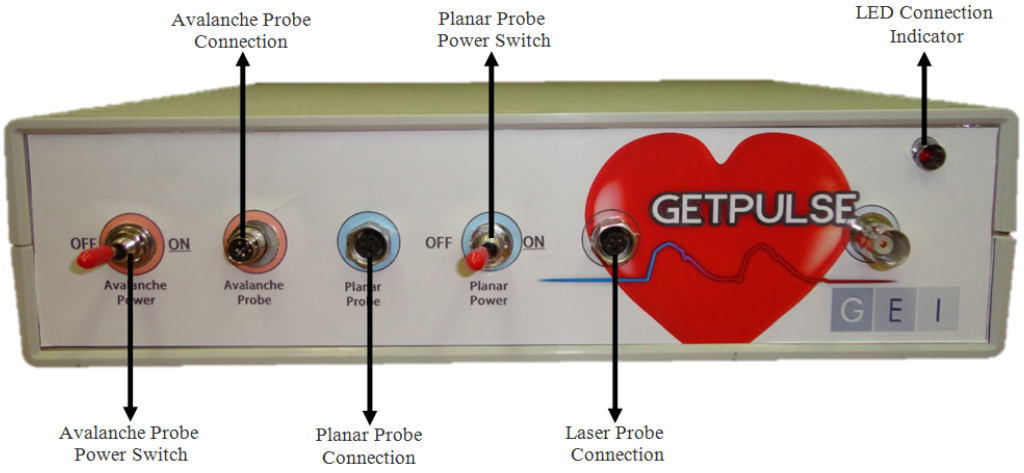

FIGURE 3.21: Front panel of the *GetPulse* acquisition box.

The LEP prototype was abandoned in the first tests benches (section 5.1) and was not included in acquisition box.

3.3.1 Power Supply

To accomplish the requirement of a completely portable system able to be carried to health centres and hospital units in large-scale validation studies, the system should be portable and power supplied by an USB port. In this way, all the components are directly or indirectly supplied by USB port. USB supplies a 5V DC electric power with a maximum current intensity of 500 mA [112].

For the three prototypes, as the APD and LD probe has to be supplied with ± 15V and the PPD probe has to be supplied with ± 12V, two conversion circuits were integrated in the acquisition box (Murata® NDTD 0515C and XP Power® IR 0512S converters, respectively) [113], [114]. The converter NDTD0515C Murata® Power Solutions supports a 5V DC input and provides two outputs of +15V and -15V with a maximum output power of 3W and minimum efficiency of 75 %. The converter XP Power® IR 0512S provides the ± 12V with a maximum output power of 3W and minimum efficiency of 85%.

The PPD probe needs a different power supply in result of *in vivo* tests, for the acquisition in the human skin in the Caucasian persons. In this case a saturation of signal generated by the photodetector was observed and the solution passes through the decrease of the LEDs power supply voltage. This effort decreased the luminous intensity and solved the saturation problem *in vivo* acquisition.

3.3.2 Anti-aliasing Filter – Laser Probe

Prior to the signal acquisition, a filtering stage is extremely important to prevent aliasing. Aliasing is a signal discretization effect that distorts the original signal. According to sampling theorem, the minimum sampling frequency needs to be higher than twice the highest interest frequency present in the signal in order to prevent aliasing.

For the LD probe where signals have a frequency modulation, the aliasing of higher frequencies could be a problem for the signal quality. To reduce the artefacts introduced by this effect, an anti-aliasing filter based on TL081 op-amp was implemented for the self-mixing signals (Figure 3.22) [92].

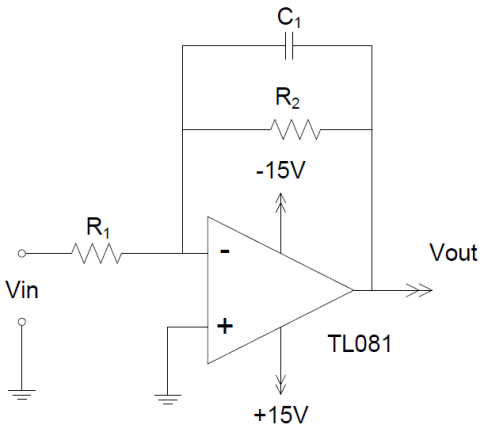

FIGURE 3.22: Schematic diagram of anti-aliasing filter.

This op-amp configuration has a DC gain of $-R_2/R_1$ and the stop band drops off -20 dB per decade because it is a first-order filter. The selected cut off frequency was 50 kHz and the gain was -1. The cut off frequency was selected according to the sampling frequency of the acquired self-mixing signals.

3.3.3 Data Acquisition System

In order to digitize the probe signals, a commercial data acquisition system was used. In this work the NI USB-6361 was used to acquire all the data [115]. This module has a resolution of 16 bits and a maximum sample rate of 1MS/s with multiple channels and 2MS/s if only one channel is performing the acquisition [115]. This platform is connected to a host computer running Matlab® R2011a data acquisition toolbox. Through Matlab® it is possible to control the acquisition parameters such as sampling frequency, number of channels to acquire, total time of acquisition and recording the signals for posterior analysis.

3.4 Database and Graphic User Interface

With the first acquisitions, when the collection of signals becomes larger and some data could be loss or become unsystematic emerge the necessity to create a structured database. Storing the data in a relational database brings several benefits, such as the possibility to reduce the redundancy, to enhance the data integrity and flexibility, to facilitate the data access to users as well as improve data security.

According to the system requirements, for a several optical probes, a relational database was developed in order to store and organize the acquired data from the optical system with the patient clinical information and the acquisition characteristics, and was connected to the signal processing software in order to achieve an integrated system.

3.4.1 Database Schema

A database schema is the set of diagrams that define its entire structure of the database. A relational database schema is composed by an arrangement of tables (entities) and the relationships between them. An Entity-relationship (ER) model is a high-level database modelling method used to build a conceptual design for a database. An ER diagram illustrates the data architecture, how the attributes are arranged by different entities and gives a global view of the relationships between them.

Four entities were created: *Acquitision*, *Porbe*, *Operator* and *Subject*. The *Acquisition* entity contains the basic principle of the system requirement: a patient could be submitted to more than one acquisition but one acquisition has to belong to one and just one subject. The *Acquisition* entity contains all the values of the obtained hemodynamic parameters, such as PWV (determined by several algorithms), AIx, SEVR, ETI or dP/dt_{max}, among others. It also comprises data that will better define the acquisition, such as which probe had been used, in which institution was the acquisition carried out, which operator had realized the acquisition, as well as time/date characteristics and the filename of the saved file (that corresponds to the acquired signal). When applicable, the values acquired by commercial devices (for comparison purposes) can also be saved.

The *Subject* entity allows to store personal data of each patient, such as biometric values, diseases and risk factors information, as well as familiar medical information. The *Probe* register which probe was used in each acquisition, and *Operator*, the whom operator did the acquisition.

As each probe could be used for more than one acquisition (or none) but one acquisition could be made with one and just one probe (mandatory), the relationship between the entity *Probe* and the entity *Acquisition* has a cardinality one to many (1:N) and is mandatory in *Probe* to *Acquisition* direction. The same is applied for the relationship between *Operator* and *Acquisition*, and between *Subject* and *Acquisition*.

Every entity has an attribute (or attributes) is named primary key and it allows the univocal identification of any record in the table. To univocally identify each record in *Acquisition* table, an incremental serial attribute was defined as primary key (*id_aquisition*). In *Subject* entity the chosen primary keys are the initials of the subject name (initials) and the Date of Birth (DOB). Preferably the primary key to univocally identify the subject should be an identification number or patient registration number. However, the identification number no guarantee the confidentiality of the subjects.

For every attribute there is the need to define the data type that will be stored and the constraints for each one. This has a special importance in maintaining the data integrity; restricting the entry of data values in a specific type help to reduce the probability of violation of the integrity rules. As mentioned before, the entities are related to each other by specific relationships. The attributes that define those relationships are foreign keys. A foreign key is an attribute (or a set of attributes) of one table that is identified as primary key in another table, allowing the record association between those tables.

The developed physical model is represented in Figure 3.23. Both the ER and the physical diagrams were designed using the Sybase PowerDesigner (v. 15.2, Sybase Inc.) software.

The Database Management System (DBMS) used to control, maintain and access the developed database is PostgreSQL 9.1 (v. 1.14.0, PostgreSQL Inc.), which consists of software that allows the access, maintenance and the control of data by one or more users. The DBMS ensures that the integrity of the data, since it guarantees that the requests made by the user to save or modify data does not infringe the defined constraints.

The user interface to a relational database is the Structured Query Language (SQL). The SQL statements permit the user to manipulate, define, control and consult the data

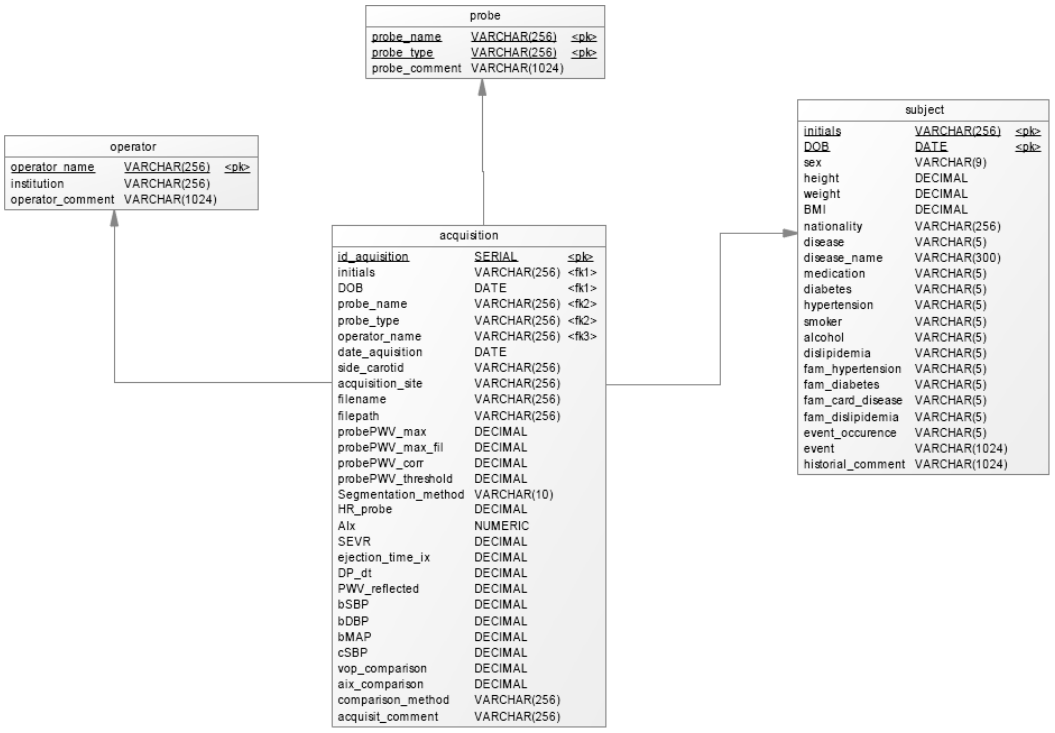

FIGURE 3.23: Developed physical diagram of database. The symbol $< pk >$ represent the primary keys of each entity and $< fk >$ represent the foreign keys. Adapted from [81].

in a database. From a physical model a set of SQL statements are generated in order to create the tables, define relationships, characterize attributes and data types and specify column constraints.

3.4.2 Graphic User Interface

The interface encloses the real time acquisition signal processing and database connection joined in a single graphic user interface that allows the user to: quickly visualization in real-time the acquired data, process and save it; visualization of the signal segmentation, as well as filter the baseline variations and change features of the peak detection algorithm; save the acquired signal for further processing with a default file name (patient name, date, time and probe); store the obtained hemodynamic parameters in the database and data acquired by another device can also be introduced in order to be able to compare the obtained values.

The Figure 3.24 shows a schematic flowchart of the principal steps of the user interface. When the user opens the software, four main options are available: *Register new patient*, *New acquisition*, *Open saved signal* and *Consult*.

In the *Register new patient* option, the user can insert a patient in the database by fulfilling a set of text fields with the patient personal data and biometric parameters and answer to several questions concerning clinical history. In each text field in which the user is asked to fill with required information, entry rules were defined for not violate the defined constraints in database and, in case, it warns the user.

In the *New Acquisition*, the real-time window will open (Figure 3.25). In this window the user can choose the patient name, the probe type, the operator name as well as the institution where the assessment is occurring. The values of the arterial blood pressure measured with a sphygmomanometer, should be inserted in the appropriate

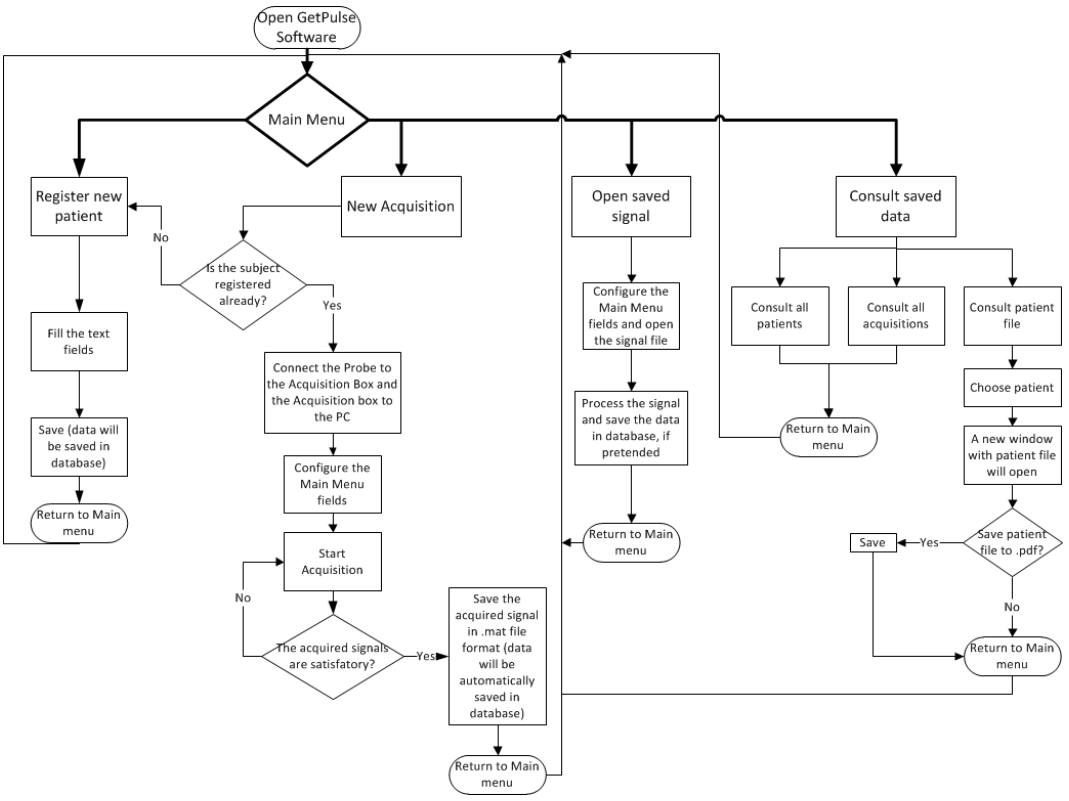

FIGURE 3.24: Flowchart of the main steps of user interface. Adapted from [81].

fields, in order to calibrate the system. In the moment of user choose the probe in use, automatically, the acquisition frequency of the signals and the channels from the data acquisition system related to the probe are selected. After setting up the main menu and be sure that the connections between the box and the probes/PC are established the user can press Start button in order to start the acquisition. A real time graphic will show, and each channel, corresponding to both photodetectors has a different colour (green and blue).

In the end of acquisition process, the user can review the entire acquired signals through the sliding bar and zoom parts of the signal with the zoom buttons. The user can choosing a part of the obtained signal to apply the processing algorithms, clicking in the data selection button of the signal acquisition environment. After the data selection, the data processing environment of the interface is automatically opened (Figure 3.26).

In the signal processing, the signals are normalized and can be filtered with a digital filter that removes fluctuations of the signal from the patient's breathing or clinician handling. Then, both maxima and minima of the signals are detected and identified in a separate plot for each signal. A parameter for peak detection improvement can also be manipulated by the user to adjust the value for the signal in analyses. The signals are segmented and and shown in two boxes each one related to a single photodetector, separate pulses (multi-color lines) and their average pulse (black line) are overlapped. The several hemodynamic parameters determined are shown in a table, and can be saved with a segment of signal analyzed.

In the Main menu, *Open saved signal*, allows the user to open and process an already saved signal press. A new window will appear and the user should choose the intended file.

Finally, in *Consult* section the user can access to the stored data in database. The user

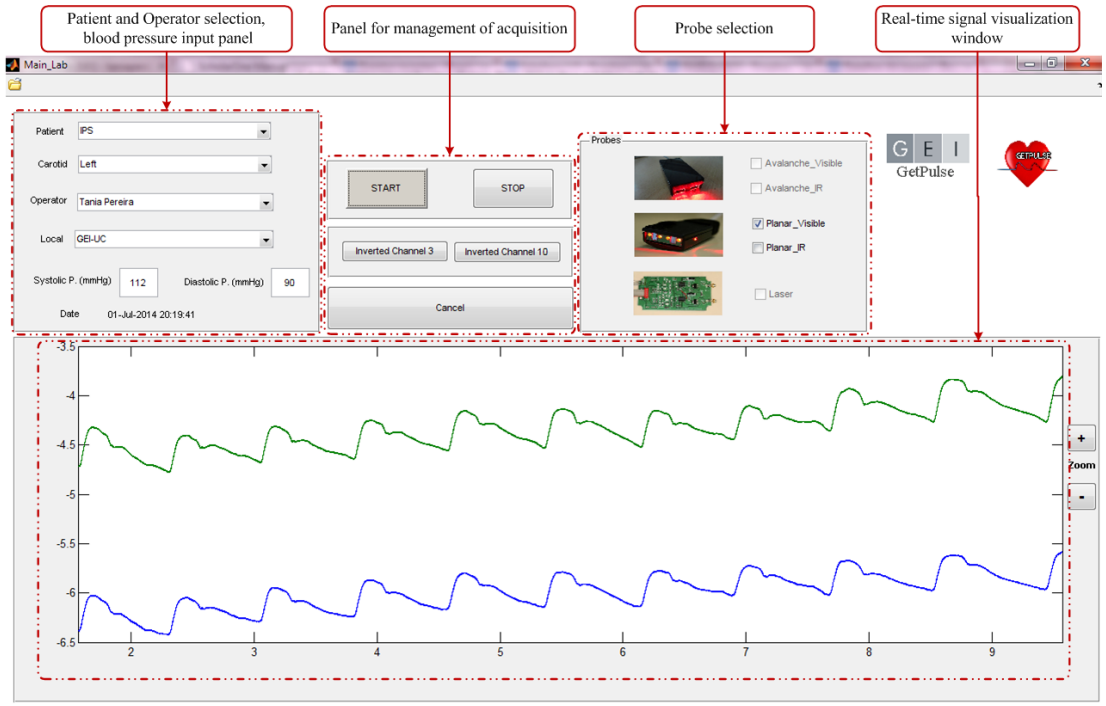

FIGURE 3.25: *GetPulse* new acquisition window.

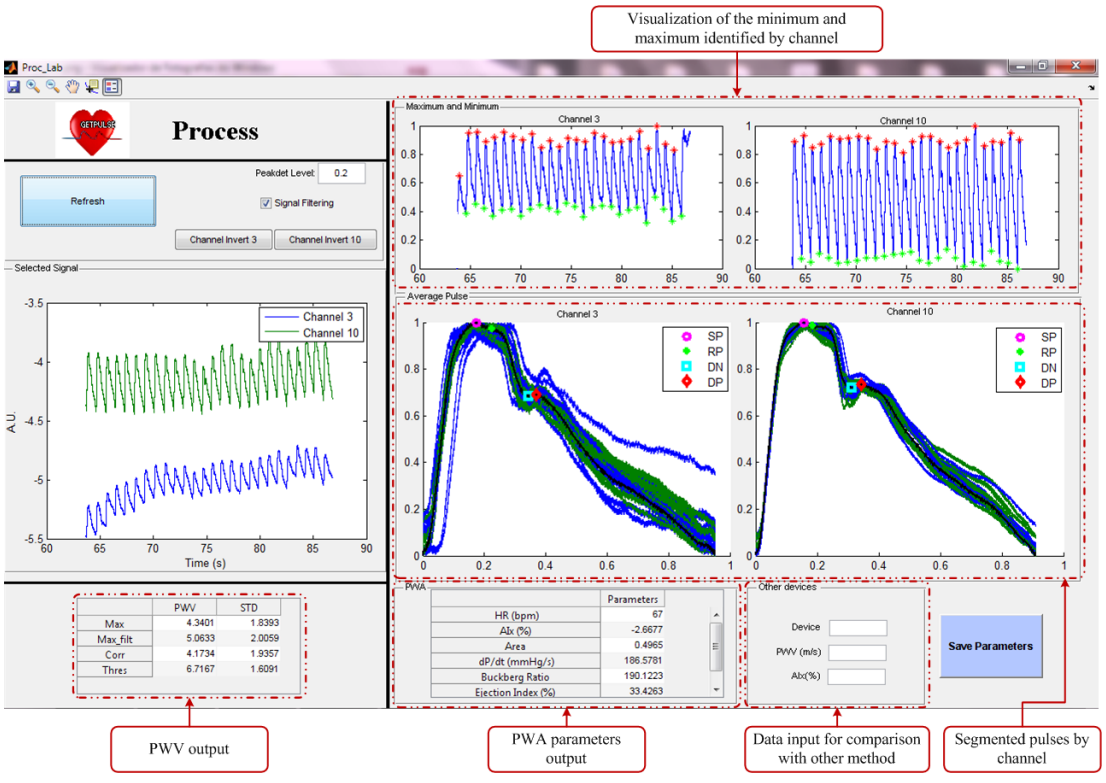

FIGURE 3.26: *GetPulse* signal processing window.

can see which patients are registered in database, how many and what acquisitions have been made, and the patient file as well as the obtained data from the signal processing.

Chapter 4

Signal Processing Algorithms

The optical probe solutions, previously described, were developed with the purpose of determining clinical relevant parameters, from an arterial distension profile signal. With this in mind, a set of algorithms was developed and optimized, tailored for each of the probe's technology features and constraints. While the prototypes based on non-coherent light generate amplitude modulated signals, the coherent light prototypes produce a distinct family of signals where the information is contained in the frequency modulation pattern. The aspects related to the development of these algorithms are comprehensively presented throughout this chapter.

4.1 Amplitude Modulated Signals

The relevant information in the signals generated by probes based on non-coherent light is contained in amplitude modulation, by the determination of the inflection points in the structure of the arterial pulse waveform (see Figure 2.4).

During one acquisition the collected data are stored directly into a portable computer. These signals are processed offline in order to parametrize the arterial pulse waveform and calculate the corresponding cardiovascular performance indexes. A schematic overview of the methods for signal processing is represented in Figure 4.1, for the Pulse Wave Analysis and for Pulse Wave Velocity determination are two different sequences of signal processing, described by the left and right route, respectively.

Concerning PWV determination (on the right side of the Figure 4.1) the full-length of chosen sequence the acquired signals from the double channel are considered. Afterwards the two signals underwent a segmentation process and the pulse wave velocity is determined by one of the four algorithms that were developed for PTT determination.

The several steps for the PWA are described in Figure 4.1 on the left side, only one of the two signals acquired by the photodetectors is used. A set of cyclic waveforms coming from one of the channels, with some seconds of duration, undergo segmentation and normalization to the diastolic–systolic pressure range. An average pulse is determined and used to compute the hemodynamics parameters. The average pulse is digitally low-pass filtered, which removes the noise, thus allowing the signal differentiation.

The feature extraction algorithm, capable to detect remarkable points of the PWA, was implemented to detect the SP, RP, DN and DP in the previously determined average pulse. For the optical system based in non-coherent light, the developed algorithm for

waveform features determination is based on differential calculus and was applied to the remarkable points as a tool to quantify arterial pulse waveform features. This method uses the consecutive zero-crossing of the first, second and third derivatives to detect inflection points that correspond to the clinically interesting features of the waveform. The last step for PWA is the linear normalization of the carotid pressure wave that was accomplished with the values collected at the brachial artery, Diastolic Blood Pressure (DBP) and Mean Arterial Pressure (MAP). It was assumed that MAP is relatively constant along the arterial tree and that DBP do not vary considerably between the carotid and brachial arteries, whereas Systolic Blood Pressure (SBP) increases along the arterial tree. These values were used to calibrate the carotid pressure waveform as recommended and according to the calibration method proposed by Kelly and Fitchett [116], [117]. After this sequence for pulse waveform analysis the AIx, SEVR, ETI, HR and dP/dt_{max} were determined.

The specific algorithms are further described in the subsequent subsections.

4.1.1 PWA Algorithms

4.1.1.1 Segmentation Algorithms

For the PWA parameter determination the segmentation procedure of the acquired signal into single pulses is fundamental. Three algorithms were developed in order to segment the set of acquired pulses for the hemodynamic parameters determination, namely the the windowed systolic peak, minimum point and upstroke threshold methods.

In this section only the algorithms developed for signal segmentation in the PWA are considered. In this way, they are only applied to the signal acquired by just one photodetector and do not have to preserve the time delay information between both channels, contrasting with the segmentation procedure for PWV determination. The segmentation methods for PWV computation will be further presented in subsection 4.1.2.

Windowed Systolic Peak

The windowed systolic peak method consists in a window defined by a typical proportions of a regular waveform, before and after the maximum peaks of the set of pulses, as represented in Figure 4.2 (upper). The method uses the automated peak detection function in Matlab® (Peakdet from the Mathworks, by Tom McMurray) [118]. The Peakdet function analyses the selected signal and detects all the local maxima and minima in the acquisition prior to any filtering. The time difference between consecutive maximum was determined and the window of pulse was defined by the point in the waveform that corresponds 20% of time before the SP and 60% after that.

Minimum Point

This method is based on the determination of the lowest values of the set of pulses,represented in Figure 4.2 (lower), by a peak detection function, Peakdet. Each local minima, foot of waves, were used to segment the signals. The set of pulses is cut attending to the detected points. This method enables the segmentation at the level of the corresponding diastolic pressure ensuring, in this way, the segmentation of the signal in the end of each cardiac cycle, *i.e.*, in the end of each diastole. However in some waveforms, when there are baseline variations or with a low SNR in the diastolic part of the signal, the minimum method could lead to erroneous determinations.

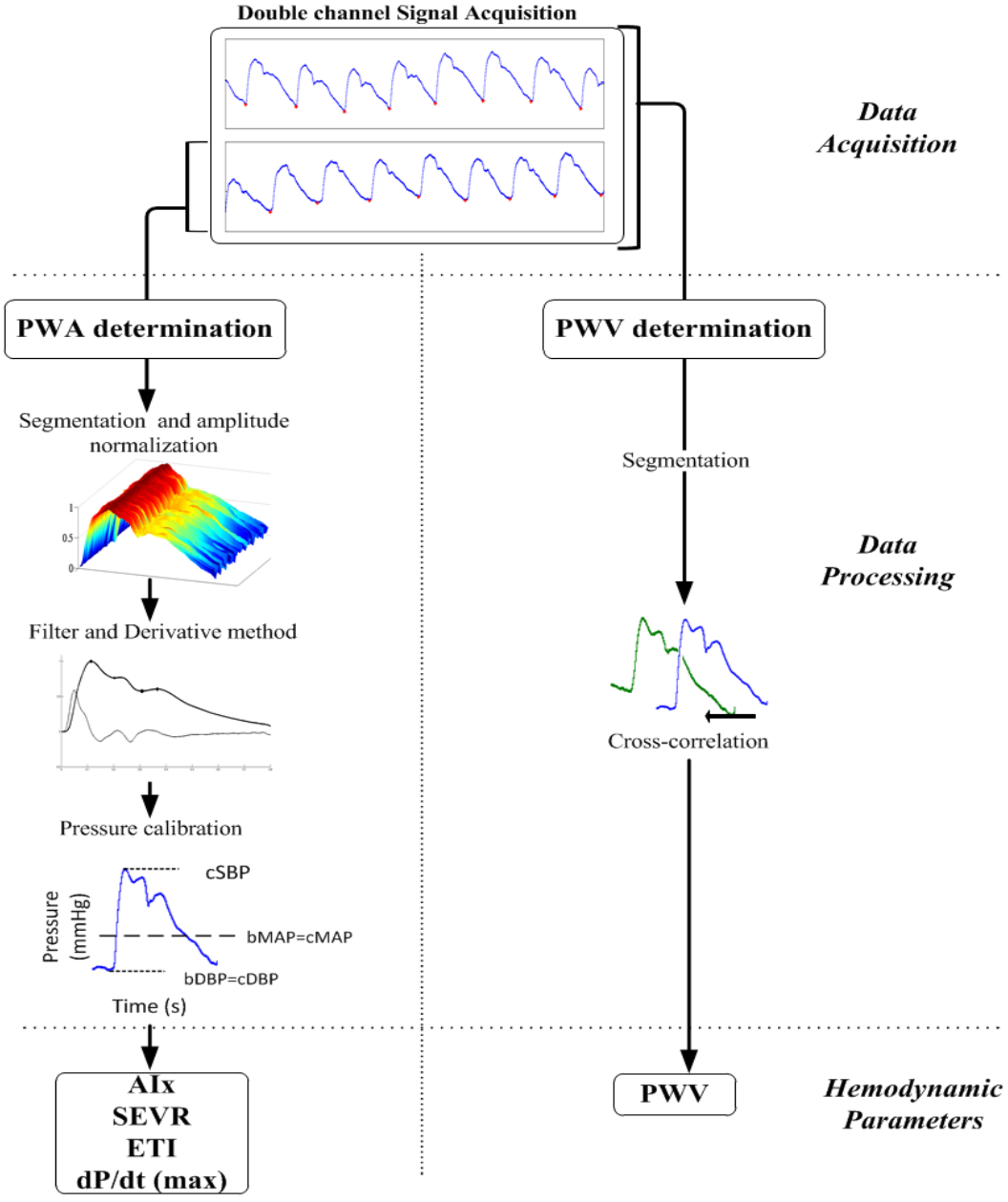

FIGURE 4.1: Schematic overview of the data processing workflow to determine the hemodynamic parameters.

The method of minimum point takes the assumption that all the pulses have the same proportion between diastolic and systolic duration, which does not comprises all physiological cases. The extraction of a part of pulse waveform and not the total of the pulse, could eliminate a fraction of the latter diastolic baseline, but the diastolic fraction of the wave does not consist of a determinant region of interest for extraction of parameters in the pulse wave analysis. However, if the upstroke is cut it will compromise the determination of several parameters.

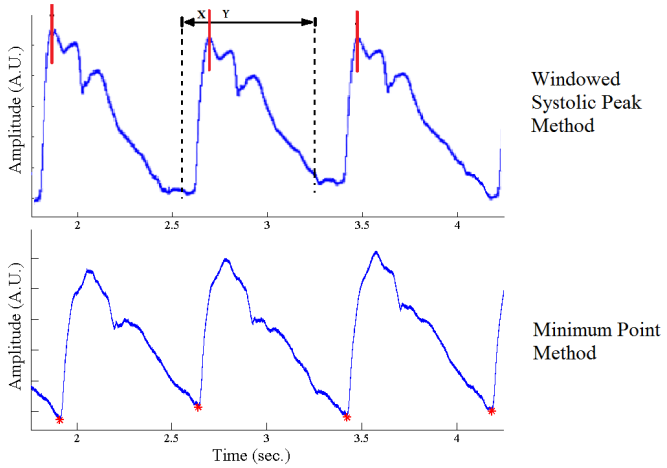

FIGURE 4.2: Segmentation algorithms. Schematic representation of the windowed systolic peak method for signal segmentation (upper). Minimum segmentation method in a set of pulses (lower). Adapted from [81].

Upstroke Threshold

This method segments the pulses at the instant when the upstroke reaches 10% of its total amplitude. This value cannot be neither too low, because the baseline variations would compromise the segmentation; nor too high, or, in the cases that the reflected peak occurs before the systolic peak, the RP might not be considered. However this method has the drawback of cutting part of the total amplitude of the upstroke, preventing the determination of several important PWA parameters, such as dP/dt_{max}, AIx or SEVR.

For these reasons, and due to the simplicity and the minimum point method efficacy on a major number of types of waveform, this was the chosen method used to segment the signal in order to determine the hemodynamics waveform features.

4.1.1.2 Brachial to Carotid Artery Pressure Calibration

The calibration method is currently still a demanding challenge for optoelectronics probing techniques such as the hereby presented [119]. The determination of a number of hemodynamics parameters, specially the dP/dt maximum rate, leads to the requirement of pressure calibration. Currently, the amplitude of the obtained arterial pulse waveform through this optical system has to be scaled with the pressure measured inside the carotid artery. With this purpose, an algorithm that allows the calibration of the carotid pulse waveform using the measured brachial blood pressure (brachial Diastolic Blood Pressure (bDBP) and brachial Systolic Blood Pressure (bSBP)) by sphygmomanometry was implemented and is schematized in Figure 4.3.

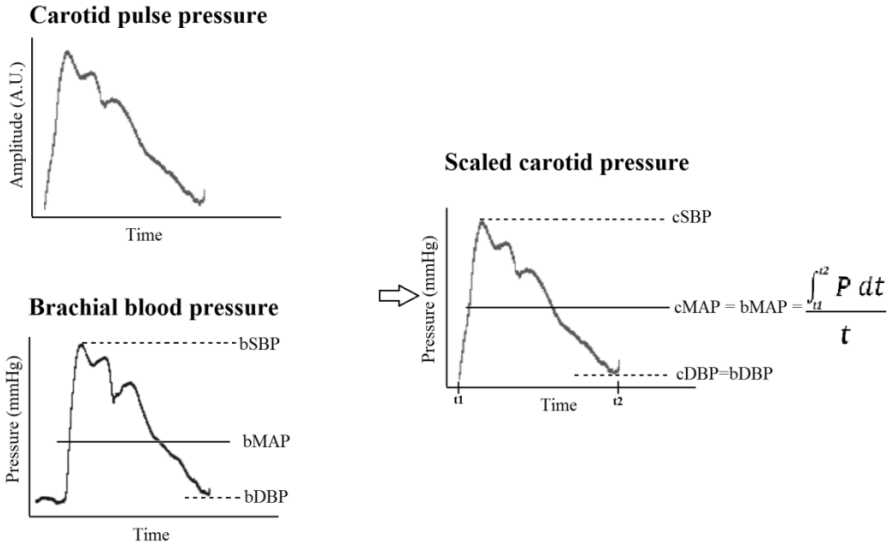

FIGURE 4.3: Brachial to carotid blood pressure calibration procedure. Adapted from [81].

As it was previously referred, in section 2.2.1, the arterial pulse pressure changes throughout the arterial tree, suffering an increase in the whole amplitude of the pulse pressure when it travels to a distal vessel, due to an amplification of SBP whereas the DBP do not vary considerably between carotid and brachial arteries [64], [116], [117].

The method proposed by Kelly and Fitchett (1992) was used for calibrate the carotid pressure waveform [116], [117]. This method was based on the assumption that the bDBP and carotid Diastolic Blood Pressure (cDBP) have the same pressure value and the carotid Mean Arterial Pressure (cMAP) corresponds to the mean pressure along a cardiac cycle. One can determine graphically the mean pressure of carotid waveform cMAP in the wave function (arbitrary units), through the division of the numerical integration by the length of the pulse 4.3.

Using the measured bDBP and the graphically determined brachial Mean Arterial Pressure (bMAP), the carotid waveform is calibrated and the carotid Systolic Blood Pressure (cSBP) is determined. This calibration procedure is a recognized calibration method, based on proven physiological findings and avoids the use of complex transfer functions that always need to be validated.

4.1.1.3 Filter and Derivative Method

For detecting the remarkable points of the pulse waveform a feature extraction algorithm was implemented to identify the systolic peak, reflection point, dicrotic notch and dicrotic peak. This algorithm is based on differential calculus and it is implemented over an average segmented pulse acquired by only one of the photodetectors available on a double probe.

The pulse waveform could vary significantly with the subject. In some cases the reflected peak occurs after the systolic peak, while there are others where it occurs before, as in the case of elderly people or in those cases of subjects presenting arterial severe stiffness.

The algorithm is based on first, second and third derivative tracing to identify the remarkable points as a tool to quantify arterial pressure waveform features, based on those proposed by other authors [33], [120], [121], [122]. In order to remove the noise

and to allow the signal differentiation a filter is applied to the determined average pulse. The signal was filtered using low-pass filter with a cut frequency of 30 Hz to remove the high frequency noise that might be present in the signal [123]. Lower values for the filter were tested but have not be sufficient to allow the remarkable points detection by the derivative method.

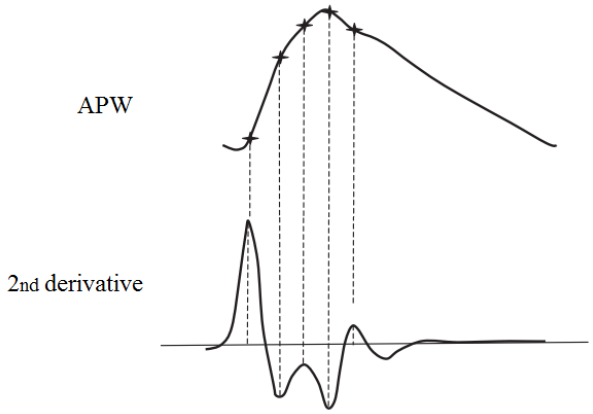

FIGURE 4.4: The arterial pulse waveform (APW, upper panel) and its second derivative ($d^2\text{APW}/dt^2$, lower panel). Adapted from [124].

The zero-crossing of the three first derivatives of the pulse are determined to further describe completely every inflection or variation that occurs in the pulse and the feature points (SP, RP, DN and DP) are identified. The zeros of the first three derivatives are used for the determination of inflection points, even the most tenuous inflections are identified, as in the situation of type A waveform (described in section 2.2). An example are represented in the Figure 4.4, the inflection points in the upstroke could be identified by the zero-crossing of third derivative.

The parameters AIx, SEVR, dP/dt_{max} and ETI are then determined by the expressions presented in table 2.1, using the location information (time and amplitude) of these points in the arterial wave.

4.1.2 Pulse Wave Velocity

The time delay determination between the signals acquired by each photodetector constitutes the main goal for an accurately local PWV determination. To achieve this, a number of algorithms were tested. PWV is computed dividing the distance between the photodetectors by the corresponding determined pulse transit time. For PTT determination it is of foremost importance to preserve the time delay between the two signals when segmenting, for this, one of the acquired signals is segmented by its minima (Figure 4.5) and the segmentation in the second signal is made taking into account the corresponding time period of the segmentation of the first signal.

For the set of cyclic waveforms detected, segmented and normalized for PWV, four different algorithms for extraction of the time delay from the two signals were applied. They are referred to as Foot-to-foot, Maximum, Threshold, Phase Spectra and Cross-Correlation algorithms. Their basis derives from the homonymous mathematical functions which is simply explained in the next sections. The foot-to-foot, maximum and threshold algorithms focus solely on the first part of the waveform (systolic period) while, the cross-correlation takes into account all the length of the pulse. All these methods are sensitive to the reflections in the structure of signal. The phase spectra is an frequency domain analysis, and less sensitive to this phenomena.

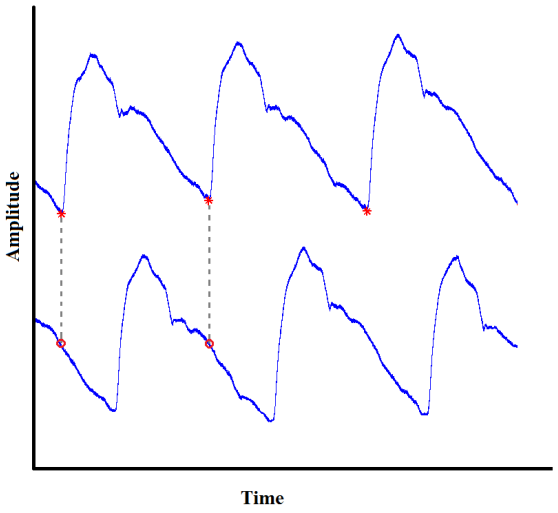

FIGURE 4.5: Schematic representation of the segmentation process for PTT determination. Note that the time delay is overrepresented to exemplify, since the original time delay is in the order of few miliseconds. Adapted from [81].

4.1.2.1 Foot-to-foot Method

The foot-to-foot technique is the most common used for the transit time estimation in tonometric studies [85]. In the foot-to-foot method, and, in spite of more complex methods, a simple detection of the time lag between the start of the upstroke of the two consecutive pulses is carried out [125]. The foot of the pulse wave is the point of minimal diastolic pressure before upstroke of the pulse wave in the new cardiac cycle.

The "derivative method" and the "intersecting tangent method" are the most reproducible computer algorithm available for the determination of the foot of the pulse wave [26], [125], [126]. This is possible due to the well behaved nature and low noise levels of signals. A different situation usually occurs in signals collected from a patient, mostly due to baseline drift and affected by the superimposed reflections (Figure 4.6). The foot point of the arterial pulse waveform is such a trivial task as it may look at first sight. It is known that, depending on a chosen measuring point, the arterial pulse waveform reflections distort the arterial pulse waveform foot to a certain degree.

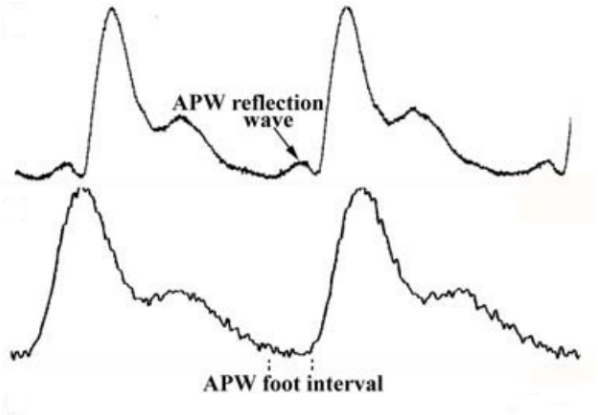

FIGURE 4.6: Arterial pulse wave with a main problems in foot detection, a reflection wave (upper) and signals with higher noise level. Adapted from [125].

Figure 4.6 shows that the arterial pulse waveform foot is long and flat, and the differences between nearby values are small. Consequently, even a slight noise or interference difficults the task of determination of the foot point in the arterial pulse waveform [125].

A method based on an automated peak detection function in Matlab® (Peakdet from the Mathworks, by Tom McMurray) was implemented with this propose. The algorithm analyzes a window of several pulses and detects all the local minima and maxima in signals from two photodetectors. The transit time is determined by the difference between the minima point, foot of each waveform. An average value is calculated and the PWV obtained through this algorithm is displayed.

4.1.2.2 Maxima Method

The maxima algorithm is based in the same automated peak detection function in Matlab® (Peakdet from the Mathworks, by Tom McMurray), however uses the maximum of waveform from each photodetector for estimation of the time delay. Similarity to the minima algorithm, this method provides an average value for each set of two pulses, originated by the two distinct photodetectors.

Since the PTT determination is based in a single point on both signals, the limitations of this algorithm become evident, if one considers the noise effect in the maxima determination. Indeed, the noise is responsible for many wrong PTT determinations in signals with low SNR. With the purpose of testing an alternative for the maxima point algorithm problem an digital low-pass filter was tested (cutoff - 30 Hz, the same that was tested for the PWA agorithm, presented in the section 4.1.1.3) [123]. Even though, it is recognized the main drawback of using a filter, since the signal undergoes a temporal shift which involves a loss of important information for the original assignment of PWV determination. The conclusion is that the filtered signal is corrupted by the noise leading to miscalculations of PTT. Besides, the use of filter does not ensure that the signal is not being delayed.

As the systolic peak detection showed to be too sensitive to the noise presence, this algorithm was not considered preferable to determine PWV.

4.1.2.3 Threshold Method

The threshold algorithm consists of determining the time delay between the points that assumedly corresponds to 20% of the systolic upstroke amplitude of the normalized set of pulses acquired by each photodetector. The value of 20% threshold of the systolic upstroke was chosen considering that this part of upstroke do not suffer modifications the reflections or baseline artifacts.

This algorithm is also based in the detection of a single point and it has the inherent drawback in signals with low SNR. Moreover, as the pulses are normalized, the 20% point of the upstroke in the pulse acquired by one photodetector might not necessary correspond to the analogous point on the other waveform. This issue assumes special importance when there is a significant discrepancy between their amplitude, which represents an advantage when for the time delay determination.

4.1.2.4 Cross-Correlation Method

The cross-correlation method is based on the property of the peak of cross-correlogram that allows delays to be calculated by subtracting the peak time position from the pulse length. The two waveforms are normalized and then temporal difference is calculated by the equation (4.1),

$$C_{sg} = \sum_{t=0}^{t=T} s(\tau)g(t+\tau), \tag{4.1}$$

where t is the sweep of distal waveforms for successive correlations, 0 and T denote end diastole of a waveform, and end diastole of the subsequent waveform, respectively and s and g are the two waveforms from each photodetector [127].

With each set of two pulses (coming from each photodetector) two correlograms are obtained; one from the auto-correlation (correlation between the same pulse) and cross-correlation (correlation between the pulses originated by both photodetectors), as illustrated in Figure 4.7.

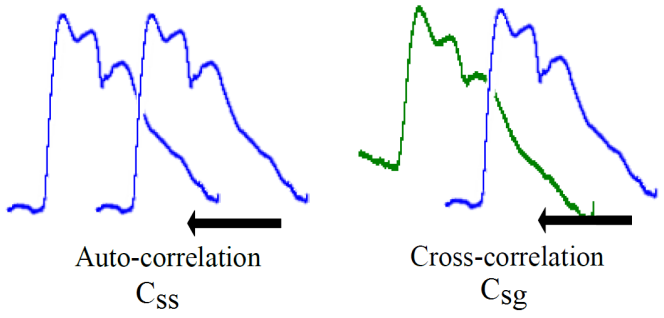

FIGURE 4.7: Schematic representation of auto-correlation and cross-correlation. Adapted from [81].

$$PTT = t_{maxC_{ss}} - t_{maxC_{sg}} \tag{4.2}$$

The PTT is determined subtracting the time delay of the maximum point of the auto correlograms and cross correlogram (equation 4.2). A generic correlogram is displayed by the number of points that corresponds to the length of the pulses against the amplitude of the correlation between each set of pulses. As the correlogram implies the correlation between two signals, the total length of it is twice the length of just one pulse less one point (2N-1). The PTT is extracted by subtracting the number of points between both peaks of the correlograms.

The correlation function used belongs to the Matlab® core (*xcorr*) that generates the cross-correlation making direct use of the cross-correlation theorem [128].

The main advantage of using cross-correlation over other waveform identification methods (foot-to-foot, maximum and threshold) is that the cross-correlation calculates the time delay of the wave using all of the data points of the waveforms rather than identifying the arrival of the wave by a single point. In this way, errors from poor wave arrival time estimations can be minimized [129].

The cross-correlation is a technique to compare two waveforms. The pulse wave at each vessel location is affected by the arrival time and reflection amplitude changes in the waveform shape along the arterial tree. For the optical system the waveforms detected by the two sensors have similar shapes, since are measured in adjacent locations (carotid vessel) rather than comparing the waveforms from different vessels. Dissimilar shapes in cross-correlation analyses introduce inconsistency in the results [129]. In the distension waveform the upstroke region is less susceptible to interference from reflected waves, and the noise could be affecting same parts of wave that introduce an error in the PWV determination. To overcome this expected problems the cross-correlation was applied in the variable sliding window of pulse waveform.

Cross-Correlation Algorithm: Sliding window

This method consists in a sliding window consecutively smaller that cuts the corresponding set of two pulses from each photodetector in smaller portions, where only a percentage of pulse pressure was analyzed and at each iteration the proportion of pulse decreases down to 50% which comprises approximately the region of upstroke in the wave. The set of those portions for each set of two pulses are submitted to cross-correlation, and the average PTT value is extracted. In this way, the contribution of errors in the PTT determinations, that were influenced by reflected waves or regions with more noise, are diminished in the average calculus.

4.1.2.5 Phase Spectra Method

The fifth method uses data in the phase spectra of the signals. Since the estimation is conducted in the frequency domain. In this method, the exact frequency of the signal's harmonics is firstly identified, using the amplitude spectra, and then, extract the corresponding phase angles from the phase spectra. The phase angle, θ, is related with angular frequency of the phase spectrum, ω and with the time delay, t, according to:

$$\theta = \omega t, \tag{4.3}$$

On its turn, the time delay is computed from the phase angles of the same harmonic in the phase spectra of each signal, θ_1 and θ_2:

$$t = \frac{(\theta_1 - \theta_2)}{\omega}. \tag{4.4}$$

Despite the fact that, theoretically, the time delay can be determined at any harmonic of the complete spectrum, the practice, however, differs, given that they are difficultly affected by noise. This method is used for time delay estimation in deterministic signals, namely, a single complex sinusoid [130].

4.2 Frequency Modulated Signals

The main application for the entire system is to record and analyze the pulse pressure waveform in human carotids and extract the clinical information.

Self-mixing signals frequencies are related with the Doppler effect and velocity absolute value of the target object. Due to that information encoding, a reconstruction algorithm is needed to transform the frequency information carried by self-mixing signals into velocity information. Since the self-mixing signal is correlated with the absolute value of the velocity, it is relevant to present the absolute value of the derivative of membrane movement.

A global vision of Doppler signals processing was described in Figure 4.8. The Doppler signals require a time–frequency analysis to extract most of the physiologically important parameters. An algorithm based on the Short-Time Fourier Transform (STFT) and EMD, was used to find the feature points of the pulse waveform.

4.2.1 Maximum Power Density Profile

The first step in the signal processing is the time-frequency analysis (Figure 4.8). The self-mixing signal presents a frequency change when the target object varies its velocity.

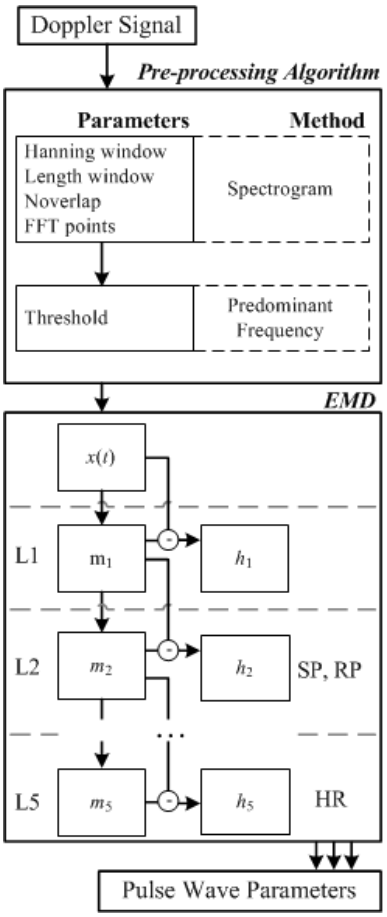

FIGURE 4.8: Schematic overview of the algorithm developed. Algorithm for pre-processing the Doppler signals and several levels of the EMD.

These frequency variations encode the most important information of the distension waveform, so a time-frequency analysis is needed.

The short time Fourier transform is a powerful tool to analyze non-stationary signals. The STFT has been used to process self-mixing signals in hemodynamic applications by several authors [76], [104].

In the continuous-time case, the function to be transformed is multiplied by a window function which is nonzero for only a short period of time. The Fourier transform (a one-dimensional function) of the resulting signal is taken as the window is slid along the time axis, resulting in a two-dimensional representation of the signal. Therefore, the STFT is mathematically defined as:

$$STFT\{x(t)\}(\tau,\psi) \equiv X(\tau,\psi) = \int_{-\infty}^{\infty} x(t)\Psi(t-\tau)e^{-j\psi t}dt, \tag{4.5}$$

where $\Psi(t)$ is the window function, commonly a Hann window or Gaussian window bell centered around zero, and *x(t)* is the signal to be transformed. $X(\tau,\psi)$ is essentially the Fourier transform of $x(t)\Psi(t-\tau)$, a complex function representing the phase and magnitude of the signal over time and frequency. Often phase unwrapping is employed along either or both the time axis, τ, and frequency axis, ψ, to suppress any jump discontinuity of the phase result of the STFT. The time index τ is normally considered to be "slow" time and usually not expressed in as high resolution as time *t*. Another important role for the windows function is their spectral leakage prevention. The most

common window functions are Hamming window, Hanning window, Blackman window and rectangular window. The Hamming and Hanning windows present a more balanced performance comparing to Blackman and rectangular windows [131].

The designed algorithm uses a 124-point length Hanning window and a 100-point segment overlap for high temporal resolution. The use of this type of window is referred in literature for self-mixing signal analysis [75], [104].

The STFT was performed in Matlab® through the usage of *Spectrogram* function. The spectrogram provides visual information of the STFT results by using a colormap to illustrate the STFT coefficients for each time and frequency (Figure 4.9). It is a two-dimensional plot of the energy of the frequency content of a signal as it changes over time. A waveform similar to the pulse pressure waveform derivative is evident in the spectrogram but a strong DC component is also visible. The DC component was expected because the original signal has small amplitude variations compared to the DC electric potential value and no high-pass filter was used. This component does not have significant information. In order to determine the most predominant frequency, in the self-mixing signal, along time, it is necessary to remove the DC component. This component is removed using a threshold to cut off the coefficients of small frequencies according to the resultant spectrogram.

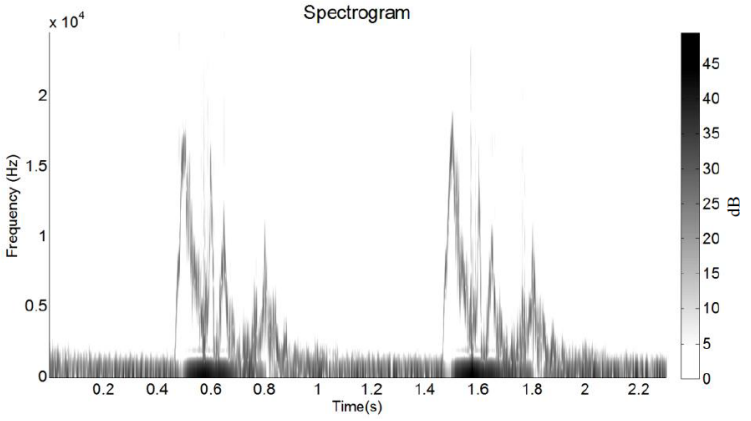

FIGURE 4.9: Spectrogram of the original signal. The image of spectrogram results on a conventional grey scale representation with 50 dB corresponding to the signal maximum value.

By finding the higher coefficient along time and register the respective frequency it is possible to obtain a reconstructed signal of most predominant frequency *vs* time. The Figure 4.10 shows the waveform presented in the spectrogram image. The noise is a repercussion of DC removing threshold once some zero spikes are noticed during the signal oscillation.

An example of a time domain Doppler signal from a single pulse pressure waveform and the corresponding Doppler spectrogram is shown in the next Figure 4.11 [6]. The Doppler relation states that the Doppler frequency is related to the velocity of the moving target. In this case, the frequency is proportional to the velocity of skin vibration (that corresponds the distension of artery wall). The skin vibration (Figure 4.11a) is related to the first derivative of the blood pressure pulse (dP/dt) in Figure 4.11b. Applying a STFT over the Doppler signals, a Doppler spectrogram can be obtained, which presents the Doppler frequency shift as a function of time, that is comparable to dP/dt of the original waveform. This is shown in Figure 4.11d) [6].

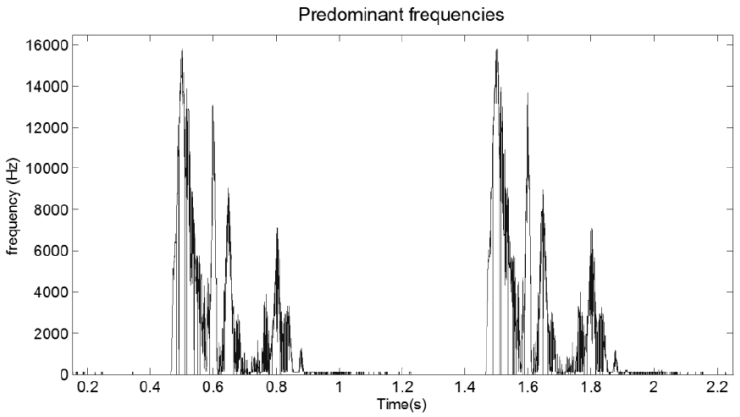

FIGURE 4.10: Predominant frequencies along time.

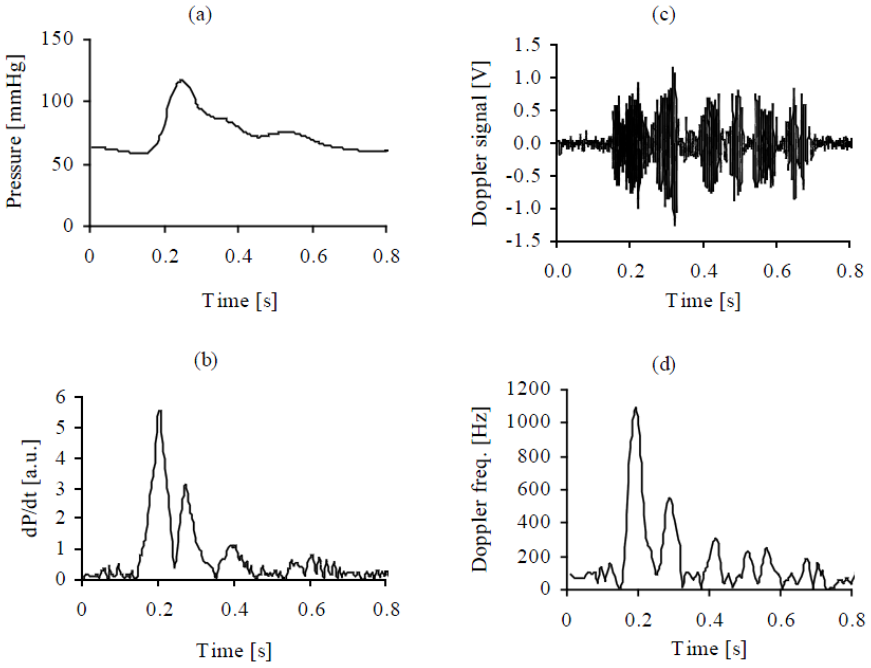

FIGURE 4.11: Processing Doppler signal and arterial distension waveform. (a) Normal blood pressure pulse and (b) first derivative of the pulse, (c) Doppler signal of the blood pressure pulse and (d) spectrogram of the Doppler signal. Adapted from [6].

The maximum Doppler frequency can be located to the rising edge of the blood pressure pulse, where diastolic blood pressure changes to systolic. In the pulse the maximum frequency is 1.1 kHz (measured with a laser-diode of λ=810 nm), which corresponds to 445 μm/s radial velocity determined by the equation 3.4 [6].

4.2.2 Empirical Mode Decomposition

After a visual analysis of the frequency decomposition algorithms result it is very difficult to determine the feature points of arterial pulse waveform. To remove the noise component of the signals a low-pass filter would be the simplest manner. Low-pass filters introduce a time delay in the system so, since time occurrence of the feature points is the information to be extracted, they are not a good option. An empirical mode decomposition was used to remove the signal noise for posterior feature points

determination (Figure 4.8). This method is capable of decomposing a signal into a finite number of Intrinsic Mode Functions (IMF) creating a multistate decomposition and time-frequency analysis of the original signal [132]. The pulse pressure waveform undergoes great variability in the shape and duration between individuals; for these reasons a self-adaptive algorithm, such as EMD represents an advantage in this analysis comparatively to Wavelet-Transform [133]. The computation of the EMD does not require any previous known value of the signal, which accounts to be an eligible tool for that purpose.

The EMD and wavelet-transform, which represent standard techniques, provide the decomposition of a signal into different time scales. The main difference is that the EMD performs the signal decomposition adaptively and based exclusively on the available time series, whereas the wavelet-transform uses a set of pre-fixed filters based on the choice of a mother wavelet function and scale [134].

The arterial pulse pressure signals are the result of several biological processes (cardiac activity and arterial function) that correspond to different time scales in the analyzed signal. According to the EMD procedures, data are decomposed into several fundamental components (decomposition layers), each with a distinct time scale, sequential extraction of energy associated with various intrinsic time scales of the signal starting from finer temporal scales (high frequency modes) to coarser ones (low frequency modes). The iterative process explores sequentially the natural constitutive scales of the signal [135], giving an almost direct insight into the physiological mechanisms undergoing in the arterial propagation process.

The applied algorithm is an iterative computation where the upper and lower wave envelopes of the signal are computed using, in this case, a cubic interpolation. Then the mean value of the upper and lower envelopes (m) is subtracted from the original signal (x) yielding h_n, expressed in equation 4.6. In this case, the main goal is to find the feature points of the pulse waveform, the residue (h_n) is negligible and the envelope (m) is considered a new signal to decompose (Figure 4.8). Once the highest frequency is removed from a signal, the same procedure is applied on the residue signal to identify the next highest frequency. The stop condition implies that the number of zero crossings of m is equal, or differs by 1, to the number of the extremes [132]; otherwise it considers m as x and repeats the envelope procedure, equation 4.6.

$$h_n(t) = x(t) - m_n(t), \tag{4.6}$$

$$x(t) = m_n(t). \tag{4.7}$$

After the decomposition, for each level two data sets were obtained. The smooth effect was obtained from the envelope of higher levels, so m data represents the filtered signal. The extracted data appeared on the m signal. Due to the cubic interpolation, the decomposed signal's boundaries tend to have very large absolute values which are characteristic of the cubic functions. To solve this problem, the edges of the processed signal were removed was not introduced for the analysis and parameters determination.

Chapter 5

Non-coherent Light Probes Characterization

The current chapter presents the probe characterization tests for the prototype based in non-coherent light. Several test benches were assembled in order to evaluate three optical probes prototypes along with the dedicated algorithms. The APD and PPD probes performances were compared with the gold standard, based on ultrasound transduction, for assessment of the carotid distension waveform. The performance of the probes, both with visible and infrared light sources, was evaluated in a test setup that simulates the fatty tissues between skin and the artery, commonly seen in the obese people. Finally, an automatic method to select the signals, that contain relevant information from acquired data during clinical tests, was implemented.

The three optical probes developed with non-coherent light, using the PPD, APD and LEP was characterized in test benches in order to find the sensor with most adequate features for acquire the arterial pulse waveform in the carotid vessel and the with temporal resolution with adequate algorithm for PWV determination.

An algorithm based on a classifier that could distinguish valid data signals containing arterial pulse waveform and which part has no relevant information from signals acquired by the optical probe, represents an great advantage. There is a great potential in clinical applications for a system that assessment the arterial pulse waveform by combining the non-contact optical probe and advanced machine learning to automatic detection the signals. Another great challenge was, to study the new features and provide more information about the arterial pulse waveform. As an initial attempt in this direction, was used a substantial feature subsets that could provide an extensively study for this type of signal.

5.1 Characterization of Lateral Effect Photodiode

To characterize the probe based on LEP, both spatial and temporal resolution need to be determined and two different test setups were design for that purpose.

5.1.1 Spatial Resolution

The spatial resolution of the LEP was determined by computing the sensor's response to a laser sweep along its surface. The laser was moved by two linear actuators precision positioners (T-LA28A from ZABER® Linear Actuator, 28 mm travel, RS-232 interface) that allow precise control of the position of the laser, however, due to mechanical platform where they are inserted only 1.5 cm of the movement was allowed. The combination of both actuators in order to increase total spark of actuator origins a central artifact on the LEP response (Figure 5.1) [136].

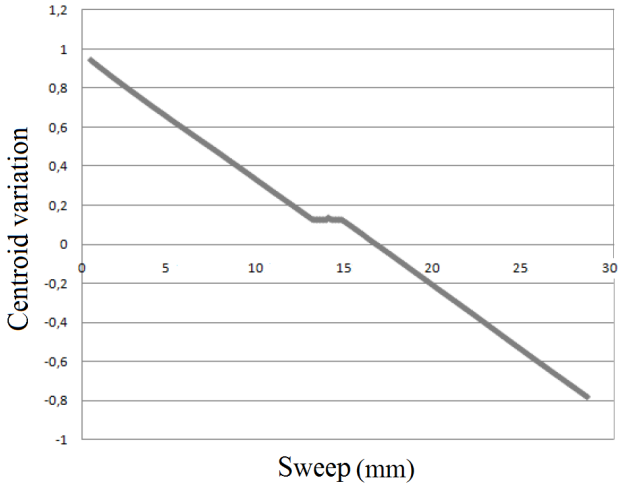

FIGURE 5.1: LEP response to a laser sweep. Adapted from [136].

Figure 5.1 shows an absence of boarding effects, which allows the use of the entire LEP area. The actuators moved 0.1μm at each step that were discriminated by the centroid position, showing a 0.1μm spatial resolution for the LEP.

5.1.2 Temporal Resolution

Temporal resolution was also determined using another test setup, consisting in a set of seven aligned LEDs that are switched on-off sequentially and independently (Figure 5.2), by a counter with a 8 outputs, CMOS Counter CD4022B [137]. An entire cycle lasted 1 millisecond, corresponding to a 30 ms^{-1} velocity, that embraces all normal and pathological PWV values.

As an entire loop of turning on-off of the seven LEDs lasted 1 ms, the frequency of LED change needed to be 7 kHz. A range of frequencies (from 0.5 to 400 Hz) were tested and some results from 1, 64, 200 and 400 Hz are shown in Figure 5.3. LEP currents are represented as blue and green lines and the centroid position is the red line.

At 1 Hz frequency, the difference between the on and LEDs is accurately determined by the variation in the centroid position, that clearly describes the steps related to each LED illumination. With the frequency increasing, these differences become less defined and, at higher frequencies, it is difficult to distinguish the steps of light variation. In Figure 5.3, the centroid position along time (red line) at 64 Hz frequency does not define clear transitions of LED illumination, as the transitions are less steeper and round shaped. For 200 Hz, these transitions are difficultly determined and the centroid position describes a clear rounded shape along the entire time interval, that is even more pronounced at 400 Hz, situations away from the conditions required with 7 kHz that represents the interest value for PWV measurement.

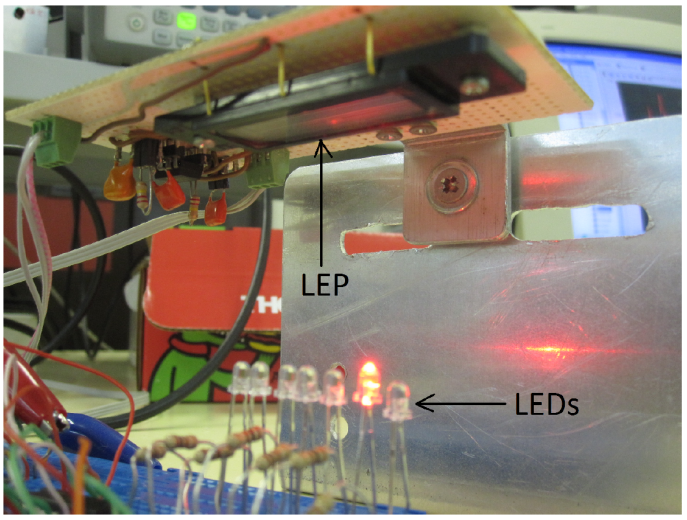

FIGURE 5.2: Test bench for temporal resolution determination. Adapted from [136].

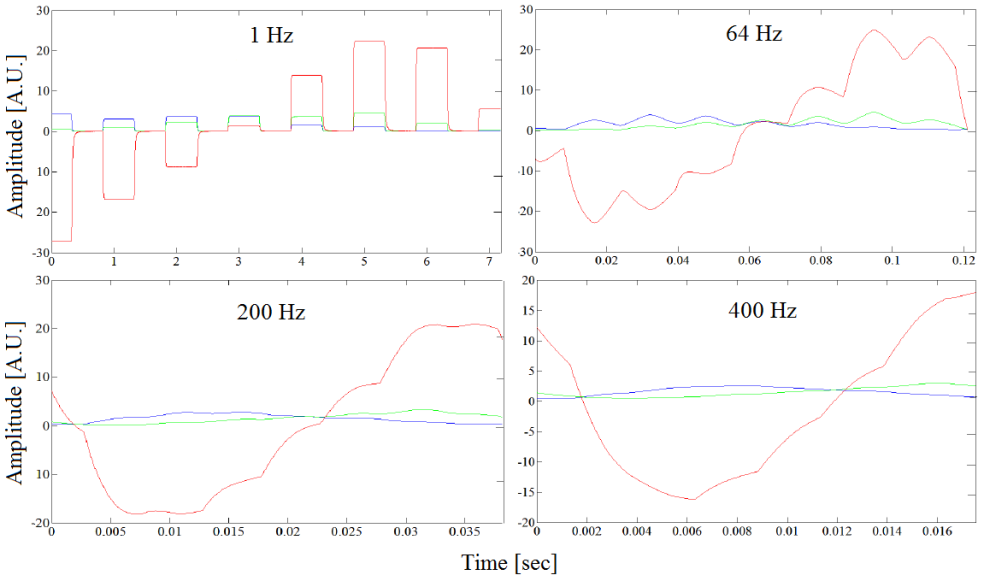

FIGURE 5.3: LEP response for a set of on-off LEDs. Adapted from [136].

This results show as the LEP response for the required frequencies did not accurately discriminate the light position transitions, from which can conclude that temporal resolution of LEP was not enough for PWV assessments.

The capacitance is therefore proportional to junction area, a high capacitance inherent to the photodiode reduces the frequency bandwidth for the detection [138]. Generally, larger devices are slower time response than smaller ones, capacitance give a definite limit on how fast they can respond to modulated light [139]. On the other hand, the size of photodector represents one limitation for an ergonomic probe configuration, essential feature for clinical applications. For theses reasons the LEP was not considered as a value sensor for one probe requirements.

5.2 PWV Algorithm Evaluation

In this study two optical probe prototypes were evaluated. These probes are dedicated to pulse transit time and three algorithms for its assessment. Although the tests were carried out at the test bench, where "well behaved" signals can be obtained, the transition to a probe for use in humans is also considered.

5.2.1 Test Bench

PWV is assessed by measuring the time delay between the signals of the two photosensors using three algorithms: foot-to-foot, cross-correlation and phase spectra. For the correlation two different functions are used: one nature from Matlab® core (xcorr) and another that generates the cross-correlation making direct use of the cross-correlation theorem (Fcorr).

The test bench was designed to assess the two main parameters of in PWV measurements: linearity and time resolution. Their assessment was carried out in a test setup where illumination is provided by two LEDs whose light intensities reproduce the same signal with a variable time delay between them, generator by two arbitrary waveform generators, Agilent 33220A (AWG1 and AWG2), are synchronously triggered by an external signal. The waveform generators have been previously loaded with the same typical cardiac waveforms, the time delay between the signals was selected in order to simulate different pulse transit times (Figure 5.4) and was controlled by adding a time delay on one of the wave generators. These signals must be added to a small offset of the order of the magnitude of the forward voltage drop of the LED, so that the resulting light intensity is linearly modulated by the LED signal current.

In the test setup, the probe is placed in front of a test device, see Figure 5.4, which holds the two modulated LEDs and provides light isolation to prevent crosstalk. During the tests, the LEDs of the probe itself are deactivated and all light comes from the LEDs in the test device.

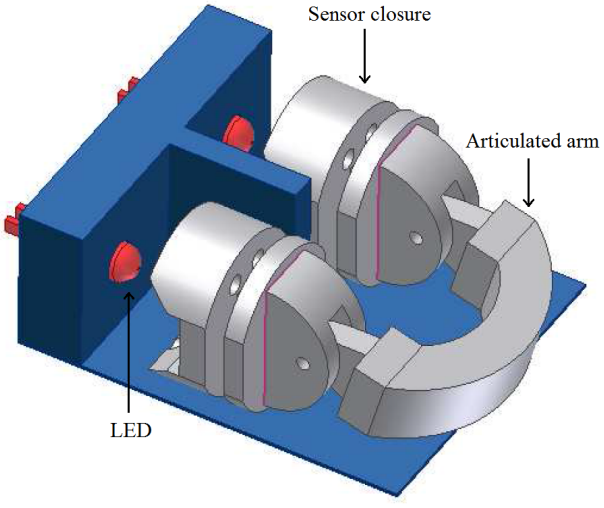

FIGURE 5.4: Schematic drawing of the test setup.

Figure 5.5 shows a typical set of signals generated and detected in the test setup of Figure 5.4.

To assess the operational limits of the probes and algorithms, three different tests were designed. In the first one, signals with frequency similar to the normal heart rate

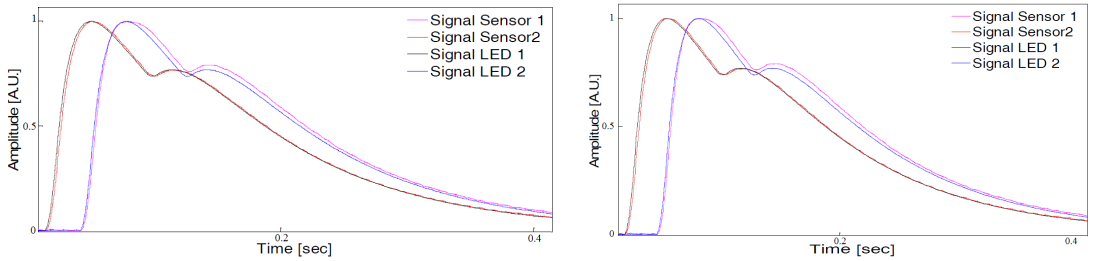

(a) Results for PPD probe.

(b) Results for APD probe.

FIGURE 5.5: Excitation and detector responses for each probe.

but with delays within the interesting PTT range are fed to the system to investigate the integral linearity error. This test was performed at a constant frequency of 1.5 Hz and time delays varying from 1 ms to 100 ms, corresponding to PWVs in a 30 ms^{-1} to 0.3 ms^{-1} interval. This range of values includes the normal PTT range of values in humans.

In the second test was assess the robustness of the algorithms to noise. To accomplish this, was added white noise of amplitudes ranging from 1% to 50% of the signal amplitude in 2% steps, to the isolated pair of pulses. For each noise level, 1000 samples were produced in order to obtain reasonable statistics. The resulting PTT distribution was then studied.

The third test was intended to validate our algorithm's operability under a wide range of frequencies (simulating different heart rates) with a time lag far greater than the maximum PTT seen in humans. It consisted of varying the output frequency (1 Hz to 200 Hz) of the cardiac pulses keeping the time lag between the two signals at 1.1 ms.

5.2.2 Results

5.2.2.1 Integral Linearity

By definition, integral linearity is the maximum deviation of the results from the reference straight line, expressed as a percentage of the maximum. In this test was explore delays in the 1 to 100 ms interval, this range includes physiological PTT values. The results are shown in Figure 5.6. A higher number of points are taken close to the origin since this is the interesting range of values in human PTT studies using the optical probes.

For both probes, all the algorithms produce highly linear (better than 1%) results as well as low error agreement with the reference time delay.

5.2.2.2 Pulse Transit Time Error

Error plots, expressed as a percentage of the corresponding reference value, are shown in Figures 5.7(a) and 5.7(b).

The main differences between the PPD and the APD probes are analyzed. While the PPD probe exhibits lower than 8% error, the APD based probe never exceeds the 4% limit. Cross-Correlation theorem based algorithm (Fcorr) can be identified as the best performing algorithm with a relative error never exceeding 1% in any probe. In the APD probe, the phase angle detection method also yields very good (lower than 1%) error, but poor performance for the PPD probe, mainly in the small time lag region.

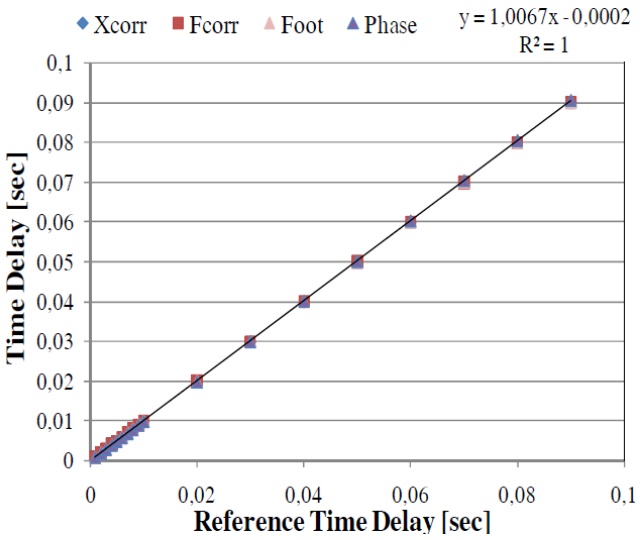

FIGURE 5.6: Reference Delay *vs* measured delay for the PPD probe. The APD curve practically coincides with this one.

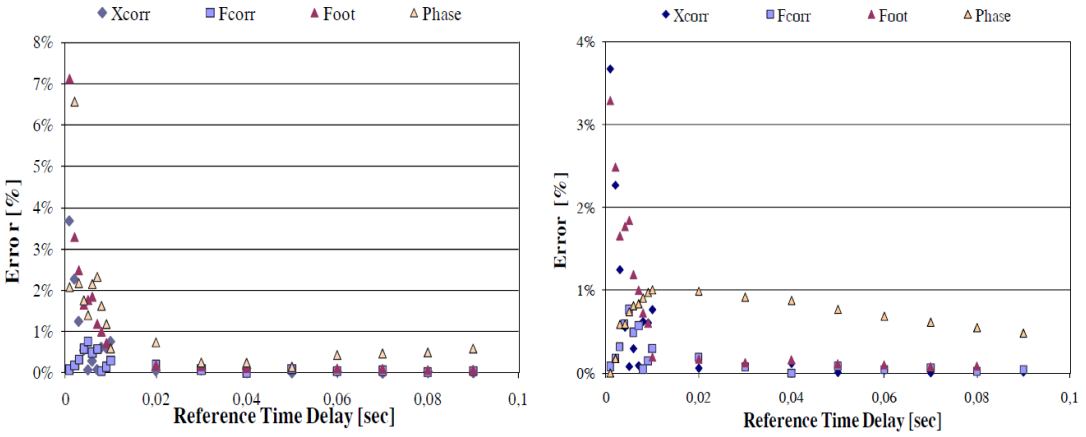

(a) PPD probe results.

(b) APD probe results.

FIGURE 5.7: Relative errors by algorithm.

As expected all the algorithms performed almost perfectly for higher than 10 ms time delays.

5.2.2.3 Noise Tolerance

The tests to determine the algorithm was less influenced by noise in the signals was important step in the selection of algorithm for PWV.

Robustness of the algorithms to noise is assessed by adding normal distribution noise to the photodiode readings and studying the resulting effect on the algorithm output.

This test was performed just for the correlation and phase methods. It was not used in foot-to-foot detection, because, as long as added noise is of the order of magnitude of the threshold used to detect the upstroke, the upstroke will not be detected at all.

Data collected by the PPD and APD probes was submitted to this test using the following procedure: for each noise level, the algorithm under test was run 1000 times,

with an independent noise vector affecting each run. In total, 25 relative noise levels, from zero to 0.5 of peak amplitude, were explored.

The overall performance of probes and algorithms is shown in Figure 5.8 where the probabilities of the algorithm returning a PTT value with less than 5% and less than 10% error are plotted as a function of noise. Results, expressed as a percentage, are derived from 1000 runs per curve. Data in Figure 5.8 confirms the superior robustness of the phase method for both probes.

All algorithms can deliver all the measurements (100%) within the specified error threshold, up to a certain noise level where the curves show a turning point and start decaying towards zero. The phase algorithm not only shows a higher turning point but also decays slower as noise increases, denoting extra robustness to noise.

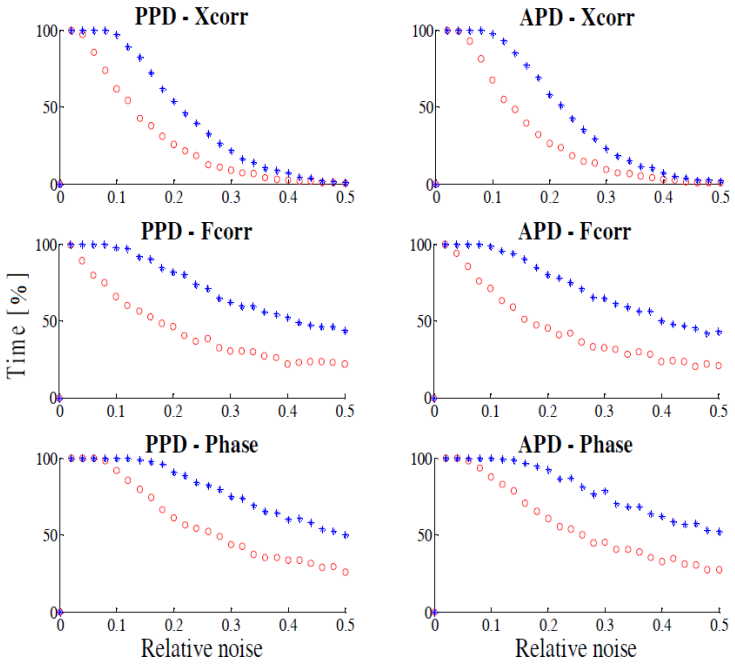

FIGURE 5.8: Measurements with less than 5% error (blue dots) and less than 10% error (red circles) *Vs* relative noise.

5.2.2.4 Algorithm Robustness to Heart Rate

The effect of different heart rates on the performance of the developed algorithms was studied as a robustness measure. In fact, all the data mentioned so far was acquired at a rate of 1 pulse per second, thus, any conclusive notes might not be valid for other acquisition rates. Accordingly, the referred test was performed for signal repetition rates varying from 1 to 200 Hz, without artificial noise added to the readings and for a known constant time delay.

The value used for the time delay, 1.1 ms, was selected by mere convenience. At this point it's important to remark that the AWG2 can define the time delay as an angle, the delay angle, with a precision of a tenth of a degree. On the other hand, for the specific set of used repetition rates, the value of 1.1 ms yields feasible values for delay angles that, otherwise, could not be loaded by the equipment.

In conclusion, as Figures 5.9(a) and 5.9(b) reveal, the APD probe performs superiorly (note that the vertical scales of the figures are different). It is also noticeable that the

Fcorr and the phase algorithms produce the best results if the entire range of repetition rates is considered.

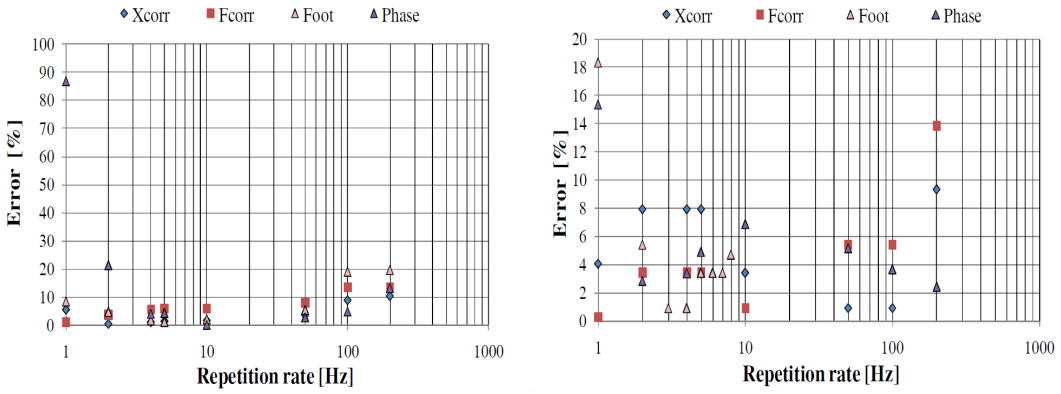

(a) Results for PPD probe.

(b) Results for APD probe.

FIGURE 5.9: Relative errors for each algorithm for a range of frequencies of signal, for PPD and APD probes.

The natural follow-up of this work was start the acquiring pulse data in humans. Figure 5.10 shows a preliminary acquisition in a human subject, in the carotid site, using the APD probe. The shape of the pulses is very clear, not too much affected by noise and allows the anticipation of good results.

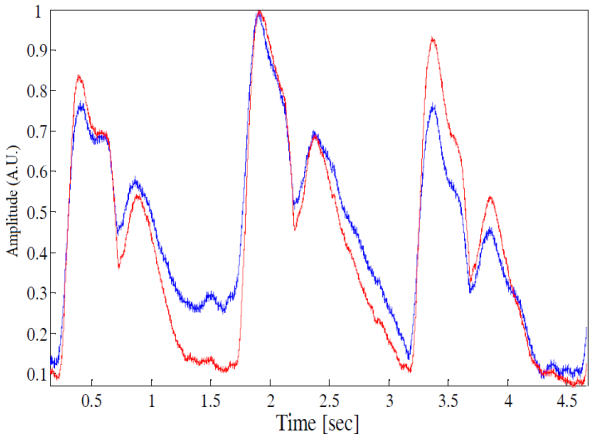

FIGURE 5.10: Preliminary results of the APD probe acquiring data in humans.

5.3 Ultrasound Comparison

Performance of the probes is evaluated in an especially developed test setup and *in vivo*, at the carotid site of humans. In this study two methods for measuring the distension waveform was compared; the gold standard ultrasound and the developed method based on optical probes. Accordingly, distension waveforms were obtained from both ultrasound data and optical probes in a test bench setup (able to reproduce the typical cardiac waveforms), as well as in human carotid arteries.

The gold standard for assessment of the carotid distension waveform is the ultrasonography, which is an established source of clinical and experimental information. The main

scanning mode for vascular analysis is the B-mode, where reflected ultrasound echo signals are mapped as a 2D scale image. The ultrasound system measures the intensity of the echo providing information about the type of structures in the scanning region. A grayscale map evidences the density differences in the B-mode section and an approximate anatomical image becomes recognizable. The technology is especially accurate at probing the interface between solid and fluid filled spaces, which is a key requirement for vascular analysis. Superficial structures such as vessels, muscles, tendons, breast and the neonatal brain are imaged at a higher frequency (7 to 18 MHz), which provides better axial and lateral resolution. On the other hand, deeper structures such as liver and kidney are imaged at a lower frequency (1 to 6 MHz) with lower axial and lateral resolution but greater penetration depth. The quality of the produced ultrasound image depends on image axial and lateral resolution [140]. Axial resolution refers to the ability of representing two points that lie along the direction of ultrasound propagation, and depends on the frequency of the beamed waveforms.

As the purpose of this study is to measure a superficial vessel (carotid artery) one should use a high frequency (10 MHz) which provided reasonable resolution to detect the vessel distension caused by the propagation of the pressure waves. The equipment used in the tests was *Vivid e*® cardiovascular ultrasound system, from the *GE Ultrasound Vivid*® product line [141].

5.3.1 Test Bench

The test bench was designed to evaluate if the optical probes were able to measure distensions with the same magnitude of the ones observed at the carotid (Figure 5.11). The test waveforms were generated by an Agilent 33220A arbitrary waveform generator, AWG in Figure 5.12, which feeds an Actuator (ACT), 700 μm Physik Instrumente GmbH, P-287, High Voltage Linear Power Driver (HV Amp), Physik Instrumente GmbH, E-508.

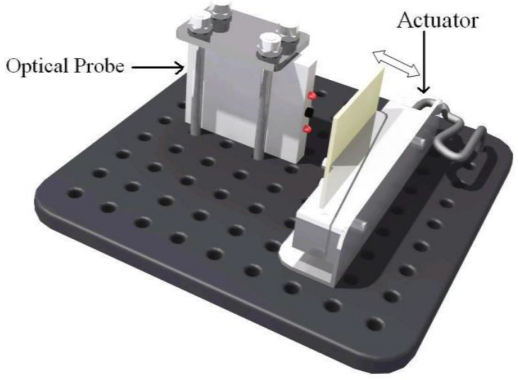

FIGURE 5.11: Schematic drawing of the test bench.

The actuator describes an arterial waveform of type C, and moves a Mechanical Structure (MS), lined with a silicone membrane that reflects the light emitted by the optical probe, similarly to human skin. The optical probe is positioned in front of a mechanical structure and detects variations of the reflected light. The illumination scheme the photodetector and their driving Electronic Circuitry (EC), compose the optical probe.

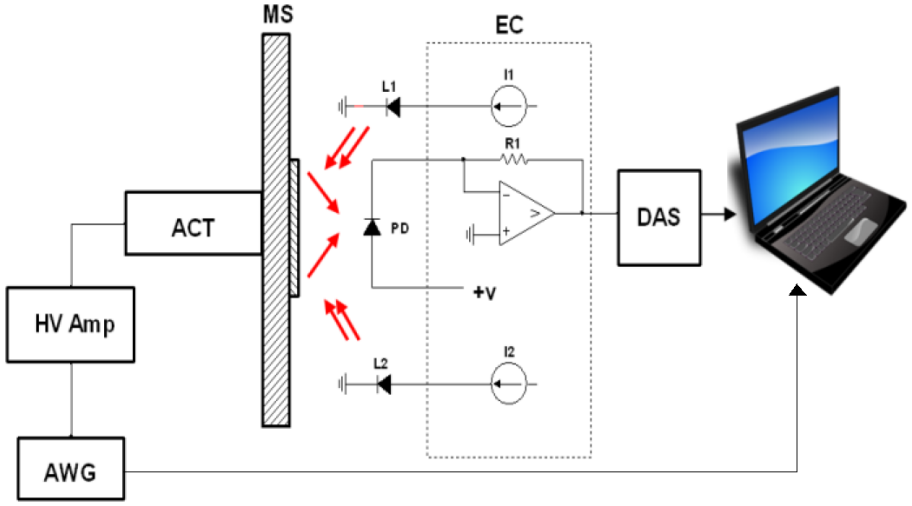

FIGURE 5.12: Schematic of test setup. Connection of the mechanical structure with the various electronic subsystems.

5.3.1.1 Optical Sensors in Test Bench

The results obtained in the test setup are shown in Figures 5.13(a) and 5.13(b) for the PPD and APD probes, respectively. These results show that the optical sensors can detect the distension wave faithfully, reproducing the waveform with Root Mean Square Error (RMSE) less than 6% for both probes. The correlation index between the two signals (actuator waveform and optical response of each of the two probes) is always greater than 0.99 for the four different types of waves described in literature and showed before in Figure 2.2, and for the two optical probes under study (PPD and APD).

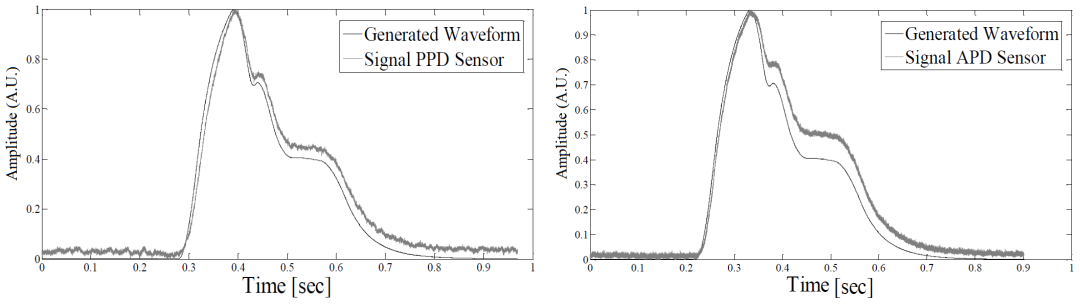

(a) Results for PPD probe.

(b) Results for APD probe.

FIGURE 5.13: Distension and detector responses for each probe.

5.3.1.2 Ultrasound in the Test Bench

All the studies were performed using a real-time B-mode cardiovascular US image system, *Vivid e*® with 9L linear probe, at a 10MHz frequency. In the test setup the specific module was developed and applied to detect the waveform displacement of the structure. All US images were digitized the B-mode (640-by-480 pixels, at 8 bit grayscale, 30 fps).

Signals were obtained placing the probe in front and very close to the moving structure, with a gel layer contact interface. The observed image obtained with this setup shows the defined structures along with the displacement induced by the actuator.

For the reconstruction of the distension wave detected by US, a Region-of-interest (ROI) was marked at the image and selected for analysis. The vertical grayscale level sum over the lines of the ROI shows a cumulative profile in this region. The selection of a high contrast area eases the identification of the moving part which is done by means of the differentiated signal (Figure 5.14). The minimum (red circle in Figure 5.14) of the differentiated signal was computed for each frame in the US sequence. The obtained minima vector in this sequence is plotted over time, where the waveform described by the actuator becomes clearly visible (Figure 5.15(a)).

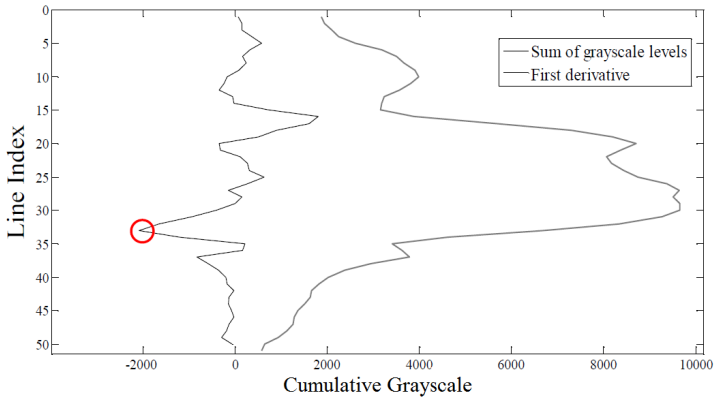

FIGURE 5.14: Grayscale sum profile and its first derivative (minimum marked with a red circle) for the image section.

The obtained waveform is thus segmented by the minimum algorithm and after, each individual pulse, as well as the average pulse, can be plotted to describe the characteristics of the waveform generated by the actuator. As expected, all pulses exhibit poor resolution since it is derived from a 30 fps sequence (Figure 5.15(b)).

Comparing the results from the US system with the ones from the optical probes, it is evident that the optical sensors can measure the distension waveform with much higher resolution. Nevertheless, the data obtained this way follow the directly observed profiles registered with the low-resolution US system, in the same time frame.

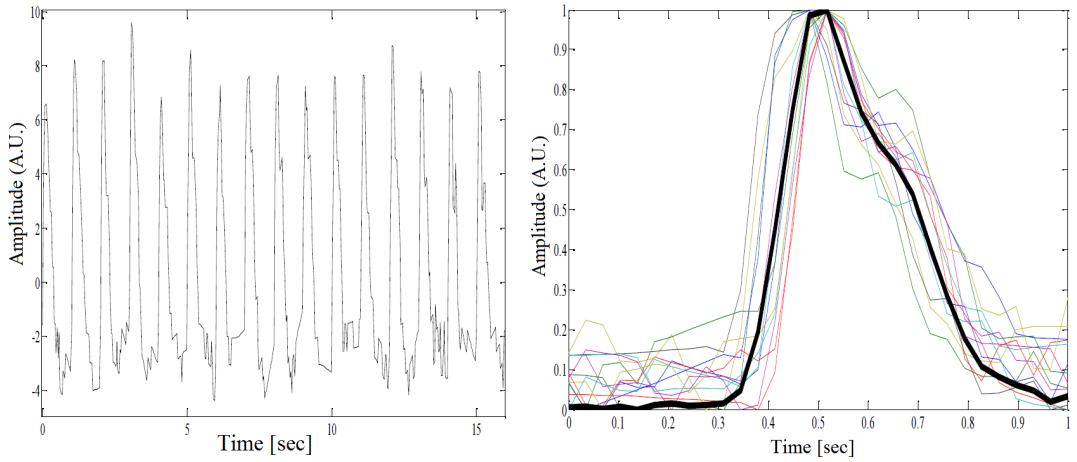

(a) Signals from US system on the test setup.

(b) Average pulse.

FIGURE 5.15: Set of periodic waveforms detected with the US system on the test setup and its average, black line.

5.3.2 *In vivo* Carotid Measurements

Following the preliminary tests with both systems, a set of *in vivo* carotid measurements is necessary to validate the optical probe as a distension profiler. Once again, this was performed in a comparative way with the gold standard ultrasound system.

5.3.2.1 Ultrasound Based Waveform Profiling

A set of longitudinal section of carotid images were acquired with a cardiovascular ultrasound system with a linear probe. During the exam, the patient was in the supine position and the images were stored for offline analysis.

In this study, a sequence of carotid images was used to reconstruct the distension waveform. From the original image, that contained not only the carotid artery but also the jugular vein, a ROI of the original image was again used to select only desired segment of the carotid artery. To compute the diameter time-variation, the sequence of images was analyzed on the frame basis and the proximal and distal walls were detected by analysis of the longitudinal grayscale level sum profile in each frame. The diameter variation is determined through the relative displacement between the minimum and maximum of the differentiated grayscale sum (red circles in Figure 5.16), allowing the reconstruction of the diameter variation in the artery over time (Figure 5.16).

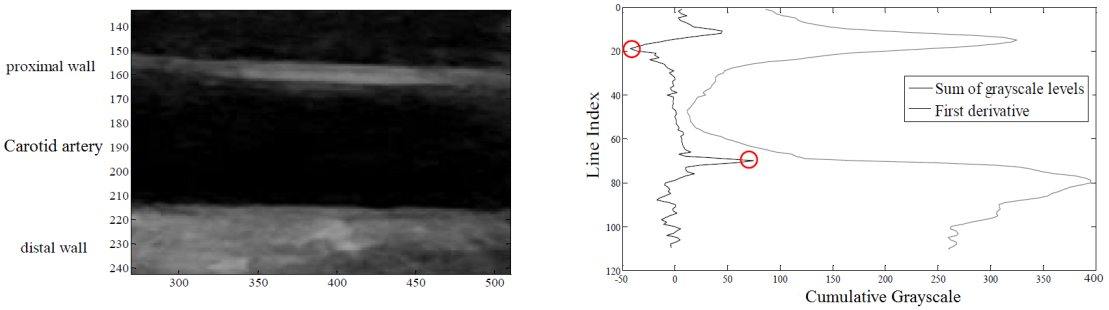

FIGURE 5.16: Ultrasound image of the carotid artery (left) and respective grayscale sum profile and its first derivative (right).

The resulting waveform was obtained along several cardiac cycles (Figure 5.17(a)), with a baseline drift caused by the patient's natural movements (such as breathing) and by the operator's handling, that were removed by the application of a digital high-pass filter that removes the lower frequencies of the signal (cut 0 to 0.5 Hz). To improve the waveform curve, a smoothing spline was applied, with a smoothing parameter, p, equal to 0.55 and a 0.9212 *r-square* fit. The final waveform is show in Figure 5.17(b).

To allow the comparison of the signals obtained with both the optical and ultrasound probes, the average pulse of the signals also computed. The signals exhibit high variability and, as a consequence, the remarkable points are lost in the average pulse waveform.

5.3.2.2 Optical Probes Measurements

The waveform is measured in the carotid artery by a near contact placement using the same preliminary procedures described for the US tests.

A baseline drift was affected the signals and had to be removed by the digital high pass filter referred before that cuts the frequency lower than 0.5 Hz, and remove the

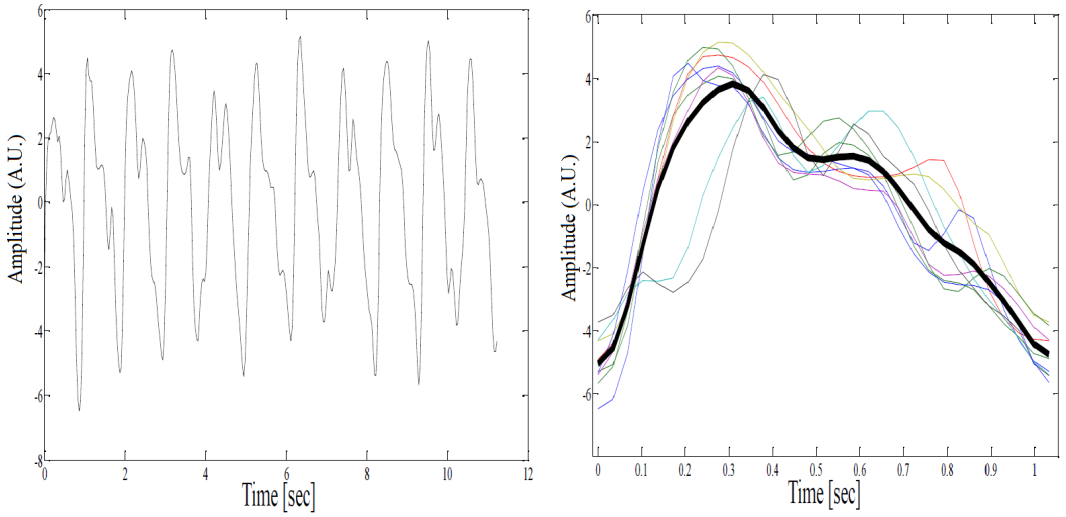

(a) Set of carotid signals from US system.

(b) Average pulse.

FIGURE 5.17: Set of cyclic carotid pulse pressure waveforms detected by ultrasound system its average, black line.

breath rate. After baseline removal, the signals clearly show the characteristic carotid waveform.

The shape of pulse obtained by the PPD probe is very consistent over time and with high signal-to-noise ratio. The average pulse was computed and is shown in Figure 5.18, lower left, black line. Its close similarity with the individual pulses is very clear.

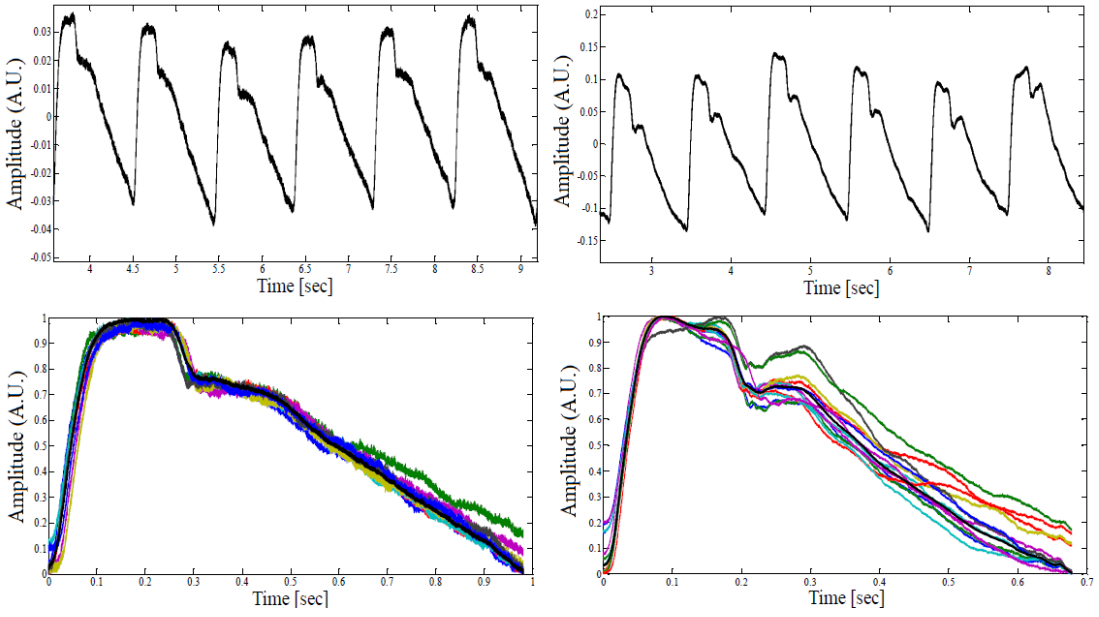

FIGURE 5.18: Distension waveform obtained by PPD in human carotid (left) and by APD (right) and its respective average pulse (black line).

For the APD probe (right panels of Figure 5.18) a remarkable consistency in morphology and a noise level lower than in the PPD pulses is clear. This can be accounted by the much larger light detection area of PPDs when compared to the almost punctual area of the APD. The much smaller skin section intercepted by the APD solid angle of

detection decreases the errors associated to the measurement and, therefore, decreases the noise level.

The average pulse for the APD probe (black line in Figure 5.18, lower right panel) exhibits a very well defined profile, very close to the one of individual pulses, with clearly visible remarkable points.

For both optical probes, each patient showed his own characteristic waveform, with high pulse-to-pulse consistency and clear definition of the remarkable points, as show in the signals of Figure 5.18, all concerning the same patient.

5.3.3 Comparison of Results

The carotid pressure waveforms derived from the US system, from a healthy individual, were compared with the same waveforms obtained with both, the APD and the PPD optical probes.

Signals derived from ultrasonography data exhibit very poor time resolution, due to the low frame rate of the system, and higher inter-pulse variability when compared to the ones retrieved with the optical probes. This lack of resolution and variability strongly affects the resulting average pulse and, consequently, comparison of the carotid pressure waveforms greatly favours the optical probes.

Figures 5.19(a) and 5.19(b) show the ultrasound average pulse overlapped with the PPD and APD probes average pulse, respectively.

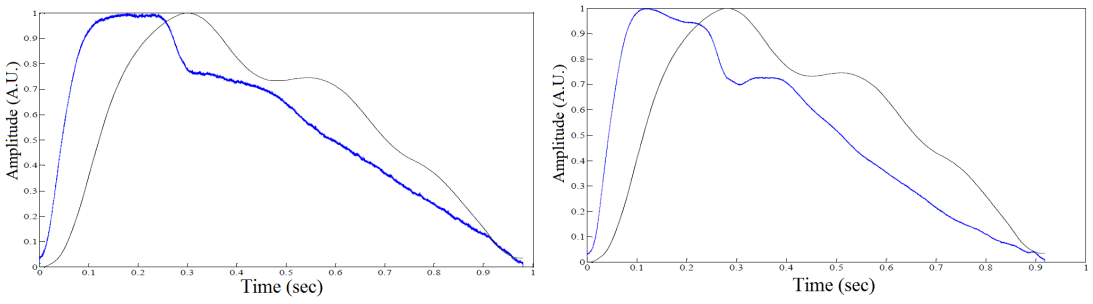

(a) PPD signals *Vs* US system.

(b) APD signals *Vs* US system.

FIGURE 5.19: Overlapping of average pulse for distension waveform obtained by optical probe (blue) and ultrasonography (black) in human carotid.

Figure 5.19(a) shows the overlapping of the average pulse from the PPD probe with the ultrasound average pulse. Analysing the two waveforms, a typical carotid pressure waveform is present in both signals, with particular emphasis to the notability of the characteristic points and inflections of the pressure waveform.

Both signals closely deliver the morphology of a carotid pressure waveform with seemingly potential of allowing extraction of remarkable points and other clinically relevant parameters. The APD probe signal shows a more accentuated inflection in the dicrotic notch region (Figure 5.19(b)) when compared to the PPD probe signal.

5.4 Visible and Infrared Optical Probes Comparison

In the case of obese people, the detection of the pressure wave with the existing methods is rather difficult or impossible. The applanation tonometry in obese subjects is very difficult, as this technique needs a rigid structure to sustain the artery and therefore, fatty structures between the artery and the bone should be avoided [27].

Situations where the carotid artery is not near the skin surface require wavelengths able to optically penetrate the tissues in order to allow the determination of the distension waveform. To fulfill those needs, probes fitted with infrared illumination were developed, in addition to the ones using visible light.

The penetration depth of light into a biological tissue is an important parameter for the correct determination of the signal detected by the photodetectors. The near-infrared region of the electromagnetic spectrum provides a window of opportunity with greater tissue penetration. In the 700–1000 nm wavelengths range the tissue penetration is on the order of 10–15 mm [142]. The normal carotid arteries lie 10 mm beneath the skin [143]. As in the plethysmography principle, in this optical system the pulsatile changes in the light transmission through the living tissues occur due to the changes in the arterial blood volume on that tissue. The measurement of the pulsatile component would eliminate the variations of the light absorption by the tissues, skin, pigment, etc. Thus, only the pulsatile absorbance between the light source and the photodetector corresponds to the pulsatility of the arteries in the resultant signal [144].

The main absorber in skin tissue is the melanin pigment, a highly effective absorber of light, particularly in the UV and visible wavelength ranges. Most of the scattering in blood is also due to the red blood cells, although there are also small contributions from the leucocytes, the platelets and from the large albumin molecules. The carotid tissue is mainly composed of elastin and collagen fibers and, as expected, it is very thick and consequently responsible for the large scattering and reflection of the light [145].

The current study describes the optimization process of four optical probes configuration, PPD and APD probes with visible and IR version, used for the measurement of the distension profile, over time, at the carotid artery site.

5.4.1 Skin Emulation Model

The different tissues that compose the skin (essentially fatty deposits and muscle) have particular optical properties. The indices of light absorption and reflection for each structure allow the understanding of the penetration depth of each wavelength, from the skin to the carotid artery.

There is an optical window in the skin on the region of 600–1300 nm. Wavelengths below 600 nm are strongly absorbed by proteins, melanin, acids and DNA while infrared wavelengths can easily cross the skin and fat barrier before reaching the carotid artery [146].

In this work, only the LED light wavelengths, capable of crossing the epidermis (melanin layer) and eventually fat structures, up to its reflection at the carotid artery, were selected. The ideal optic window is in the IR wavelength.

For obese subjects, independently of the cardiovascular condition, acquiring signals at the carotid site using optical sensors can be a hard task to accomplish. In this sense, the use of IR light allows tissue penetration and captures the distension waveform deeper than in the case of visible light that is mostly reflected at the skin surface level (Figure 5.20).

Silicone rubber has optical and mechanical properties similar to those of the human skin and is often used to build phantoms in human tissue optical studies [147]. For this reason, silicone layers were used in the developed test bench in order to simulate the thickness of the structures that make up the skin and fatty accumulations.

The optical absorption measured across the wavelength range of 300 to 1700 nm, shows that the silicone has strong absorption bands in the mid-infrared spectrum range,

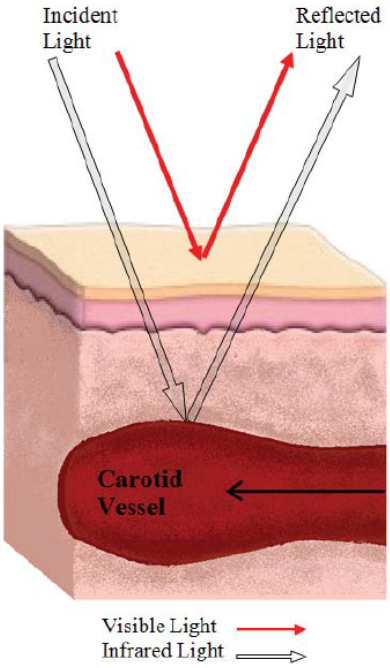

FIGURE 5.20: Structure at the carotid site and its interaction with radiation.

with a maximum at 1260 nm, and has a high refractive index and a lower absorption (1%) in the visible spectrum [148], [149].

To better understand the IR performance three different wavelengths (635, 830 and 940 nm) were considered along with two photodetectors (APD and PPD) for the assessment of the distension waveform at the carotid site.

5.4.2 Test Setup

The test setup was designed to evaluate the optical ability of the developed probes in measuring distensions with the same magnitude of the ones observed at the carotid site. Different number of silicone layers were placed in front of the probes, to simulate the fat structures that can be accumulated in the neck, between the skin and the artery.

The Arbitrary Waveform Generator (AWG), Agilent 33220A, in Figure 5.21, was previously loaded with typical cardiac waveforms, as described in the literature [24], which feeds an ACT, 700 μm Physik Instrumente GmbH, P-287, driven by a HV Amp, Physik Instrumente GmbH, E-508.

The cardiac waveforms generated in the test setup were of two types; one corresponding to an healthy individual, type C and one with pathological features, type A [24]. The actuator describes this waveforms and moves a MS separated from the probe by a variable number of static layers of silicone rubber.

In the probe, light is produced by two LEDs (L1 and L2). The lighting system uses a current regulator, based on transistors, to ensure uniform target illumination. Variations of the reflected light are detected in the photodiode and driven to dedicated EC, which complete the optical probe as a whole.

5.4.2.1 Results

On the test setup, each silicone layer has a 1 mm thickness and the tests were conducted using 2 to 10 layers (10 mm). The signals were acquired for cardiac shaped pulses of

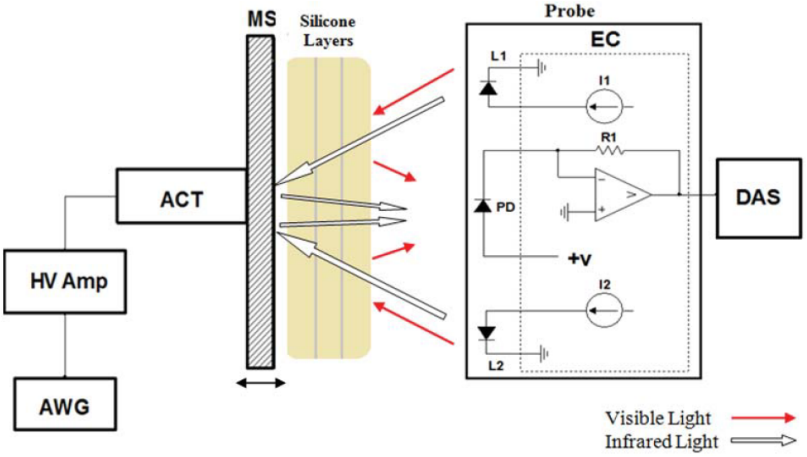

FIGURE 5.21: Schematic of test setup. Light interaction with silicone layers and photo detection circuit.

frequencies 0.5, 1 and 1.5 Hz, to ensure that healthy and pathological cardiac frequencies were covered. This range was chosen to enclose possible heart rate at rest, normal conditions in the acquisition of signals. Signal acquisition was made in human carotid arteries in order to compare the results obtained with the analysis in the test setup.

The signals were obtained for both red and infrared lights, transmitted through two, four, six, eight and ten silicone layers. Figure 5.22 shows the waveform, type C with 1 Hz, detected by the PPD with different number of silicon layers.

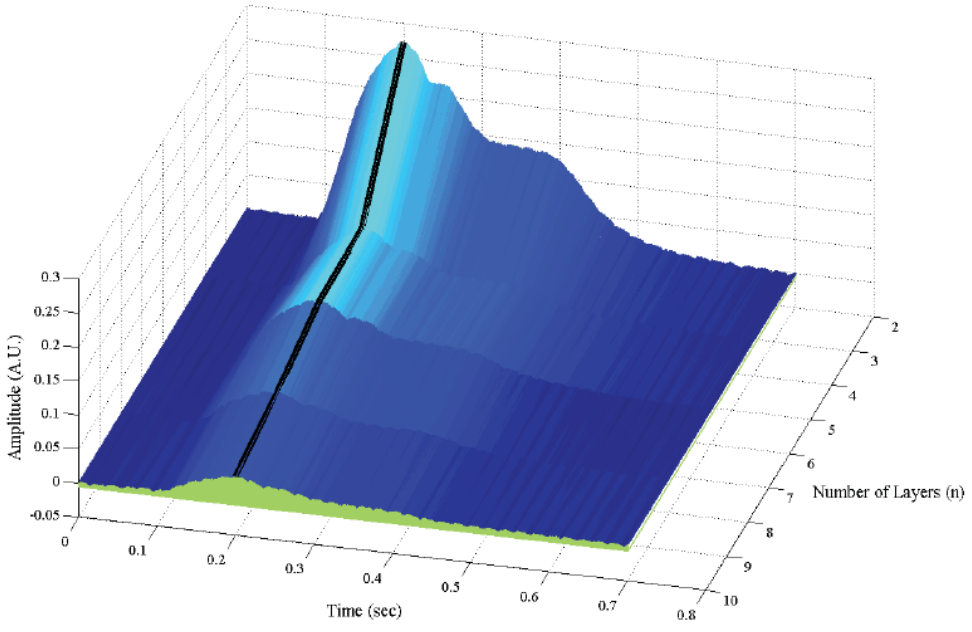

FIGURE 5.22: PPD signals with visible light for different number of silicone layers and exponentially attenuation (black line).

The reflected radiation that reaches the photodetector is composed by the light reflected on the surface of the silicone and by the component that is reflected in the deeper layers. The reflection from the top surface corresponds to the DC component of the signal detected and the AC component captures the reflected light at the pulsating

mechanical structure in movement. The DC component was removed from the acquired signals. The main objective of these probes is the measurement of the pressure waveform, and the layers have a low pass filter effect that doesn't affect the waveform profile but decreases the signal amplitude and the SNR level.

The intensity of the transmitted light decreases exponentially with the increasing number of layers, *i.e.*, the thickness of the homogeneous body. Lambert's law (equation 5.1) describes the amount of attenuation (absorption) that the radiation undergoes passing through a thickness of material, where μ is the linear absorption (or attenuation) coefficient

$$I = I_0 e^{-\mu n}. \tag{5.1}$$

In equation 5.1, the measured intensity I transmitted through a silicone layer with thickness n is related to the incident intensity I_0 according to the inverse exponential power law.

The attenuation coefficient (μ) is a quantity that characterizes how easily a material can be penetrated by light. A large attenuation coefficient means that the beam is quickly "attenuated" as it passes through the material, and a small attenuation coefficient means that the material is relatively transparent to the beam. The attenuation coefficient was determined for the two probes with visible and infrared light sources.

The black line, in Figure 5.22, is the attenuation suffered by the detected radiation with the increasing number of silicone layers. Using an exponential fit to this curve, it is possible to determine the attenuation coefficient for each wavelength. For visible light this attenuation coefficient is $\mu_{visible} = 0.5930\ mm^{-1}$ and for infrared light is $\mu_{IR} = 0.3971\ mm^{-1}$. The augmentation of the radiation absorbed by the silicone layers and the decreasing of the transmitted light that reaches the photodetector are evident in the increasing of the computed attenuation coefficient. For the APD probe with visible or infrared light the behavior is similar. For the signals obtained in the test bench, a spectral analysis was performed in order to determinate the attenuation provided by the silicone layers. Figure 5.23 shows the spectrum obtained for signals acquired with the avalanche photodetector with visible light, without silicone (grey line) and with 10 layers (black line).

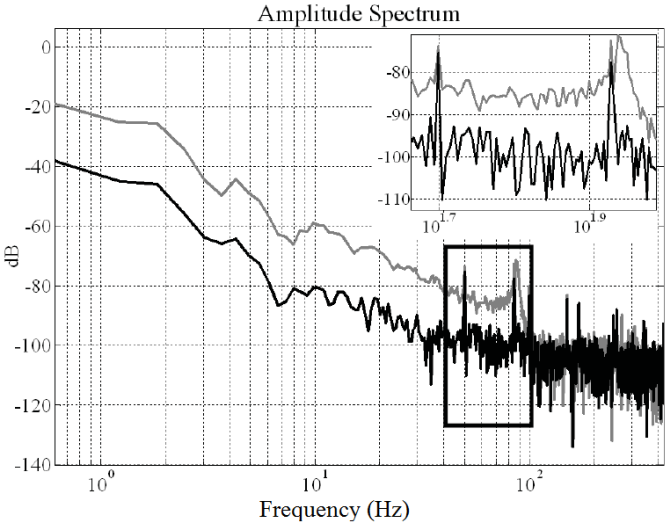

FIGURE 5.23: Amplitude spectrum for APD signals with visible light without silicone layers (grey) and with 10 silicone layers (black).

TABLE 5.1: Maximum RMSE between the signals from the waveform generator and the signals detected from each probe.

	Visible	IR
PPD	7.19%	6.13%
APD	7.95%	5.66%

In the frequency window of interest for the analyzed signal, bellow 100 Hz, there is a nearly constant attenuation at about 20 dB for signals acquired with ten silicone layers. It is possible to identify, in the spectrum, the frequencies which correspond to the electronic interference detected by the optical sensors, such as the frequencies of the light bulbs (50 Hz) or monitors used during the acquisition (87 Hz). For the IR light, the attenuation also occurs at low frequencies with smaller impact, at an almost constant attenuation level of less than 10 dB. In the case of the planar probe, the spectral analysis of the acquired signals showed the same attenuation at low frequencies (20 dB for of visible light and 10 dB for IR light). The signals from four and ten silicone layers for waveform types A and C acquired at 1 Hz are shown in Figure 5.24. The signals acquired by the APD probe with infrared light, exhibit higher amplitude as well as a better waveform resolution. The signals acquired with visible light, marked in red, show smaller signal amplitude and a higher noise interference imparting lower resolution to the waveform, mainly in the morphological features that enclose a great clinical importance.

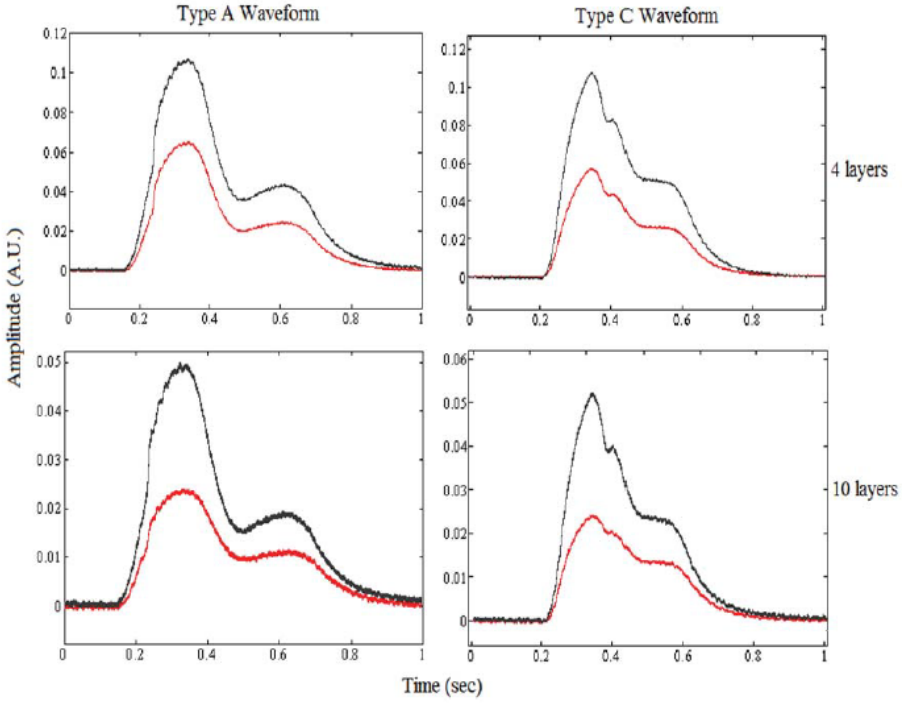

FIGURE 5.24: APD signals for four and ten layers, with visible (red line) and IR light (grey line).

Once again, IR light exhibits a better performance (table 5.1), with the lower RMSE values, although there is not a clear distinction between the photodetectors used.

Another parameter that is used to quantify how much a signal has been corrupted by noise is the SNR. Its value in dB is computed by the relation between signal amplitude

and noise amplitude. The experimental determination of this parameter was accomplished by acquiring signals from the photodetector with the movement of the actuator and in static conditions. The last one yields just the noise since there is no signal while the first is the signal plus noise component. Results from the two probes for A and C waveform types for different frequencies are shown in Figure 5.25(a).

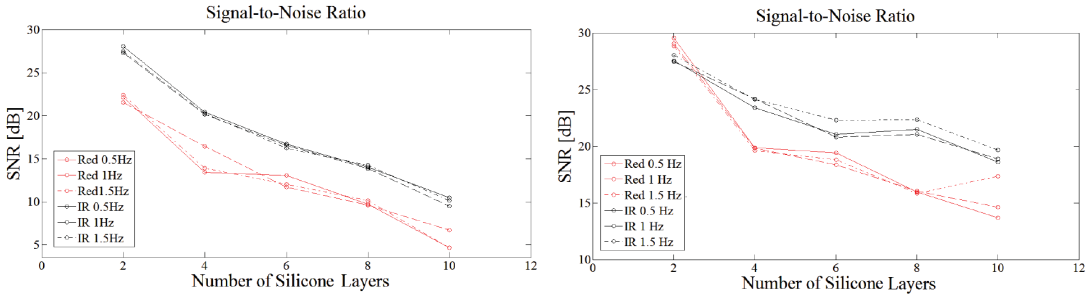

(a) SNR for PPD.

(b) SNR for APD.

FIGURE 5.25: SNR for each probe with different number of silicone layers.

The SNR from the PPD probes, for the red and infrared wavelengths, decrease with the increment of the number of silicone layers. It is also noticeable that the SNR obtained with infrared light is always greater than its counterpart obtained with red light. SNR values for PPD probes are shown in Figure 5.25(b). For two silicone layers, (low fat accumulation), visible and IR light perform similarly. However, as the number of silicone layers increases, IR light probe show higher SNR values and thus a better performance.

Carotid *In vivo* Measurements

Following the preliminary tests with both systems, a set of measurements at the carotid site were carried out in order to validate the use of the optical probes for *in vivo* conditions.

The radiation spectrum of a person is the same as the one of a blackbody. The Wien's Law allows the determination of the maximum wavelength of radiation for a human (body temperature of 37 °C), that is 9700 nm. This wavelength corresponds to the infrared radiation, also known as body heat. This wavelength is well above the electromagnetic spectrum range used by the optical probes, as the spectral range of sensitivity of both, the planar and avalanche photodiodes, is between 400 and 1100 nm. The influence of the infrared radiation emitted as animal heat, in this specific case the human body, is thus negligible [150].

The waveform was measured in the carotid artery by a near contact placement. Measurements were performed while subjects were in a quiet environment after at least 10 minutes of supine rest.

The acquired signal, can be interpreter if considered to have two distinct components: the DC component which represents the light absorption of the tissue, venous blood, and non-pulsatile arterial blood, and the signal has a baseline drift caused by the patient's natural movements (such as breathing); and the AC component which is related to the pulsatile arterial blood.

The resulting waveforms obtained along several cardiac cycles show that the infrared probes allow the acquisition of cardiac waveforms with lower noise and, consequently, better definition at the morphological features (Figure 5.26). Another, not so obvious,

advantage of the IR lit probes is that it eases the operator's task since the detection of the optimal positioning of the probe becomes faster. This effect assumes great importance in practice since it can determine the overall time spend in acquiring data from a patient.

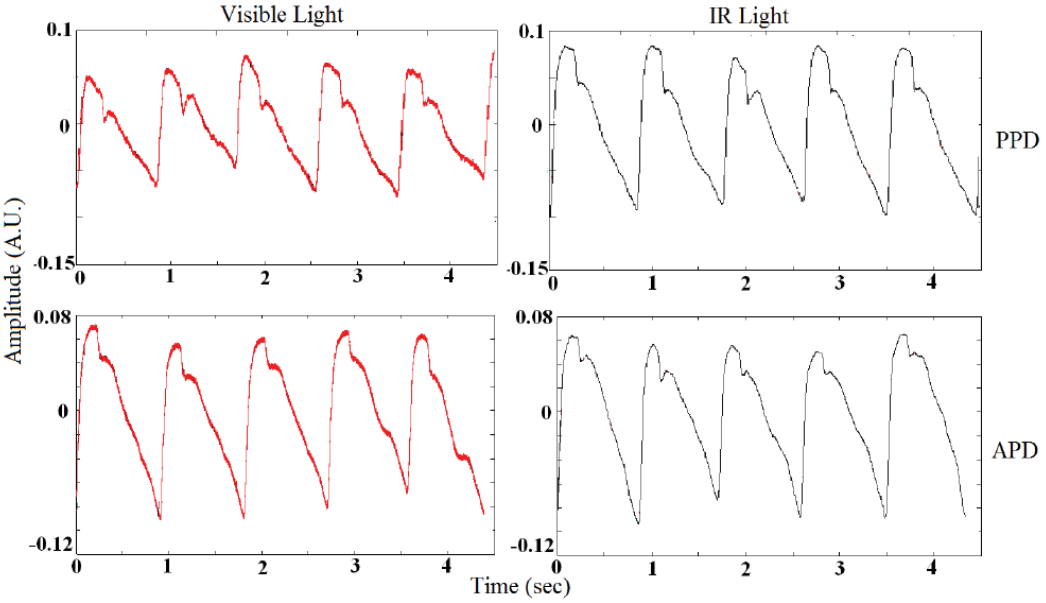

FIGURE 5.26: PPD and APD signals obtained at the human carotid using visible (red line) and infrared light (grey line).

5.5 Automatic Detection of Pulse Waveforms

Independently of the selected probe an automatic method to select the arterial pulse waveforms, greatly improves data collection efficiency during a clinical exam.

Machine learning techniques have been successfully employed in automatic classification of several physiological signals, including those related with cardiovascular diseases [151]. Following similar approach of acquired data validation two methods are considered using supervised learning and perform the implementation of two types of classifiers: K-Nearest Neighbors (KNN) and Support Vector Machine (SVM) are described.

SVMs take into account an effective classification method with significant advantages. They proved to be very useful in a variety of pattern classification tasks, like handwritten character recognition, classification of ECGs signals, speaker verification and image retrieval [152], [153], [154]. Usually, higher classification performances are achieved using this type of algorithms.

An alternative pulse classification method is the KNN. The Nearest Neighbor application has been extensively explored in the field of Geographical Information Systems [155], computational geometry, detection of cardiovascular signals like heart arrhythmia [156], movement classification from Electroencephalograms (EEGs) data, implemented on brain computer interface technologies [157].

To perform a robust classification platform is fundamental to perform a sequence of tasks are described in the following sections: data acquisition and pre-processing, features creation, features selection and training of the classifier. The fulfillment of these steps is directly related with the improvement of classification accuracy.

5.5.1 Pulse classification Sequence

5.5.1.1 Data pre-processing

The main purpose of pre-processing is to segment each Arterial Pulse Waveform (APW) from the entire raw data stream. The method was based on an automated peak detection function in Matlab® (Peakdet from the Mathworks, by Tom McMurray) [118]. The algorithm analyzes a window of 10 second and detects the local maxima and minima in the acquisition. Each local minimum detected corresponds a foot of wave, which were used to segment the signals that comprise 1 second after the foot of wave.

The dataset used in this work was acquired by the PPD probe in 213 patients and consisted in an overall of 1752 acquisitions. The study protocol was approved by the ethical committee of the Centro Hospitalar e Universitário de Coimbra, Portugal, and all the subjects were volunteers and gave a written informed consent.

5.5.1.2 Features creation

The optical signals were parameterised by means of 37 pulse features divided in the following subsets: amplitude features (systolic peak; reflection point; full width at half maximum), time domain statistics (mean; median; standard deviation; variance; interquartile range; skewness; kurtosis; root mean square; entropy), cross-correlation features (maximum of cross-correlation with template waveform), wavelet features (relative power at six levels of wavelets for two mother wavelets, Haar and Db4), and frequency domain statistics (first to four-order moments in the frequency domain; median frequency; spectral entropy; total spectral power and peak amplitude in frequency band) [158], [159], [160], [161]. Most of this features are summarized in the Table 5.2.

Table 5.2: Feature subsets and expressions.

Group	Feature	Expression
Amplitude features	Reflection Point (RP)	x'(RP)=0 but is not the absolute maximum (x' is the first derivative)
Time domain statistics	Mean (M)	$M = \frac{1}{n}\sum_{i=1}^{n} x_i$ (n is the number of elements in the sample)
	Standard deviation (σ)	$\sigma = ((\frac{1}{n-1})\sum_{i=1}^{n}(x_i - M)^2)^{1/2}$ (where M is the mean of x)
	Variance (Var)	$Var = E[(x-M)^2]$ (E represents the expected value)
	Skewness (s)	$s = \frac{E(x-M)^3}{\sigma^3}$ (where σ is the standard deviation of x)
	Kurtosis (k)	$k = \frac{E(x-M)^4}{\sigma^4}$

TABLE 5.2: (continued)

Group	Feature	Expression
	Root mean square (RMS)	$RMS = \sqrt{\frac{1}{n}\sum_{i=1}^{n}(x^2 i)}$
	Entropy (H)	$H = -\sum_{i=1}^{n} p(x_i) log_{10} p(x_i)$ (where p(x_i) is a probability of x)
Cross-correlation features	Cross-correlation (CC)	$CC = max \sum_{m=-\infty}^{\infty} x[n+m] y*[m]$ (y is the signal template, y* denotes the complex conjugated of y)
Wavelet features	Relative power for each decomposition detail (P_j)	$P_j = \int D_j^2 dt$ (D_j is the reconstructed signal detail at the j th level)
Frequency domain statistics	Moments in the frequency (M1f)	$M1f = \sum_{l=1}^{L} f_l PSD(f_l)$ (where L is the length of FFT and f representing the frequency component)
	Median frequency (MF)	$MF = 0.5 \sum PSD(f)$
	Spectral entropy (SE)	$SE = -\sum p_j ln(p_j)$ (p_j is the normalised value of PSD at each frequency)
	Total spectral power (PT)	$P_T = \sum PSD(f)$
	Peak amplitude (PA)	$PA = max(PSD(f))$

For the amplitude features creation, a low-pass filter (with a cut-off frequency of 30 Hz) was used [123], with the intent of removing the noise, thus improving the signal differentiation that is essential for the detection of the inflection points in the waveform. The reflection point represents the amplitude of the inflection point in the pulse pressure waveform corresponds to the arrival of the reflected component that added to the incident wave. The full width at half maximum further is determined by the difference between the two values at which amplitude is equal to half of its maximum value.

In the time domain statistics: mean and median quantitatively represent the magnitude of each signal variable, whereas standard deviation, variance and interquartile its variability. Skewness and kurtosis reflects the shape of the amplitude distribution [158], [161], while the root mean square measures the magnitude of a varying quantify [160].

The maximum of cross-correlation with a template signal measures a coupling between two time series. Differences in the structure of arterial pulse waveform indicate an alteration of cardiovascular system. Four types of pulse pressure profile are described and identified with arterial stiffness [24], [162]. The waveform templates, used for the cross-correlation tests, belong to four waveforms groups classified as A, B, C and D, and which represent the most relevant clinical relevant types [24]: type A, systolic peak appears after the peak of the wave, type B, corresponds to cases of pronounced artery stiffness where the systolic peak appears after the inflection point (although the difference between them is very close to zero); type D, waves are similar to type A waveforms, but the inflection point can not be identified; type C waveforms, where the systolic peak appears before the inflection point, are commonly seen in healthy individuals that have low arterial stiffness and high elasticity [24].

The wavelet features capture relative energies in the different spectral bands. Two mother wavelets (Haar and Db4) were tested and the relative power for reconstructed signal detail was determined [24], [163], [164]. The choice of wavelet depends upon type of application. Generally, a wavelet similar in shape to the signal being analyzed is considered suitable for the analysis. The mother wavelet function Doubechies 4 is the most commonly used for the arterial pulse waveform analysis [24], [164], [165]. Although Haar function does not have the character of excellent time-frequency localization, it is more suitable for analysis that requirement of peak detection [166], [167].

Figure 5.27 shows the pulse waveform measured by the optical probe decomposed in 6 levels using the Haar wavelet. In this case, the details D1, D2, D3 and D4 embed the information of the pressure pulse that contains the signature of effects of wave travel and reflection. For the analysis of the Figure 5.27, typical morphological features of the pulse waveforms, e.g., the systolic peak and the dicrotic notch, are included in details D1–D4. Maximum information in the first levels while D5 and D6 only provide residual information. The normalized power of the details was used, resulting from wavelet decomposition, as a synthetic descriptor of the morphological differences among pressure pulses.

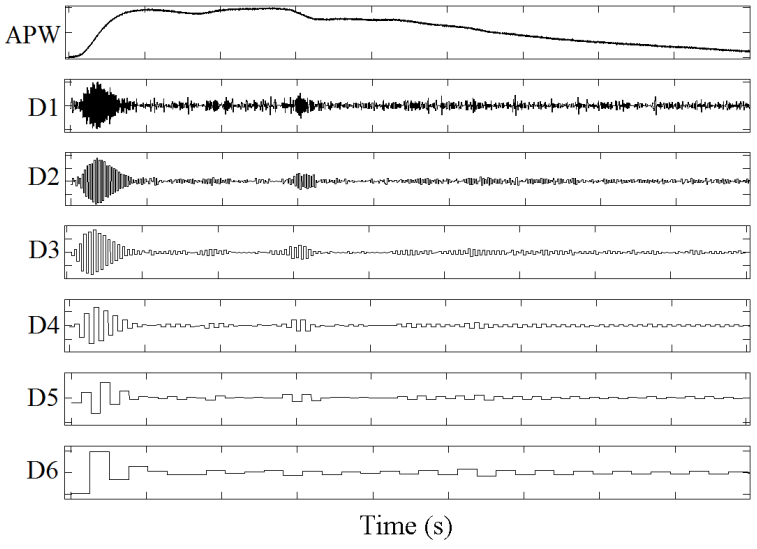

FIGURE 5.27: Wavelet decomposition up to 6 detail coefficient using Haar mother wavelet. Arterial pulse waveform is original signal.

First to four-order moments in the frequency represents the amplitude of the Power Spectral Density (PSD) at each single spectral component. The median frequency is

defined as the spectral component which comprises 50% of the signal power, with higher values corresponding to signals with significant spectral components at higher frequencies. The spectral entropy is a disorder quantifier related to the flatness of the spectrum. The total spectral power is computed as the total area under the PSD. The peak amplitude is the local maximum of the spectral content in the frequency range [158], [167].

All the features sets are then concatenated to produce a single feature vector. However, due to the great difference in the characteristics of the feature components a normalization procedure is required. This task has a strong impact on KNN and SVM classification algorithms [168]. The normalization consists in subtracting the mean over all training values and dividing by the corresponding standard deviation [168].

5.5.1.3 Features selection

The choice of the most relevant features reduces the computational complexity and improves of the classifier's generalization ability. In an initial stage of a pattern recognition project, it is desirable to discard features with no significant contribution. There are methods that generate new features from the existing ones that retains the most meaningful attributes, a process called features extraction. An example is the Principal Component Analysis (PCA) algorithm. On the contrary, features selection algorithms preserve the most significant features contained in the original features vector [169].

PCA must be applied for feature extraction with caution because there are some disadvantages related with its use. This method could discard components with negligible contribution to the overall variance, which may nevertheless provide a crucial contribution to pattern discrimination and, inadvertently, impair the classification accuracy [168].

Feature selection algorithms are divided into two types: filter methods and wrapper methods. The first one is based on indirect measurements, for example with distances, reflecting segregation between classes. Wrapper methods, on the contrary, select a subset of features based on the classification accuracy, which means they are dependent of the used classifier. The Support Vector Machine Recursive Feature Elimination (SVM RFE) algorithm is wrapper method based on a recursive process of features elimination. Starting with all available features in the original data, it determines each feature's contribution in terms of the classification performance. The algorithm eliminates the feature with the least impact on the classification accuracy until a stopping criterion, indicating that a good solution has been found, is reached [170]. At the end of process, the algorithm returns a features ranking, sorted by order of significance in terms of the classification accuracy [171]. In this work a linear kernel function in SVM RFE was used. The computational time is smaller in this case, due to the absence of kernel parameters. Only the Regularisation Constant (RC) has to be tuned and it has been demonstrated that very low values can improve the performance of SVM RFE [172]. The recursive features elimination techniques have been successfully applied to physiological signals, with the aim to find features subsets with high diagnostic relevance [159], [170]. The SVM RFE algorithm was adopted in the current project, and the SPIDER toolbox for Matlab® was used to perform the features selection [173].

5.5.1.4 Classifiers

In biomedical data classification systems is frequent that the classifier which is applied may not be suitable for the given data set [174]. For this reason, two types of classifiers, KNN and SVM, were explored to find out which one guarantees the best classification performance.

SVM is defined as a classifier that can be linear or non-linear. When applied to data it can distinguish two different types of classes by finding a separating hyperplane with the maximal margin between two classes [174]. SVMs are defined by two general attributes: C, a hyper-parameter that controls the trade-off between having large normalized margin and having less constraint violation; and kernel, a function that map training data into a higher dimensional space [169]. The kernel function is used to train the SVM and, usually, the most common kernel types are the linear and the Gaussian (Radial Basis Function, RBF) [169]. In this study, the last one was adopted because the Gaussian kernel is considered the best option on the biological context [151], [175]. By using SVMs with this type of mapping function a third parameter must be optimized: sigma, the width of the Gaussian function. Therefore, it is always necessary to define the best combination of the two hyper-parameters, C and sigma, that define the kernel RBF model.

Contrary to SVM, KNN does not make any assumptions about the underlying data pattern distributions. It is an algorithm used for object classification based on closest training examples in the problem space [168]. The object is then assigned to the most common class among its k nearest neighbours. KNN is considered the simplest algorithm of all machine learning techniques, where the function used is only approximated locally [176].

Generally, the performance of SVM classifier is better than KNN but a comparing study between them was made, on the current study, to select the best model. The Statistical Pattern Recognition Toolbox for Matlab® was used to design both the KNN and SVM classifiers [177].

5.5.1.5 Performance evaluation

In this phase a set of tests is usually performed in order to estimate the performance of each classifier. Some data from the original data set is selected randomly and the model build predicts its output values. Therefore, the predicted values are compared to the real ones. Performance analysis is conducted under Accuracy (A), Specificity (Sp), Sensitivity (Se) and F-Measure (F-M) that are explain in the Table 5.3.

In general, the performance of a binary classifier as the ones analyzed here, can be evaluated taking in account the following quantities: TP, TN, False Positive (FP) and False Negatives (FN). In the context of the data set analyzed, a 'positive' denotes a part of the signal classified as having a waveform profile and 'negative' denotes noise. Consequently, a TP is a portion of the signal which was correctly classified as having a waveform profile, and a FP is a portion of the signal with noise which was wrongly classified as having a waveform profile.

A high sensitivity guarantees that the algorithm rarely miss a 'positive' sample when it appears. A high specificity ensures a very low rate of false alarms (when a 'positive' event is classified as a 'negative' one). A classifier is considered as having a good performance if it simultaneously has a high sensitivity and a high specificity [168]. F-M reflects indirectly the sensitivity and the specificity of the method. Therefore, having a good classifier means that it has a high F-Measure. Globally, the aim of the performance evaluation task is to find the method that ensures the highest Accuracy and F-Measure values. In some cases it is important to consider Se and Sp measures individually. For example, when the data set used is unbalanced as the one that was explored here.

To select a good classifier from a set of classifiers (model selection) is necessary to adopt an accuracy estimation method. Its implementation is important to predict the

Table 5.3: Performance measurements.

Performance measure	Definition	Expression
Accuracy	The fraction of True Positives (TP) and True Negatives (TN) in the population of all instances.	$A = \frac{TP+TN}{TP+TN+FP+FN}$
Sensitivity	Dictates how sensitive the decision method is in the detection of a 'positive' event. A high sensitivity guarantees that the algorithm rarely miss a 'positive' sample when it appears.	$Se = \frac{TP}{TP+FN}$
Sensitivity	Informs how specific the classification decision is in the detection of the 'negative' event. A high specificity guarantees a very low rate of false alarms (when a 'positive' event is classified as a 'negative' one).	$Sp = \frac{TN}{TN+FP}$
Precision (PR)	Denotes the proportion of predicted 'positive' cases that are correctly real 'positives'.	$PR = \frac{TP}{TP+FP}$
Recall (R)	The same as specificity.	$R = Sp$
F-Measure	The harmonic mean of precision and recall, and reflects indirectly the sensitivity and the specificity of the method.	$FM = \frac{2.PR.R}{PR+R}$

classifier's future prediction accuracy and to calculate the above performance measures. Hold-out and cross-validation are the methods chosen in the current study.

Hold-out method divides the data into two mutually exclusive subsets – the training set and the test set. The training set corresponds to a percentage of the whole data set, and the test set is defined as the remaining data. Changing the data proportion can lead to different values of accuracy. The error estimate is obtained from the validation set, and therefore suffers from bias and variance effects originated by the finiteness of the training set and the finiteness of the test set, respectively [168]. The hold-out method is a pessimistic estimator. Only a portion of the data is given to the inducer for training and the more instances are chosen for the test set, the higher the bias of the estimate [178]. Usually, the larger is the training data set the better is the classifier. In the hold-out method, the accuracy of the error estimate is directly related with the length of the test set. Ideally both training and test sets should be large. To obtain more reliable results, the hold-out method can be repeated several times and the estimated accuracy is then computed by averaging the runs [178].

Cross-validation is one of the most common methods [178]. In this method the whole data set is randomly split into n different subsets (folds). The classifier is trained and tested n times. In each iteration, one subset is used as the validation set, being the classifier trained with the other n-1 subsets. A subset assigned as part of the test set will be used as the training set in the next iteration. The overall estimated accuracy is the average among the n iterations and it depends on the number of folds n. Usually, 5-fold or 10-fold cross-validation displays lower variance. Cross-validation ensures nearly unbiased estimate of the prediction error rate and avoids overlapping test sets [179].

5.5.2 Classifier Performance

This section contains the results obtained after thorough testing the two classifiers for several combinations of different values of parameters.

TABLE 5.4: Overall KNN and SVM accuracy for different parameters in the SVM RFE.

RC	1×10^{-7}				5×10^{-7}				1×10^{-6}			
N	5	10	25	30	5	10	25	30	5	10	25	30
KNN Hold-out	0.983	0.980	0.980	0.983	**0.995**	0.983	0.978	0.991	0.983	0.980	0.980	0.983
KNN Cross-validation	0.921	0.919	0.919	0.926	0.932	**0.933**	0.930	0.924	0.923	0.923	0.924	0.923
SVM Hold-out	0.991	0.983	**0.992**	0.983	0.979	0.979	0.979	0.983	0.979	0.991	0.983	0.983
SVM Cross-validation	0.947	0.948	**0.952**	0.948	0.942	0.949	0.947	0.949	0.946	0.950	0.949	0.948

The KNN classifier was tested for 1 to 50 nearest neighbours and 5 to 10 folds in cross-validation method. For the hold-out method the length of test set varies between 50 % to 90 %. For the SVM classifier tests were used the values of a constraint factor between 0.01 to 200, the sigma of the 0.01 to 100, 5 to 10 folds in cross-validation and 50% to 90% for the length of test set in hold-out method. The best results obtained for the accuracy for all combinations of these parameters in test are represented in the Table 5.4.

Three values for small RC of the SVM RFE were tested, for 1×10^{-7}, 5×10^{-7} and 1×10^{-6} and for different features numbers. The best performance of classifiers was found for the lower values of RC. Similar results were also described in another studies that used very low values for the regularisation constant in order to improve the performance of SVM RFE [172], [180].

In the simplest case, hold-out sets are constructed just by splitting some original dataset into more than one part, but the evaluations obtained in this case tend to reflect the particular way the data are split up. The solution is the cross-validation that uses statistical sampling to get more accurate measurements. The advantage of using cross-validation is the combination of a large training set with several independent test sets. The cross-validation method is the standard procedure for classification error estimation [181], [182], for this reason the next discussion of the results is made taking into account only the cross-validation method.

It can be observed, from Table 5.4, that the overall accuracy is higher than 0.9, for both classifiers. For the KNN the higher accuracy (0.933) was evaluated for 4 nearest neighbours using 5-fold cross-validation scheme. In the SVM classifier with a cross-validation method the best value of accuracy is the 0.952, and the best combination of parameters for the SVM RFE, results for a small regularisation constant 1×10^{-7} and 25 selected features. The evolution of the accuracy results corresponds to the combination of sigma and constraint values in the SVM classifier and is represented in Figure 5.28. The maximum value in the figure occurs for the values mentioned above from reading the Table 5.4, for a constraint factor of C = 180 and $\sigma = 0.1$ with 5-fold cross-validation scheme. For sigma values higher than 2 there is a great decay of the accuracy results and from $\sigma = 4$ stabilizes at a low performance results. Very small values of sigma keep a high score of performance for a wide range of constraint values.

From Table 5.4 it was possible to identify the best accuracy value for each classifier and number of features in the study. For each accuracy measure was identified a value of Sp, Se and F-M. These values are summarized in Table 5.5 for the cross-validation

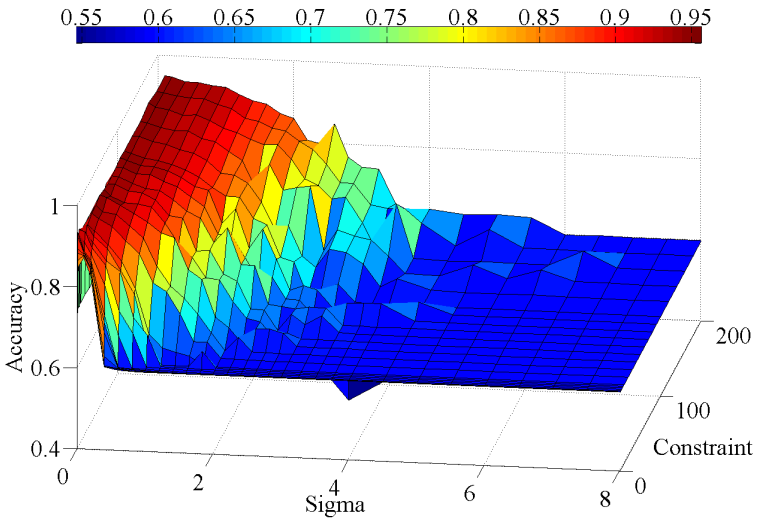

FIGURE 5.28: Grid search showing the accuracy of SVM classifier for a wide range of σ and C for data set, and the colour code represents the accuracy result.

TABLE 5.5: Validation results for KNN and SVM classifiers for different parameters of SVM RFE.

RC	N		Sp	Se	F-M		Sp	Se	F-M
1×10^{-7}	5		0.9018	0.9290	0.9347		0.9259	0.9623	0.9560
	10		0.9018	0.9337	0.9339		0.9203	0.9672	0.9569
	25		0.8992	0.9337	0.9336		**0.9312**	**0.9665**	**0.9600**
	30		0.8619	0.9743	0.9395		0.9253	0.9640	0.9568
5×10^{-7}	5		0.8942	0.9624	0.9432		0.9115	0.9624	0.9515
	10	KNN	**0.8921**	**0.9658**	**0.9446**	SVM	0.9221	0.9668	0.9572
	25		0.9054	0.9629	0.9426		0.9221	0.9644	0.9559
	30		0.8649	0.9583	0.9369		0.9214	0.9672	0.9573
1×10^{-6}	5		0.8500	0.9748	0.9372		0.9183	0.9647	0.9549
	10		0.8953	0.9355	0.9370		0.9297	0.9648	0.9585
	25		0.8325	0.9747	0.9381		0.9253	0.9648	0.9572
	30		0.8943	0.9471	0.9371		0.9253	0.9640	0.9568

method, the best selected values are highlighted. From this table it can be observed that all the algorithms achieved a good performance, once the overall results for Sp, Se and F-M are extremely high.

It was expected a lower performance of KNN classifier when compared to SVM. A good performance of a classifier can be considered when its values of Sp and Se have some balance between them. The best values of specificity and sensitivity were selected for each algorithm. In all cases, the value of Se is higher than 0.9 which means that the False Negative rate is very small, showing that the classifiers are identifying the signal in the correct class. On the other hand, for SVM higher values of Sp, were obtained indicating, again, that SVM classifier have a much stronger performance than KNN classifier. The high values of Se ensure that a small number of signals are classified as noise, and this affords an important characteristic of the classifier for this type of problem, ensuring that good signal segments are not disposed.

The parameters that lead to best accuracy were selected for more detailed testing of the implemented algorithm, to each group of selected features. For these parameters, the graphic illustrated in Figure 5.29 shows the evolution of accuracy with the number

of features chosen from SVM RFE, for the two different classifiers under study with cross-validation method. It can be observed that the best values of accuracy were obtained for the SVM algorithms, which are in agreement with the previously performance analysis and confirms that KNN has a weaker behaviour. Besides that, this illustration gives important information about the number of features that should be selected from SVM RFE.

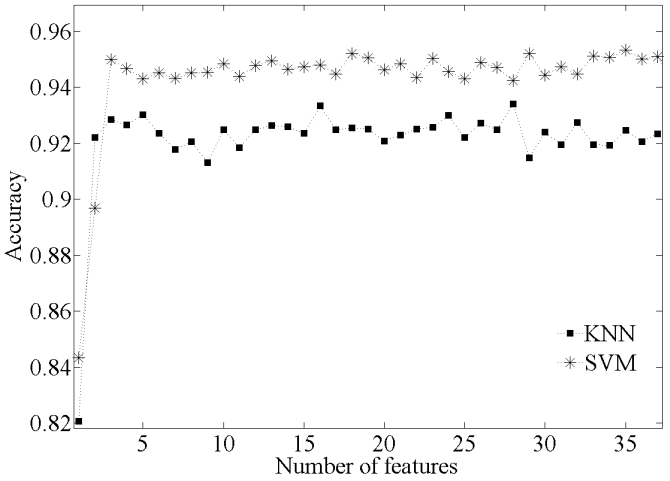

FIGURE 5.29: Accuracy for two classifiers obtained for different numbers of features extracted from SVM RFE.

It is clearly visible that accuracy has a strong increase until 5 features, but from that point it does not suffer substantial changes in the accuracy results indicated that extracting a higher number of characteristics will not affect the classifiers performance. There is therefore a lot of redundancy in the signal features extracted. Through this analysis it can be concluded that the first selected features, from SVM RFE, will have enough information to make a correct and safe distinction between clear and noisy signals. This point has important practical consequences for the classifier implementation, since, being only 5 features necessary processing can be much faster.

The most important features identified by the SVM RFE procedure are: Root Mean Square (RMS); cross-correlation with signal template C and D; relative power for the first two levels decomposition in the wavelet analysis using the mother wavelet function Haar. These 5 features are sufficient for the classifier distinguish between signal and noise.

The Figure 5.30 shows the scatter plots between features, it is observed that the features extracted from signals and noise acquisitions are almost distinguishable.

5.6 Conclusions

Three optical probes specifically designed to measure PTT have been developed, however in the first tests with LEP demonstrated to have a low temporal resolution, not enough for measure the PWV expected in pathological cases. The PPD and APD probe was tested along with three different signal processing algorithms. All three tested algorithms can measure PTT with an error below 8%. Tests show that although both probes are capable of measuring PTT accurately, the APD based one is more precise and accurate.

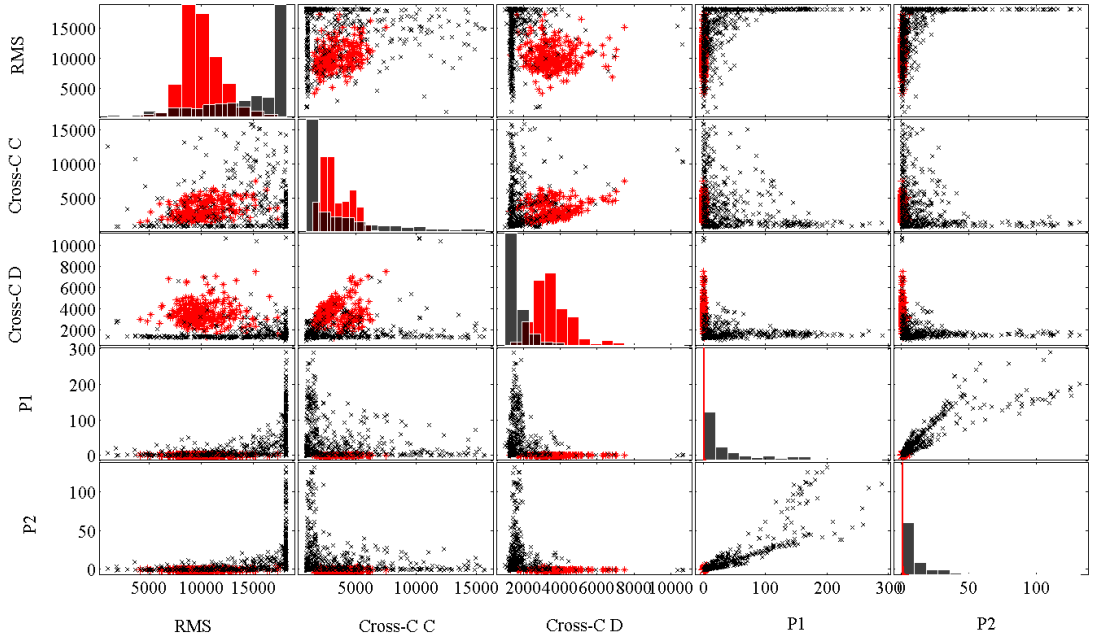

FIGURE 5.30: Scatterplot matrix of the five variables distinguished by class, signals are marked in red and noise with black. The diagonal plots show the histogram of each feature. List of features: RMS; Cross-C C represents cross-correlation with signal template C; Cross-C D represents cross-correlation with signal template D; P1 is the relative power for the first level of decomposition with mother wavelet function Haar; P2 is the relative power for the second level of decomposition with Haar mother wavelet.

The pulse waveform obtained by optical probes, PPD and APD probes, were compared with US in a test bench and *in vivo* at the carotid site. Although both systems, optical and US, allow the reproduction of the arterial waveform, the overall results clearly favour the optical solution. The optical probes are able to reproduce the pressure waveform and respective characteristic points with great consistency and resolution, APD probe exhibits a better performance as well as a lower noise profile, when compared to the PPD probe.

The probes developed with infrared light show better results with the progressive increase in the number of silicone layers. They also provide better resolution in the waveform features and higher SNR and lower RMSE when compared to the signals acquired with visible light.

The APD has an inner gain of 50 due to its intrinsic avalanche effect and is considered almost point-like (1 mm^2). On the other hand, the PPD has a detection area of 52 mm^2, which is 52 times larger than the APD detection area. However, as the PPD does not have any inherent gain, we can consider that the gain of the APD compensates the detection area of the PPD and thus, the signals can be comparable. APD probes exhibit a better performance for both visible and IR lighting, with better SNR when compared to the signals from the PPD probes. On the other hand, the APD has a stronger electric field which allows the decreasing of the drift velocity, a fast response time and an increased bandwidth response.

The study of the attenuation coefficient showed that there is a greater absorption of visible light, when compared to the infrared light, in the silicone layers for both the APD and PPD probes: $\mu_{visible} > \mu_{IR}$. For the probes with visible illumination, a lower amount of light is transmitted when compared with infrared illumination, and the signal

detected is poorer, demonstrating the preference for the ability of the infrared light in tissue penetration, in order to detect the signal in cases of fat accumulation.

The good results obtained with the PPD combined with the far lower cost of the PPD detector makes the LED/PPD combination the best solution.

An algorithm based on a classifier was developed for distinguish valid data signals containing arterial pulse waveform and which part has no relevant information from signals acquired by the optical probe.

The 37 created features which allow the data characterization were divided in different subsets: amplitude features, time domain statistics, wavelet features, cross-correlation features and frequency domain features. The SVM RFE was implemented for feature selection in order to reduce the computational complexity and to improvement of the classifier's performance.

Two classifiers architectures were tested, KNN and SVM, and compared to find the one that guarantees the highest classification performance. The SVM classifier obtained the higher accuracy (0.952) with a specificity of 0.9312, sensitivity of 0.9660 and F-Measure of 0.9600, for a constraint factor of C = 180 and $\sigma = 0.1$.

Chapter 6

Coherent Light Probe Perform Evaluation

This chapter presents the validation tests of a probe based on the self-mixing effect. These tests encompass the electrical and optical crosstalk tests, along with the tests that allow the evaluation of the algorithms' performance for signal processing based on Short-Time Fourier Transform and Empirical Mode Decomposition when applied to self-mixing signals. The next test determines the ability, of this kind of probes, to measure velocity, and other characteristics, of the movement described by a target. The last study represents a novel approach to obtain the mixing effect outside the laser cavity using an external photo-detector.

The optical probe, based on laser Doppler technology, is composed by two LDs. This fact implies the need for electrical and optical crosstalk tests in order to prove the robustness and galvanic isolation of the electric circuits and non influence of optical axis between the LDs.

The main objective of the optical probe developed is the use self-mixing signals to obtain the arterial pulse waveform measured in the carotid artery, of to determine the temporal occurrence of the feature wave points with dedicated algorithms. To achieve these goals, a STFT algorithm and EMD were applied to the self-mixing signals and the performance of the method was evaluated.

The self-mixing probe was tested with two different test benches in order to determine its ability to accurately measure velocity and other movement characteristics of a moving target. These tests included the characterization and analysis of piezoelectric actuators and piezoelectric transducers used in the tests setup.

Some problems could be expected while acquiring signals in the human carotid artery with an optical probe using the self-mixing principle. In order to improve the acquisition a new approach was tested for obtain the self-mixing signals using an external photodetector such as a planar photodiode. This configuration was intended to increase light collection efficiency and therefore SNR.

6.1 Cross-talk Tests

6.1.1 Electrical Crosstalk Results

The probe construction was realized with two independent and identical circuits of driver and trans-amplification. The common points between the channels are the ground and power supply. In order to evaluate the electrical robustness of the probe, the test setup was performed with a devoted test bench. This consists on putting one LD sensor in front of the silicone membrane while keeping the other laser-diode covered with a non reflective material represented in Figure 6.1. Both sensors are switched on but only one of them illuminates the membrane surface.

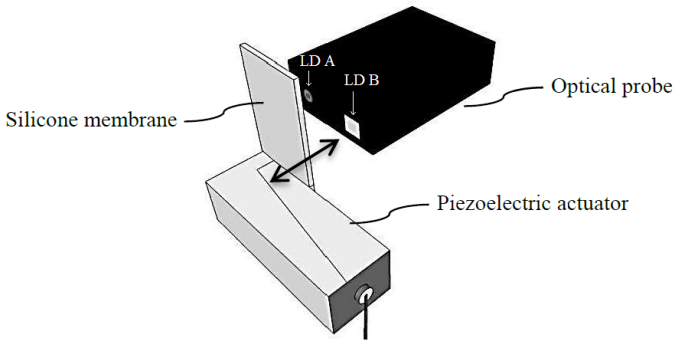

FIGURE 6.1: Electrical crosstalk test bench. The probe has an open laser-diode sensor and a closed laser-diode sensor. Adapted from [183].

The silicone membrane executes a controlled movement that tries to simulate the skin displacement of healthy subject, *i.e.* describes a pulse pressure waveform of C type (see section 2.2). The generated waveform has a period of 1 second, which tries to simulate a heart rate of 60 bpm, and a maximum displacement of approximately 470 μm (refereed value for the carotid distension) [184]. The acquired self-mixing signals are shown in Figure 6.2. LD A corresponds to the opened sensor, emitting light to the membrane, and LD B corresponds to the closed sensor. By analyzing these results it is clearly visible in LD A signal, the modulation caused by the membrane movement (Figure 6.2(a)). In contrast, the LD B signal shows no amplitude modulations correlated with the membrane movement.

6.1.2 Optical Crosstalk Results

When two optical emitters/receivers are used proximal to each other or in the same area, it is important to study the influence of the emitted light from one component in the sensing operation of another component in the vicinity. Due to this problem another test was idealized (Figure 6.3). In this case, the two sensors are open and pointing to silicone membranes. One of the membranes is moving with the pulse pressure profile and the other is fixed. LD A is pointing to the moving membrane and LD B is pointing to the stopped membrane.

Acquired signals from both sensors are showed in Figure 6.4. In the signals is clearly visible the amplitude modulation in the LD A signals due to the membrane movement. In the LD B signals does not exists any indication of this amplitude modulation. In the frequency analysis, by the spectrogram, no components were identified in the signal from LD B. These results prove that laser light reflected by the moving membrane do

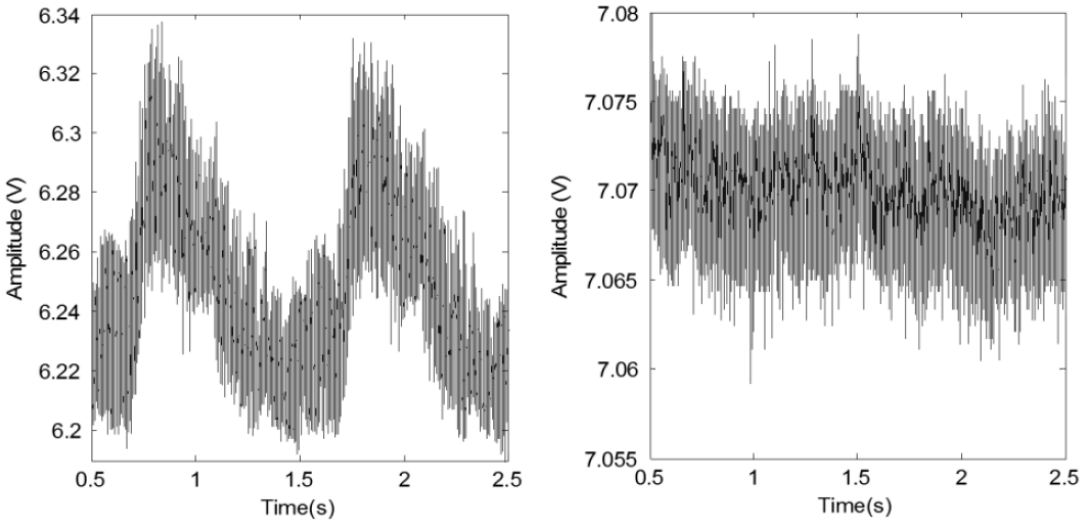

(a) Test setup signals.

(b) Detail of the signals.

FIGURE 6.2: Acquired signals in crosstalk tests. a) Signal of the LD A (opened). b) Signal of the LD B (closed). Adapted from [183].

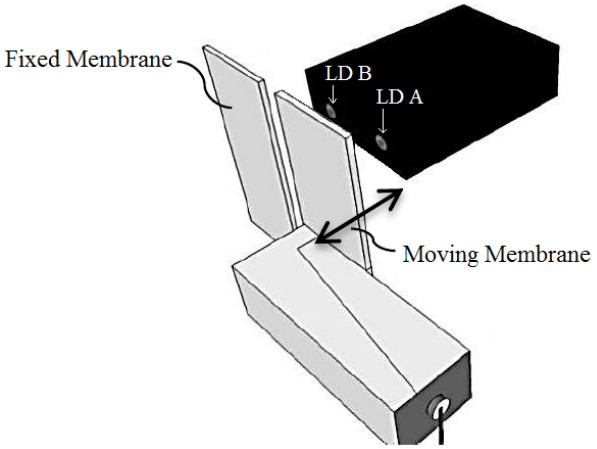

FIGURE 6.3: Optical crosstalk test bench. The probe is placed in front of two silicon membranes. The moving membrane, with a pulse pressure waveform movement and the fixed membrane, without movement. Adapted from [183].

not reach the LD which is pointed to a fixed surface. This fact occurs due to the small area of aperture of the LD, the photodiode is a point-like sensor.

6.2 Empirical Mode Decomposition Results

6.2.1 Test Setup

The test setup, schematically represented in Figure 6.5, was designed to evaluate if the optical probe was able to measure distensions of the same order of magnitude as the ones observed at the skin over the carotid site. The test waveforms were generated by an Agilent 33220A arbitrary waveform generator, which feeds an actuator, biased by a high voltage linear power driver. The actuator moves a mechanical structure, MS as

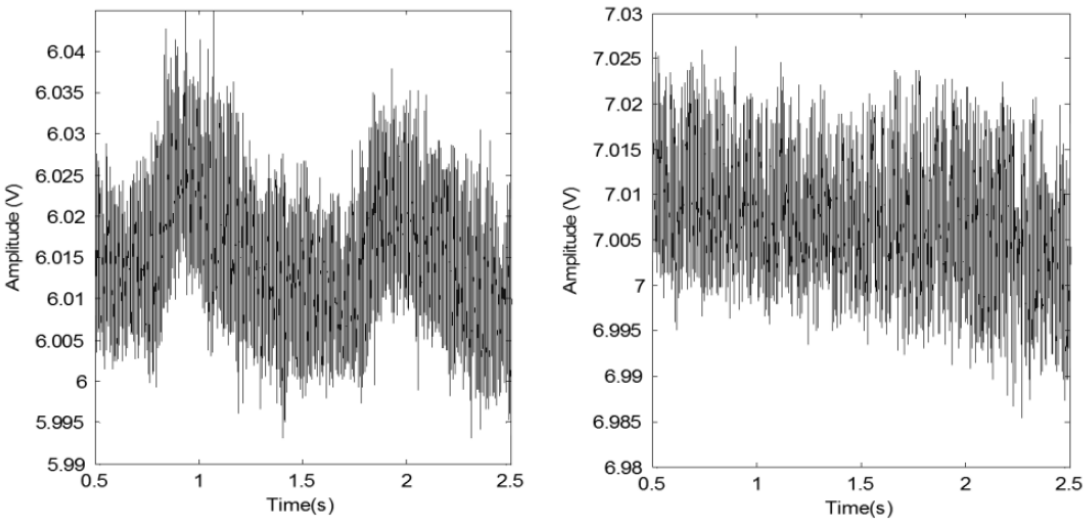

(a) Test setup signals.

(b) Detail of the signals.

FIGURE 6.4: Acquired signals with optical probe. a) LD A pointing to a moving membrane. b) LD B pointing to a fixed membrane. Adapted from [183].

shown in Figure 6.5, lined up with a silicone membrane that reflects the light emitted by the laser-diode, similarly to human skin. Each silicone layer was 1 mm thick and the tests were conducted using four layers (4 mm). The cardiac-like waveforms, generated in the test setup are similar to healthy individual cardiac waveforms. The actuator reproduces these waveforms with a maximum displacement of 500 μm. The optical probe was positioned in front of the MS and detected variations of the reflected light.

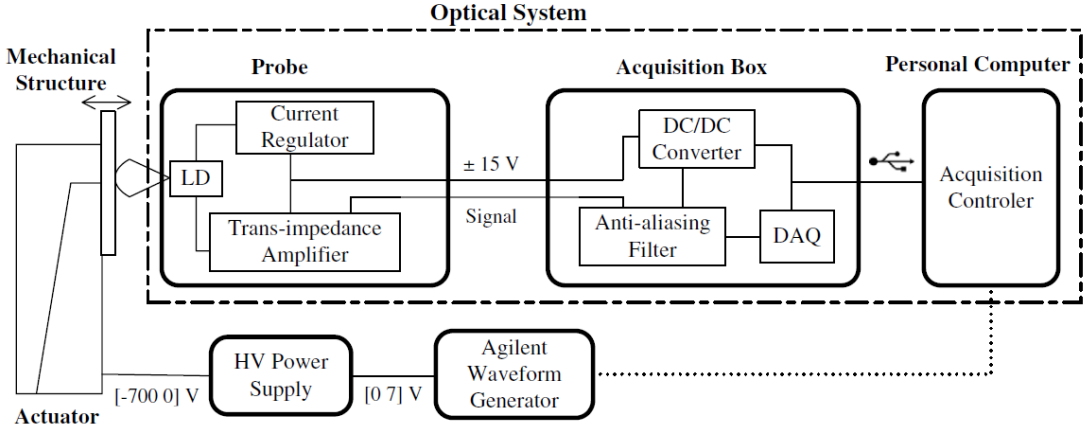

FIGURE 6.5: Block diagram of the optical system and all its minor components and simple diagram of the implemented test setup. Adapted from [183].

Self-mixing signals were acquired in a long range of sampling frequencies (from 20 kHz up to 200 kHz) [76], [185], [186]. The sampling frequency set must ensure that it is always higher than twice the Doppler frequency to be measured with this system. In the arterial pulse pressure, the velocity expected for the carotid movement is approximately 4500 μms^{-1} [187], that corresponds approximately to a maximum Doppler frequency of 20 kHz. A 100 kHz sampling frequency was elected for the acquisition of the signals since it ensures the best compromise between signal quality and computational effort,

according to a shape waveform RMSE test. As mentioned before, section 4.2, the self-mixing signals are a non-stationary type of data due to their high dependence on the Doppler effect [75]. The typical signals acquired in the test setup are shown in Figure 6.6 and the solid line represents the actuator displacement.

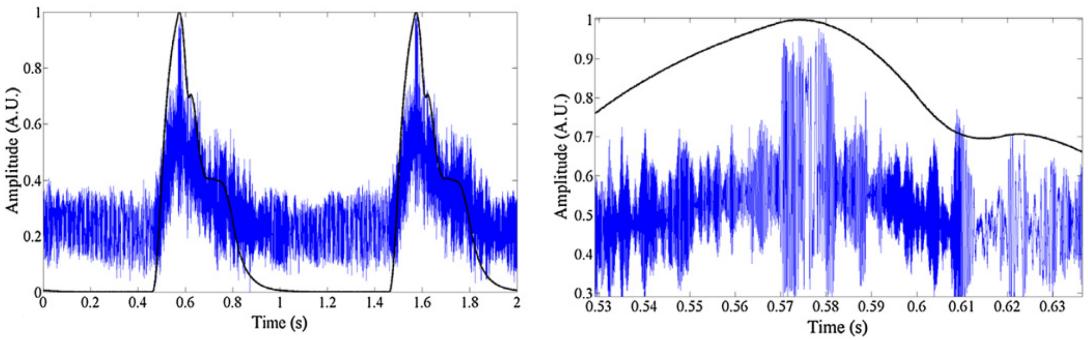

(a) Test setup signals.

(b) Detail of the signals.

FIGURE 6.6: Test setup signals. (a) Self-mixed laser signal acquired in the test setup and the waveform described by the actuator marked by a solid line. (b) Detail of the signals, self-mixing effect.

The Doppler signals require a time–frequency analysis to extract most of the physiologically important parameters. To find the time of occurrence of the clinically relevant feature points of the pulse pressure waveform a STFT was performed. This algorithm was used with a 124-point length Hanning window and a 100-point segment overlap for high temporal resolution [104]. The Fourier length was 1024 points using zero padding of the analyzed signal to obtain a better frequency discretization and the resulting spectrogram is shown in Figure 6.7(a), a two-dimensional matrix with the coefficients representative of the frequencies present in each time window. After these processing stages, a two-dimensional signal was constructed for a good visualization of the time–frequency spectrum (Figure 6.7(b)). Numerically, this is achieved by finding the maximum value in every column and representing its values on a time scale. Since the dc value of the signal is extremely high, the zero frequency is the predominant at every window. However, as the zero frequency does not bear significant information, it was excluded from this search of frequencies in order to find the correct Doppler shift frequency using this algorithm. In addition, a threshold was defined to prevent the determination of image artifacts as predominant frequencies. Thereafter, a Doppler shift frequency was reconstructed along time from the original self-mixing signal. The reconstructed signal represents the most predominant frequency of the original self-mixing signal over time, which corresponds to the Doppler frequency shift.

Figure 6.7(b) shows the reconstructed signal which evidences a strong correlation with the derivative of the signal fed to the actuator, despite the presence of high noise level. To remove the noise present in the reconstructed signal an EMD-based algorithm was conducted. This method intended to create a multiscale decomposition and a time–frequency analysis of the reconstructed signal [132].

Figure 6.8 represents the decomposition levels with relevant information in EMD processing. The smoothing effect of this algorithm is clearly evident as the signal is decomposed. In the first levels, noise spikes are removed and the waveform is preserved, in the last levels do not show the main waveform, but the frequency presented in the envelope of level 5 is the fundamental frequency of the original signal. The level 6 of decomposition has no longer relevant information.

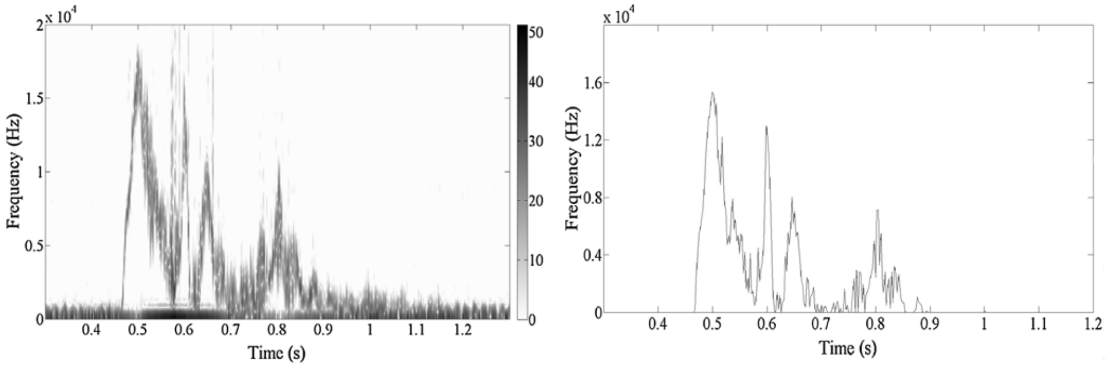

(a) Spectrogram.

(b) Wave reconstructed.

FIGURE 6.7: Spectrogram of the original signal. (a) Spectrogram in a conventional gray scale representing the top 50 dB of the signal. (b) Wave reconstructed from the image spectrogram.

TABLE 6.1: RMSEs between the turning points from the waveform generator and the temporal features determined by the EMD in the first level.

data sets	1st	2nd	3rd	4th	5th
Systolic peak e_{RMS} (ms)	2.5	2.7	2.9	4.7	2.9
Reflected wave e_{RMS} (ms)	1.4	1.3	1.9	2.1	3.0

6.2.2 Error Evaluation

The described algorithm was applied to five different data sets. For every test, data were acquired in the test setup and, between the data acquisition, the probe was withdrawn from the forward-facing of the membrane and re-aligned. Such variations of the initial conditions permit the understanding of the influence of the probe's positioning and alignment in the final results. The data sets are composed of the generated original signal, the self-mixing signal and time correspondence.

After the signal processing, a few quality parameters were extracted by comparing the reconstructed and the original data in order to evaluate the performance of the presented algorithm. Since temporal coherence is the objective of this work, the temporal occurrence of the SP and the reflected wave were previously determined for all data sets. Each data set has ten SP and ten reflected waves because the synthetic pulse waveform period is 1 s. Besides this, the corresponding SP and reflected wave occurrence time were computed in the reconstructed signal using a semi-automatic method. For each peak, the time lags were calculated by subtracting the original time occurrence from the reconstructed time occurrence.

Finally, the RMSEs for the SP and RP were calculated for each data set. For every data set, the first and second levels of decomposition were considered. The first decomposition level achieves the best performance in all cases and the errors were computed for this decomposition level.

In terms of RMSEs (table 6.1), it is important to note the high precision in the point time determination of the reflected wave. For this event, the maximum mean error was 3 ms for the fifth data set. Between data, small differences in errors occurred. This fact is understandable because the probe alignment influences the quality of the extracted signal but, despite this, the reconstructed algorithm showed high robustness.

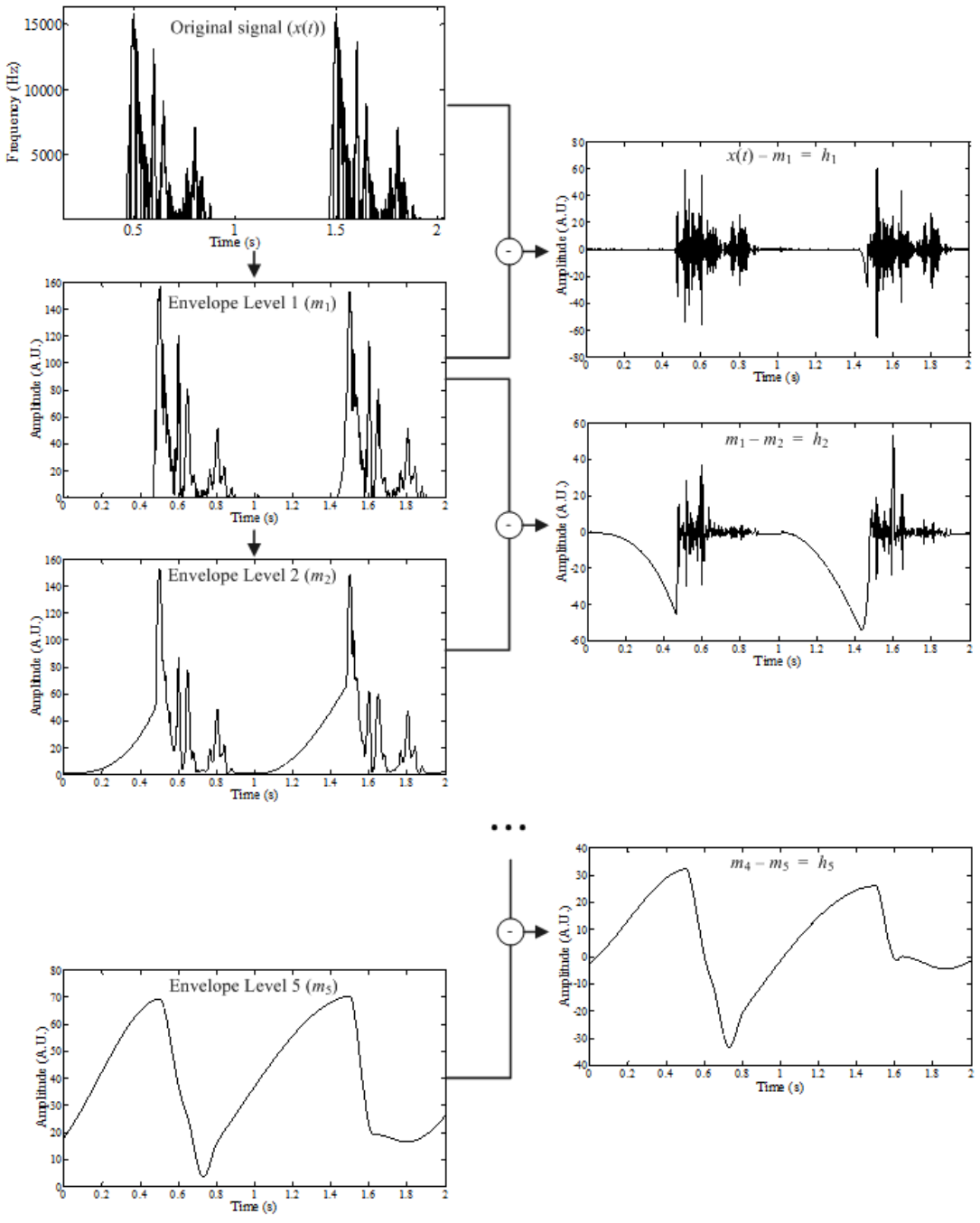

FIGURE 6.8: EMD first, second and fifth levels. The envelope and the residue result for each level.

With regard to the systolic peak, the RMSEs were slightly larger in almost all sets and never exceeded 3 ms. The high RMSE in their fourth data set is an outlier probably originated by an under optimization of the alignment in the test setup. Lastly, all time errors were small if one considers that under physiological conditions the pulse waveform has a period between 1 and 0.5 s, which is equivalent to 60 and 120 beats per minute. Data sets were composed of ten SP and ten reflected waves that made a total of 50 feature points for each data set. To get information about the dispersion of the time errors, a histogram (Figure 6.9) was constructed with the time errors of all analyzed data, separated by the feature points (SP and RP).

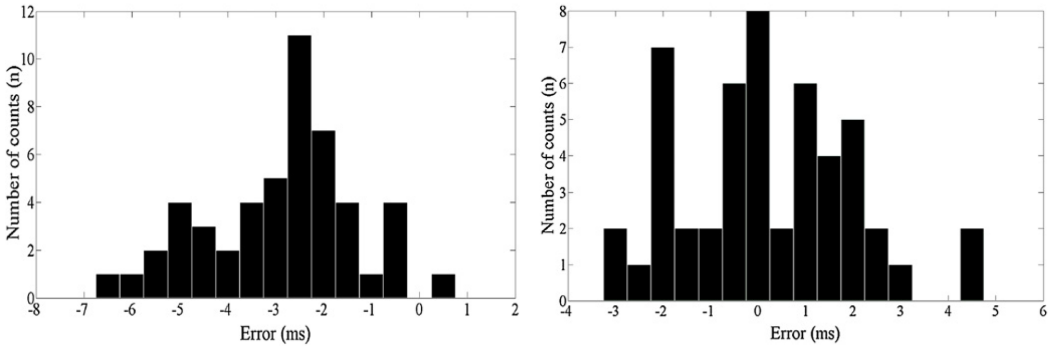

(a) Error dispersion for the SP.

(b) Error dispersion for the RP.

FIGURE 6.9: Error dispersion plots for each temporal feature determined by the algorithm. (a) Error dispersion for the SP determination. (b) Error dispersion for the RP.

Considering the histogram of the single errors, a strong conclusion needs to be made. At the time of the determination of the SP, almost all errors had a negative signal. This means that all points were identified with a small delay. This conclusion is acceptable because the spectrograms do not permit to split the original signal into an infinite number of windows. Another cause for this delay is the strong dc component present in the original signal. The need to remove this signal component causes some information loss. Nevertheless, in the reflected wave point histogram, a more balanced distribution of the errors is present. This fact happens because the reflected wave has two rapid turning points (local maximum and local minimum) and the reconstruction algorithm, in some cases, can only identify one of them.

6.2.3 *In vivo* Carotid Measurements

The expected follow-up of this work started with the acquisition of pulse data in humans, in the carotid artery. Measurements were carried out after 15 minutes of rest period in a temperature controlled environment (25 °C). Each exam procedure consisted in the acquisition of a set of cardiac cycles at the carotid artery during 2-3 minutes, with the patient lying in supine position.

Figure 6.10 shows a preliminary acquisition in humans using the optical probe. Data were collected directly into a portable computer for a few minutes. The signals show great consistency in the waveform of the pressure wave (Figure 6.10(a)). The self-mixing effect is clearly visible in the Doppler signal (Figure 6.10(b)).

The one-dimensional signal reconstructed from the spectrogram of the set of acquired pulses is shown in Figure 6.11. The reconstructed signal shows the periodic structure of the wave, proportional to the velocity of the distension of the carotid wall.

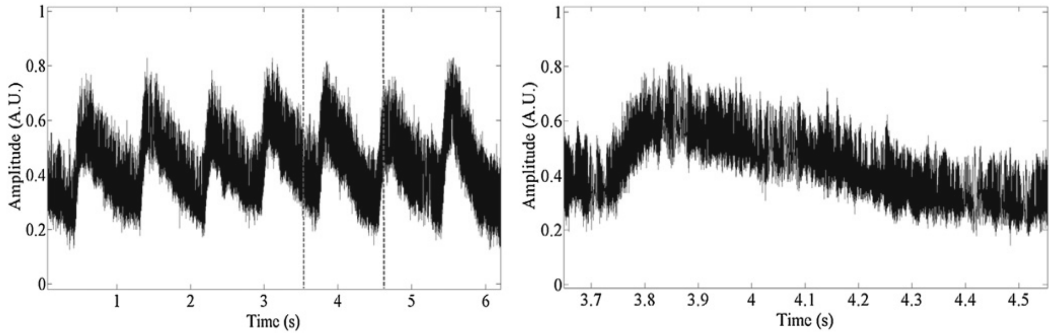

(a) Set of cyclic laser Doppler signals.

(b) Detail of the pulse detected.

FIGURE 6.10: *In vivo* carotid measurements. (a) Set of cyclic self-mixed laser Doppler signals from the movement of the carotid artery. (b) Detail of the pulse detected by the optical probe.

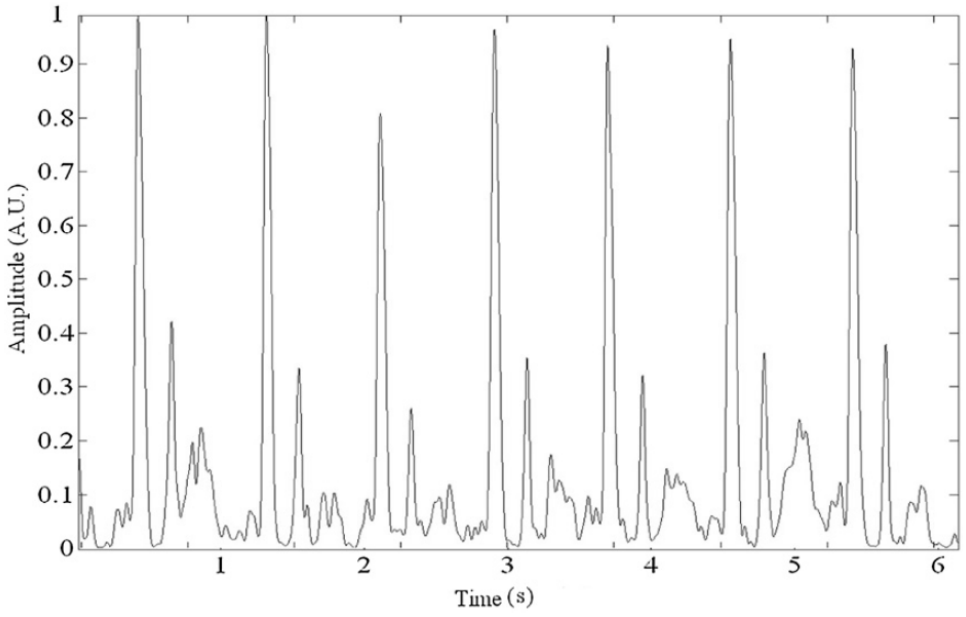

FIGURE 6.11: Reconstructed signal from the STFT and EMD.

6.3 Sub-micron Doppler Vibrometry

The capabilities of the optical probe measurement vibration was tested in extreme conditions, sub-micron amplitude vibrations and high frequencies. This probe was tested with two test bench apparatus that enhance its precision performance, with a linear actuator at low frequency (35 μm, 5 - 60 Hz), and its dynamics, with disc shaped transducers for small amplitude and high frequency (0.6 μm, 100 – 2500 Hz).

Doppler shifted scattered light is proportional to the component of its axial velocity with a magnitude that may be evaluated by measuring the frequency of the beats produced by the scattered light [100]. The readout LD signal is converted in a Doppler spectrogram, using a short-time Fourier transform and overall spectrogram represents the estimated signal power distribution in the time-frequency plane, and each instantaneous time has a corresponding instantaneous frequency. The velocity of a target is not constant and the statistical distribution of the successively measured Doppler shifts is proportional to the Probability Density Function (PDF) of the object velocity. The

maximum Doppler frequency corresponds to the maximum velocity of the target. The peak of the curve on the power spectrum corresponds to the dominant frequency and can be related with the scattered velocity [188], [189].

Based in the information given by the Doppler spectrogram and power spectrum from the selfmixing signal it is possible to determine the velocity and the amplitude of the moving target, and consequently it is possible to reconstruct the movement equations described by the target vibrations [76].

6.3.1 Test Benches

The optical probe was tested in two different test setups, where two types of displacement transducers were used. The first one is based on a piezoelectric actuator whose movement can be electronically controlled, biased by a HV Amp. This test allows an error evaluation by comparing the original values defined in the system with the measurements obtained by the self-mixing signals.

The second bench test is based on a disc shaped piezoelectric element driven by an oscillating electronic circuit and was conducted to study the capability of the probe for measurement a sub-micro vibrations.

6.3.1.1 Test Bench I - Sensibility characterization

The test bench I, which is represented in Figure 6.12, was based on a piezoelectric actuator mechanically coupled to a mirror surface that acts as the moving target. For bench procedure, a sinusoidal driving signal was used thus providing a single frequency oscillatory movement. This test was designed to evaluate the ability of the optical probe to measure the velocity and amplitude in a micron range.

The sinusoidal movement signal was provided by an actuator (ACT in Figure 6.12) driven by the HV Amp; that amplifies to the appropriate high voltage level the Agilent® 33220A output. The mirror attached to the actuator reproduced a pure sinusoidal movement with 35 μm amplitude. In the velocity study, several frequencies, from 5 to 60 Hz, were tested with the optical probe axis perpendicular to the mirror surface in order to detect the Doppler frequency modulation imposed to the reflected light.

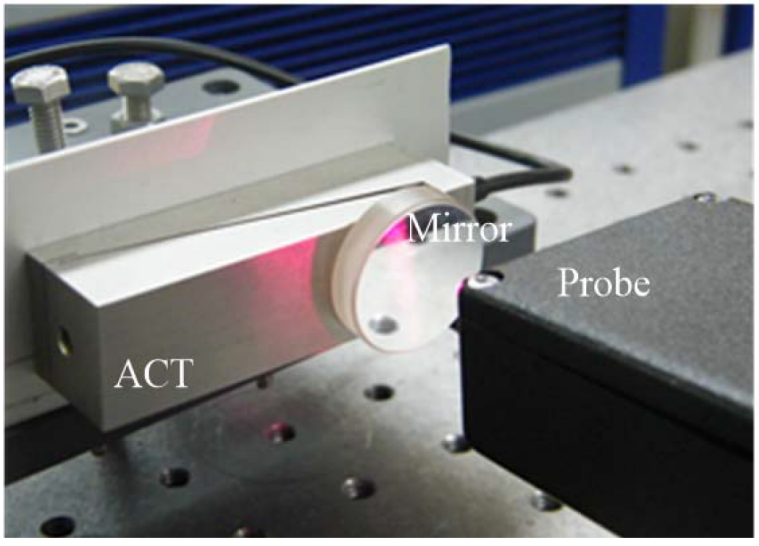

FIGURE 6.12: Photo of the experimental setup with ACT, mirror and the optical probe.

6.3.1.2 Test Bench II - Vibration Response Characterization

In the second test bench the ACT was replaced by a piezoelectric disc, finely polished to improve the reflection properties of the vibrating surface. A circularly-shaped piezoelectric sounder, MURATA® 7BB-35-3, with 23 mm electrode size diameter and 2.8 ± 0.5 kHz resonant frequency, was used.

To determine the characteristics of the Piezoelectric (PZ) vibration, a sinusoidal voltage from an Agilent® 33220A arbitrary waveform generator, was used as a driving signal for the sounder. Figure 6.13 depicts this test bench apparatus with a three axis linear precision positioner (T-LA28A from ZABER® Linear Actuator, 28 mm travel range with RS-232 interface) that allows precise control of the actuator position relative to the probe. The PZ is welded at two points at the edge of the metal disc to guarantee free vibration of the piezo wafer.

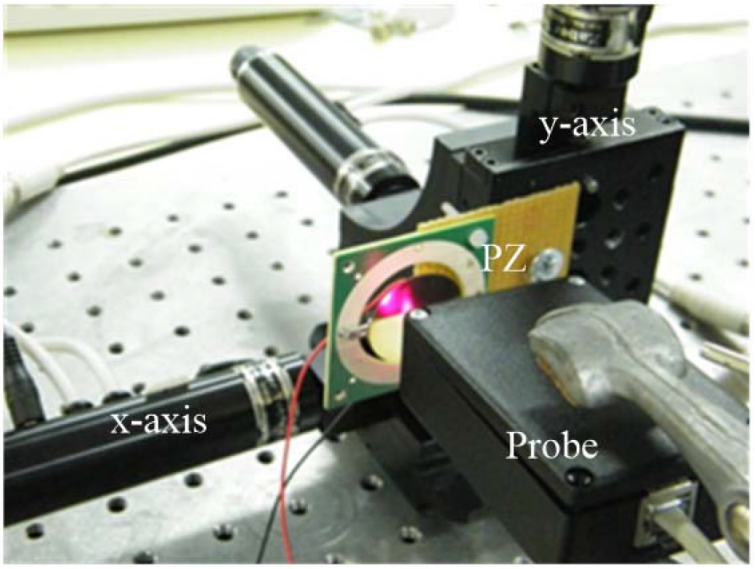

FIGURE 6.13: Photo of the experimental setup with PZ disc fixed in three linear actuators in front of optical probe.

6.3.2 Results and Discussion

The self-mixing signals readout from the optical probe, were processed in order to characterize the mechanical dynamics of the target. Complementally, a study of the errors associated to this measure was performed.

6.3.2.1 Actuator Velocity Determination

The self-mixing signals were sampled at 100 kHz. Figure 6.14 shows the power spectrum of the self-mixing signals obtained when the sinusoidal frequency, that drives the ACT, is swept from 5 to 60 Hz, with a constant amplitude of the 35 μm . The Doppler frequency is computed as the maximum peak in the power spectrum calculated for the signals (magenta dots). It is clearly visible that the Doppler frequency increases when the ACT velocity also increases. However there is a non-linear correlation between these two variables that were expected to be linearly correlated. This behaviour results from the operating limits the HV Amp when it drives high capacitive loads. Regarding the inherent electrical capacitance of the actuator (290 nF ± 20%), the response curve of the HV Amp presents a decreasing amplitude for frequencies values higher than 45 Hz.

In Figure 6.14 it is also possible to identify another frequency component, which is twice the Doppler frequency, representing a second harmonic generated by the multiple reflections at the dielectric mirror used in the test setup. An interface between two different dielectric media is a source of second and third-harmonic components which are clearly visible in the spectrogram (Figure 6.14) [16]. In the power spectrum plot the presence of a strong component at 28.52 kHz and at 42.97 kHz is also clear, for all the analysed signals. This effect results from an interference in the DAS, which is easily proved since the two peaks remain in the spectrum even for acquisitions with the probe turned off. However, these interference peaks don't affect the conclusions on the target's dynamics, if properly considered during processing.

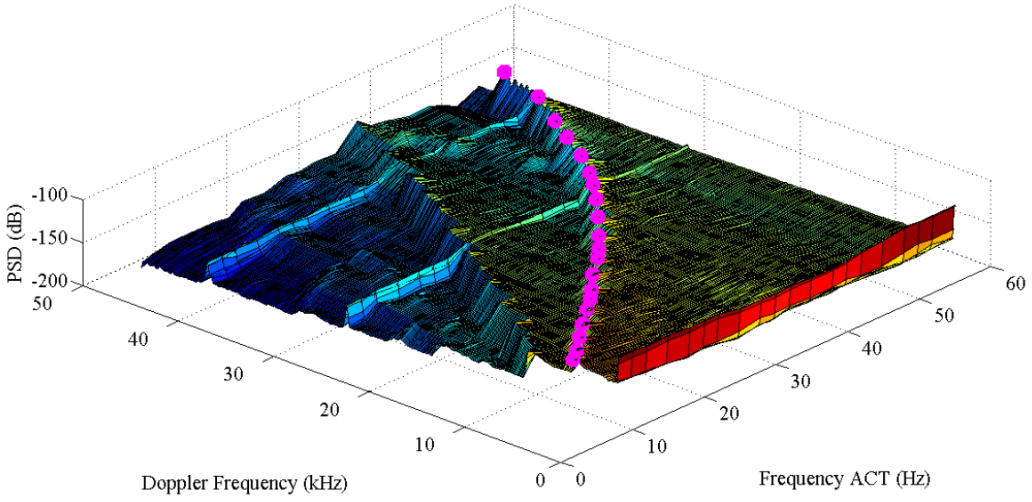

FIGURE 6.14: Power spectral density generated by the self-mixing signals for a sinusoidal vibration of the ACT (movement frequencies between 5 to 60 Hz). The power spectral characteristics evidence the behavior of Doppler frequency with the ACT frequency marked with magenta dots.

The theoretical relationship for the Doppler frequency, equation 3.4, allows the determination of the ACT velocity. To solve the equation that describes the sinusoidal movement, the amplitude of the ACT displacement needs to be assessed. The spectrogram is considered the most valuable tool to derive the target movement from the self-mixing signals. This time dependent spectral description of the signal is obtained through a sequence of STFT over the analysis interval, providing a two-dimensional matrix with the coefficients proportional to the frequencies present in each time window (Figure 6.15). In this grey scale plot the predominant frequencies are represented by the darker colours (50 dB). The successively attenuated harmonics are clearly visible as lighter traces on the STFT plot. The period of the original signal can be estimated from the spectrogram analysis considering the double frequency of the self-mixing signal, arises from the rectified effect results the Doppler technique.

From equations 6.1, 6.2 and 6.3 that describe the sinusoidal movement:

$$x(t) = A\sin(\omega t), \tag{6.1}$$

$$v(t) = A\omega\cos(\omega t), \tag{6.2}$$

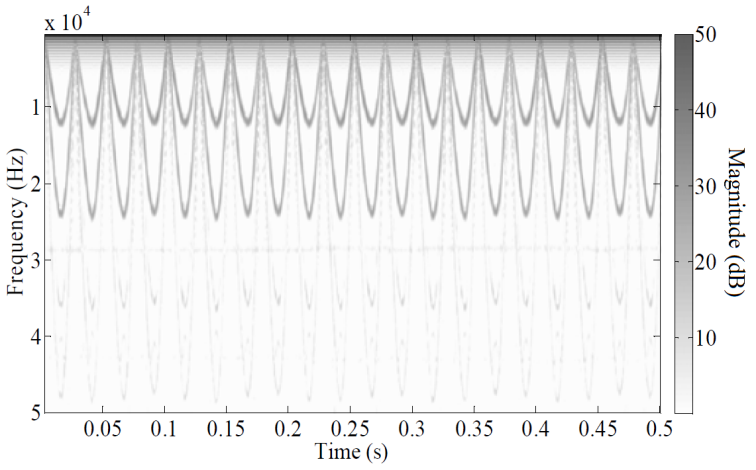

FIGURE 6.15: Spectrogram for a self-mixing signal at a 20 Hz vibration of the actuator ACT. Conventional gray scale representing the top 50 dB of the signal.

$$a(t) = -A\omega^2 \sin(\omega t), \tag{6.3}$$

These expressions are related to equation 3.4 leading to the equation that describes the velocity $\nu = A\omega$.

6.3.2.2 Error Evaluation

For the results obtained with optical signals processing was important quantify the error and study their origin. The velocity computation, according to the previously described expressions, revealed a particular distribution illustrated by Figure 6.16. The comparison between these values obtained from the self-mixing signal analysis and the real values, imposed on the actuator shows an average error of 10% for the amplitude and velocity values. This error is inversely proportional to the ACT driving frequency for values bellow 45 Hz and quickly increases above this value. This behaviour is explained by the performance degradation of the actuator for this frequency range, as mentioned earlier.

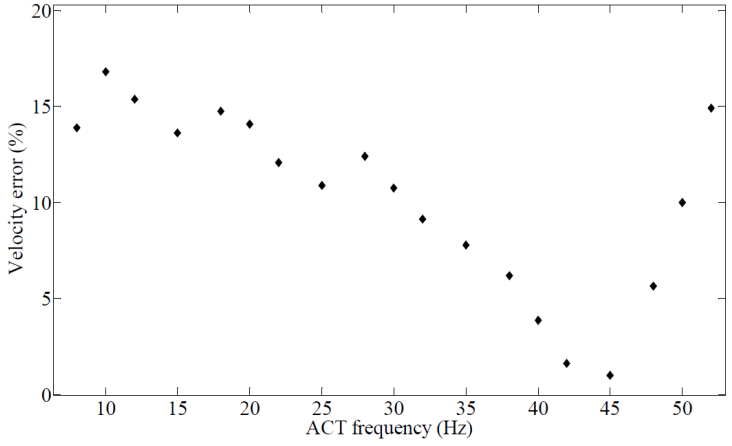

FIGURE 6.16: Error evolution for the velocity determined in the different frequencies tested.

The relative error is higher at lower velocities and decreases when the velocity increases. Similar results obtained by other authors [105], [190], [191] support these observations. It is shown that the method is not sensitive to slow movements, *i.e.* low frequencies, since the Doppler frequency is too close to the fundamental frequency and consequently cannot be clearly distinguished.

The movement amplitude is estimated from two variables extracted from the self-mixing analysis: ν and ω. The amplitude mean value obtained is 33.8 μm with standard error of 5.6 μm. The error associated to these values produces an amplitude error of less than 20% in all measurements.

6.3.2.3 Piezoelectric Velocity Measurements

Higher Doppler frequencies are expected for the test bench II in order to test the capability of optical probe to measurement sub-micron vibrations. As the sampling frequency must always be higher than twice the measured beat frequency (from the Nyquist–Shannon theorem), the self-mixing signals were sampled at the higher possible frequency supported by the DAS, *i.e.* 500 kHz.

To study the PZ vibration it was necessary to select the best surface region on the PZ to acquire the signals. In order to build the PZ vibration profile, a systematic disc surface scan was performed. The axis linear precision positioners were used in 28 incremental steps, both in x and y axis, resulting in a square image (28x28 *pixel*). The signals were acquired for a fixed vibration frequency of 600 Hz, which is far enough from the PZ resonance frequency expected to be around 2.8 $\pm$ 0.5 kHz. The Doppler shifted frequencies determined are represented by a colour scheme in Figure 6.17. From the observation of this image it can be concluded that points near the disc fixation site (left and right peripheral points) present low vibration, *i.e.*, the determined Doppler frequency is close to zero. This vibration absence, corresponds to a null velocity, and account for the elliptical shape of the vibration area.

The vibration amplitude, in the centre of disc was estimated to be 0.6 μm by using the central Doppler information presented in the PZ disc scanning.

The Figure 6.17, obtained from the surface scan, can be used to identify the vibration mode of the PZ disc and explains the deflection directions on the disc. The vibration mode (0,1) acts like a monopole source, and represents the most efficient mode concerning the transfer of vibrational energy [192].

The frequency spectrum of the PZ measured by the optical probe is shown in Figure 6.18. The PZ disc transducer was swept by frequencies from 100 to 2500 Hz, and, for each scan, four slightly different amplitudes were tested. Frequencies above 2.5 kHz were tested but the power spectrum of the self-mixing becomes very complex, making the Doppler frequency determination very hard most likely due to the resonance effect expected for these frequencies.

The behaviour of the Doppler frequency curve (Figure 6.18) shows an inflection point when the PZ vibrates at 1 kHz that can be properly understood considering the impedance analysis of the PZ (section 6.3.2.4).

In the test bench the piezoelectric layer converts electrical energy into mechanical energy. When excited at the resonant frequency, the PZ will resonate freely with higher amplitude than at any other frequencies. In the vicinity of this resonant frequency, an anti-resonant frequency is expected, with a consequent impedance maximum and, therefore, minimum oscillation amplitude.

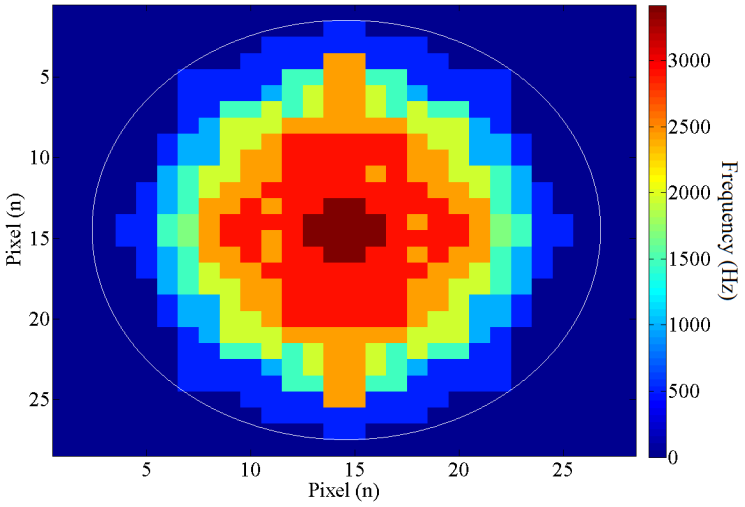

FIGURE 6.17: The mode shape (0,1) of the PZ disc vibration obtained by the Doppler frequencies. The scales represent the number of pixels, and the colour code represents the Doppler frequency (in Hz) for each pixel.

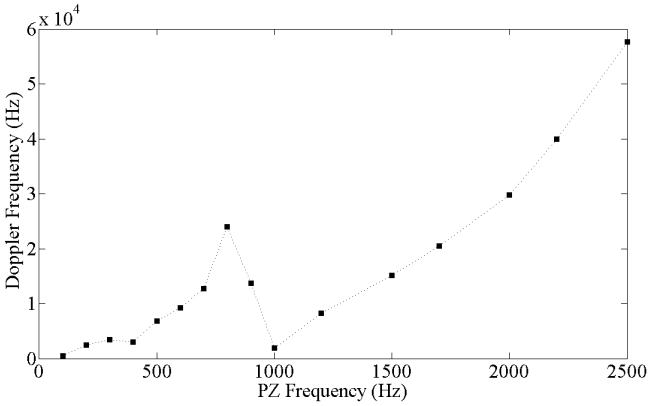

FIGURE 6.18: Typical curve response for the Doppler frequency obtained from the self-mixing signals for different frequencies in the PZ movement.

6.3.2.4 Piezoelectric Impedance Measurements

The ability to transform electrical energy into mechanical energy depends on the frequency response of the PZ and can be measured through the impedance spectrum. The impedance analysis implies the measurement with an electrical impedance spectroscopy Electrical Impedance Spectroscopy (EIS) system [193] being the obtained results represented in Figure 6.19.

The resonant frequency, i.e. minimum of impedance, occurs at 3 kHz which corresponds to the value expected for the PZ used in this study. The anti-resonant frequency, *i.e.* maximum impedance, occurs immediately afterwards, at about 3.3 kHz. For the anti-resonant frequency, the PZ disc shows almost no displacement and no reproductive behaviour to the applied voltage, showing minimum conversion of electrical energy into mechanical energy. There is another maximum in the impedance curve that explains the particular behaviour for the determined Doppler frequencies. At around 1 kHz (red dot mark in Figure 6.19 the Doppler frequency is close to zero due to the higher impedance of PZ. The dashed box in Figure 6.19 defines the frequency window that is represented

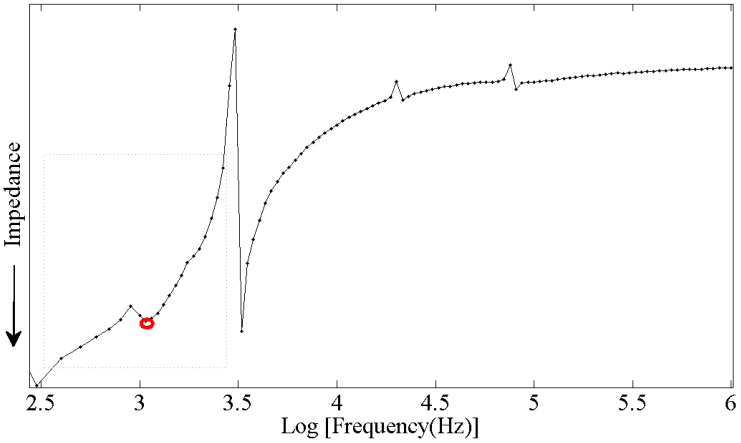

FIGURE 6.19: Impedance of a piezoelectric disc for several frequencies. The frequencies are represented in logarithmic scale. Dashed box define the frequency window that corresponds to the frequencies analyzed for the PZ response, red dot makes a second anti-resonance point in 1 kHz.

in Figure 6.18 8 and exhibits the same wave profile, which explains the behaviour of PZ vibration and Doppler frequencies obtained.

6.3.2.5 Piezoelectric Energy Study

The electric to mechanical energy conversion in the actuator accounts for the mechanical movement (oscillation) of the piezo element and its adjacent materials, when the sinusoidal voltage is applied. The electric power delivered to the PZ is evaluated by measuring its electrical current using a sense resistor. The instantaneous electric power for a 600 Hz frequency was found to be 2.9 x 10^{-3}W.

The mechanical power was computed as the sum of the power of each pixel, as seen in Figure 6.17, $P = \Sigma m_p a_p v_p$ where a_p and v_p are acceleration and velocity, respectively, directly derived from the corresponding Doppler frequencies, and m_p is the mass of the vibrating pixel, estimated from its dimensions and from the physical properties of the disc [194]. A total mechanical power of 6.01 x 10^{-6}W was computed.

The efficiency of the energy conversion process, understood as ratio between the electrical input and the mechanical output powers, was computed to be 2.07 x 10^{3}. A significant part of the electric energy seems to be lost due to the source-load impedance mismatch at 600 Hz, which is very far from equality, the condition for maximum power transfer. The low conversion efficiency of piezoelectric materials also contributes to these final results that are similar to others [194], [195].

6.4 Out-of-cavity Self-Mixing Approach

During the *in vivo* tests, some difficulties were verified in the acquisition the signals in the human carotid artery with an optical probe using the self-mixing effect. The laser-diode has a small aperture area which means that, for physiological sensing techniques, can be considered to act as a point of light detection. This feature causes difficulties in recording good quality signals in physiological conditions, *i.e.* it is difficult to place the sensor exactly above the carotid artery. On the other hand, some limitations on the power of the optical probe are imposed by the security rules of laser exposure. Light output power cannot exceed values for which there is risk of damage of organic tissues,

such as skin [109]. The high power for the LD improves the SNR of the acquired signals; however, the medical devices have security limitations.

In order to avoid the problems in the *in vivo* tests, an external PD with a large area is coupled to the probe, collecting more photons reflected from the skin and then improving the quality of the signal producing a higher SNR. However, a high capacitance inherent to the photodiode reduces the frequency bandwidth for the detection. For this reason the size chosen for the photodetector is defined by the balance between the area for the collection of photons and the frequency bandwidth which allows the obtention of the self-mixing effect.

The aim of this work is to demonstrate the possibility of acquiring self-mixing effect signals outside the laser cavity, using an external photodetector such as a planar photodiode. For this purpose, a test bench setup was designed. The developed probe is based on a LD component that emits the coherent light required for the self-mixing effect and a planar photodetector that receives the final signal. For the test bench the presence of two reflectors is mandatory. The first one was fixed and that reflects the light beam with the same frequency of the original one, and the second one that is movable in order to reflect a light beam with a different frequency.

6.4.1 Test Benches

Two test benches were designed in order to obtain a self-mixing effect outside the laser cavity, using an external photodetector. To prove this concept, two simple test benches were constructed. In both cases, the aim was to have a fixed reflective surface, acting as a reference for that conserved the original frequency, and another moving surface that reflects the light corresponding to the Doppler effect. The interference between the beam with Doppler shift frequency and the original beam, the self-mixing effect, occurs in the planar photodetector.

For this purpose the test bench A used a fixed mirror that reflects the beam with the original frequency, and the test bench B used an optical wedged beam splitter to reflect a multiple beam with the original one. In both cases, a moving mirror was used to produce the Doppler shifted frequency beam.

6.4.1.1 Test Bench A

Test Bench A: Characterization

In the first test bench the LD and the photoreceptor were positioned in the same plan. The Fixed Mirror (FM) was positioned between the LD and the speaker, making a defined angle, in order to reflect the light beams from the LD to the photoreceptor. The Moving Mirror (MM) was placed just behind the FM, bonded in a loudspeaker to reflect the light over to the photodetector. The MM is attached to the loudspeaker which moves with a sinusoidal profile. Light from the fixed mirror was reflected with the same frequency as the original beam and the light reflected from the movable mirror was reflected with a different frequency (Doppler shifted). Figure 6.20 presents a 3D model of the experiment with the light beam representation.

Test Bench A: Signals

The signals that were acquired on the test bench A are represented in Figure 6.21 which shows a typical set of signals detected by the planar photodetector. Several data sets were recorded for alignment and positioning changes.

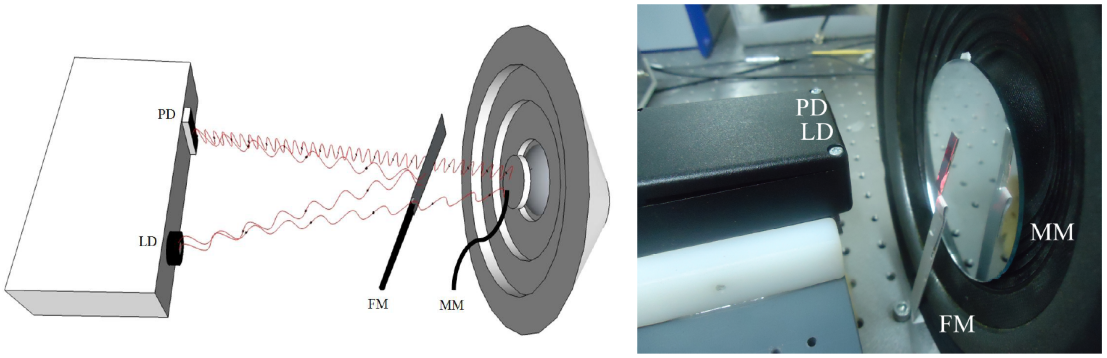

(a) Drawing of 3D model of the experiment.

(b) Photo of the experimental setup.

FIGURE 6.20: Test bench A. a) Diagram model of the operating mechanism. b) Photo of the experimental setup with FM, MM, PD and LD. The light beam is represented with the red waves.

Figure 6.21 shows the photodiode signals acquired from the described experiment (Figure 6.20). . This amplitude modulation is extremely evident in the planar PD, due to its large photo sensitive area of the planar photodiode 6.21(a). The approximation and withdrawal of the mirror causes variation in the number of photons reflected directly to the photodiode. Figure 6.21(b) shows the self-mixing effect manifestation in the turning points of the main profile. The fringe number increases with the velocity increase of the movable mirror [76], *i.e.* the Doppler frequency is proportional to the mirror velocity. In the turning point (stopping of the mirror), is clearly seen a decrease in the signal frequency oscillations which is consistent with the self-mixing effect [103].

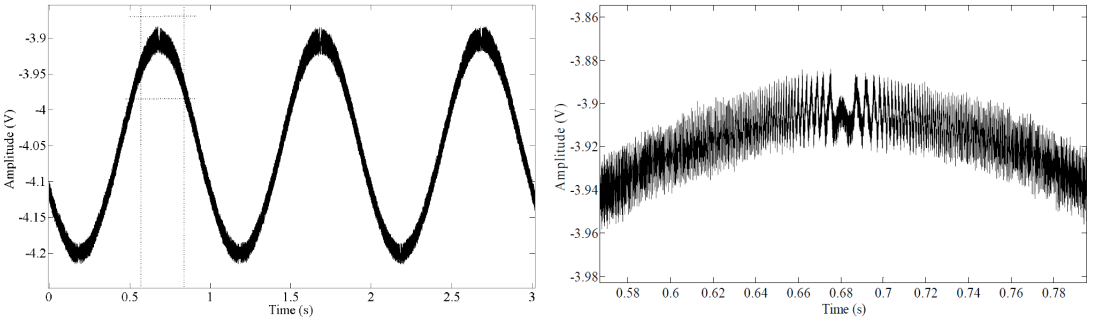

(a) Set of cyclic laser Doppler signals.

(b) Detail of the pulse detected.

FIGURE 6.21: Planar photodiode signal form test bench A. a) Row of pulses with amplitude and frequency modulation. b) Turning point magnification.

The acquired signal was filtered using a two pole high-pass Butterworth filter with a cutoff frequency of 10 Hz. This filter removes the strong constant frequency component (DC value) and the amplitude modulation for a better visualization of the frequency modulation. The Doppler spectrogram, represented in Figure 6.22, shows the changes in frequency along the time that correspond to the modulus of the derivative of the mirror movement.

Analyzing the Doppler spectrogram from the test bench A signals, the frequency changes along time are evident. The obtained profile is related with the MM velocity absolute value. The highest frequency (4000 Hz) occurs when the target moves with

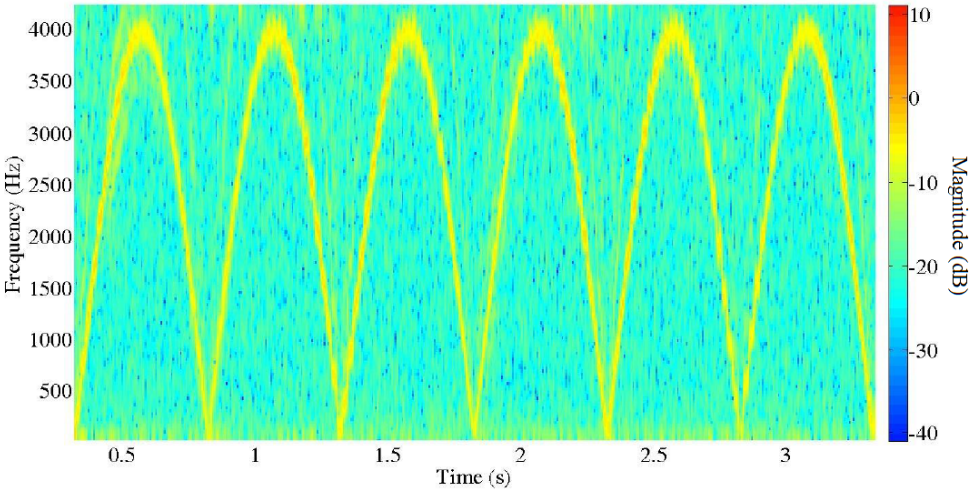

FIGURE 6.22: Detail of the Doppler spectrogram from the planar photodetector.

the maximum velocity and the zero frequency is the most predominant when the target stops.

6.4.1.2 Test Bench B

Test Bench B: Characterization

Test bench B arises from the need to find an arrangement of optical elements without any leftover areas such as those generated by the fixed mirror on the movable mirror. Thus, the ideal would be to have an element that is responsible to reflect the part of beam light and to transmit part of beam to mobile mirror. This new assembly is based on Wedged Plate Beamsplitter (WSB) from Thorlabs® (BSF2550) which ensures the separation of a single input beam into multiple copies through successive reflections and refractions. The wedge is formed using a 5 ° apex angle, which is designed to provide good separation between the multiple outputs, and offers a transmission over a large broad wavelength range (from 185 nm to 2.1 μm). The refraction index depends on the wavelength, and for the LD used in the optical probe (635 nm) is 1.46. The rectangular shape allows a precise positioning of the WSB for a full control of the output beams direction. The WSB is parallel to a mirror surface, which allows numerous copy beams to be created.

The test bench composed by the optical WSB is represented in Figure 6.23. The LD emits the coherent light, and some light waves are reflected by the planar surface of the WSB, and other light beams are transmitted through the WSB and reach the movable mirror. The mirror reflects this light with a Doppler frequency shift due to its sinusoid movement. The photodetector receives the light reflected by the WSB, with the original frequency, and reflected by MM, with the Doppler frequency shift. In the PD, the MM reflected beams are coupled with the original beams and produce interference patterns describing the self-mixing effect. In Figure 6.23, the red lines represent the main pathways that beams may take, when they interact with the successive surfaces of the test bench, specifically in the beamsplitter and contribute to the mixing effect in the PD. The photons which are reflected by the WSB, maintain the original frequency, on the other hand, the photons reflected by the movable mirror show a Doppler frequency shift. These pair of photons that go through each of the tracks are responsible for the generation of the self-mixing effect signal.

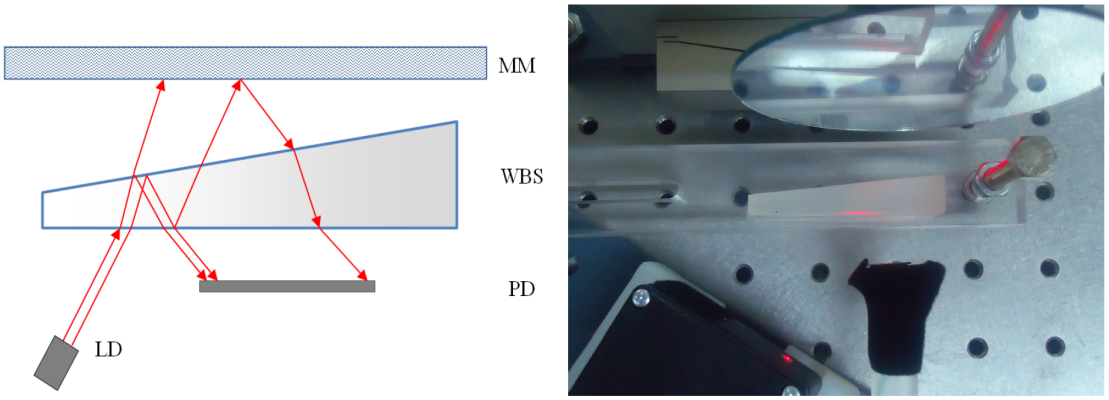

(a) Drawing of 3D model of the experiment.

(b) Photo of the experimental setup.

FIGURE 6.23: Test bench B. a) Schematic drawing. b) Photo of the experimental setup with MM, WSB, PD and LD.

Test Bench B: Signals

The signals represented in Figure 6.24 were acquired in test bench B by the planar photodiode of the probe. These data show the amplitude modulation of the signal in a set of cycles (Figure 6.24(a)) and in detail (Figure 6.24(b)) the interference patterns characteristics of the self-mixing effect are visible.

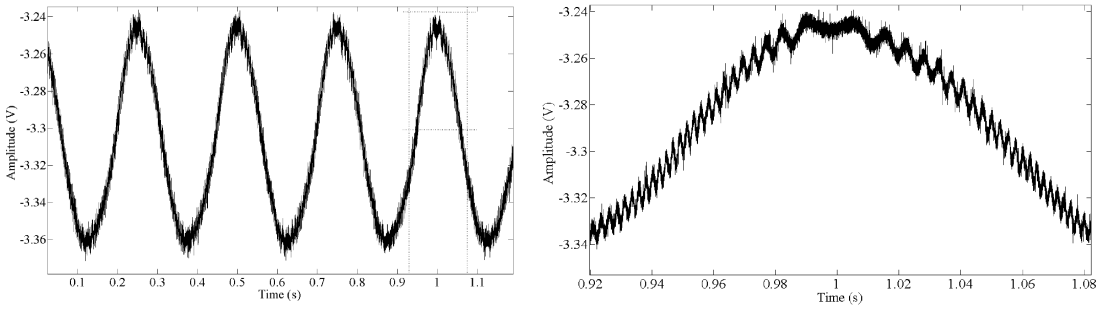

(a) Set of cyclic laser Doppler signals.

(b) Detail of the pulse detected.

FIGURE 6.24: Planar photodiode signal from test bench B. a) Row of pulses with amplitude and frequency modulation. b) Turning point magnification.

The Doppler spectrogram is represented in Figure 6.25. Frequency decomposition was reconstructed along time from the original self-mixing signal, obtained by the planar photodetector. The reconstructed signal represents the most predominant frequency of the original self-mixing signal over time which corresponds to the Doppler frequency shift.

The self-mixing signals obtained in the test bench B have a poor SNR compared with the signals of the test bench A. The large frequency band presented in the signal along time makes it difficult to identify in a unique way which is the correct Doppler frequency shift. It happens due to the high number of reflection and refraction in the WSB, which cause some of the input power to be lost. Hence, the WSB acts as an attenuator.

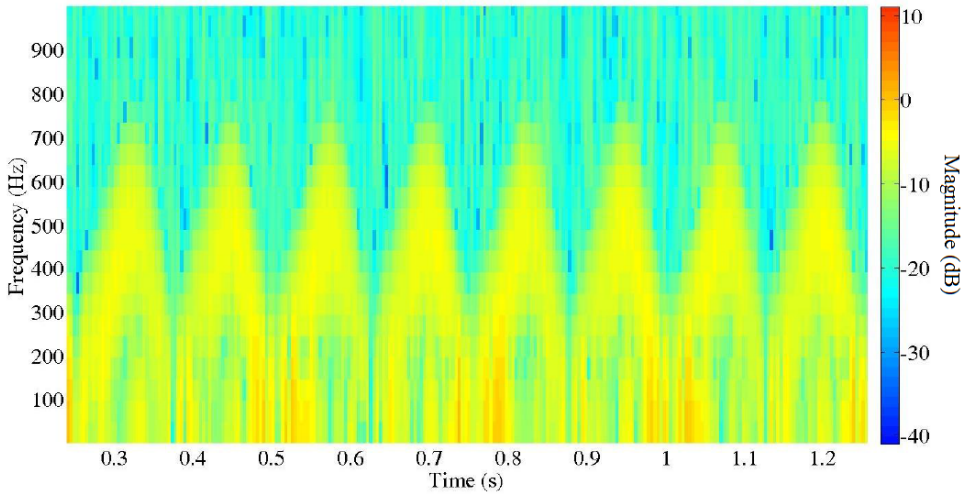

FIGURE 6.25: Detail of the Doppler spectrogram from the planar photodetector.

6.5 Conclusions

For the optical probe, two crosstalk tests were performed (electrical and optical) and significant interference were not found between the LDs that composed the probe.

For the probe's validation, a test setup system was designed, developed and characterized. This test is capable of controlled generation of cardiac pressure waveforms, and well suited to validate feature-extracting algorithms for hemodynamic studies. The developed optical probe has demonstrated good performance in the test setup system.

In addition, the developed algorithm uses well established methods for signal processing of self-mixing Doppler signals, such as the STFT and EMD, to remove noise and apply semi-automatic peak detection. The decomposition levels of the EMD permit the extraction of different pieces of information. The first level allows an easy detection of the feature points in contrast to the fourth/fifth levels that clearly show the basic oscillation frequency. The developed instrumentation and the reconstruction algorithm allow the identification of the pulse waveform feature points with an accuracy of a few milliseconds and high performance in the identification of the reflected wave.

The use of several data sets, by changing the alignment between the probe and the silicone membrane, are evidence of the robustness of the system. As the developed probe uses an optical signal, it is relevant to note that tests were performed to assess if the room illumination conditions influence the self-mixing signal. No changes in the signal were observed between the dark and illuminated rooms.

In the *in vivo* carotid measurements, the operator hand vibration needs to be minimized because the laser is a point-like sensor and the pulse pressure waveform needs to be recorded precisely above the carotid site.

The low-cost optical system, able to acquire a self-mixing signal from a vibration target, was used to develop an algorithm for estimation of the movement features. The STFT and PSD algorithm used for determination of the features of the movement, allows the estimation of the movement equations of target and the evaluation of velocity and amplitude with an average error less than 10%.

The optical probe was also used to evaluate the vibration modes of a piezoelectric disc membrane. The results obtained by the Doppler signals enabled the construction of the

vibration curve of the PZ. Its behaviour was confirmed by the impedance spectroscopy analysis. The scan of all regions of the PZ disc allowed the identification of its main vibration mode (0,1) and explained the deflection directions in the disc.

Finally, it has been demonstrated that a laser vibrometer based on the self-mixing effect, with a simple optical apparatus, can accurately perform measurements of velocity and displacements in sub-micron vibrations amplitudes.

Due to the potential interest to use a photodetector with a larger area that can improve the quality of the signal, with a better signal-to-noise ratio and which may have biomedical applications, an optical system capable of generating a self-mixing signal outside the optical laser cavity was created.

The two test benches designed to obtain the self-mixing effect demonstrated that is possible to reach the mixing effect outside the laser cavity, using a planar photodiode that detects the interference between the original beam and a beam with Doppler shifted frequency.

Tests developed in the test benches opened the possibility to construct a probe that uses a planar photodiode with a large area for the collection of medical signals and improve the quality of the acquisition and expected a better SNR.

Chapter 7

Towards Clinical Analysis

The current chapter presents several studies for a preliminary evaluation of an optical system devoted to the clinical environment. These studies attempt to validate the proposed optical system as a reliable tool and method to non-invasively assess local PWV and PWA parameters in the carotid artery. These tests were performed using the PPD and APD probes.

This chapter consists of several tests for the experimental validation and a clinical feasibility for a non-invasive and multi-parametric optical system for evaluation of the cardiovascular condition. Two prototypes, based on two different types of photodetectors (planar and avalanche photodiode) were tested in a several groups of volunteers, and several main hemodynamic parameters were measured. These parameters including such as pulse wave velocity and indexes of pulse waveform analysis: the Augmentation Index, Subendocardial Viability Ratio and Ejection Time Index.

The first tests in this chapter evaluate the probe performance for clinical data. The fisrt one estimates the repeatability of the parameters determined by the developed system in a small group of volunteers during 4 weeks and infer about its clinical feasibility. Other test compares the local PWV measured by the optical probe with the regional PWV obtained with Tonometry probe. The reproducibility tests of pulse pressure profile was performed for both inter-operator (systematic differences among the observers) and intra-operator (deviations of a particular observer's score on a particular patient) variability.

The following tests were performed in a clinical environment and represent an important step for the clinical validation of optical system. These tests allowed the assessment the values for local PWV, to establish its reference values for the carotid artery in a young and healthy population and find correlations between hemodynamic parameters and population characteristics.

A comparative test between the acquired signals from optical probe and an intra arterial catheter in the ascending aorta, allowed to study the relationship and the correspondence between the distention profile and the pulse pressure waveform.

In the end of this chapter one case study is presented that evidence the modifications of arterial pulse pressure in consequence of changes in arterial system, and the possibility of detection with the optical system.

All studies presented in this chapter have a study protocol approved by the Ethical Committee of the Centro Hospitalar e Universitário de Coimbra, EPE Portugal. All the

subjects were volunteers and gave a written informed consent.

All the data were analyzed as mean ± Standard Deviation (SD) with Predictive Analytics Software Statistics 18 (SPSS, Inc, Chicago, IL).

7.1 Probe Performance for Clinical Data

7.1.1 Optical Probe Performance

A preliminary test was made to evaluate the optical system capability in determining the hemodynamic parameters. The main objective of the this study was to estimate the repeatability of the parameters determined by the developed system as a preliminary evaluation test with a small group of volunteers and infer about its clinical feasibility. Signals were acquired with non-commercial prototype optical probes during 4 weeks in 10 volunteers and the results for the different parameters were evaluated.

In vivo tests were performed in a set of healthy individuals. The main purpose of these tests was to assess the capability of the system in determining the pressure waveform features and pulse wave velocity.

Each exam procedure consisted in the acquisition of a set of cardiac cycles at the carotid artery during a few minutes, with the patient in the supine position.

The acquisitions for each volunteer is weekly based, with the two developed probes (PPD and APD, described in the section 3.2.1), during four consecutive weeks. The procedure was continued for each of the acquisitions, and the different hemodynamic parameters were determined.

For the set of cyclic waveforms detected, segmented and normalized for PWV, three different algorithms for extraction of the time delay from the two detector's signals were applied. They are referred to as Maximum, Threshold and Cross-Correlation algorithms.

The algorithm of phase spectra, described in section 4.1.2.5, was abandoned in the first *in vivo* acquisitions, due to large measurement errors in PTT determination, probably because the algorithm is used for sinusoidal signals and not for this type of structure as the pulse pressure waveform [130].

For each acquisition, the three algorithms mentioned above were used for the PWV determination. Further tests were made to compare the results and study the variability between different measures and subjects.

7.1.1.1 Study Population

The characteristics of the volunteers are presented in table 7.1. The group consisted of 10 subjects (5 male and 5 female), normotensive and with no documented history of cardiovascular disorders or diabetes, with average (± SD) age of 24.4 ± 2.5 years old.

7.1.1.2 Results

A reliable estimation of PWV, AIx, ETI, HR and dP/dt_{max}, and area under the curve were obtained in all the subjects with the two probes of the optical system. The values of systolic and diastolic pressure were obtained from brachial pressure measurement with sphygmomanometer (blood pressure cuff) using a commercial system.

Reproducibility of PWV

The results from the three algorithms for local PWV determination were compared to select the one that exhibits the best results. The average PWV, obtained by the

TABLE 7.1: Main characteristics of the volunteers.

Characteristics	Values
n, Males/Females	10 (5/5)
Age (years)	24.4 ± 2.5
Height (cm)	168.1 ± 10
Weight (kg)	63 ± 11.2
BMI (kg/m^2)	22.2 ± 2.6
Brachial SBP* (mmHg)	104.6 ± 11.1
Brachial DBP* (mmHg)	68.0 ± 8.6
Heart Rate* (bpm)	64.6 ± 8.4

Values are numbers or mean ± SD.
BMI body mass index.
SBP systolic blood pressure.
DBP diastolic blood pressure.
** Measure in brachial with a sphygmomanometer.*

Maximum algorithm, is 4.37 ms^{-1} with SD of 1.79 ms^{-1}, for the Cross-Correlation method the result is 4.58 ± 1.29 ms^{-1} and for Threshold method 4.78 ± 1.89 ms^{-1}. All algorithms exhibit a good performance, and the correlations between all of them were evaluated. The best correlation was found for the Cross-Correlation and Threshold methods, as shown in Figure 7.1(a).

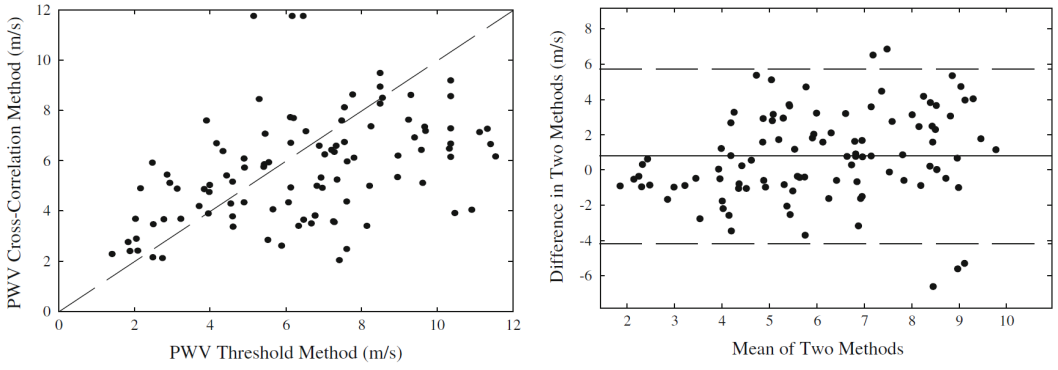

(a) Correlation between the two methods for PWV. (b) Bland–Altman plot between two methods.

FIGURE 7.1: Comparison between Threshold and Cross-Correlation methods. a) Correlation between the two methods for PWV; b) Bland–Altman plot displaying the difference between two methods.

The average difference between the two methods, Threshold and Cross-Correlation, was 0.78 ms^{-1} with a SD of 2.52 ms^{-1} as shown in a Bland–Altman plot in Figure 7.1(b). The Cross-Correlation method analyzes the pulse pressure waveform as a whole, incorporating all moments of the arterial pulse, while the Threshold is based on a pulse by pulse single point identification (at the diastole) followed by for time delay assessment. For this reason the Threshold method should be more sensitive to noise and artifacts on the baseline [196]. Due to lower SD for the values obtained with the Cross-Correlation, this method was preferred for the PWV determination. The values of pulse wave velocity determined by the optical system are slightly lower than those reported in the literature [53], [197]. However, the values mentioned above are for a regional PWV while the values determined here are for local PWV and there is no consistent reference for this type of measurement.

Reproducibility of AIx

The distribution of AIx values was also assessed for each subject (Figure 7.2). The results show that the AIx values are consistently negative, except for one of the subjects. This is consistent with the waveform observed for each subject, since the subject 8 always shows an early reflected peak that corresponds to a positive Augmentation Index and could indicate a case of arterial stiffness.

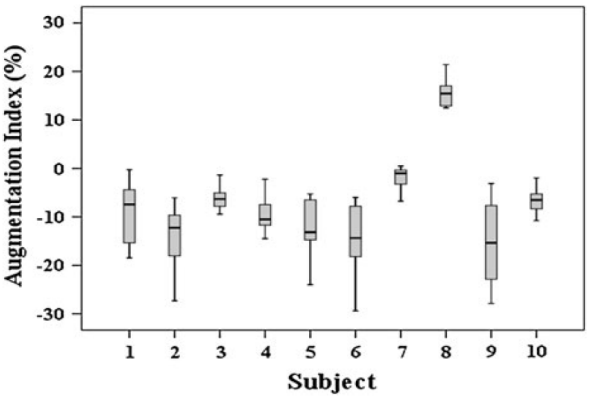

FIGURE 7.2: Box plot of data from the AIx determined for the all the subjects.

The correlation between AIx and heart rate was evaluated. The results of Pearson-Correlation test were compatible with a significant negative correlation, between HR and AIx at a 0.01 level (2-tailed), as it was found in other studies [36], [37]. Even though the strength of the relationship found between these two variables is medium, since the Pearson Correlation is -0.315.

It should be noticed that the obtained values by the proposed system are predominantly negative, and therefore lower than those found in previous studies [37]. However, it is significant that in these studies, the mean age of the sample population (63 years) is much higher comparing to this sample, which have an mean age of 24.4 years (range 20–29 years), which may explain this trend to lower values. Once again, the subject who had higher values of AIx (subject 8) is the oldest in this sample.

Reproducibility of other PWA Parameters

The other parameters described before, such as HR, area under the curve, dP/dt_{max}, SEVR and ETI were determined by the optical system with a PWA algorithm; all data was analyzed as mean $\pm$ SD and is shown in table 7.2. The SD presented in table for the PWA parameters represents the standard deviation for each volunteer during the different measures of the four consecutive weeks. The results obtained for the subjects submitted to this study are consistent over time for all parameters. For the area under the normalized curve, the values obtained are closer than described in literature, 0.54–0.58 [42], in spite of the differences in volunteers of the study. This fact suggests that there is no variation over gender for the area under the pressure curve.

For the dP/dt_{max} and SEVR parameters the values obtained were within the range expected for a sample of healthy individuals. For the SEVR parameter were expected values for healthy individuals greater than 100%, in which the perfusion of the heart is made during a time period longer than the period of contraction, which is energy consumption. In some volunteers, the perfusion period is twice the time of contraction (systole) and the SEVR is about 200%. There is a consistency between the trials for ETI and that there are no large variations in its value to the same subjects. The expected

TABLE 7.2: Hemodynamic parameters obtained for each subject.

Subject	HR (bpm)	Area	dP/dt_{max} (mmHg/s)	SEVR (%)	ETI (%)
1	63.2 ± 19.3	0.5 ± 0.10	566.0 ± 187.6	201.1 ± 41.4	30.93 ± 1.75
2	84.5 ± 8.2	0.3 ± 0.04	731.6 ± 83.2	117.5 ± 15.6	44.59 ± 3.70
3	67.5 ± 5.0	0.5 ± 0.04	509.3 ± 93.6	167.7 ± 21.4	35.90 ± 3.05
4	66.9 ± 3.1	0.5 ± 0.10	682.7 ± 105.0	143.3 ± 26.9	32.87 ± 9.70
5	56.8 ± 6.0	0.5 ± 0.10	541.2 ± 83.1	221.2 ± 30.3	28.97 ± 3.23
6	76.3 ± 12.0	0.4 ± 0.10	570.0 ± 113.7	171.2 ± 29.6	35.16 ± 5.33
7	73.5 ± 6.4	0.5 ± 0.10	466.3 ± 110.0	173.7 ± 30.9	35.83 ± 4.34
8	64.2 ± 3.4	0.5 ± 0.05	504.1 ± 93.1	197.3 ± 18.8	32.98 ± 1.62
9	64.6 ± 3.8	0.5 ± 0.10	746.6 ± 150.0	176.3 ± 29.5	33.86 ± 0.65
10	76.8 ± 8.0	0.4 ± 0.10	790.8 ± 269.0	189.8 ± 7.40	29.49 ± 3.69
Total	69.7 ± 10.8	0.5 ± 0.10	620.0 ± 166	171.7 ± 36.2	34.06 ± 3.71

values are included between 30 and 42% in other studies [34], [35]. The results obtained by the optical system are within the expected range.

Comparison Results between Two Probes

The developed multi-parametric system is composed of two types of probes, PPD and APD, used in this study for all subjects. The parameters previously obtained were determined from acquired data with the two probes. To allow certain values in their differentiation the comparison was made in the PWV values determined for the three algorithms under study.

The results showed a carotid PWV mean value (± SD) of $4.72 \pm 1.22\ ms^{-1}$ for planar probe while avalanche probe showed a mean PWV value of $4.32 \pm 1.38\ ms^{-1}$, represented in Figure 7.3(a). In Figure 7.3(b) it is visible that there are no major variations between the PWV values obtained by the two probes for each subject.

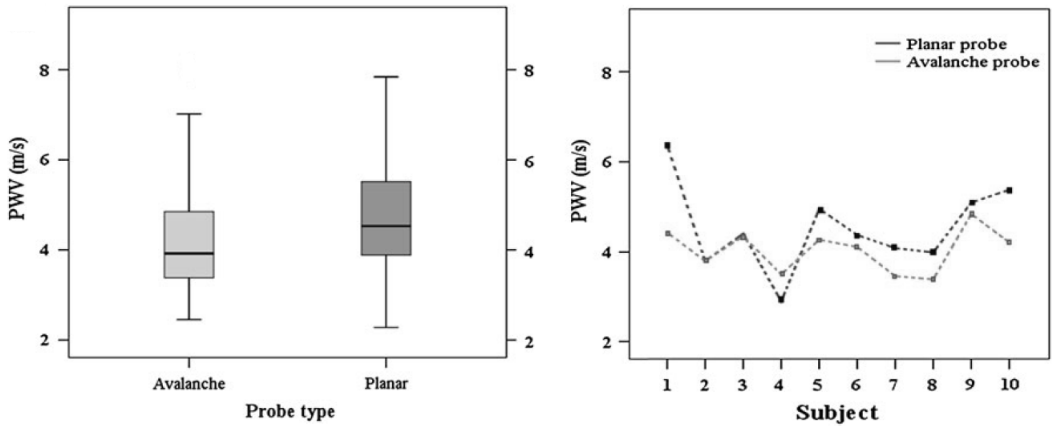

(a) Box plot for comparison of PWV.

(b) Mean of PWV values for each subject.

FIGURE 7.3: PWV determined by two probes. a) Box plot for comparison of PWV determined by Cross-Correlation for the two optical probes, Avalanche and Planar; b) mean of PWV values for each subject.

The results obtained for PWV suggest an underestimation of values in the case of the APD probe. The avalanche photodiodes are almost punctual and the signal-to-noise ratio is worse, therefore increasing the difficulty in the determination of the delay between the two acquired signals.

The good results obtained with the PPD combining with the much lower cost of the PPD detector than the APD and the fact that in the acquisition of signals *in vivo* with APD probe was more difficult than with the PPD probe, the solution based in the planar photodiodes becomes the best option.

7.1.2 Comparison with Tonometry Probe

In this test was made a comparison between the optical system and the gold-standard in the regional PWV assessment, a Complior Analyse® device, to explore the correlations and differences in the results obtained using the two techniques of measuring the pulse wave velocity. In spite of this comparison, it is worth to point out that the nature of the PWV determination is different in the optical system, that is based on local assessment (carotid artery measure) and the Complior® system, which is based on a regional assessment (carotid-femoral measures).

Based on what has been discussed previously, the probe composed of the planar photodiode along with the Cross-Correlation method represents the best combination for PWV determination. In order to validate the data obtained by the developed optical system, a number of volunteers had been previously submitted to a signal acquisition procedure, using simultaneously the proposed optical device and a gold-standard in the PWV assessment, a Complior Analyse® device. This study was undertaken in 14 healthy subjects (9 females/5 males, average age 23.2 ± 5.5 years).

Using a non-parametric correlation analysis between the values obtained from the two systems, the Pearson correlation value is 0.819, which is a strong correlation and significant at the 0.01 level (2-tailed).

The agreement between the PWV values obtained by the Complior® and the optical probe is shown in Figure 7.4(a). The values of PWV obtained by the two systems are correlated ($r^2 = 0.67$) being the average difference between the two systems, Complior® and optical probe, was -1.8557 ms^{-1} with a SD of 0.5744 ms^{-1} as shown in a Bland–Altman plot in Figure 7.4(b). As shown in Figure 7.4(a), there is a shift towards a have systematic lower values from the optical probe device in comparison to those of Complior®. This may be due to the fact that the parameters correspond to slightly different PWV determination processes (local *vs* regional) and lower values are expected for PWV in the carotid than the PWV in a carotid-femoral measure. This issue could explain the obtained associated error [53], [60], [61].

Altogether, these results allow the use of the proposed optical system as a reliable method to determine local carotid PWV.

The PWV obtained by the developed optical system was validated by comparing results with Complior® that showed a great consistency between the PWV obtained with the two devices, even though their direct comparison should be carefully taken due to the fact that they refer to different PWV parameters (Complior® is regional PWV, while the designed probes measure local PWV at the carotid).

It should be noted that the parameters assessment in this study is local, *i.e.*, only at the carotid artery and, unlike some commercial system (*e.g.*, Complior®), does not require measurements at two distant points to determine PWV. This represents an important advance because it allows the analysis of this type of parameter without the coarse approximations of the distance between test points in arteries. In the local PWV

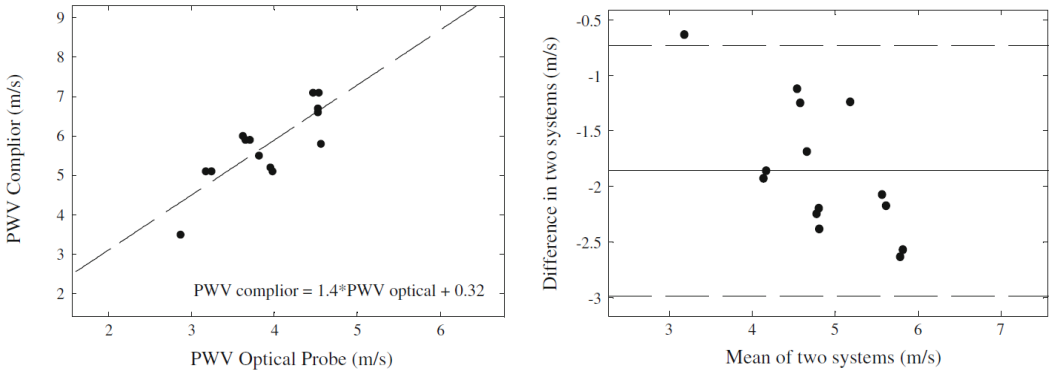

(a) Correlation between the two systems for PWV.

(b) Bland–Altman plot displaying.

FIGURE 7.4: Comparison between the Complior® and Optical probe. a) Correlation between the two systems for PWV determination; b) Bland–Altman plot displaying the difference between the two systems (Complior and Optical probe) as a function of the average of the determined PWV.

approach the detectors equally are spaced by a fixed distance and the outcome gives a glimpse over the physiological status of a particular arterial segment.

7.1.3 Reproducibility Tests by Operator

In this study was investigated the reproducibility of pulse pressure profile, and both inter-operator (systematic differences among the observers) and intra-operator (deviations of a particular observer's score on a particular patient) variability analysis were performed. Thus the aim of the present study is to assess intra- and inter-operator reproducibility.

Reproducibility was evaluated in 13 healthy subjects by two senior operators, and evaluates the degree of closeness of the repeated measurements made on the same subject either by the same instrument [198].

This is a preliminary study to investigate the reproducibility of the optical system by comparing the results obtained by the two operators and not a statistical study, thus it was used a limited cohort of 13 volunteers. This is a prospective study and similar studies of this kind presents a sample of the same magnitude [199], [200], [201].

The reproducilbity study covering inter-operator and intra-operator variability analysis. Inter-operator variability refers to systematic differences among the observers. Intra-operator variability refers to deviations of a particular observer's score on a particular patient that are not part of a systematic difference.

This work contributes to the design a protocol for this type of non-invasive probes used in determination of hemodynamic parameters, which contains the required guidelines to assessment test for the operator variability.

7.1.3.1 Methods

Study Population

The group consisted of 13 healthy human volunteers (7 males and 6 females), normotensive and with no documented history of cardiovascular disorders or diabetes, that had undergone signal acquisitions with the optical probe. The characteristics of the volunteers are presented in table 7.3.

Table 7.3: Main characteristics of the volunteers.

Characteristics	Values
n, Males/Females	13 (7/6)
Age (years)	24.1 ± 2.2
Height (cm)	166.6 ± 8.0
Weight (kg)	63.8 ± 12.8
BMI (kg/m^2)	22.8 ± 2.9
Brachial SBP* (mmHg)	113.5 ± 12.5
Brachial DBP* (mmHg)	73.2 ± 9.1
Heart Rate* (bpm)	65.4 ± 11.4

** Measure in brachial with a sphygmomanometer.*

Study Protocol

Two trained blinded operators (further referred as 'A' and 'B') alternatively undertook 2 measurements each, in the same location, using the same probe in the same day, over a short period of time.

The subjects rested for 10 minutes in supine position, reached the physiological baseline conditions, in a standardized temperature environment and then, both operators measured BP before each measurement and acquired signals in alternate order (ABAB or BABA). Each trial consisted of few acquisitions, usually between 2 and 4, and the values of each trial were further averaged.

Similar reproducibility studies have been carried out with same protocol, that accepted as rigorous approach this evaluation of PWA and PWV repeatability [35], [202], [203]. As expected BP, pulse pressure waveform and consequently the hemodynamic indices remained, are stable during the assessment period.

The sequence of operator was random, which reduce bias will have tended to compromise intraoperator variability.

Statistical Analysis

The data are reported as mean values ± standard error with 95% confidence intervals and percentages were used to describe qualitative variables. The Bland-Altman approach for "95% limits of agreement" was used in inter and intra-operator differences in paired measurements.

Reproducibility was assessed by Intraclass Correlation Coefficients (ICC), Coefficients of Variation (CoefV), Standard Error of Measurement (SEM) and Limits of Agreement (LA) [204], [205].

Intraclass correlation coefficient was computed for repeatability studies, based on one-way analysis of variance (ANOVA). ICC describes how strongly measurements in the same group resemble each other. The CoefV expresses the variation between measurements in relation to the mean value of all measurements. The LA provides direct information about the absolute measurement error. The standard error of measurement takes the amount of measurement error into consideration [206].

7.1.3.2 Results

Pulse wave analysis and pulse wave velocity were successfully undertaken in consecutive series from 13 subjects and the results are summarized in the next sections.

TABLE 7.4: PWV mean values obtained by each operator A and B, per trial.

Trials	Operator	Range (min-max) (ms^{-1})	Mean (ms^{-1})	SD (ms^{-1})	Var
1	A	(3.090 - 5.463)	4.263	0.734	0.539
	B	(3.616 - 5.699)	4.629	0.714	0.510
2	A	(2.932 - 5.710)	4.568	0.649	0.422
	B	(3.558 - 5.729)	4.517	0.663	0.440

Ope: operator; Var: variance.

PWV Results

The normality of the variables distribution for each trial/operator were assessed using the test of normality Shapiro-Wilk, all the sets of PWV values follow a normal distribution (Significance value $\geq$ 0.169, p <0.05) [207]. The correlation between the PWV values obtained by both operators is plotted in Figure 7.5(a).

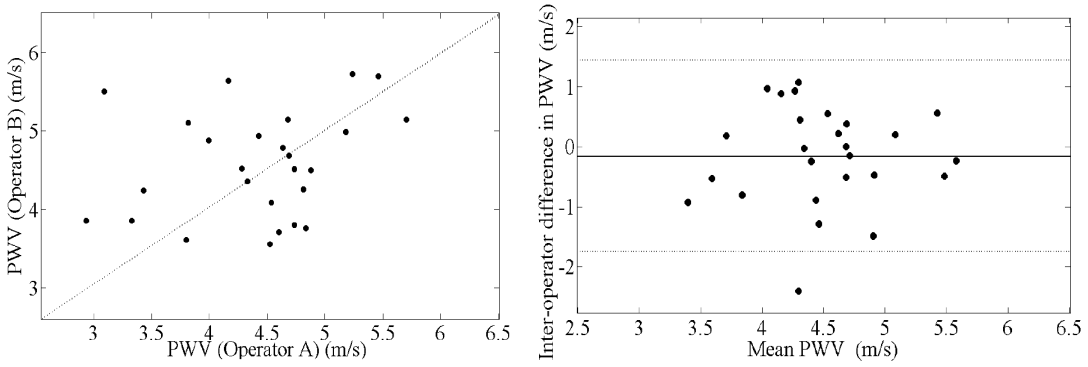

(a) Correlation between the operators for PWV.

(b) Bland-Altman plot.

FIGURE 7.5: Comparison between two operators (A and B). a) Correlation between the operators for PWV measurements. b) Bland-Altman plot displays the interoperator interoperator difference for the two operators (A and B) as a function of the mean of the determined PWV.

The mean difference between the two operators is 0.1570 ms^{-1} with a SD of 0.8160 ms^{-1} as shown in a Bland-Altman plot (Figure 7.5(b)). This difference represents approximately 3% of the arithmetic average of the means obtained by each operator per trial. The between-operator ICC of 0.602 (95% from 0.12 to 0.82) revealed a moderate agreement between classes (measurement made by operator A and operator B).

Considering all measurements there is only one that has a difference greater than 2 ms^{-1}, and just 4 measurements have a difference higher than 1 ms^{-1}.

According to Figure 7.5 the acceptable intraoperator PWV differences (<1 ms^{-1}) are observed in 22 measurements (85%).

Considering variance results, in table 7.4, there is no evident variation depending on the operator. However, considering the values between trials, the trial 2 shows lower variance comparing to trial 1 for each operator. Furthermore, the coefficients of variation obtained for inter-observer and intraobserver reproducibility were less than 15%.

The graph represented in Figure 7.6 shows that values obtained by operator A are very similar to the operator B. Also the mean values for PWV from different trials of each operator have very close values.

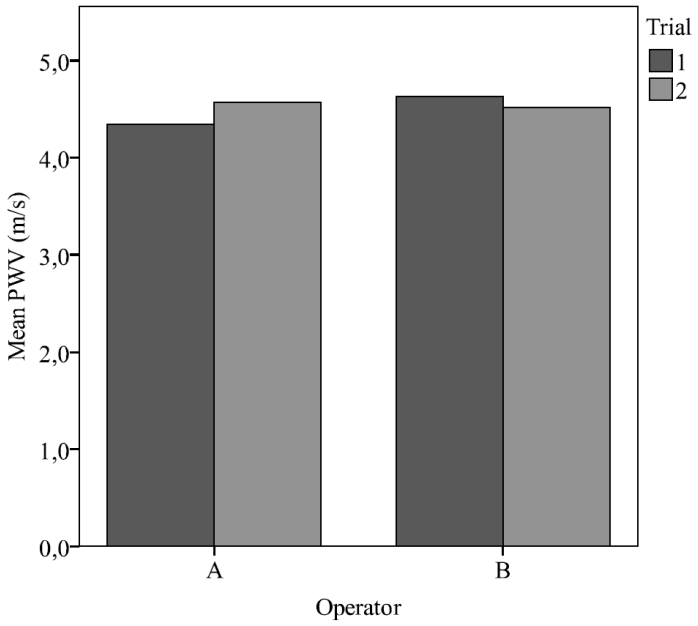

FIGURE 7.6: Bar graphs for mean values of PWV by operator.

In spite of this apparent difference, the ICC for both trials per operator shows that for operator A there is a moderate agreement between trial 1 and 2 (ICC=0.674; 95% CI from 0.01 to 0.82) and for operator B this coefficient has a similar value of agreement (ICC=0.654; 95% CI from -0.17 to 0.89).

To better understand the variability of the PWV values, the values obtained within each operator and between trials are represented in the Figure 7.7.

No significant association between the PWV intra-operators values was found after a correlation analysis. The average difference between the two trials assessed by the operator A was -0.30 ms^{-1} with a SD of 0.73 ms^{-1} as shown in a Bland-Altman plot in Figure 7.7(b). This limit of agreement (from -1.78 to 1.17 ms^{-1}) represents at most 6.9% of the mean PWV for this operator.

The average difference between the two trials assessed by operator B was 0.11 ms^{-1} with a 0.68 SD of ms^{-1} as shown in a Bland-Altman plot in Figure 7.7(d). This limit of agreement (from -1.25 to 1.47 ms^{-1}) represents at most 7.6% of the mean PWV value for operator B.

PWA Results

Relatively to the other PWA parameters the values determined in this dataset by the optical system are shown in Table 7.5.

For the all parameters the values obtained were within the range expected for healthy population, since they are coherent with those reference values. The resulting values for dP/dt_{max} differ substantially from the ones presented as reference. Actually, the mean value for this parameter was relatively low, a wider range than the expected and a smaller mean value is evident, probably originated by the differences in the calibration method used. The values for other parameters are very similar between operators.

The more reliable the measurement response, the less error variability around the mean is verified. The standard deviation of measurement errors is therefore a reflection of the reliability of the test response [206]. The SEM is expressed in the actual units

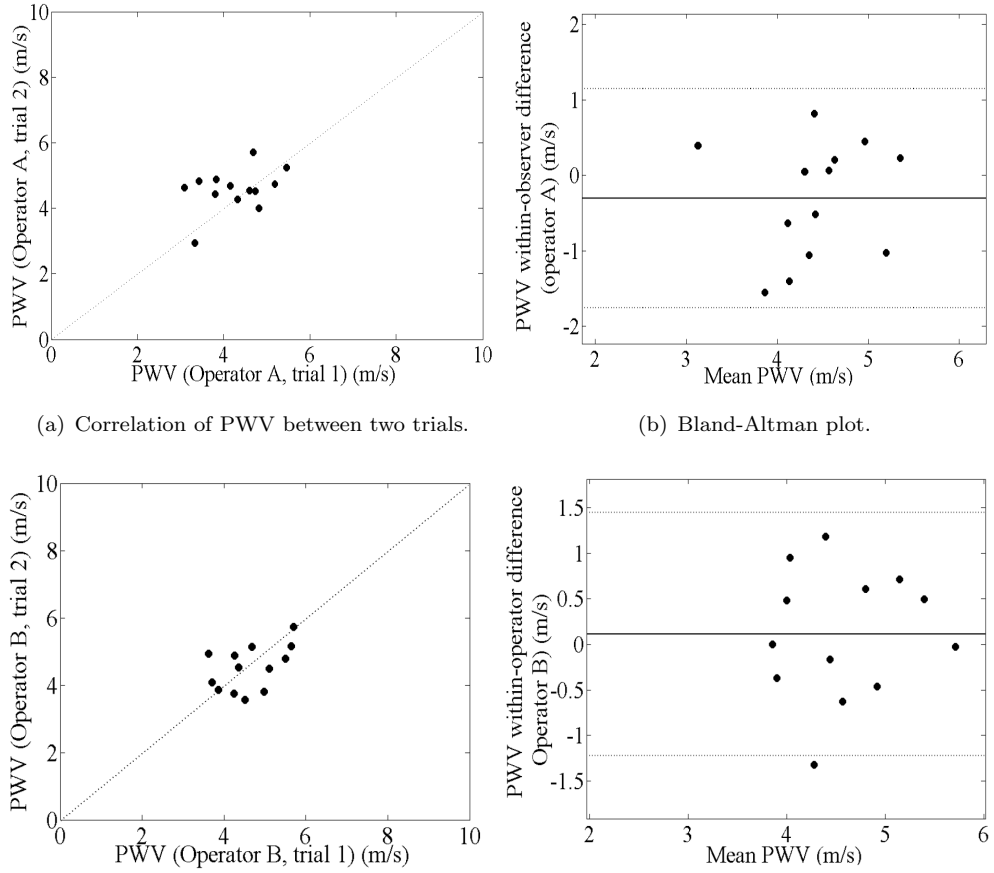

(a) Correlation of PWV between two trials.

(b) Bland-Altman plot.

(c) Correlation of PWV between two trials.

(d) Bland-Altman plot.

FIGURE 7.7: Comparison between two trials for two operators (A and B). a) Correlation of PWV between two trials acquired by Operator A. b) Bland-Altman plot displays the intra-operator difference for the Operator A. c) Correlation of PWV between the two trials acquired by Operator B. d) Bland-Altman plot displays the intra-operator difference for the Operator A.

TABLE 7.5: Mean values of PWA hemodynamic parameters for each operator.

	Operator	Mean	SEM	95% CI	SD
HR (bpm)	A	65.41	1.47	62.48 to 68.35	11.18
	B	64.95	1.79	61.34 to 68.57	11.90
AIx (%)	A	-1.57	1.70	-5.15 to 2.00	13.61
	B	-4.19	1.89	-7.99 to -0.39	12.51
SEVR (%)	A	149.4	9.38	130.98 to 168.53	71.20
	B	152.9	13.04	126.63 to 179.84	86.53
dP/dt_{max} (mmHg/s)	A	328.4	20.75	286.92 to 370.00	158.00
	B	347.7	19.59	308.29 to 387.25	129.94
ETI (%)	A	42.24	1.96	38.31 to 46.16	14.93
	B	42.61	2.27	38.04 to 47.18	15.04

TABLE 7.6: Inter-operator repeatability of PWA: based in the differences correspond to operator A measurement minus operator B measurement.

	ICC^a	95% CI	Mean Diff	SD (2SD)	Limits of $agreement^b$
HR (bpm)	0.976	0.95 to 0.99	-0.279	3.52 (7.03)	-7.31 to 6.75
AIx (%)	0.734	0.41 to 0.88	-1.929	10.01 (20.02)	-21.95 to 18.09
SEVR (%)	0.472	-0.20 to 0.77	7.173	152.26 (304.52)	-151.75 to 166.09
dP/dt_{max} (mmHg/s)	0.581	0.09 to 0.81	-2.660	14.96 (29.91)	-263.61 to 345.44
ETI (%)	0.442	-0.24 to 0.75	0.014	0.09 (0.19)	-32.57 to 27.25

a Intraclass correlation coefficient (ICC) using an absolute agreement definition.
b Limits of agreement for differences= mean difference ± 2SD.
Mean diff means Mean of difference between measures.

of measurement, making it easy to interpret, *i.e.* the smaller the SEM, the greater the reliability and the values obtained for HR, AIx and ETI parameter are low values, only in the case of dP/dt_{max} and SEVR were presents slightly higher values for the SEM.

Inter-Operator Repeatability

The proximity of the mean values Inter-operator is expressed in the ICC results (table 7.6). Some parameters showed good agreement. As one can observe, the HR and dP/dt_{max} had shown high ICC values, concordant with almost perfect agreement. On the other hand for SEVR and ETI parameters, the determined low ICC is congruent with fair agreement.

Concerning AIx, its corresponding ICC values show a moderate level of between-operator agreement.

In Figure 7.8 the results for AIx measurements for all subjects for operator A and operator B are represented. It is visible that there are not major differences between AIx values obtained by the two operators for each subject.

The results in the Figure 7.8 show a common trend between the values obtained for AIx parameter by two operators measurement for each subject. A convention for the signal of AIx, defines when the reflected wave arrival occurs earlier than the systolic peak the AIx have positive value while a negative value of AIx indicates that the reflected wave arrives after the systolic peak.

A positive Augmentation Index could indicate a case of arterial stiffness. With an increase in stiffness there is a faster propagation of the forward pulse wave as well as a more rapid reflected wave, a positive AIx means that the reflected wave arrival occurs earlier than the systolic peak is [208].

Depending on the AIx value (positive or negative) the pulse wave type is defined as follows: when a negative value occurs the pulse shows characteristic of healthy subjects and when a positive value occurs the pulse have characteristic of subjects suffering from arterial stiffness [209].

Intra-Operator Repeatability

Comparing the ICC results from table 7.7 with those presented in table 7.6, which are referent to within-operator differences, one could see that there are no major discrepancies, except for AIx that has a lower ICC and dP/dt_{max} that is slightly higher.

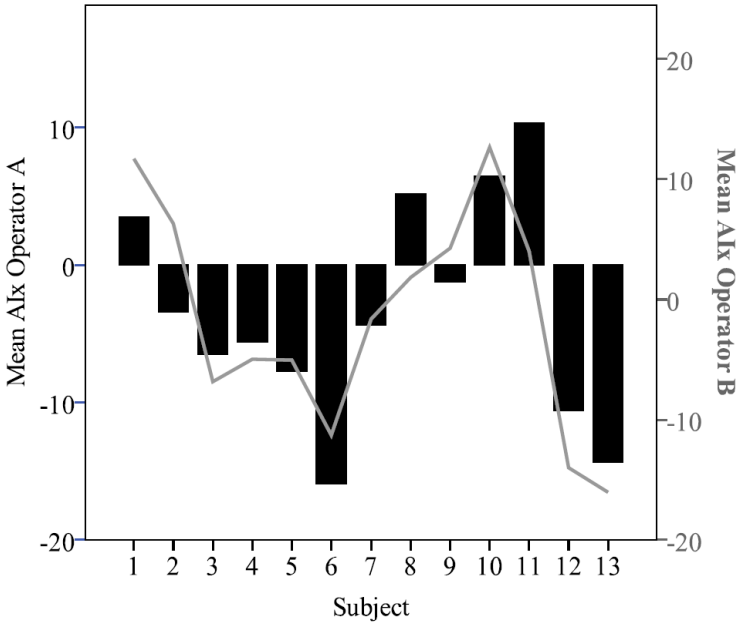

FIGURE 7.8: Trends in AIx measurements: mean of values for each subject by operator A and operator B.

TABLE 7.7: Intra-operator repeatability of PWA, based in the differences corresponds to trial 1 measurement minus trial 2 measurement.

	ICC^a	95% CI	Mean Diff	SD (2SD)	$Limits of agreement^b$
HR (bpm)	0.926	0.83 to 0.97	1.837	5.73 (11.46)	-9.62 to 13.20
AIx (%)	0.448	-0.23 to 0.75	-2.398	13.00 (26.00)	-28.40 to 23.61
SEVR (%)	0.473	-0.20 to 0.77	-4.804	79.53 (159.05)	-163.86 to 154.25
dP/dt_{max} (mmHg/s)	0.678	0.27 to 0.86	6.902	141.85 (283.70)	-276.80 to 290.60
ETI (%)	0.494	-0.16 to 0.78	0.740	14.63 (29.27)	-28.53 to 30.00

7.2 Test with Clinical Populations

7.2.1 Validation in Population

The objective of this study was to assess the values for local PWV, to establish its reference values for the carotid artery in a young and healthy population and validate the technology for hemodynamic parameters assessment from the pulse pressure waveform. The study also aimed to find correlations between hemodynamic parameters with the population characteristics such as age, gender, smoking, body mass index, blood pressure or heart rate: main characteristics described in the literature and have significant impact in the cardiovascular system evaluation.

The complete study database contains 131 subjects constituting a representative cohort of 18–35 year old subjects randomly sampled.

Measurements were performed after a rest period in a temperature-controlled environment. Each exam procedure consisted in the acquisition of a set of cardiac cycles at the carotid artery during 2-3 minutes, with the patient lying in supine position. The assessment of the arterial BP by conventional measurement using an automated digital oscillometric sphygmomanometer (Omron Matsusaka Co., Ltd., Japan) was performed

TABLE 7.8: Main characteristics of the volunteers.

Characteristics	Values
n, Males/Females	131 (69/62)
Age (years)	22.6 ± 5.3
Height (cm)	169.2 ± 10
Weight (kg)	64.5 ± 13.2
BMI (kg/m^2)	22.4 ± 3.2
Brachial SBP* (mmHg)	113.3 ± 14.5
Brachial DBP* (mmHg)	72.7 ± 9.9
Brachial MAP* (mmHg)	86.2 ± 10.4
Estimated Carotid SBP** (mmHg)	99.1 ± 12.2
Heart Rate* (bpm)	69.0 ± 11.7

** Measure in brachial with a sphygmomanometer.*
*** Determined using the calibration method*

prior and after the exam for reference purposes. The diastolic and systolic pressures of arm blood pressure were used to calibrate the system.

7.2.1.1 Study Protocol

The characteristics of the volunteers are presented in table 7.8. The group consisted of 131 subjects (62 men and 69 women), normotensive and with no documented history of cardiovascular disorders or diabetes, with mean (± SD) age of 22.6 ± 5.3 years old.

7.2.1.2 Results

The results for the parameters that were assessed by the optical probe are presented in the next sections. Data are reported as mean values (± SD) or 95% confidence intervals, with $P<0.05$ considered significant unless stated otherwise. The Shapiro-Wilk test of normality was used to assess the normality of the variables distribution. Mean differences between variables were assessed using ANOVA. The strength of the association between two variables was assessed using Pearson Correlation, for normal distributions, unless stated otherwise.

Carotid PWV Results

In a total of 131 subjects the mean value for PWV is 3.33 ± 0.72 ms^{-1} (range of 2.00-5.13 ms^{-1}). The results obtained for PWV approximated a normal distribution. Statistically negligible differences between genders were found. For females the mean of PWV is 3.31 ± 0.64 ms^{-1} and for males is 3.35 ± 0.81 ms^{-1}.

It is well documented in other studies that PWV tends to increase with age [53]. Since the population under study is young we categorized it in three groups: under 20 years (22 subjects), 21-29 years (93 subjects) and over 30 years old (16 subjects).

The correlation between PWV and age is weak (0.244) but significant with a 2-tailed significance value of 0.008 ($p<0.01$). The comparison of PWV mean values among the different age categories using ANOVA shown this statistically significant difference, with a significance value=0.024 ($p<0.05$). The PWV mean value (± SD) for each age category is 2.96 ± 0.52 ms^{-1} for the less than 20 years old group, 3.38 ± 0.7 ms^{-1} for the 20-29 years group and 3.58 ± 0.7 ms^{-1} for subjects above 30 years old (Figure 7.9).

It was hypothesized whether there is a statistically significant difference for PWV, between smoker and non-smoker subjects. The data analysis shows that smoking influences significantly the PWV.

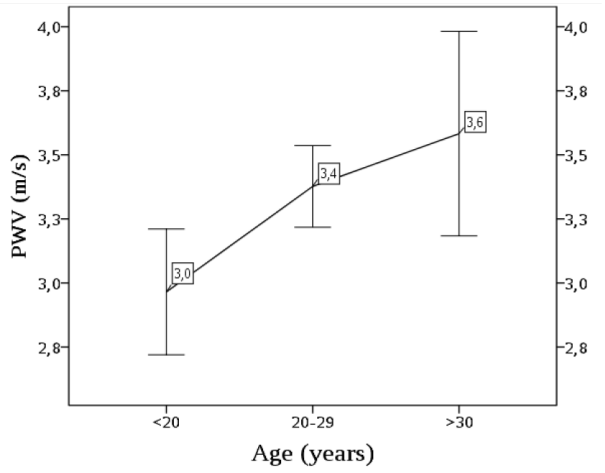

FIGURE 7.9: PWV by age category. The continuous line connects mean values; error bars indicate the 95% confidence interval of the sample mean.

These results show a small but significant correlation between PWV and smoking with a 2-tailed significance value of 0.016 ($p<0.05$). Non-smoker subjects presented a PWV mean value ($\pm$ SD) of 3.29 $\pm$ 0.72 ms^{-1} while smoker subjects showed a mean PWV value of 3.81 $\pm$ 0.6 ms^{-1}, represented in Figure 7.10.

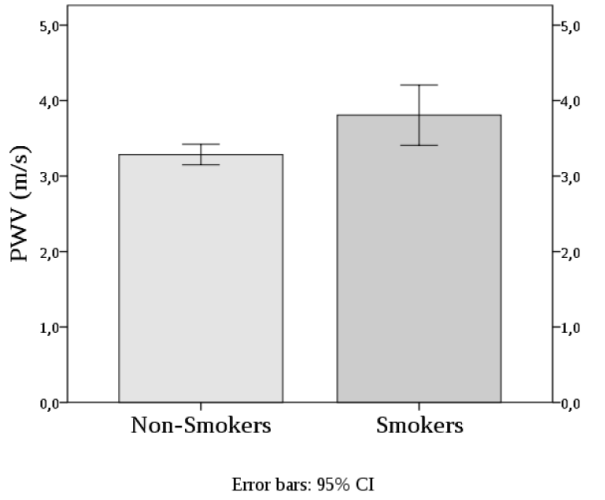

FIGURE 7.10: Bar plot of PWV by smoking status. The error bars indicate the 95% confidence interval of the sample mean.

The comparison of PWV mean values among these two groups using ANOVA confirms the statistically significant difference between the obtained PWV for smokers and non-smokers, with a significance value = 0.021 ($p<0.05$).

The data suggests that, in spite of having a young population, smoking would significantly influence the arterial stiffness, thus leading to increased PWV. Similar findings have been reported by N. Jatoi et al. [210].

Contrary to expectations, no significant correlation between blood pressure and PWV was found. This contrasts with other studies where this correlation is verified [211], [53].

AIx Results

For the total of the subjects in study, the mean value for AIx is -6.1 ± 11.5% (range -44.3% to 24.3 %).

Small differences between genders were verified, as the female mean of AIx is -5.6 ± 1.4% and the male is -6.9 ± 1.6%. However, this difference did not reach the statistical significance threshold ($P > 0.05$).

Also for this parameter, as well as for PWV, statistically differences between smoker and non-smoker subjects were found. AIx is higher for smokers (-4.3 ± 4.4%) than for non-smokers (-6.4 ± 1.0%), this shows that for smokers the reflected wave arrives earlier in time, which is consistent with a slight higher arterial stiffness.

The negative correlation between the AIx and the heart rate was described in other tests [37], [162] and was confirmed in this study (Figure 7.11). The results of Person-Correlation test were compatible with a significant negative correlation, between heart rate and AIx at a 0.05 level (2-tailed). Nevertheless, the strength of the relationship found between these two variables is medium, since the Pearson Correlation is significant with a 2-tailed significance value of -0.226 ($p < 0.05$). The comparison of AIx mean values among these three groups using ANOVA confirms a statistically significant difference, with a significance value = 0.024 ($p < 0.05$).

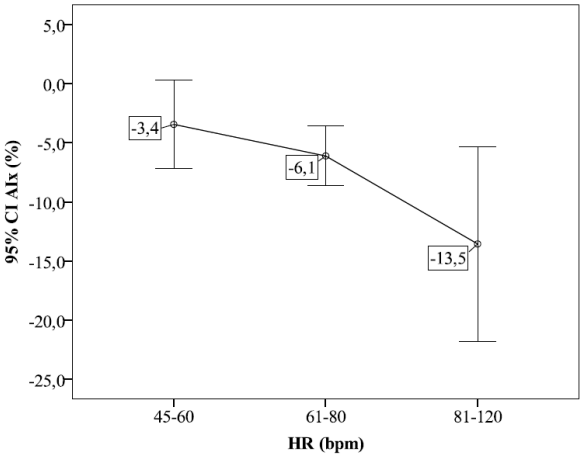

FIGURE 7.11: The continuous line connects plots of AIx mean by heart rate category, with error bars representing the 95% confidence interval of the sample mean.

The negative correlation between these two parameters is explained due to the early return of the reflected wave in systole when HR is lower, and the long period of heart contraction.

Other Hemodynamic Parameters Results

The ETI, SEVR and dP/dt_{max} are other hemodynamic parameters assessed by the optical system, and the results for the population in study are shown in table 7.9.

It is remarkable that the mean values of SEVR and ETI stay within the range presented by other studies (table 2.1) even though it is clear that they show a wide variation. For the SEVR parameter it was also verified a decrease with the heart rate (Figure 7.12) with a significant variance (ANOVA, P=0.01) and a significant Pearson correlation at 0.01 level (2-tailed).

The derived values for dP/dt_{max} differ substantially from the ones presented by other studies [33]. A wider range than the expected and a smaller mean value is evident

TABLE 7.9: Hemodynamic parameters obtained with the optical system.

	Min.	Max.	Mean	SD
SEVR (%)	86.41	412.25	176.86	53.44
dP/dt_{max} (mmHg/s)	212.59	953.33	443.92	151.68
ETI (%)	14.33	47.17	33.96	6.37

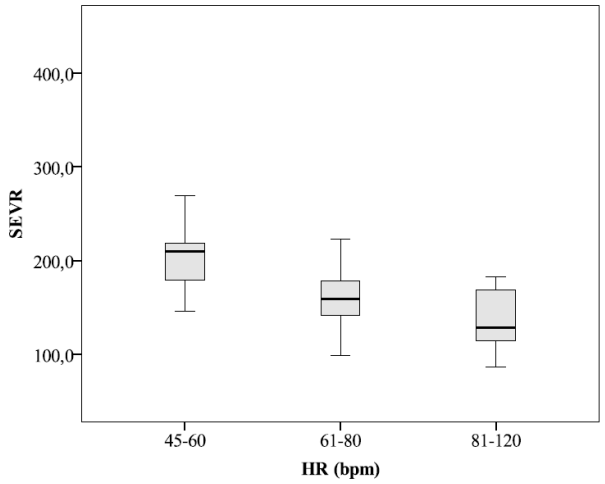

FIGURE 7.12: Box plot of data from the determined SEVR versus heart rate categories.

probably originated by the differences in the calibration method used. However, a relation between dP/dt_{max} and gender, was found, since the Pearson Correlation is -0.408. The female subjects showed lower values for this parameter, which are represented in Figure 7.13.

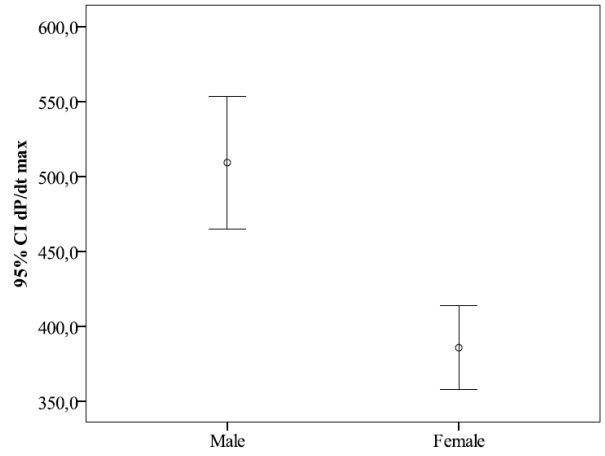

FIGURE 7.13: Error plots of dP/dt_{max} mean values according to gender. The error bars represent the 95% confidence interval of the sample mean.

The dP/dt_{max} values decrease significantly with subjects' age, this allows the inferring that with the increasing age the velocity of the myocardial contraction is lower, meaning that there is a decrease in the myocardial performance.

For the ETI parameter there were verified slight differences between gender, the mean vales for the females is $36.80 \pm 0.72\%$ and for males $33.60 \pm 0.85\%$. This suggests

Table 7.10: Brachial blood pressures and calibrated carotid systolic pressure.

	Range (Min. to Max.)	Mean	SEM	SD	Variance
bSBP (mmHg)	69 (80 to 149)	113.31	1.26	14.46	209.06
bDBP (mmHg)	56 (48 to 104)	72.71	0.86	9.88	97.67
bMAP (mmHg)	54.33 (58.67 to 113)	86.24	0.91	10.38	107.73
cSBP (mmHg)	66.91 (68.34 to 135.26)	99.12	1.07	12.21	148.98

that there is a shorter systole during cardiac cycle in males than in females. Also for this parameter, a significance correlation with heart rate was found since the Pearson Correlation is -0.408.

Brachial-to-Carotid Pressure Calibration Results

In table 7.10 are shown the assessed brachial blood pressures as well as the obtained carotid systolic blood pressure, resultant of the implemented calibration algorithm (presented in section 4.1.1.2). The values are reported to the large sample (n= 131 participants).

The calibrated cSBP determined using the developed algorithm revealed average values 12.52% lower than brachial systolic pressure. This result is not so different of that presented by McEniery *et.al.* (2008) in which the difference between aortic and brachial blood pressure was assessed in a significant cohort of healthy people [212].

According to these authors the brachial/aortic systolic pressure is within the range 5-15%. Considering that the systolic pressure does not vary significantly from aorta to carotid artery due to their proximity and due to the fact that carotid artery is considered a central artery. Another study, with healthy subjects shown that the carotid mean pressure is 12% lower than brachial mean pressure [213]. The obtained value for the implemented calibration algorithm is in accordance of the values presented by the mentioned studies.

7.2.2 Invasive Comparison

In the current study, an optical probe developed for measuring the distension waveform of the carotid artery was compared with the invasive profile of the pulse pressure acquired by an intra arterial catheter in the ascending aorta, during cardiac catheterization procedures, in order to validate the new optical device. Direct blood pressure monitoring with an arterial catheter is currently considered to be the most accurate method, but its invasive nature has several disadvantages. This work was designed to determine the correlation between the two waveforms and analyze the differences obtained from PWA parameters based on time intervals of the cardiac cycle and corresponding areas in the arterial pulse pressure of 16 subjects [214], [200].

7.2.2.1 Methods

Study Population

The characteristics of the volunteers in this study are presented in table 7.11. This is a preliminary study for correlation of the two measures and not a statistical study, and therefore a limited cohort was used. This is a prospective study and similar studies of this kind presents a sample of the same magnitude [200], [201], [199].

TABLE 7.11: Main characteristics of the volunteers.

Characteristics	Values
n, Males/Females	16 (12/4)
Age (years)	65.2 ± 12.3
Height (cm)	163.3 ± 6.0
Weight (kg)	72.3 ± 7.0
BMI (kg/m^2)	27.1 ± 2.6

Study Protocol

Measurements were performed in a study population of 16 patients, with a cardiovascular pathology, who had undergone cardiac catheterization. In all cases, simultaneous invasive (in the aortic root) and non-invasive measurements were performed. The study protocol was approved by the ethical committee of the CHUC, Portugal.

Subjects were allowed to rest for 15 minutes in the supine position at a temperature controlled environment before the angiography proceeds. Each exam procedure consisted on the acquisition of a set of cardiac cycles at the carotid artery during a few minutes with the optical system. The measurements were taken by a senior physician who was trained to operate the optical probe device.

After the optical acquisition, the arterial catheter was used to monitor the blood pressure during the surgery and it was positioned to record the pulse pressure at the aorta. These tests make use of a 6-Fr Judkins right catheter that was connected to a pressure transducer using a saline infusion system. After flushing and transducer calibration, the hemodynamic polygraph was set to 200mmHg/10 cm sensitivity and a 100mm/s registry speed. The system used was a Siemens® Artis Zee with AXIOM Sensis hemodynamic recording system. Data were resampled at 200 Hz for waveform analysis, during 10s to cover at least two respiratory cycles. The invasive pulse pressure waveform acquired was stored and processed with Matlab®.

Hemodynamic measurements

To compare the two waveforms acquired with the two systems with different amplitudes and time duration, it is convenient to normalize both over amplitude and time. After this process, the inflection points for the extraction of the parameters were determined. The end of systole was determined by the identification of the dicrotic notch, which marks the beginning of the diastole. The areas under the curve of the pulse wave represent the cardiac performance and the potential for coronary perfusion enabling the cardiac workload. The indices under analysis were: the AUC, the Area during Systole (AS) and Area during Diastole (AD) their ratio (AD/AS) and the ETI [200]. In a non-invasive approach of the global cardiac function time intervals from the cardiac cycle were used [214].

7.2.2.2 Results

The correlation in shape and hemodynamic parameters under study were compared between the two pulse pressure waveforms acquired (invasive and non-invasive). The mean value of HR from the optical measure is 69 ± 8.80 and for the invasive measure is 71 ± 7.81, with a mean difference of 5 bpm between them. HR remained unchanged during the surgery procedures, consequently the hemodynamic indices are also stable during the assessment period.

Comparison of the Pulse Pressure Waveform

The waveforms obtained with the new optical system, placed externally over the carotid artery have a very similar contour to the pressure curve obtained with a catheter, placed inside the aortic artery (Figure 7.14). The dicrotic notch is marked with a small square at the represented waveforms (Figure 7.14).

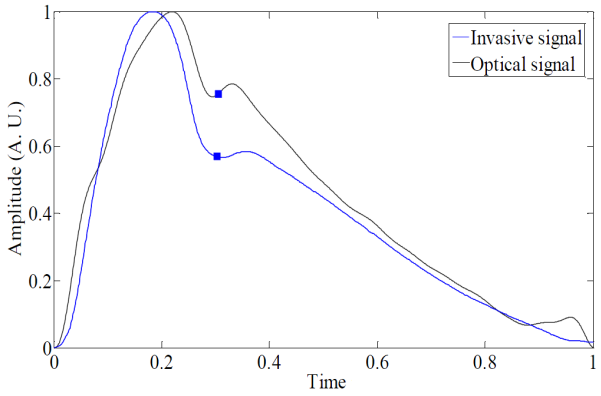

FIGURE 7.14: Invasive aortic pulse pressure waveform and non-invasive carotid waveform.

The small effect of signal amplification in the carotid results from a phenomenon that occurs throughout the arterial tree. In clinical practice, it is recognized an increase in the whole amplitude of the pulse pressure when it travels distally, *i.e.*, a gradual widening of the pulse pressure between two sites of the arterial tree [30]. This amplification of the pressure wave with distance (spatial amplification) does not require additional energy input in the arterial system, and so, by definition, is more a distortion than a true amplification, translated as an alteration in the morphology of the waveform [31]. Between the two arteries that are close to each other, the distortion is very small but significant, due to the structural arterial differences as can be seen in the performed analysis [215].

The results show that invasive and non-invasive signals are correlated and show good overall similarity, for all patients, with less than 20% RMSE, and the mean value for the RMSE in all analyzed samples was 13%. The R-Squared value, coefficient of determination, for the profile of the signals under analysis is approximately 0.8 in all cases.

The strength of the correlation of pulse pressure waveforms is expressed by the coefficient of correlation (1 means that the two signals are identical), and for the signals varies in the range of 0.9202-0.9959, thus demonstrating the strong correlation.

The signals frequency study showed great similarity in the modulus. The power spectral density analysis showed attenuation for the invasive signals and confirms the amplification effect in the optical signals. In the frequency window of interest for the analysed signals (below 100 Hz) there is a nearly constant attenuation for signals acquired with the invasive system for all patients. Therefore, there is no frequency modulation able to distort pulse waveforms in a significant way, in the scope of the presented analysis.

Comparison of hemodynamics parameters

The comparison between the areas under the curves allows the assessment of the differences between the phases of the cardiac cycle, systole and diastole. Figure 7.15 shows a biparametric plot of the invasive signal versus the non-invasive signal. For both systems a mean of the pulse pressure from the sample in analysis is represented. When the two

signals are the same, the result would be the bisector of the first quadrant, the line y=x. The plotted curve shows that in the upstroke of the waves, part of the systole period marked in black has a greater proximity to the y=x, these means that in this zone the signals are almost equal.

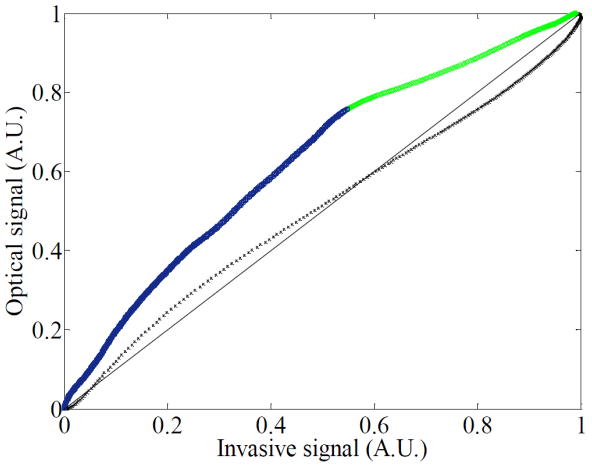

FIGURE 7.15: Plot of the invasive signal *vs* optical signal. The upstroke of the pulse pressures are marked in black, the systolic period segment is comprised by the black and green, the diastolic period is in blue and the solid line marked the x=y segment.

There was a close relationship between the Optical (diameter)–Invasive (pressure) slopes obtained for all subjects and represented by the mean curve in Figure 7.15. However, comparing the change shown by a slope obtained some differences were detected.

After the systolic peak, differences between the two signals are more obvious and during diastole, after the dicrotic notch marked in blue segment, the difference is more substantial. This means that in this cycle phase, the optical signal exhibits greater amplitude than the non-invasive signal, or in other words, there is a higher difference between the structures of the two analyzed waves.

The arterial wall has both elastic and viscous properties. The difference is related to the time-dependent response to the stress–strain relationship (pressure change–diameter change). In a purely elastic artery, this relationship is time-independent, and after the removal of stress, the arterial diameter dimensions would return to the initial dimensions. In the presence of wall viscosity, the arterial wall retains part of the deformation. The arterial viscous properties are responsible for part of the left ventricular energy dissipation characterized by the hysteresis of the pressure–diameter loop represented in Figure 7.15 [201], [17], [216]. The surface between ascending and descending parts of the loop is hysteresis representing the energy dissipation due to the viscous properties of the arterial wall, which could indicate an alteration of the mechanical properties of the arterial vessel [217].

Arterial compliance reflects the ability of an artery to expand and recoil with cardiac pulsation and relaxation [17]. The increasing age of the sample at study leads to changes in the structural components of the aorta walls, and reduces compliance. This change in compliance has significant implications in the pulse type contour analysis and contributes to the hysteresis verified in Figure 7.15 [17], [218].

Evaluating the whole area under the curve, there is an over-estimation of the values for the non-invasive method. The optical system presented an AUC mean value ($\pm$ SD) of 0.51 ± 0.04, while the invasive system showed of 0.42 ± 0.04, as shown in Figure 7.16.

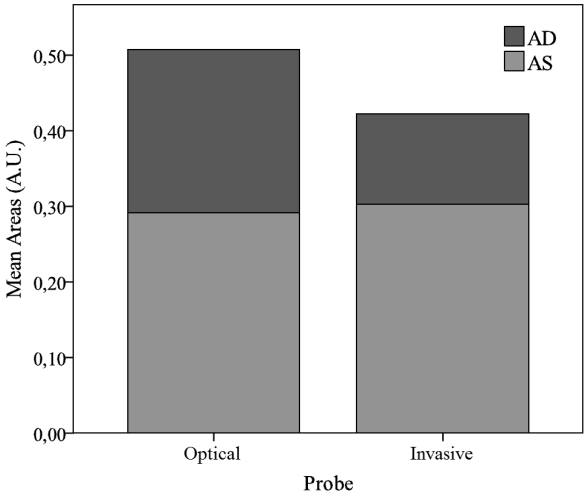

FIGURE 7.16: Bar plot of AS and AD determined by the two systems.

The area during the diastole is the responsible component for the difference between the AUC, the sum of the two components, in the two systems. During the systolic period the AS mean values are very similar, 0.30 ± 0.05 for the optical method and 0.29 ± 0.04 for the invasive system. The variability of values measured by the two systems for each subject under the study was compared and represented in Figure 7.17.

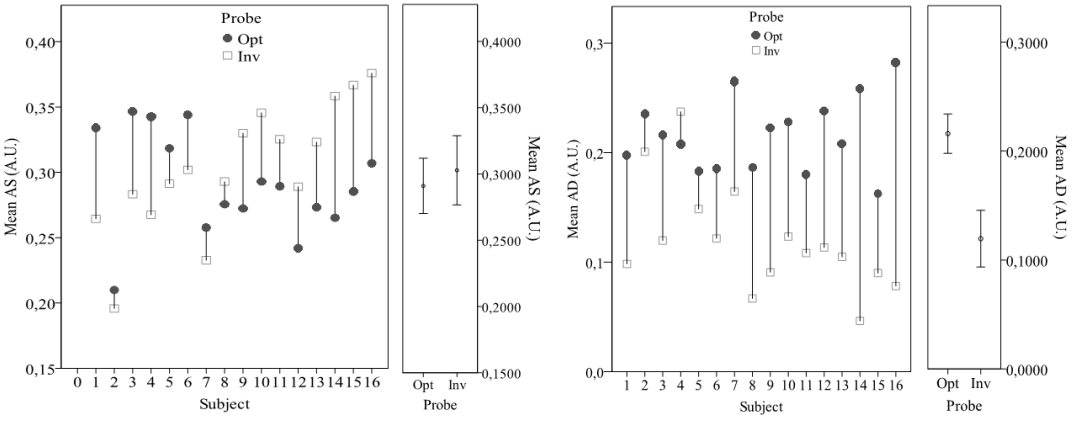

(a) Variability in AS.

(b) Variability in AD.

FIGURE 7.17: Variability of two systems within each individual subject and mean values by acquisition method, with error bars representing the 95% confidence interval of the sample mean.

The variability over the measures was assessed by the coefficient of variation which is defined by a ratio of the SD of measures divided by their mean value. For the optical and invasive systems, these coefficients are similar (13% *vs* 16%) with a lower variability for the optical probe.

Figure 7.18 represents the curve of mean differences during the cardiac cycle, between the two systems for all subjects. For the pressure pulse samples in analysis, the average systolic peak occurs approximately after 0.2 seconds, marked in a dashed line in Figure 7.18. After that, the difference begins to be more significant, as a result of the energy dissipation, due to viscous properties of the arterial wall. After the removal of stress, the

arterial diameter dimensions would return to their initial dimensions but, the arterial wall retains part of the deformation.

The average difference between the two systems along the cardiac cycle is 0.0875. A Pearson-Correlation analysis between the areas of signals shows a significant correlation of 0.847 at a 0.01 level (2-tailed).

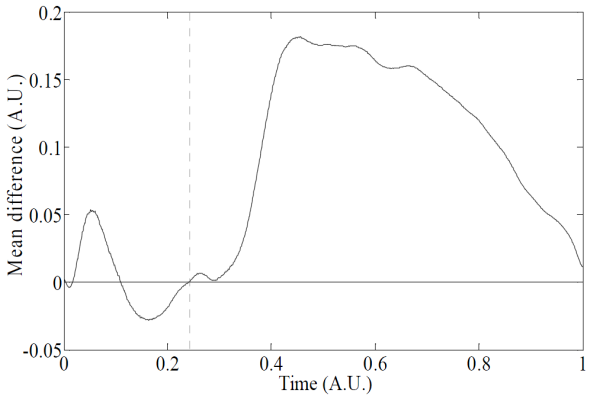

FIGURE 7.18: Mean difference between the optical and the invasive signals during a heart cycle.

The ratio AD/AS demonstrates, again, the differences (optical system 0.76 ± 0.19; invasive system 0.42 ± 0.25) explained by the discrepancies originated during the diastole.

The ETI values obtained are correlated but there is a trend to have systematic lower values from the optical probe device. The ETI mean value (± SD) is 45.64 ± 7.80% for the invasive measurements and 41.40 ± 6.53% for the optical signals. The mean values for the ETI obtained by the two optical systems are slightly higher than the expected. Patients with systolic dysfunction have been found to have higher values of ETI, the prolonged ejection time is primarily due to the increased afterload [35], [219].

7.2.3 Case Study: Carotid Stenosis

The main purpose of the tests on this particular case study was to assess the capability of the system in determining the pressure waveform features.

The tests were performed in a patient who had undergone a carotid angiography, and the assessment trials were made before and after the endovascular angioplasty procedure.

7.2.3.1 Description of Case

The subject under study is a 76-year-old woman with a of 90% left internal carotid artery stenosis, as well as hypertension and type II diabetes. The body mass index is 22.8, and at the time of the surgical procedure she had heart rate of 36.6 °C of temperature and 69 beats per minute. An obstruction of 90% causes a significant decrease in the blood flow that passes through this vessel (Figure 7.19), which consequently causes variations of the arterial pulse pressure waveform. The patient was subject to an endovascular angioplasty and stenting procedure.

The carotid pressure waveform was recorded with the optical probe before the surgery, and the detected waveform revealed a modified profile when compared to the normal range, with a large increase of pressure before the systolic peak (Figure 7.20(a)).

Figure 7.20(a) evidences the presence of a reflected wave, marked in blue for the RP, prior to the systolic peak that is caused by the reflection of the pressure wave in

FIGURE 7.19: Angiographic image of the patient in the case study showing the carotid artery with stenosis, marked with a white arrow.

the atherosclerotic plaque of the internal carotid artery wall. Because this plaque is nearby the assessment location, the return of the backward reflected wave is detected almost immediately its occurrence, *i.e.*, even before the systolic peak. Along the detected waveform there are few inflections indicate that multiple reflections are occurring. In the end of the diastole it is noticed an increase of pressure, that is not common in normal pressure waveforms and will be analyzed below.

After the procedure, few pressure waveform signals were acquired once again, with the optical probe at the carotid site, for comparison with the pre-surgery signals. The pulse pressure waveform changed with the intervention and the abnormal inflection in the wave, during the diastole, has disappeared (Figure 7.20(b)).

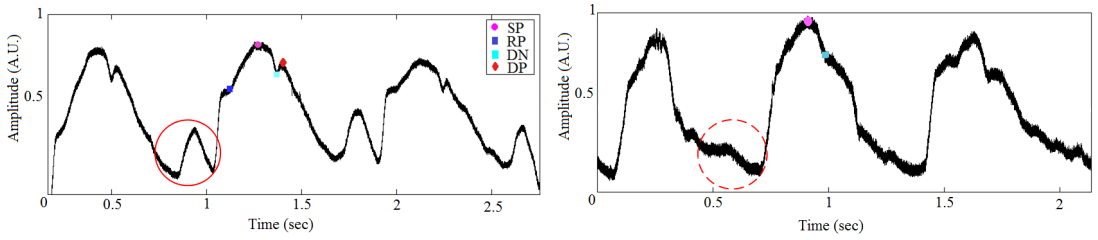

(a) Before the surgical procedure.

(b) After the surgical procedure.

FIGURE 7.20: Set of a few heart beats detected with the optical probe at the carotid site. (a) Before the surgical procedure. Main features marked in the waveform and abnormal effect marked in red circle. (b) After the surgical procedure. The abnormal effect disappears from the region of the end-diastole in the waveform, marked with the dotted circle.

The waveform acquired after the surgery presents the characteristics of a normal arterial pulse pressure waveform, which seems to indicate that the anomalous inflections disappeared with the correction of the diameter of the vessel. However, small inflections

continue to appear in the pulse pressure upstroke, probably originated by the different compliance in the vessel wall in the local of stent.

7.2.3.2 Discussion

In particular, this case illustrates the variation of the pulse pressure waveform in a stenosis intervention case. The pulse pressure waveform reflects the interaction between the left ventricle ejection and the physical properties of the arterial circulation. Its behavior demonstrates that the atherosclerotic plaque buildup is responsible for wave reflection events.

As already stated, in the pressure waveform acquired before the surgical procedure, it is notable an early wave reflection that occurs due to the severe obstruction in the internal carotid artery. In fact, due to the proximity of the atherosclerotic plaque to the assessment local, this reflection was expected and is actually easily observed immediately before the systolic peak. However, in the later diastole a phenomenon of augmented pressure is visible (red circle in Figure 7.20(a)). This event is unexpected in these pressure waveforms and hypothetical explanations for the occurrence of that were theorized. The fact that the pressure increases in the end of the diastole is likely corroborative with a distal event, otherwise, if the cause of this phenomenon was nearby the local of assessment, the pressure augmentation would be detectable earlier, most probably during the systole.

The hypothetical justification that can be given to explain this occurrence is based in collateral circulation confirmed by the angiography data. It is known and described that in cases of severe internal carotid artery stenosis, cerebral collateral circulation can take place [220], [221], [222]. The collateral circulation consists on a supplying of blood flow to the ischemic regions, which is in when the principal pathway of circulation is compromised. This phenomenon compensates the lack of perfusion, through existing anastomoses, namely the circle of Willis [220], [223]. In the pathological cases of intracranial artery stenosis, this mechanism of compensation of blood flow can occur in order to maintain the cerebral tissue perfusion and prevent ischemic episodes [222].

Once the distal region of the stenotic artery has lower pressure than the proximal segment of the artery, the blood tends to flow downstream from anastomose towards the distal end of the plaque. Hence, a hypothesis could be made and the increase of pressure in diastole may be explained by a latter backward blood flow in the stenotic internal carotid artery, due to the collateral circulation.

Altogether, the optical probe proved to be a very useful tool for a non-invasive monitoring of the arterial pressure waveform and could help in the early diagnosis of cardiovascular diseases. In particular, this probe is able to detect stenosis events and can be used in the diagnostic and monitoring of this cardiovascular pathology.

The natural follow-up of this work would be to compare the distension waveform in carotid obtained with Ultrasound in cases with different levels of stenosis severity, with the signals being acquired by the optical system, in order to quantify the changes of pulse pressure waveform with the stenosis severity.

In the future, a study of other cardiovascular pathologies will be interesting to classify the differences in waveform arising from physiological variations. A system able to make an assessment of the cardiovascular system without resorting to expensive and invasive techniques will be an important tool in the clinical context.

7.3 Discussion and Conclusions

In this chapter was intended to select the best combination: probe/algorithm for acquire the arterial waveform in the carotid site and determine the main hemodynamic parameters. After selecting the probe, it was necessary to extensively test for evaluate the robustness of the optical probe and validates the capability to measurement the arterial pulse waveform.

The tests were carried out over 4 weeks, in a small group of volunteers with two types of optical probes, APD and PPD, allowed the selection of the best algorithms for PWA and PWV computing.

The shown algorithms, developed for the determination of PWV have a good overall performance. The best results was obtained for Cross-Correlation method while the algorithm based on differential calculus for PWA allows the determination of the main hemodynamic parameters used in clinical practice.

The two types of probes in study proved to be able to reliably measure the pulse pressure waveform at the carotid site. However, the determination of the PWV with the APD probe evidences an underestimation of this parameter. Furthermore, the acquisition of signals *in vivo*, with the APD probe, was more difficult than with the PPD probe, because the SNR is significantly lower. This is due to the fact that the sensitive area of the avalanche photodiodes is almost a point, which makes positioning of both photodiodes over the carotid artery tougher. The good results obtained with the PPD, combining with the much lower cost of the PPD, does the solution based in the planar photodiodes the best option.

The major limitation of this type of technology is the inability to direct calibration of the waveform obtained by the optical probe. For the determination of parameters like AIx, SEVR, ETI and dP/dt_{max}, it was necessary to calibrate the system with the systolic and diastolic pressure. With this purpose each evaluation was preceded of brachial blood pressure measurement with a clinical sphygmomanometer.

These preliminary tests allowed a study of repeatability of the parameters inferred by the system validation, showing great consistency over time for different subjects.

The validation test on a small sample showed the clinical feasibility of the optical probes, preceding a large study of healthy subjects.

The comparison test between the optical system and Complior Analyse® device show a strong correlation for the values of PWV obtained, however, these devices measure different PWV parameters that is responsible for some discrepancies in the results.

The reproducibility study was performed in 13 volunteers by two trained operators. The main limitations of this study are its small size and the inclusion of healthy volunteers rather than patients. However it is common to evaluate emerging techniques in volunteers initially and these studies are important platforms for further method improvement and subsequent patient studies.

The PWA repeatability results are considered high for HR, strong for AIx, moderate for dP/dt_{max} and low for SEVR and ETI. Actually, for all analysis the resulting values for dP/dt_{max} and SEVR differ substantially from the ones presented as reference and show the lower values for reproducibility evaluation, probably originated by the calibration method used.

The PWV results had a good inter and intraoperator reproducibility judged by the Bland-Altman plots as well as the test of differences between measures.

The factors such as the position of two photodetectors in the carotid vessel, tremors in the hands of an operator, respiratory movements of the volunteers could introduce

differences in the measurements between operators and trials. These factors might affect the measurements and are possible to quantify making changes in the probe by the introducing an accelerometer or a respiratory band in the volunteers, however escaped to the objective of this work.

The newly developed optical system showed good reproducibility as evaluated by both inter and intra-operator methods.

The trial tests, in a large group of young and healthy subjects, has attempted to validate the proposed optical system as a reliable method to assess non-invasively local PWV in the carotid artery, to establish reference values of the local PWV as well as other mentioned parameters in this type of population.

Even though the sample consists of young subjects with a relatively narrow age distribution, this result generally agrees with those obtained in other studies. The PWA parameters revealed the important relations between some characteristics of the population and the arterial system status.

All the correlations obtained in this study showed that the age contributes to the arterial stiffness as reflected in the values found for the various parameters. Smokers appear to have higher arterial age, and therefore increased cardiovascular risk.

The optical system under study proved to be a good choice for the determinations of hemodynamic parameters in a non-invasive and non-contact assessment, which allows a better knowledge about the cardiovascular condition and the management of many disease states.

The proposed method exhibits a very high patient hit success. In fact, for 119 out of 131 patients (90%) it took around 1 to 2 mins to start acquiring reasonable quality signals, each take lasting for 30 seconds.

The study between the measurements obtained with invasive system and the optical method, emphasizes the effect of the energy dissipation due to the viscous properties of the arterial wall that occurs during the heart cycle characterized by the hysteresis in the pressure–diameter loop. In the presence of wall viscosity, the arterial wall retains part of the deformation that results of in part of the energy dissipation by the arterial viscous properties.

The displacement of the pressure–diameter loop, indicating changes in the vessel function and these data can be used to provide the response of a large elastic vessel to the blood pressure changes within a cardiac cycle and thus on large elastic arterial mechanical properties.

The results show that the two pulse waveforms obtained by the two systems have a strong correlation and the mean values of the area analysis during the systolic period are very similar. The diastole is the period at which the biggest differences between the two waves are observed which might be explained by the mechanical energy dissipation during the heart cycle.

This study validates the capability to estimate the arterial pulse waveform with a non-invasive way with a new contactless optical probe, in a carotid measure. The differences between the two systems are due to the different measures in study, diameter and pressure.

Chapter 8

Conclusions and Future Work

8.1 Conclusions

The main objective of this work was demonstrate that an optical system is capable of contactless measure of pulse pressure waveform in carotid artery along with algorithms for determination of the temporal specific features, for PWA and PWV estimation which may allows a rigorous cardiovascular diagnosis.

All the system was built from scratch with clinical requirements. The most important characteristics of this system are its high portability, a compact size, ergonomic configuration probes, user-friendly and non-invasive, with a truly non-contact operation capability, and allows measurements without complex patient preparation and the absence of complex optical constituents. All the optical system is portable, lightweight and it was designed with low power consumption and low cost materials, in order to be considered as an interesting solution for commercial purposes.

Four prototypes were developed in this work: three based in non-coherent light and one based in coherent light.

The probes based in non-coherent light were tested for three different photodetectors: avalanche photodiode, planar photodiode and lateral effect photodiode. The last one was abandoned due to low temporal resolution and therefore not enough to measure the expected PWV in pathological cases. The optical probes based in planar and avalanche photodiodes were extensively evaluated in bench tests and *in vivo* acquisitions. Theses optical probes, APD and PPD, specifically designed to measure PWV have been developed and tested along with three different signal processing algorithms for PTT determination. The algorithm based in Cross-Correlation method delivers PTTs with the lowest errors in the bench test. These results were confirmed with in *in vivo* tests.

The APD and PPD probes proved to be reliable in detecting the distension waveforms either in the test bench or *in vivo* tests at the carotid site where they reflect the propagating pressure wave. In order to evaluate the capability of the developed optical device to accurately detect the pulse waveform, a comparison test was carried out between an ultrasound image system, as source of reference data, and the optical probes. This study demonstrated that the optical probes allow the reproduction of the arterial waveform with a higher resolution.

Probes with infrared light sources were developed for situations where the carotid artery is distant from the skin surface. These cases require wavelengths able to optically penetrate the tissues in order to allow the determination of the distension waveform. The probes with infrared light show better results with the progressive increase in the number of silicone layers that simulates the fatty accumulation levels. They also provide

better resolution in the waveform features, higher SNR and lower RMSE when compared to the signals acquired with visible light.

The good results obtained with the PPD in the benches tests, combined with the lower cost of the PPD detector compared to the APD and the easy bias voltage of 15 V, makes the solution LED/PPD combination the best option.

The several studies carried out along this project have proved the feasibility and the potentiality of this optical system in the clinical practice.

All clinical studies follow a protocol approved by the ethical committee of the Centro Hospitalar e Universitário de Coimbra, EPE Portugal. All the subjects were volunteers and gave a written informed consent.

The tests carried out over 4 weeks in a small group of volunteers led to an experimental validation of the optical system under study composed by two types of optical probes, APD and PPD. This study allowed the selection of the best algorithms for PWV computing based on the cross-correlation method. The acquisition of *in vivo* signals with APD probe was harder than with the PPD probe. The solution based in the planar photodiodes becomes the best option and the following studies were made only with PPD probe.

The PWV obtained by the developed optical system was validated by comparing results with gold-standard tonometry probe Complior® that showed a great consistency between the PWV obtained with the two devices. The Pearson correlation value is 0.819 that represents a strong correlation. However, in these trials, the obtained values for local carotid PWV are substantially lower than the regional carotid-femoral PWV. This systematic shift towards overvalues from Complior® was expected since it is known that the femoral PWV is higher than carotid PWV.

The developed optical system showed good reproducibility as evaluated by both inter-operator and intra-operator methods. This study could be extended by comparing PWV and PWA values from patients with vascular risks.

One limitation identified *in vivo* tests was due to the two photodetectors (placed at a precise and well-known distance of 20 mm) that detect the pulse wave propagation, along the arterial segment. This distance could be a limitation only in cases were a small segment of carotid artery is accessible, which difficults the position of two photodetectors centred on the artery.

A large study was performed in 131 young subjects to establish the reference values for several hemodynamic parameters and to find correlations between these and the population characteristics. The results proved that the use of this new technique is a trustworthy method to determine PWV and PWA parameters.

The mean value for PWV is $3.33 \pm 0.72\ ms^{-1}$ measured by the optical probe, and confirmed a significant increase of PWV with age. The PWA parameters revealed the important relations between some characteristics of the population and the arterial system status. The negative correlation between the AIx and the heart rate were verified in this study also differences between gender and smokers/non-smokers were found. For the SEVR parameter it was also verified a decrease with the heart rate. The dP/dt_{max} analysis showed a difference with gender, with lower values for the female subjects, and this parameter decreased significantly with age. All the correlations obtained in this study showed that the age contributes to the arterial stiffness as reflected in the values found for the various parameters. Smokers appear to have higher arterial age, and therefore increased cardiovascular risk.

The optical probe developed was compared with the invasive profile of the pulse pressure acquired by an intra arterial catheter in the ascending aorta during cardiac catheterization procedures in order to validate the new waveform acquired by the optical

device. The results show that the waveforms obtained by the two systems have a strong correlation (mean value of 0.958) and the mean values of the area analysis during the systolic period are very similar (0.30 - 0.05 for the optical method and 0.29 - 0.04 for the invasive system). The diastole is the period at which the biggest differences between the two waves are observed which might be explained by the mechanical energy dissipation during the heart cycle.

The analysed case study suggests that the optical prototype is able to detect a waveform distorted due to the presence of severe carotid stenosis. This finding constitutes an important milestone in the development of this prototype, extending its capabilities and potentiality in the diagnosis of cardiovascular diseases.

The probe based in Doppler technique was designed with two LDs. For this probe, based in coherent light, tests were performed in order to evaluate the performance of the probe and the specific algorithms for frequency analysis.

The crosstalk tests were performed (electrical and optical) and significant interferences were not found.

To extract most of the physiologically important parameters from the Doppler signals, an algorithm based on the short time Fourier transform and empirical mode decomposition was used. The decomposition levels of the EMD permit the extraction of different pieces of information. The first level allows an easy detection of the feature points in contrast to the fourth/fifth levels that clearly show the basic oscillation frequency. The first decomposition level wave envelope achieves a feature points identification with a maximum RMSE of 4.7 ms for SP and 3 ms for RP, a minimum RMSE of 2.5 ms for SP and 1.3 ms for RP.

The coherent optical probe demonstrated that a laser vibrometer based on the self-mixing effect, with a simple optical apparatus developed, can accurately perform measurements of velocity and displacements in the sub-micron vibrations amplitudes, confirming the multiple utility of this method for this kind of measurements.

Another configuration for the probe based in Doppler effect was tested, for the potential interest to use a photodetector with a larger area that can improve the quality of the signal which may have biomedical applications. The mixing effect was obtained outside the laser cavity, using a planar photodiode that detects the interference between the original beam and a beam with Doppler shifted frequency, and opened the possibility to construct a new probe with this new configuration.

To conclude, the non-invasive and non-contact method proposed by the optical solutions, as well as the implementation of rapid algorithms to assess hemodynamic parameters, will permit a continuous monitoring of the cardiovascular system and give an early and accurate diagnosis about the cardiovascular conditions.

8.2 Future Work

The presented results are considered encouraging and demonstrated the great potential of the optical probes as a reliable approach for non-invasive hemodynamic parameters assessment. Nevertheless, towards the continuous development of the optical probes and its system few issues should be enhanced. Those questions could offer opportunities for further work.

During this project, several configurations were design to improve the signal acquisition process and overtake the eventual difficulties in positioning the probe in the carotid vessel. The implementation of a new configuration could represent a great advance in the

flexibility and freedom to adjust the measure (Figure 8.1). This new probe would have more degrees of freedom which would allow a better adaptation to the neck's anatomy. The probe would never touch the beating artery because the head of the probe would have a support system that could be orientated alongside the artery, preventing signal distortions. Although the optical probes allow a contactless measurement and just the box contacts the skin, to stabilize and maintain constant the distance between the photodector and the artery site, a layer of polymeric gel without optical properties to do the interface between the probe and the skin could solve hygiene problems in the use of probes without interfering with the signal that is measured.

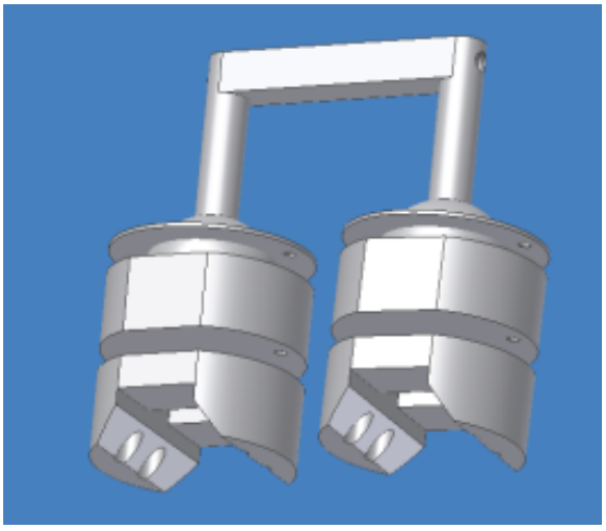

FIGURE 8.1: Schematic version of a new design PPD based probe.

The algorithm developed that provides an automatic method to select the data acquired in a clinical exam that contains the relevant information, has not been yet tested in a population in order to prove their capability to select the pulse waveforms in the data acquired.

The preliminary tests allowed the clinical feasibility of the optical probes, preceding a large study of patients with different pathologies and cardiovascular diseases. Envisaging a possible clinical use of the probes, feature extraction tests have to be carried out, in the follow-up of this work, in a multi-center medical oriented clinical trial program. Large scale clinical trials, with central hospital partners, are mandatory for the clinical validation of the optical probe systems.

The stenotic lesions could be identified and quantified by analyzing Doppler velocity spectra in combination with real-time B-mode and color-flow images of these vessels [224], [225]. Comparison of the Doppler analysis with optical system results of accumulation status in atherosclerotic plaques in cohort of patients with carotid stenosis, could confirm the results obtained in the severe stenosis case and proved the potential of this new technique to be able to detect a distorted wavefom due to the presence of atherosclerotic in this vessel segment.

Optical Coherence Tomography (OCT) is an imaging method used to take high-resolution pictures of blood vessel walls. OCT provides detailed images of the plaques (build-up of cholesterol and other materials) in blood vessel walls and the distension of wall during of cardiac cycle could be access. This detailed information about artery wall distension can be compared with the results obtained with optical probes. These tests

would focus on comparing distension waveforms of the carotid artery from an invasive method and the optical probe.

For the probe based in Doppler technique, where the signals are modulated in frequency, some hardware improvements could be implemented in order to substitute algorithms steps and to allow an online data analysis. It is expected that the inclusion of a frequency-to-voltage converter will substitute the time frequency analysis, which is currently performed with algorithmic analysis. The hardware time-frequency analysis will reduce the software computational effort.

This work demonstrated the possibility to generate self-mixing signals outside the optical laser cavity using a photodetector with a larger area. That fact can improve the quality of the signal in biomedical applications, using a configuration that may allow data acquisition *in vivo*. This approach still remains to be explored.

Appendix A

Schematics of Probes

In this appendix is represented the schematics of circuits for all prototypes developed during this project.

A.1 Prototypes Based in Non-coherent Light

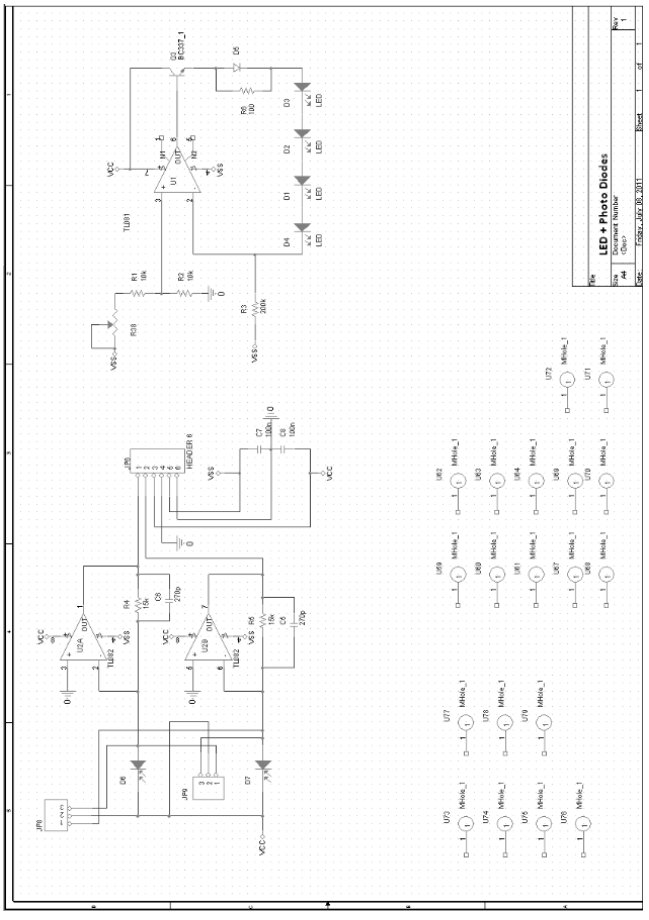

FIGURE A.1: Schematic of the PPD Probe.

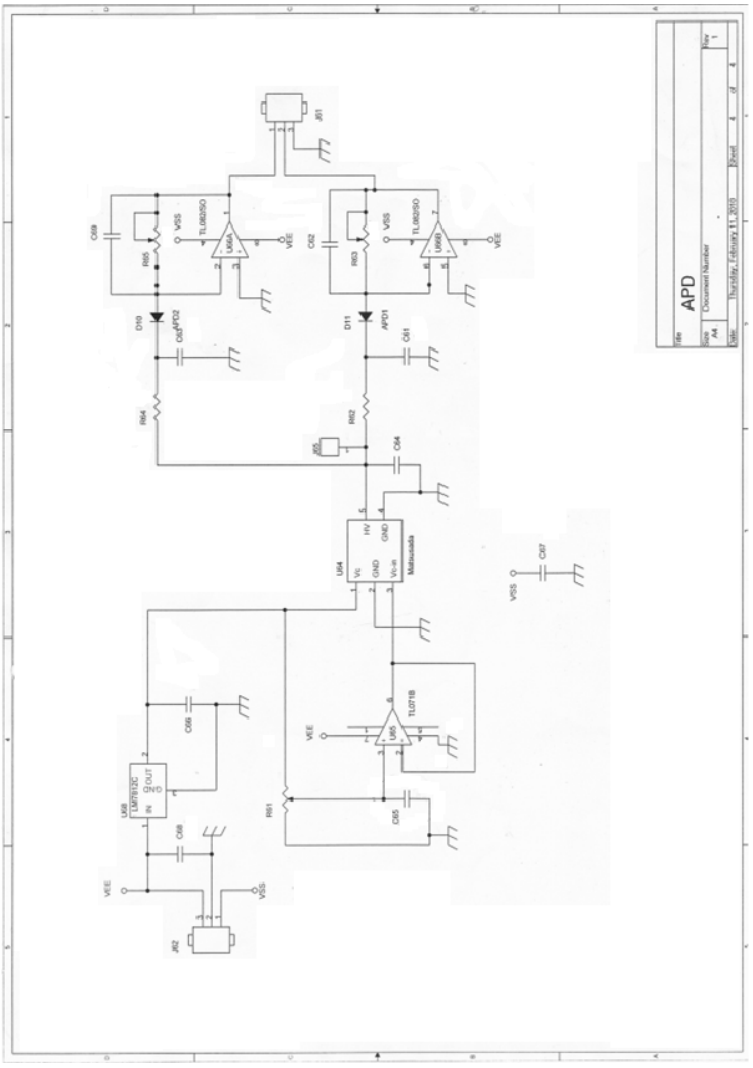

FIGURE A.2: Schematic of the APD Probe.

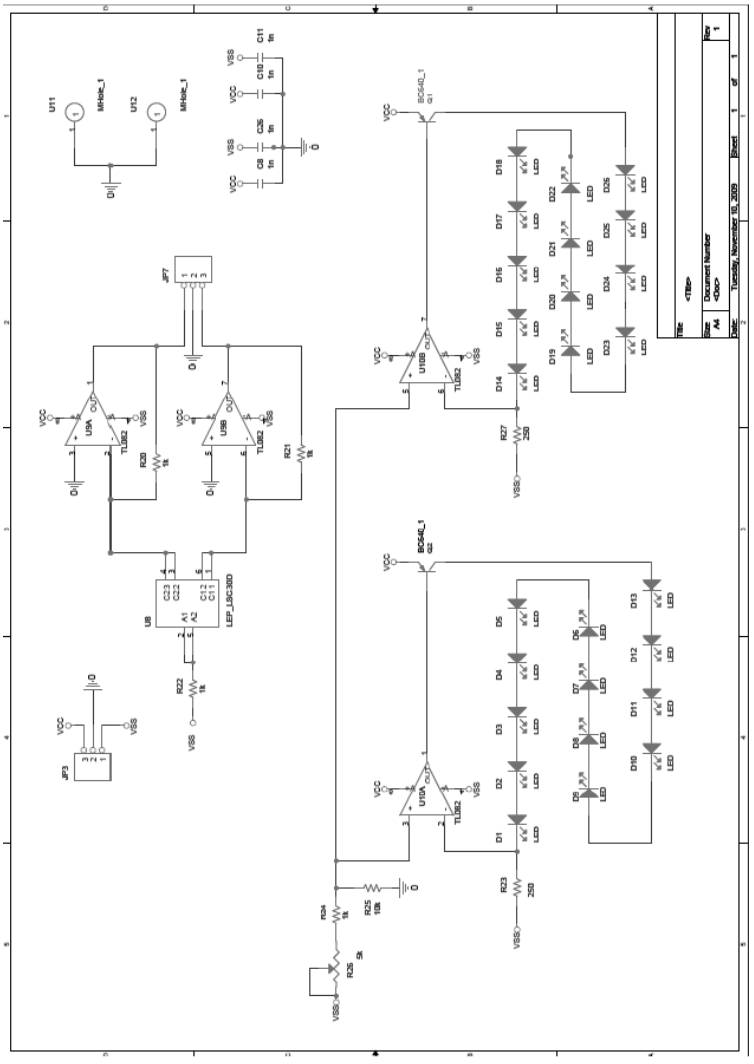

FIGURE A.3: Schematic of the LEP Probe.

A.2 Prototype Based in Coherent Light

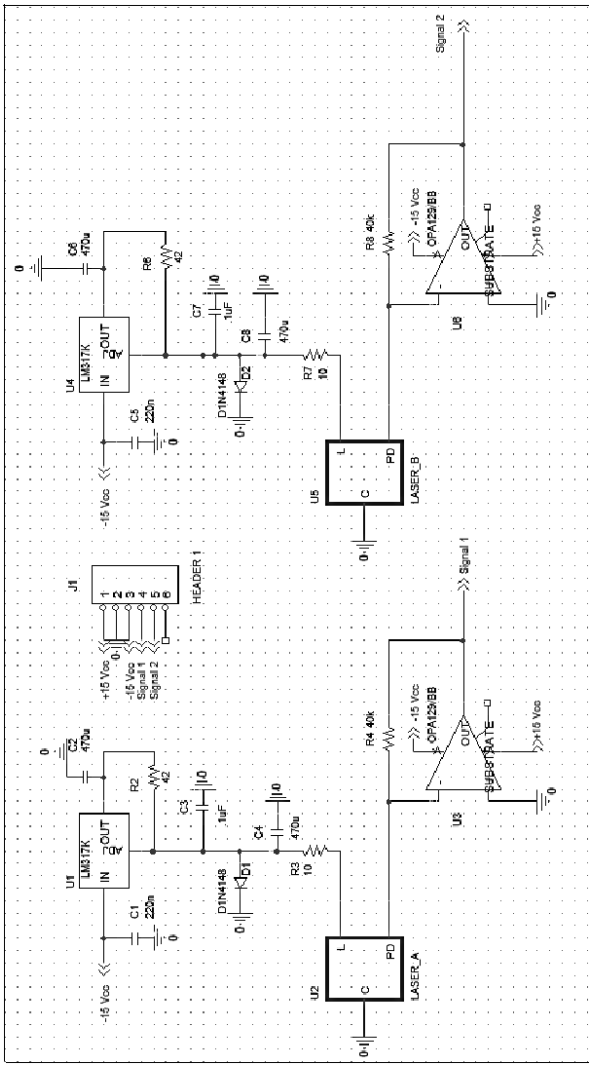

FIGURE A.4: Schematic of the LD Probe.

Appendix B

Schematics of Acquisition Box Modules

In this appendix is represented the schematics of circuits from different modules of acquisition box.

B.1 Power Supply

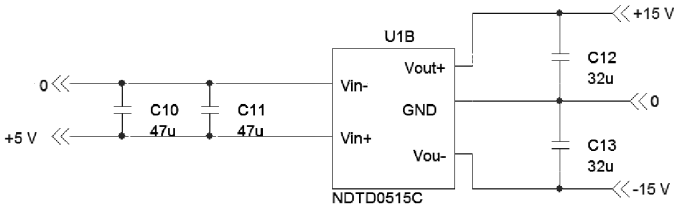

FIGURE B.1: Convertion circuit for ±15V probe power supply (Murata NDTD 0515C converter).

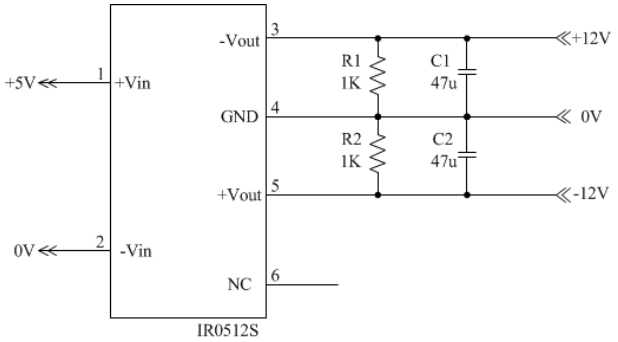

FIGURE B.2: Convertion circuit for ±12V probe power supply (XPpower IR 0512S converter).

B.2 Anti-aliasing Filter

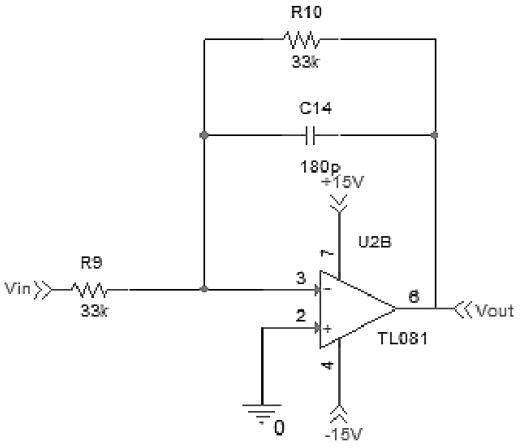

FIGURE B.3: Schematic of the anti-aliasing filter.

Bibliography

[1] C. D. Mathers and D. Loncar, "Projections of global mortality and burden of disease from 2002 to 2030," *PLoS medicine*, vol. 3, no. 11, p. e442, Nov. 2006.

[2] A. Bitton and T. Gaziano, "The Framingham Heart Study's Impact on Global Risk," *Prog Cardiovasc Dis.*, vol. 53, no. 1, pp. 68–78, 2010.

[3] A. Alwan, Ed., *Global status report on noncommunicable diseases.* World Health Organization, 2010.

[4] A. P. Avolio, M. Butlin, and A. Walsh, "Arterial blood pressure measurement and pulse wave analysis–their role in enhancing cardiovascular assessment." *Physiological Measurement*, vol. 31, no. 1, pp. 1–47, 2010.

[5] P. Boutouyrie, S. Laurent, X. Girerd, A. Benetos, P. Lacolley, E. Abergel, and M. Safar, "Common Carotid Artery Stiffness and Patterns of Left Ventricular Hypertrophy in Hypertensive Patients," *Hypertension*, vol. 25, no. 4, pp. 651–659, 1995.

[6] J. HAST, "Self-mixing interferometry and its applications in noninvasive pulse detection," Doctoral Thesis, University of Oulu, 2003.

[7] N. Christodoulides, F. N. Pierre, X. Sanchez, L. Li, K. Hocquard, A. Patton, R. Muldoon, C. S. Miller, J. L. Ebersole, S. Redding, C.-K. Yeh, W. B. Furmaga, D. a. Wampler, B. Bozkurt, C. M. Ballantyne, and J. T. McDevitt, "Programmable bio-nanochip technology for the diagnosis of cardiovascular disease at the point-of-care." *Methodist DeBakey cardiovascular journal*, vol. 8, no. 1, pp. 6–12, Jan. 2012.

[8] H. Federation, *Global Atlas on cardiovascular disease prevention and control*, P. P. Shanthi Mendis and B. Norrving, Eds. Geneva: World Health Organization, 2011.

[9] J. Perk, G. De Backer, H. Gohlke, I. Graham, Z. Reiner, M. Verschuren, C. Albus, P. Benlian, G. Boysen, R. Cifkova, C. Deaton, S. Ebrahim, M. Fisher, G. Germano, R. Hobbs, A. Hoes, S. Karadeniz, A. Mezzani, E. Prescott, L. Ryden, and M. Scherer, "European Guidelines on cardiovascular disease prevention in clinical practice (version 2012)," *European heart journal*, vol. 33, no. 13, pp. 1635–701, Jul. 2012.

[10] D. M. Lloyd-Jones, "Cardiovascular risk prediction: basic concepts, current status, and future directions," *Circulation*, vol. 121, no. 15, pp. 1768–77, Apr. 2010.

[11] D. B. Panagiotakos and V. Stavrinos, "Methodological issues in cardiovascular epidemiology: the risk of determining absolute risk through statistical models." *Vascular health and risk management*, vol. 2, no. 3, pp. 309–15, Jan. 2006.

[12] S. M. Hussain, B. Oldenburg, Y. Wang, S. Zoungas, and A. M. Tonkin, "Assessment of Cardiovascular Disease Risk in South Asian Populations," *International journal of vascular medicine*, vol. 2013, p. 786801, Jan. 2013.

[13] G. Mancia, R. Fagard, K. Narkiewicz, J. Redon, A. Zanchetti, M. Böhm, T. Christiaens, R. Cifkova, G. De Backer, A. Dominiczak, M. Galderisi, D. E. Grobbee, T. Jaarsma, P. Kirchhof, S. E. Kjeldsen, S. Laurent, A. J. Manolis, P. M. Nilsson, and E. Al., "2013 ESH/ESC guidelines for the management of arterial hypertension: the Task Force for the Management of Arterial Hypertension of the European Society of Hypertension (ESH) and of the European Society of Cardiology (ESC)." *European heart journal*, vol. 34, no. 28, pp. 2159–219, Jul. 2013.

[14] M. E. Hock Ong, C. H. Lee Ng, K. Goh, N. Liu, Z. X. Koh, N. Shahidah, T. T. Zhang, S. Fook-Chong, and Z. Lin, "Prediction of cardiac arrest in critically ill patients presenting to the emergency department using a machine learning score incorporating heart rate variability compared with the modified early warning score." *Critical care (London, England)*, vol. 16, no. 3, p. R108, Jul. 2012.

[15] J. J. Oliver and D. J. Webb, "Noninvasive assessment of arterial stiffness and risk of atherosclerotic events," *Arteriosclerosis, thrombosis, and vascular biology*, vol. 23, no. 4, pp. 554–66, May 2003.

[16] M. E. Safar, "Arterial Stiffness : A Simplified Overview in Vascular Medicine," *Atherosclerosis, Large Arteries and Cardiovascular Risk*, vol. 44, pp. 1–18, 2007.

[17] G. M. London and B. Pannier, "Arterial functions: how to interpret the complex physiology," *Nephrol Dial Transplant*, vol. 25, no. 12, pp. 3815–23, Dec. 2010.

[18] N. a. Shirwany and M.-h. Zou, "Arterial stiffness: a brief review," *Acta pharmacologica Sinica*, vol. 31, no. 10, pp. 1267–76, Oct. 2010.

[19] H. Groen, "Atherosclerotic Plaque And Shear Stress In Carotid Arteries," Ph.D. dissertation, Erasmus University of Rotterdam, 2010.

[20] M. Paciaroni, V. Caso, M. Acciarresi, R. W. Baumgartner, and G. Agnelli, "Management of asymptomatic carotid stenosis in patients undergoing general and vascular surgical procedures." *Journal of neurology, neurosurgery, and psychiatry*, vol. 76, no. 10, pp. 1332–6, Oct. 2005.

[21] L. Stoner, J. M. Young, and S. Fryer, "Assessments of arterial stiffness and endothelial function using pulse wave analysis," *International journal of vascular medicine*, vol. 2012, p. 903107, Jan. 2012.

[22] B. Syeda, M. Gottsauner-Wolf, S. Denk, P. Pichler, K. Aliasghar, and D. Glogar, "Arterial Compliance: a Diagnostic Marker for Atherosclerotic Plaque Burden?" *American Journal of Hypertension*, vol. vol. 16, pp. 356–362, 2003.

[23] J. Blacher and M. E. Safar, "Large-artery stiffness, hypertension and cardiovascular risk in older patients," *Nature clinical practice. Cardiovascular medicine*, vol. 2, no. 9, pp. 450–5, Oct. 2005.

[24] M. De Melis, U. Morbiducci, E. R. Rietzschel, M. De Buyzere, A. Qasem, L. Van Bortel, T. Claessens, F. M. Montevecchi, A. Avolio, and P. Segers, "Blood pressure waveform analysis by means of wavelet transform." *Medical & biological engineering & computing*, vol. 47, no. 2, pp. 165–73, Feb. 2009.

[25] T. Nagasaki, S. Yamada, Y. Wakita, Y. Imanishi, Y. Nagata, K. Okamoto, K. Yoda, M. Emoto, E. Ishimura, and M. Inaba, "Clinical utility of heart-carotid pulse wave velocity in healthy Japanese subjects," *Biomedicine & Aging Pathology*, vol. 1, no. 2, pp. 107–111, Apr. 2011.

[26] J. Blacher, R. Asmar, S. Djane, G. M. London, and M. E. Safar, "Aortic Pulse Wave Velocity as a Marker of Cardiovascular Risk in Hypertensive Patients," *Hypertension*, vol. 33, no. 5, pp. 1111–1117, May 1999.

[27] I. S. Mackenzie, I. B. Wilkinson, and J. R. Cockcroft, "Assessment of arterial stiffness in clinical practice," *QJM : monthly journal of the Association of Physicians*, vol. 95, no. 2, pp. 67–74, Mar. 2002.

[28] J. a. L. Pittman, J. S. Ping, and J. B. Mark, "Arterial and central venous pressure monitoring." *International anesthesiology clinics*, vol. 42, no. 1, pp. 13–30, Jan. 2004.

[29] P. Boutouyrie, "New techniques for assessing arterial stiffness," *Diabetes & metabolism*, vol. 34 Suppl 1, no. 2008, pp. S21–6, Mar. 2008.

[30] A. P. Avolio, L. M. Van Bortel, P. Boutouyrie, J. R. Cockcroft, C. M. McEniery, A. D. Protogerou, M. J. Roman, M. E. Safar, P. Segers, and H. Smulyan, "Role of pulse pressure amplification in arterial hypertension: experts' opinion and review of the data." *Hypertension*, vol. 54, no. 2, pp. 375–83, Aug. 2009.

[31] D. Agnoletti, Y. Zhang, P. Salvi, C. Borghi, J. Topouchian, M. E. Safar, and J. Blacher, "Pulse pressure amplification, pressure waveform calibration and clinical applications," *Atherosclerosis*, vol. 224, no. 1, pp. 108–12, Sep. 2012.

[32] A. Siebenhofer, C. Kemp, A. Sutton, and B. Williams, "The reproducibility of central aortic blood pressure measurements in healthy subjects using applanation tonometry and sphygmocardiography." *Journal of human hypertension*, vol. 13, no. 9, pp. 625–9, Sep. 1999.

[33] R. a. Payne, R. C. Hilling-Smith, D. J. Webb, S. R. Maxwell, and M. a. Denvir, "Augmentation index assessed by applanation tonometry is elevated in Marfan Syndrome." *Journal of cardiothoracic surgery*, vol. 2, p. 43, Jan. 2007.

[34] O. Istratoaie, R. Mustafa, and I. Donoiu, "Central Aortic Pressure Estimated By Radial Applanation Tonometry in Hypertensive Pulmonary Oedema," *Journal of Hypertension*, vol. 28, 2010.

[35] M. Crilly, C. Coch, M. Bruce, H. Clark, and D. Williams, "Indices of cardiovascular function derived from peripheral pulse wave analysis using radial applanation tonometry: a measurement repeatability study." *Vascular medicine (London, England)*, vol. 12, no. 3, pp. 189–97, Aug. 2007.

[36] J. E. Sharman, J. E. Davies, C. Jenkins, and T. H. Marwick, "Augmentation index, left ventricular contractility, and wave reflection." *Hypertension*, vol. 54, no. 5, pp. 1099–105, Nov. 2009.

[37] I. B. Wilkinson, H. MacCallum, L. Flint, J. R. Cockcroft, D. E. Newby, and D. J. Webb, "The influence of heart rate on augmentation index and central arterial pressure in humans," *The Journal of physiology*, vol. 525 Pt 1, pp. 263–70, May 2000.

[38] D. Chemla, A. Nitenberg, J.-L. Teboul, C. Richard, X. Monnet, H. le Clesiau, P. Valensi, and M. Brahimi, "Subendocardial viability ratio estimated by arterial tonometry: a critical evaluation in elderly hypertensive patients with increased aortic stiffness." *Clinical and experimental pharmacology & physiology*, vol. 35, no. 8, pp. 909–15, Aug. 2008.

[39] A. M. Weissler, W. S. Harris, and D. Clyde, "Systolic Time Intervals in Heart Failure in Man," *Circulation*, vol. 37, pp. 149–159, 1968.

[40] A. M. Weissler, R. G. Peeler, and W. H. Roehll Jr., "Relationships between left ventricular ejection time, stroke volume, and heart rate in normal individuals and patients with cardiovascular disease," *American Heart Journal*, vol. 62, no. 3, pp. 367–378, 1961.

[41] S. Kara, M. Okandan, G. Usta, and T. Tezcaner, "Investigation of a new heart contractility power parameter." *Computer methods and programs in biomedicine*, vol. 76, no. 2, pp. 177–80, Nov. 2004.

[42] R. S. Miller, C. B. Rudra, and M. a. Williams, "First-trimester mean arterial pressure and risk of preeclampsia." *American journal of hypertension*, vol. 20, no. 5, pp. 573–8, May 2007.

[43] C. V. Wilmer W Nichols, Michael F O'Rourke, *McDonald's Blood Flow in Arteries - Theoretical, Experimental and Clinical Principles*, H. A. Publications, Ed. CRC Press, 2005.

[44] G. L. Woolam, P. L. Schnur, C. Vallbona, and H. E. Hoff, "The pulse wave velocity as an early indicator of atherosclerosis in diabetic subjects." *Circulation*, vol. 25, pp. 533–9, Mar. 1962.

[45] R. Isnard, B. Pannier, S. Laurent, G. London, B. Diebold, and M. Safar, "Pulsatile Diameter and Elastic Modulus of the Aortic Arch in Essential Hypertension : A Noninvasive Study," *Reports on Hypertension*, vol. 13, no. 2, pp. 399–405, 1989.

[46] R. Asmar, A. Benetos, J. Topouchian, P. Laurent, B. Pannier, Anne-Marie, R. Target, and B. Levy, "Assessment of Arterial Distensibility by Automatic Pulse Wave Velocity Measurement," *Hypertension*, vol. 26, pp. 485–490, 1995.

[47] R. Asmar, A. Benetos, G. London, C. Hugue, Y. Weiss, J. Topouchian, B. Laloux, and M. Safar, "Aortic Distensibility in Normotensive, Untreated Hypertensive Patients," *Blood Pressure*, vol. 4, pp. 48–54, 1995.

[48] L. Bortolotto, M. E. Safar, E. Billaud, C. Lacroix, R. Asmar, G. M. London, and J. Blacher, "Plasma Homocysteine, Aortic Stiffness, and Renal Function in Hypertensive Patients," *Hypertension*, vol. 34, no. 4, pp. 837–842, Oct. 1999.

[49] S. Meaume, A. Benetos, O. F. Henry, A. Rudnichi, and M. E. Safar, "Aortic pulse wave velocity predicts cardiovascular mortality in subjects 70 years of age," *Arteriosclerosis, thrombosis, and vascular biology*, vol. 21, no. 12, pp. 2046–50, Dec. 2001.

[50] S. Laurent, P. Boutouyrie, R. Asmar, I. Gautier, B. Laloux, L. Guize, P. Ducimetiere, and a. Benetos, "Aortic Stiffness Is an Independent Predictor of All-Cause and Cardiovascular Mortality in Hypertensive Patients," *Hypertension*, vol. 37, no. 5, pp. 1236–1241, May 2001.

[51] P. Boutouyrie, a. I. Tropeano, R. Asmar, I. Gautier, a. Benetos, P. Lacolley, and S. Laurent, "Aortic Stiffness Is an Independent Predictor of Primary Coronary Events in Hypertensive Patients: A Longitudinal Study," *Hypertension*, vol. 39, no. 1, pp. 10–15, Jan. 2002.

[52] T. Willum-Hansen, C. Staessen, Jan Torp-Pedersen, S. Rasmussen, L. Thijs, H. Ibsen, and J. r. Jeppesen, "Prognostic value of aortic pulse wave velocity as index of arterial stiffness in the general population." *Circulation*, vol. 113, no. 5, pp. 664–70, Mar. 2006.

[53] S. J. Vermeersch, B. Dynamics, and L. Society, "Determinants of pulse wave velocity in healthy people and in the presence of cardiovascular risk factors: 'establishing normal and reference values'." *European heart journal*, vol. 31, no. 19, pp. 2338–50, Oct. 2010.

[54] J. a. Maldonado, T. Pereira, J. Polónia, J. a. Silva, J. a. Morais, and M. Marques, "Arterial stiffness predicts cardiovascular outcome in a low-to-moderate cardiovascular risk population: the EDIVA (Estudo de DIstensibilidade VAscular) project." *Journal of hypertension*, vol. 29, no. 4, pp. 669–75, Apr. 2011.

[55] J. Vappou, J. Luo, K. Okajima, M. Di Tullio, and E. Konofagou, "Aortic pulse wave velocity measured by pulse wave imaging (PWI): A comparison with applanation tonometry," *Artery Research*, vol. 5, no. 2, pp. 65–71, Jun. 2011.

[56] H. K. Hideyuki Hasegawa, Kazue Hongo, "Measurement of regional pulse wave velocity using very high frame rate ultrasound," *Journal of Medical Ultrasonics*, vol. 40, no. 2, pp. 91–98, 2013.

[57] J. P. Murgo, N. Westerhof, J. P. Giolma, and S. a. Altobelli, "Aortic input impedance in normal man: relationship to pressure wave forms," *Circulation*, vol. 62, no. 1, pp. 105–116, Jul. 1980.

[58] R. D. Latham, N. Westerhof, P. Sipkema, B. J. Rubal, P. Reuderink, and J. P. Murgo, "Regional wave travel and reflections along the human aorta: a study with six simultaneous micromanometric pressures," *Circulation*, vol. 72, no. 6, pp. 1257–1269, Dec. 1985.

[59] P. Podolec, G. Kopeć, J. Podolec, P. Wilkołek, M. Krochin, P. Rubiś, M. Cwynar, T. Grodzicki, K. Zmudka, and W. Tracz, "Aortic pulse wave velocity and carotid-femoral pulse wave velocity: similarities and discrepancies." *Hypertension research : official journal of the Japanese Society of Hypertension*, vol. 30, no. 12, pp. 1151–8, Dec. 2007.

[60] S. I. Rabben, N. Stergiopulos, L. R. Hellevik, O. a. Smiseth, S. Sløø rdahl, S. Urheim, and B. r. Angelsen, "An ultrasound-based method for determining pulse wave velocity in superficial arteries." *Journal of biomechanics*, vol. 37, no. 10, pp. 1615–22, Oct. 2004.

[61] G. L. Sorensen, J. B. Jensen, J. Udesen, and I. K. Holfort, "Pulse Wave Velocity in the Carotid Artery," *Ultrasonics Symposium, 2008. IUS 2008. IEEE*, vol. 1, no. 1, pp. 1386–1389, 2008.

[62] R. W. van der Meer, M. Diamant, J. J. M. Westenberg, J. Doornbos, J. J. Bax, A. de Roos, and H. J. Lamb, "Magnetic resonance assessment of aortic pulse wave velocity, aortic distensibility, and cardiac function in uncomplicated type 2 diabetes mellitus." *Journal of cardiovascular magnetic resonance : official journal of the Society for Cardiovascular Magnetic Resonance*, vol. 9, no. 4, pp. 645–51, Jan. 2007.

[63] P. Segers, J. Kips, B. Trachet, A. Swillens, S. Vermeersch, D. Mahieu, E. Rietzschel, M. De Buyzere, and L. Van Bortel, "Limitations and pitfalls of non-invasive measurement of arterial pressure wave reflections and pulse wave velocity," *Artery Research*, vol. 3, no. 2, pp. 79–88, Jun. 2009.

[64] P. Boutouyrie, M. Briet, C. Collin, S. Vermeersch, and B. Pannier, "Assessment of pulse wave velocity," *Artery Research*, vol. 3, no. 1, pp. 3–8, 2009.

[65] J. Calabia, P. Torguet, M. Garcia, I. Garcia, N. Martin, B. Guasch, D. Faur, and M. Vallés, "Doppler ultrasound in the measurement of pulse wave velocity: agreement with the Complior method." *Cardiovascular ultrasound*, vol. 9, p. 13, Jan. 2011.

[66] P. Salvi, G. Lio, C. Labat, E. Ricci, B. Pannier, and A. Benetos, "Validation of a new non-invasive portable tonometer for determining arterial pressure wave and pulse wave velocity: the PulsePen device." *Journal of hypertension*, vol. 22, no. 12, pp. 2285–93, Dec. 2004.

[67] M. W. Rajzer, W. Wojciechowska, M. Klocek, I. Palka, M. Brzozowska-Kiszka, and K. Kawecka-Jaszcz, "Comparison of aortic pulse wave velocity measured by three techniques: Complior, SphygmoCor and Arteriograph." *Journal of hypertension*, vol. 26, no. 10, pp. 2001–7, Oct. 2008.

[68] M. Namasivayam, B. J. McDonnell, C. M. McEniery, and M. F. O'Rourke, "Does wave reflection dominate age-related change in aortic blood pressure across the human life span?" *Hypertension*, vol. 53, no. 6, pp. 979–85, Jul. 2009.

[69] J. Baulmann, U. Schillings, S. Rickert, S. Uen, R. Düsing, M. Illyes, A. Cziraki, G. Nickering, and T. Mengden, "A new oscillometric method for assessment of arterial stiffness: comparison with tonometric and piezo-electronic methods." *Journal of hypertension*, vol. 26, no. 3, pp. 523–8, Mar. 2008.

[70] L. Joly, C. Perret-Guillaume, A. Kearney-Schwartz, P. Salvi, D. Mandry, P.-Y. Marie, G. Karcher, P. Rossignol, F. Zannad, and A. Benetos, "Pulse wave velocity assessment by external noninvasive devices and phase-contrast magnetic resonance imaging in the obese." *Hypertension*, vol. 54, no. 2, pp. 421–6, Aug. 2009.

[71] E.-S. H. Ibrahim, K. R. Johnson, A. B. Miller, J. M. Shaffer, and R. D. White, "Measuring aortic pulse wave velocity using high-field cardiovascular magnetic resonance: comparison of techniques." *Journal of Cardiovascular Magnetic Resonance*, vol. 12, no. 1, p. 26, Jan. 2010.

[72] M. F. O'Rourke and J. B. Seward, "Central arterial pressure and arterial pressure pulse: new views entering the second century after Korotkov," *Mayo Clinic proceedings. Mayo Clinic*, vol. 81, no. 8, pp. 1057–68, Aug. 2006.

[73] H. C. Pereira, T. Pereira, V. Almeida, E. Borges, E. Figueiras, J. B. Simões, J. L. Malaquias, J. a. M. R. Cardoso, and C. M. B. Correia, "Characterization of a double probe for local pulse wave velocity assessment," *Physiological measurement*, vol. 31, no. 11, pp. 1449–65, Nov. 2010.

[74] C. Pereira, J. Maldonado, T. Pereira, I. Contente, V. Almeid, B. Simões, J. a. Cardoso, and C. Correia, "A Novel and Low Cost Acoustic based Probe for Local Pulse Wave Velocity Estimation - Experimental Characterization and in-Vivo Feasibility," in *BIOSIGNALS 2013 - 6th International Conference on Bio-inspired Systems and Signal Processing, Barcelona Spain*, 2013.

[75] K. Meigas, R. Kattai, and J. Lass, "Continuous Blood Pressure Monitoring using Pulse Wave Delay," in *Engineering in Medicine and Biology Society, 23rd Annual International Conference of IEEE*, 2001, pp. 25–28.

[76] J. Hast, R. Myllyla, H. Sorvoja, and J. Miettinen, "Arterial pulse shape measurement using self-mixing effect in a diode laser," *Quantun Electronics*, vol. 32, no. 11, pp. 975–980, 2002.

[77] L. Scalise and U. Morbiducci, "Non-contact cardiac monitoring from carotid artery using optical vibrocardiography," *Medical engineering & physics*, vol. 30, no. 4, pp. 490–7, May 2008.

[78] M. De Melis, U. Morbiducci, L. Scalise, E. P. Tomasini, D. Delbeke, R. Baets, L. M. Van Bortel, and P. Segers, "A noncontact approach for the evaluation of large artery stiffness: a preliminary study," *American journal of hypertension*, vol. 21, no. 12, pp. 1280–3, Dec. 2008.

[79] Y. Li, P. Segers, J. Dirckx, and R. Baets, "On-chip laser Doppler vibrometer for arterial pulse wave velocity measurement," *Biomedical optics express*, vol. 4, no. 7, pp. 1229–35, Jul. 2013.

[80] A. Campo, P. Segers, H. Heuten, I. Goovaerts, G. Ennekens, C. Vrints, R. Baets, and J. Dirckx, "Non-invasive technique for assessment of vascular wall stiffness using laser Doppler vibrometry," *Measurement Science and Technology*, vol. 25, no. 6, p. 065701, Jun. 2014.

[81] I. Santos, "Pre-Clinical Validation Study of Optical Probes for Hemodynamic Parameters Assessment," Ph.D. dissertation, University of Coimbra, 2012.

[82] I. G. Horváth, A. Németh, Z. Lenkey, N. Alessandri, F. Tufano, P. Kis, B. Gaszner, and A. Cziráki, "Invasive validation of a new oscillometric device (Arteriograph) for measuring augmentation index, central blood pressure and aortic pulse wave velocity." *Journal of hypertension*, vol. 28, no. 10, pp. 2068–75, Oct. 2010.

[83] F. Santini, C. Palombo, C. Morizzo, E. Malshi, P. Spontoni, M. Kozakova, D. Stefano R, and A. Balbarini, "A preliminary study for the evaluation of large artery stiffness: a non contact approach," *Artery Research*, vol. 2, no. 3, pp. 100–101, Aug. 2008.

[84] H. Miyashita, "Clinical Assessment of Central Blood Pressure." *Current hypertension reviews*, vol. 8, no. 2, pp. 80–90, May 2012.

[85] S. Laurent, J. Cockcroft, L. Van Bortel, P. Boutouyrie, C. Giannattasio, D. Hayoz, B. Pannier, C. Vlachopoulos, I. Wilkinson, and H. Struijker-Boudier, "Expert consensus document on arterial stiffness: methodological issues and clinical applications." *European heart journal*, vol. 27, no. 21, pp. 2588–605, Nov. 2006.

[86] M. F. O'Rourke, J. a. Staessen, C. Vlachopoulos, D. Duprez, and G. E. Plante, "Clinical applications of arterial stiffness; definitions and reference values," *American journal of hypertension*, vol. 15, no. 5, pp. 426–44, May 2002.

[87] Silonex Inc., "Solderable Planar Photodiode SLCD-61N3 Datasheet," 2012.

[88] Advanced Photonix Inc., "Small Area Silicon Avalanche Photodiode - Datasheet," 2006.

[89] Multicomp, "High brightness visible red - Datasheet," 2012.

[90] OSRAM, "High Power Infrared Emitter (850 nm) - Datasheet," 2007.

[91] Multicomp, "Round InfraRed LED Lamp (940nm) - Datasheet," 2012.

[92] Texas Instruments, "TL081 - Datasheet," pp. 1–9, 1998.

[93] STMICROELECTRONICS, "NPN power transistors 2stn1360 - Datasheet," 2012.

[94] National Semiconductor, "LM78XX Series Voltage Regulators - Datasheet," 2000.

[95] Matsusada Precision Inc., "High Voltage Power Supplies TS Series - Datasheet," 2010.

[96] I. Moreno, C.-c. Sun, U. A. D. Fisica, and U. A. D. Zacatecas, "LED array : where does far-field begin ?" 2008.

[97] I. Moreno and C.-C. Sun, "Modeling the radiation pattern of LEDs," *Optics express*, vol. 16, no. 3, pp. 1808–19, Feb. 2008.

[98] M. Cabeleira, "Optical measurement of the Arterial Pulse Wave and determination of Pulse Wave Velocity," Ph.D. dissertation, University of Coimbra, 2010.

[99] I. Abdulhalim;, S. Millward;, G. Moores;, L. Firth;, and F. Placido, "Operation of lateral effect photosensitive position sensors using differential time delay mode," *Optical Engineering*, vol. 41, no. 12, p. 3265, Dec. 2002.

[100] G. Giuliani, S. Bozzi-pietra, and S. Donati, "Self-mixing laser diode vibrometer," *Measurement Science and Technology*, vol. 14, no. 24, pp. 24–32, 2003.

[101] J. L. Kalju Meigas , Hiie Hinrikus and R. Kattai, "Optical Self-mixing in a Diode Laser as a Method for No Touch Pulse Measurement," in *Proceedings of the Mediterranean Conference on Medical and Biological Engineering and Computing ;8th*, 1998.

[102] A. Campo, P. Segers, and A. Pwv, "Laser Doppler vibrometry for in vivo assessment of arterial stiffness," in *Medical Measurements and Applications Proceedings (MeMeA), 2011 IEEE International Workshop on*, 2011, pp. 119–121.

[103] H. D. Hong and M. D. Fox, "No touch pulse measurement by optical interferometry." *IEEE transactions on bio-medical engineering*, vol. 41, no. 11, pp. 1096–9, Nov. 1994.

[104] K. Meigas, H. Hinrikus, J. Lass, and R. Kattai, "Pulse profile registration using self-mixing in a diode laser," *Engineering In Medicine And Biology*, vol. 20, no. 4, pp. 1875–1878, 1998.

[105] L. Krehut, J. Hast, E. Alarousu, and R. Myllylä, "Low cost velocity sensor based on the self-mixing effect in a laser diode," *Opto-Electronics Review*, vol. 11, no. 4, pp. 313–319, 2003.

[106] G. Giuliani, M. Norgia, S. Donati, and T. Bosch, "Laser diode self-mixing technique for sensing applications," *Journal of Optics A: Pure and Applied Optics*, vol. 4, no. 6, 2002.

[107] L. Scalise and N. Paone, "Laser Doppler vibrometry based on self-mixing effect," *Optics and Lasers in Engineering*, vol. 38, no. 3-4, pp. 173–184, Oct. 2002.

[108] Laser Components, "AlGaInP Visible Laser Diode - Datasheet," 2005.

[109] International Commission on Non-ionizing Radiation Protection, "Revision of Guidelines on Limits of Exposure to Laser Radiation," *Health Physics*, vol. 79, no. 4, pp. 431–440, 2000.

[110] National Semiconductor, "LM337 Terminal Adjustable Negative Regulators - Datasheeet," 1999.

[111] Texas Instruments, "Ultra-Low Bias Current Difet OPA129 - Datasheet," 2007.

[112] R. Kollman and J. Betten, "Powering electronics from the USB port," p. 8, 2002.

[113] Murata Power Solutions, "NDTD 0515C - Datasheet."

[114] XP Power, "IR0512S DC/DC Converter - Datasheet," 2011.

[115] National Instruments, "NI USB-6361 Datasheet," 2012.

[116] R. Kelly and D. Fitchett, "Noninvasive determination of aortic input impedance and external left ventricular power output: a validation and repeatability study of a new technique." *Journal of the American College of Cardiology*, vol. 20, no. 4, pp. 952–963, 1992.

[117] L. M. Van Bortel, E. J. Balkestein, J. J. van der Heijden-Spek, F. H. Vanmolkot, J. a. Staessen, J. a. Kragten, J. W. Vredeveld, M. E. Safar, H. a. Struijker Boudier, and a. P. Hoeks, "Non-invasive assessment of local arterial pulse pressure: comparison of applanation tonometry and echo-tracking." *Journal of hypertension*, vol. 19, no. 6, pp. 1037–44, Jun. 2001.

[118] T. McMurray, "PEAKDETECT peak detection," 2001.

[119] S. Shah, A. Tucker, and N. Shah, "Optoelectronic blood pressure estimation: A novel principle for blood pressure measurement," in *European Society of Hypertension (ESH) 2012: 22nd European Meeting on Hypertension and Cardiovascular Protection, London, United Kingdom*, London, 2012.

[120] M. I. Oppenheim and D. F. Sittig, "An innovative dicrotic notch detection algorithm which combines rule-based logic with digital signal processing techniques." pp. 154–70, Apr. 1995.

[121] D. Korpas, J. Hálek, and L. Dolezal, "Parameters describing the pulse wave." *Physiological research / Academia Scientiarum Bohemoslovaca*, vol. 58, no. 4, pp. 473–9, Jan. 2009.

[122] J. Simek, D. Wichterle, V. Melenovský, J. Malík, S. Svacina, and J. Widimský, "Second derivative of the finger arterial pressure waveform: an insight into dynamics of the peripheral arterial pressure pulse." *Physiological research / Academia Scientiarum Bohemoslovaca*, vol. 54, no. 5, pp. 505–13, Jan. 2005.

[123] J. Sugawara, K. Hayashi, and H. Tanaka, "Distal Shift of Arterial Pressure Wave Reflection Sites with Aging," *Hypertension*, vol. 56, no. 5, pp. 920–925, 2010.

[124] S. C. Millasseau, J. M. Ritter, K. Takazawa, and P. J. Chowienczyk, "Contour analysis of the photoplethysmographic pulse measured at the finger," *Journal of hypertension*, vol. 24, no. 8, pp. 1449–56, Aug. 2006.

[125] E. Kazanavicius, R. Gircys, and S. Lugin, "Mathematical Methods for Determing the Foot Point of the Arterial Pulse Wave and Evaluation of Proposed Methods," *ISSN 1392 – 124X Information Technology and Control*, vol. 34, no. 1, pp. 29–36, 2005.

[126] M.-Y. Rhee, H.-Y. Lee, and J. B. Park, "Measurements of Arterial Stiffness: Methodological Aspects," *Korean Circulation Journal*, vol. 38, no. 7, p. 343, 2008.

[127] N. R. Gaddum, J. Alastruey, P. Beerbaum, P. Chowienczyk, and T. Schaeffter, "A Technical Assessment of Pulse Wave Velocity Algorithms Applied to Non-invasive Arterial Waveforms." *Annals of biomedical engineering*, Jul. 2013.

[128] Mathworks, "xcorr Function."

[129] S. W. Fielden, B. K. Fornwalt, M. Jerosch-Herold, R. L. Eisner, A. E. Stillman, and J. N. Oshinski, "A new method for the determination of aortic pulse wave velocity using cross-correlation on 2D PCMR velocity data." *Journal of magnetic resonance imaging : JMRI*, vol. 27, no. 6, pp. 1382–7, Jun. 2008.

[130] H. So, "A Comparative Study of Two Discrete-Time Phase Delay Estimators," *IEEE Transactions on Instrumentation and Measurement*, vol. 54, no. 6, pp. 2501–2504, Dec. 2005.

[131] S. W. Smith, *The Scientist and Engineer's Guide to Digital Signal Processing.* San Diego, California: California Technical Publishing, 199.

[132] E. Gallego-jutglà and J. Solé-casals, "Exploring mEMD for face recognition," in *Proc. 5h International Joint Conference on Biomedical Engineering Systems and Technologies*, 2012, pp. 498–503.

[133] Y. Hai, C. Wei, and Z. Hong, "TVAR Time-frequency Analysis for Non-stationary Vibration Signals of Spacecraft," *Chinese Journal of Aeronautics*, vol. 21, no. 5, pp. 423–432, Oct. 2008.

[134] A. O. Andrade, S. Nasuto, P. Kyberd, C. M. Sweeney-Reed, and F. Van Kanijn, "EMG signal filtering based on Empirical Mode Decomposition," *Biomedical Signal Processing and Control*, vol. 1, no. 1, pp. 44–55, Jan. 2006.

[135] C. Qing, "Empirical mode decomposition-based facial pose estimation inside video sequences," *Optical Engineering*, vol. 49, no. 3, p. 037401, Mar. 2010.

[136] T. Oliveira, "Construction of Optical Probes for Arterial Pulse Wave Assessment," Ph.D. dissertation, University of Coimbra, 2011.

[137] T. Instruments, "CMOS Counter/Dividers CD4022B," 2004.

[138] F. Sensor, "PSD Data Sheet," pp. 6–7, 2011.

[139] R. Johnson and C. Lentz, "2-D Optical Position Sensor," *Magazine for Computer Applications*, no. 152, pp. 1–7, 2003.

[140] V. Chan and A. Perlas, *Atlas of Ultrasound-Guided Procedures in Interventional Pain Management*, S. N. Narouze, Ed. New York, NY: Springer New York, 2011.

[141] G. E. Healthcare, "Vivid e Cardiovascular ultrasound system," GE Healthcare, Wauwatosa U.S.A., Tech. Rep., 2011.

[142] U. Mahmood and R. Weissleder, "Near-Infrared Optical Imaging of Proteases in Cancer," *Molecular Cancer Therapeutics*, vol. 2, no. 5, pp. 489–496, 2003.

[143] C. S. P. Andrew Nicolaides, Kirk W. Beach, Efthivoulos Kyriacou, *Ultrasound and Carotid Bifurcation Atherosclerosis*, S. London, Ed. Springer, 2012.

[144] V. Kamat, "Pulse oximetry," *Indian Journal of Anaesthesia*, vol. 46, no. 4, pp. 261–268, 2002.

[145] P. V. D. Zee, "Measurement and Modelling of the Optical Properties of Human Tissue in the wavelength range from 400 to 2000 nm," Doctoral Thesis, University College London, 1992.

[146] A. N. Bashkatov, E. A. Genina, V. I. Kochubey, and V. V. Tuchin, "Optical properties of human skin, subcutaneous and mucous tissues in the wavelength range from 400 to 2000 nm," *Journal of Physics D: Applied Physics*, vol. 38, no. 15, pp. 2543–2555, Aug. 2005.

[147] A. Gherardi, "A Skin Surface Characterization System Based on Capacitive Image Analysis," Doctoral Thesis, University of Bologna, 2007.

[148] J. V. DeGroot, A. Norris, S. O. Glover, and T. V. Clapp, "Highly transparent silicone materials," in *Proc. SPIE 5517, Linear and Nonlinear Optics of Organic Materials IV*, R. A. Norwood, M. Eich, and M. G. Kuzyk, Eds., vol. 5517, Oct. 2004, pp. 116–123.

[149] R. Riegler, Bill; Bruner, Stephen J.; Elgin, "Optical silicones for use in harsh operating environments," in *Sensors for Harsh Environments. Proceedings of the SPIE*, 2004, pp. 140–151.

[150] I. P. Herman, *Physics of the Human Body (Biological and Medical Physics, Biomedical Engineering)*. Springer, 2007.

[151] S. R. Alty, N. Angarita-jaimes, S. C. Millasseau, and P. J. Chowienczyk, "Predicting Arterial Stiffness From the Digital Volume Pulse Waveform," *Biomedical Engineering, IEEE Transactions on*, vol. 54, no. 12, pp. 2268–2275, 2007.

[152] J. M. Moguerza and A. Muñoz, "Support Vector Machines with Applications," *Statistical Science*, vol. 21, no. 3, pp. 322–336, Aug. 2006.

[153] G. Garg, V. Singh, M. Grover, and J. R. P. Gupta, "Review article Optimal Kernel Learning for EEG based Sleep Scoring System," *International Journal of Biological & Medical Research*, vol. 2, no. 4, pp. 1220–1225, 2011.

[154] W. Campbell, J. Campbell, D. Reynolds, E. Singer, and P. Torres-Carrasquillo, "Support vector machines for speaker and language recognition," *Computer Speech & Language*, vol. 20, no. 2-3, pp. 210–229, Apr. 2006.

[155] K. Beyer, J. Goldstein, R. Ramakrishnan, and U. Shaft, "When is Nearest Neighbor meaningful," in *'99 Proceedings of the 7th International Conference on Database Theory*, 1999, pp. 217–235.

[156] S. Karimifard and A. Ahmadian, "A robust method for diagnosis of morphological arrhythmias based on Hermitian model of higher-order statistics." *Biomedical engineering online*, vol. 10, no. 1, p. 22, Jan. 2011.

[157] S. Bhattacharyya, A. Khasnobish, S. Chatterjee, and A. Konar, "Performance Analysis of LDA , QDA and KNN Algorithms in Left-Right Limb Movement Classification from EEG Data," in *Systems in Medicine and Biology (ICSMB), 2010 International Conference on*, no. December, 2010, pp. 126–131.

[158] G. S. Nayak, "Classification of ECG Signals using ANN with Resilient Back Propagation Algorithm," *International Journal of Computer Applications*, vol. 54, no. 6, pp. 20–23, 2012.

[159] D. Álvarez, R. Hornero, J. V. Marcos, and F. Del Campo, "Feature selection from nocturnal oximetry using genetic algorithms to assist in obstructive sleep apnoea diagnosis," *Medical Engineering & Physics*, vol. 34, no. 8, pp. 1049–57, Oct. 2012.

[160] P. F. Diez, V. Mut, E. Laciar, A. Torres, and E. Avila, "Application of the empirical mode decomposition to the extraction of features from EEG signals for mental task classification." *Conference proceedings : ... Annual International Conference of the IEEE Engineering in Medicine and Biology Society. IEEE Engineering in Medicine and Biology Society. Conference*, vol. 2009, pp. 2579–82, Jan. 2009.

[161] J. Lee and R. G. Mark, "An investigation of patterns in hemodynamic data indicative of impending hypotension in intensive care," *Biomedical engineering online*, vol. 9, no. 1, p. 62, Jan. 2010.

[162] T. Weber, J. Auer, M. F. O'Rourke, E. Kvas, E. Lassnig, R. Berent, and B. Eber, "Arterial stiffness, wave reflections, and the risk of coronary artery disease." *Circulation*, vol. 109, no. 2, pp. 184–9, Jan. 2004.

[163] J. Kips, F. Vanmolkot, D. Mahieu, S. Vermeersch, I. Fabry, J. de Hoon, L. Van Bortel, and P. Segers, "The use of diameter distension waveforms as an alternative for tonometric pressure to assess carotid blood pressure." *Physiological measurement*, vol. 31, no. 4, pp. 543–53, Apr. 2010.

[164] A. Pachauri and M. Bhuyan, "Wavelet Transform Based Arterial Blood Pressure Waveform Delineator," *INTERNATIONAL JOURNAL OF BIOLOGY AND BIOMEDICAL ENGINEERING*, vol. 6, no. 1, 2012.

[165] N. Zajarevich, D. Bia, F. Pessana, J. Codnia, and R. Armentano, "Arterial pressure and diameter waveforms analysis by means of wavelet transform: application to artery de-endothelization." *Conference proceedings : ... Annual International Conference of the IEEE Engineering in Medicine and Biology Society. IEEE Engineering in Medicine and Biology Society. Conference*, vol. 2010, pp. 4550–3, Jan. 2010.

[166] W. He, S. Li, H. Xiao, C. Yu, and H. Lin, "An Arterial Elasticity Index Algorithm Based on Wavelet Transform and Curve Fitting," *Journal of Information & Computational Science*, vol. 9, no. 12, pp. 3379–3389, 2012.

[167] J. Janney and S. Sruthi.P, "Dicrotic Notch Detection and Analysis of Arterial Pulse by using Discrete Wavelet," *OSIET journal of Communication & Electronics*, vol. 4, no. May, p. 2012, 2012.

[168] J. P. Marques, *Pattern Recognition: concepts, methods, and applications*, 1st ed. Springer Verlag, 2001.

[169] Y. Liu and Y. F. Zheng, "FS_SFS: A novel feature selection method for support vector machines," *Pattern Recognition*, vol. 39, no. 7, pp. 1333–1345, Jul. 2006.

[170] X. Wang and J. Tian, "A gene selection method for cancer classification." *Computational and mathematical methods in medicine*, vol. 2012, p. 586246, Jan. 2012.

[171] S. Maldonado and R. Weber, "A wrapper method for feature selection using Support Vector Machines," *Information Sciences*, vol. 179, no. 13, pp. 2208–2217, Jun. 2009.

[172] J. Bedo, C. Sanderson, and A. Kowalczyk, "An Efficient Alternative to SVM Based Recursive Feature Elimination with Applications Bioinformatics," in *AI 2006: Advances in Artificial Intelligence*, 2006, pp. 170–180.

[173] F. S. Jason Weston, Andre Elisseeff , Gökhan BakIr, "The Spider."

[174] F. Lotte, M. Congedo, a. Lécuyer, F. Lamarche, and B. Arnaldi, "A review of classification algorithms for EEG-based brain-computer interfaces." *Journal of neural engineering*, vol. 4, no. 2, pp. R1–R13, Jun. 2007.

[175] T. Frontzek, T. N. Lal, R. Eckmiller, D. Bonn, and F. R. Germany, "Predicting the Nonlinear Dynamics of Biological Neurons using Support Vector Machines with Di erent Kernels," in *Neural Networks, 2001. Proceedings. IJCNN '01. International Joint Conference on*, 2001, pp. 1492 – 1497 vol.2.

[176] J. S. Raikwal and K. Saxena, "Performance Evaluation of SVM and K-Nearest Neighbor Algorithm over Medical Data set," *International Journal of Computer Applications*, vol. 50, no. 14, pp. 35–39, 2012.

[177] M. I. Schlesinger and V. Hlavac, "Statistical Pattern Recognition Toolbox."

[178] R. Kohavi, "A Study of Cross-Validation and Bootstrap for Accuracy Estimation and Model Selection," in *IJCAI'95 Proceedings of the 14th international joint conference on Artificial intelligence*, 1995, pp. 1137–1143.

[179] B. Wu, T. Abbott, D. Fishman, W. McMurray, G. Mor, K. Stone, D. Ward, K. Williams, and H. Zhao, "Comparison of statistical methods for classification of ovarian cancer using mass spectrometry data," *Bioinformatics (Oxford, England)*, vol. 19, no. 13, pp. 1636–43, Sep. 2003.

[180] T. M. Huang and V. Kecman, "Gene Extraction for Cancer Diagnosis by Support Vector Machines An Improvement and Comparison with Nearest," *Artificial Intelligence in Medicine*, vol. 35, no. 1-2, pp. 185–194, 2005.

[181] J. C. V. Gemert, C. G. M. Snoek, C. J. Veenman, and A. W. M. Smeulders, "The Influence of Cross-Validation on Video Classification Performance Categories and Subject Descriptors," in *Proceedings of the 14th annual ACM international conference on Multimedia*, 2006, pp. 695–698.

[182] A. Jain and R. Duin, "Statistical Pattern Recognition: A Review," *Pattern Analysis and Machine Intelligence, IEEE Transactions on*, vol. 22, no. 2, pp. 4–37, 2000.

[183] P. Vaz, "Design of an Optical Probe Based on Coherent Light to Assess Hemodynamic Parameters," Ph.D. dissertation, University of Coimbra, 2012.

[184] R. Cunha, A. Benetos, S. Laurent, M. E. Safar, and R. Asmar, "Distension Capacity of the Carotid Artery and Ambulatory Blood Pressure Monitoring," *American Journal of Hypertension*, vol. 8, pp. 343–352, 1995.

[185] D. Guo and M. Wang, "Self-mixing interferometer based on temporal-carrier phase-shifting technique for micro-displacement reconstruction," *Optics Communications*, vol. 263, no. 1, pp. 91–97, Jul. 2006.

[186] M. Wang, "Self-mixing microscopic interferometer for the measurement of microprofile," *Optics Communications*, vol. 238, no. 4-6, pp. 237–244, 2004.

[187] F. J. van Ittersum, M. T. Schram, J. J. van der Heijden-Spek, L. M. a. B. Van Bortel, J. W. F. Elte, P. Biemond, J. a. Staessen, a. J. M. Donker, and C. D. a. Stehouwer, "Autonomic nervous function, arterial stiffness and blood pressure in patients with Type I diabetes mellitus and normal urinary albumin excretion." *Journal of human hypertension*, vol. 18, no. 11, pp. 761–8, Nov. 2004.

[188] L. Scalise, Y. Yu, G. Giuliani, G. Plantier, and T. Bosch, "Self-Mixing Laser Diode Velocimetry: Application to Vibration and Velocity Measurement," *IEEE Transactions on Instrumentation and Measurement*, vol. 53, no. 1, pp. 223–232, Feb. 2004.

[189] R. Wunenburger, N. Mujica, and S. Fauve, "Experimental study of the Doppler shift generated by a vibrating scatterer," *The Journal of the Acoustical Society of America*, vol. 115, no. 2, p. 507, 2004.

[190] T. Bosch, "Optical feedback interferometry for sensing application," *Optical Engineering*, vol. 40, no. 1, p. 20, Jan. 2001.

[191] M. Laroche, L. Kervevan, H. Gilles, S. Girard, and J. K. Sahu, "Doppler velocimetry using self-mixing effect in a short Er–Yb-doped phosphate glass fiber laser," *Applied Physics B*, vol. 80, no. 4-5, pp. 603–607, Mar. 2005.

[192] M. Olfatnia, V. R. Singh, T. Xu, J. M. Miao, and L. S. Ong, "Analysis of the vibration modes of piezoelectric circular microdiaphragms," *Journal of Micromechanics and Microengineering*, vol. 20, no. 8, p. 085013, Aug. 2010.

[193] E. Borges, M. Sequeira, A. F. V. Cortez, H. C. Pereira, T. Pereira, V. Almeida, T. M. Vasconcelos, I. M. Duarte, N. Nazaré, J. Cardoso, and C. Correia, "Bioimpedance Parameters as a Risk Factor to Assess Pine Decay An Innovative Approach to the Diagnosis of Plant Diseases," in *BIOSIGNALS 2013 - 6th International Conference on Bio-inspired Systems and Signal Processing, Angers, France*, 2013.

[194] T. Jin, A. Takita, M. Djamal, W. Hou, H. Jia, and Y. Fujii, "A method for evaluating the electro-mechanical characteristics of piezoelectric actuators during motion." *Sensors (Basel, Switzerland)*, vol. 12, no. 9, pp. 11 559–70, Jan. 2012.

[195] J. Václavík, "Measurement of mechanical and electrical energy ows in the semi-active piezoelectric shunt damping system," *J. Intell. Mater. Syst. Struct.*, vol. 23, no. March, pp. 1–7, 2012.

[196] E. Hermeling, A. P. G. Hoeks, M. H. M. Winkens, J. L. Waltenberger, R. S. Reneman, A. a. Kroon, and K. D. Reesink, "Noninvasive assessment of arterial stiffness should discriminate between systolic and diastolic pressure ranges." *Hypertension*, vol. 55, no. 1, pp. 124–30, Jan. 2010.

[197] S. C. Millasseau, A. D. Stewart, S. J. Patel, S. R. Redwood, and P. J. Chowienczyk, "Evaluation of carotid-femoral pulse wave velocity: influence of timing algorithm and heart rate." *Hypertension*, vol. 45, no. 2, pp. 222–6, Feb. 2005.

[198] M. M. Shoukri, D. Colak, N. Kaya, and A. Donner, "Comparison of two dependent within subject coefficients of variation to evaluate the reproducibility of measurement devices." *BMC medical research methodology*, vol. 8, p. 24, Jan. 2008.

[199] A. D. Protogerou, T. G. Papaioannou, P. P. Sfikakis, J. Blacher, E. Karatzis, J. P. Lekakis, D. Papadogiannis, C. Stefanadis, and M. E. Safar, "Differences in pulse pressure day variability between the brachial artery and the aorta in healthy subjects," *Artery Research*, vol. 6, no. 1, pp. 34–40, Mar. 2012.

[200] S. Söderström, G. Nyberg, M. F. O'Rourke, J. Sellgren, and J. Pontén, "Can a clinically useful aortic pressure wave be derived from a radial pressure wave?" *British journal of anaesthesia*, vol. 88, no. 4, pp. 481–8, Apr. 2002.

[201] J. Vappou, J. Luo, K. Okajima, M. Di Tullio, and E. E. Konofagou, "Non-invasive measurement of local pulse pressure by pulse wave-based ultrasound manometry (PWUM)," *Physiological measurement*, vol. 32, no. 10, pp. 1653–62, Oct. 2011.

[202] M. Frimodt-Moller, A. H. Nielsen, A.-L. Kamper, and S. Strandgaard, "Reproducibility of pulse-wave analysis and pulse-wave velocity determination in chronic kidney disease." *Nephrology, dialysis, transplantation : official publication of the European Dialysis and Transplant Association - European Renal Association*, vol. 23, no. 2, pp. 594–600, Feb. 2008.

[203] N. B. Lee and C. G. Park, "Reproducibility of regional pulse wave velocity in healthy subjects." *The Korean journal of internal medicine*, vol. 24, no. 1, pp. 19–23, Mar. 2009.

[204] A. M. Euser, F. W. Dekker, and S. le Cessie, "A practical approach to Bland-Altman plots and variation coefficients for log transformed variables." *Journal of clinical epidemiology*, vol. 61, no. 10, pp. 978–82, Oct. 2008.

[205] F. H. M. Vanmolkot and J. N. J. M. de Hoon, "Reproducibility of forearm vasodilator response to intra-arterial infusion of calcitonin gene-related peptide assessed by venous occlusion plethysmography." *British journal of clinical pharmacology*, vol. 59, no. 4, pp. 387–97, Apr. 2005.

[206] J. W. Bartlett and C. Frost, "Reliability, repeatability and reproducibility: analysis of measurement errors in continuous variables." *Ultrasound in obstetrics & gynecology : the official journal of the International Society of Ultrasound in Obstetrics and Gynecology*, vol. 31, no. 4, pp. 466–75, Apr. 2008.

[207] J. Rochon, M. Gondan, and M. Kieser, "To test or not to test: Preliminary assessment of normality when comparing two independent samples." *BMC medical research methodology*, vol. 12, p. 81, Jan. 2012.

[208] F. Fantin, A. Mattocks, C. J. Bulpitt, W. Banya, and C. Rajkumar, "Is augmentation index a good measure of vascular stiffness in the elderly?" *Age and ageing*, vol. 36, no. 1, pp. 43–8, Jan. 2007.

[209] V. Almeida, J. a. Vieira, P. Santos, T. Pereira, H. Pereira, C. Correia, M. Pego, and J. a. Cardoso, "Machine Learning Techniques for Arterial Pressure Waveform Analysis," *Journal of Personalized Medicine*, vol. 3, no. 2, pp. 82–101, May 2013.

[210] N. a. Jatoi, P. Jerrard-Dunne, J. Feely, and A. Mahmud, "Impact of smoking and smoking cessation on arterial stiffness and aortic wave reflection in hypertension." *Hypertension*, vol. 49, no. 5, pp. 981–5, May 2007.

[211] J. M. Padilla, E. J. Berjano, J. Sáiz, L. Fácila, P. Díaz, S. Mercé, I. T. D. Morelia, H. P. D. Castellón, and M. V. Electromedicina, "Assessment of Relationships between Blood Pressure , Pulse Wave Velocity and Digital Volume Pulse," *Computers in Cardiology*, vol. 33, pp. 893–896, 2006.

[212] C. M. McEniery, Yasmin, B. McDonnell, M. Munnery, S. M. Wallace, C. V. Rowe, J. R. Cockcroft, and I. B. Wilkinson, "Central pressure: variability and impact of cardiovascular risk factors: the Anglo-Cardiff Collaborative Trial II." *Hypertension*, vol. 51, no. 6, pp. 1476–82, Jun. 2008.

[213] J. M. Meinders and A. P. G. Hoeks, "Simultaneous assessment of diameter and pressure waveforms in the carotid artery." *Ultrasound in medicine & biology*, vol. 30, no. 2, pp. 147–54, Feb. 2004.

[214] J. D. S. Thierry C. Gillebert, Nico Van de Veire, Marc L. De Buyzere, "Time intervals and global cardiac function. Use and limitations," *European heart journal*, no. 25, pp. 2185–2186, Dec. 2004.

[215] P. Mangell, T. Länne, B. Sonesson, F. Hansen, and D. Bergqvist, "Regional differences in mechanical properties between major arteries–an experimental

study in sheep." *European journal of vascular and endovascular surgery : the official journal of the European Society for Vascular Surgery*, vol. 12, no. 2, pp. 189–95, Aug. 1996.

[216] C. Giannattasio, P. Salvi, F. Valbusa, A. Kearney-Schwartz, A. Capra, M. Amigoni, M. Failla, L. Boffi, F. Madotto, A. Benetos, and G. Mancia, "Simultaneous measurement of beat-to-beat carotid diameter and pressure changes to assess arterial mechanical properties." *Hypertension*, vol. 52, no. 5, pp. 896–902, Nov. 2008.

[217] C. Stefanadis, J. Dernellis, M. Vavuranakis, E. Tsiamis, C. Vlachopoulos, K. Toutouzas, L. Diamandopoulos, C. Pitsavos, and P. Toutouzas, "Effects of ventricular pacing-induced tachycardia on aortic mechanics in man," *Cardiovascular research*, vol. 39, no. 2, pp. 506–14, Aug. 1998.

[218] X. Monnet, N. Anguel, M. Jozwiak, C. Richard, and J.-L. Teboul, "Third-generation FloTrac/Vigileo does not reliably track changes in cardiac output induced by norepinephrine in critically ill patients." *British journal of anaesthesia*, vol. 108, no. 4, pp. 615–22, Apr. 2012.

[219] R. J. Moene, G. a. Mook, K. Kruizinga, A. Bergstra, and K. K. Bossina, "Value of systolic time intervals in assessing severity of congenital aortic stenosis in children," *British heart journal*, vol. 37, no. 11, pp. 1113–22, Nov. 1975.

[220] D. S. Liebeskind, "Collateral circulation," *Stroke; a journal of cerebral circulation*, vol. 34, no. 9, pp. 2279–84, Sep. 2003.

[221] H. Furst, W. H. Hartl, and I. Janssen, "Patterns of cerebrovascular reactivity in patients with unilateral asymptomatic carotid artery stenosis," *Stroke*, vol. 25, no. 6, pp. 1193–1200, Jun. 1994.

[222] J. R. Romero, A. Pikula, T. N. Nguyen, Y. L. Nien, A. Norbash, and V. L. Babikian, "Cerebral collateral circulation in carotid artery disease." *Current cardiology reviews*, vol. 5, no. 4, pp. 279–88, Nov. 2009.

[223] R. Seeley, P. Tate, and T. D. Stephens, *Anatomy & Physiology*, 5th ed. McGraw-Hill Higher Education, 2000.

[224] R. a. Bucek, M. Reiter, A. Dirisamer, M. Haumer, A. Fritz, E. Minar, and J. Lammer, "Three-dimensional color Doppler sonography in carotid artery stenosis." *AJNR. American journal of neuroradiology*, vol. 24, no. 7, pp. 1294–9, Aug. 2003.

[225] M. Koga, K. Kimura, K. Minematsu, and T. Yamaguchi, "Diagnosis of internal carotid artery stenosis greater than 70% with power Doppler duplex sonography." *AJNR. American journal of neuroradiology*, vol. 22, no. 2, pp. 413–7, Feb. 2001.